

# **VORTEX INTERACTION IN FLOWS OVER BLUFF BODIES**

by

**Richard H. Mills, B.Sc, B.E. (Hons)**

**A thesis submitted for the degree of Doctor of Philosophy**

**on 28 January 1998**

**Department of Mechanical Engineering**

**Monash University**

**Clayton**

**Australia**



# Table of Contents

<b>ACKNOWLEDGMENTS</b> .....	v
<b>STATEMENT OF ORIGINALITY</b> .....	vii
<b>ABSTRACT</b> .....	ix
<b>NOMENCLATURE</b> .....	xi
<b>1 INTRODUCTION</b> .....	<b>1</b>
1.1 PREVIOUS RESEARCH AT THE CSIRO DBCE .....	1
1.1 OBJECTIVE OF THE OVERALL RESEARCH PROGRAM .....	2
<b>2 LITERATURE REVIEW</b> .....	<b>3</b>
2.1 BLUFF BODY AERODYNAMICS .....	3
2.1.1 Vortex Shedding .....	3
2.2 FLOW INSTABILITIES .....	4
2.2.1 Control of flow instabilities .....	6
2.3 FLOWS AROUND RECTANGULAR PRISMS .....	8
2.3.1 Effect of $c/t$ on shear layer development and $C_d$ .....	9
2.3.2 Reynolds number effects on separation bubbles .....	10
2.3.3 Effect of free stream turbulence .....	12
2.4 VORTEX SHEDDING FROM RECTANGULAR PRISMS .....	14
2.4.1 Impinging Leading Edge Vortex (ILEV) instability .....	17
2.5 THE EFFECT OF PERIODIC FLOW DISTURBANCES ON BLUFF BODY FLOWS .....	23
2.5.1 Forced oscillations of bluff bodies .....	24
2.5.2 Acoustic resonance associated with vortex shedding .....	29
2.5.3 The effect of external velocity perturbations on vortex shedding .....	36
<b>3 EXPERIMENTAL APPARATUS AND METHOD</b> .....	<b>41</b>
3.1 OPEN JET WIND TUNNEL .....	41
3.1.1 Tunnel Design .....	41
3.1.2 Tunnel Characteristics .....	43
3.1.2.1 Velocity Profile .....	43
3.1.2.2 Longitudinal Turbulence Intensity .....	44
3.1.3 Experimental Instrumentation and Models .....	46
3.1.3.1 Data Acquisition and Processing .....	46
3.1.3.2 Pressure and Velocity Measurement .....	47
3.1.3.3 Hot Wire Anemometer .....	50
3.1.3.4 Wind Tunnel Models .....	51
3.1.3.5 Smoke Wire .....	52
3.1.4 Transverse Velocity Perturbation .....	54
3.1.4.1 Signal Generator, Amplifier and Speakers .....	54
3.1.4.2 Measurement of Transverse Perturbation using LDV .....	55
3.2 WATER TUNNEL .....	57
3.2.1 Tunnel Design .....	57
3.2.2 Tunnel Characteristics .....	60
3.2.3 Water Tunnel Models .....	60
3.3 PARTICLE IMAGE VELOCIMETRY (PIV) .....	61
3.3.1 Flow seeding and illumination .....	62
3.3.2 Image acquisition .....	64
3.3.3 Bias Velocity mirror .....	65

3.3.4	Image Processing .....	66
3.3.4.1	Interrogation window size and local velocity gradient.....	66
3.3.4.2	Interrogation grid spacing.....	67
3.3.4.3	Autocorrelation technique.....	68
3.3.5	Post Processing .....	68
3.3.5.1	Data spatial filtering.....	68
3.3.5.2	Vorticity calculation.....	69
3.3.5.3	Calculation of circulation of vortex structures.....	70
3.3.5.4	Generation of velocity vector plots and vorticity contour plots.....	71
3.3.6	Flow Visualisation.....	72
<b>4</b>	<b>RESULTS AND DISCUSSION .....</b>	<b>73</b>
4.1	PLATES WITH NO LEADING EDGE VORTEX SHEDDING .....	73
4.1.1	Surface pressure measurements.....	73
4.1.1.1	Effect of transverse velocity perturbations upon $C_{p_b}$ .....	75
4.1.1.2	Effect of varying perturbation level.....	77
4.1.1.3	Effect of higher frequency perturbations .....	77
4.1.2	Particle image velocimetry measurements.....	79
4.1.2.1	No transverse velocity perturbations .....	79
4.1.2.2	Transverse velocity perturbations applied.....	84
4.1.2.3	Relationship between circulation and base pressure.....	89
4.1.3	Three dimensional effects .....	92
4.2	PLATES WITH RECTANGULAR LEADING AND TRAILING EDGES .....	95
4.2.1	Surface pressure measurements and smoke wire flow visualisation.....	95
4.2.1.1	Effect of transverse velocity perturbations .....	98
4.2.1.2	Effect of plate length on variation of $C_{p_b}$ in response to perturbations .....	105
4.2.1.3	Effect of perturbation level on $C_{p_b}$ .....	114
4.2.1.4	Effect of Reynolds number on $C_{p_b}$ .....	120
4.2.2	Particle image velocimetry (PIV) results and flow visualisation .....	126
4.2.2.1	Natural vortex shedding (no perturbations applied).....	126
4.2.2.2	Transverse velocity perturbations applied at natural ILEV frequencies.....	133
4.2.2.3	Transverse velocity perturbations applied at non ILEV frequencies .....	145
4.2.3	Reconciling the experiments of Nakamura <i>et al.</i> (1991) and Stokes & Welsh (1986) .....	154
4.2.4	Similarity in vortex shedding $St$ for three seemingly independent experiments .....	159
<b>5</b>	<b>CONCLUSIONS .....</b>	<b>163</b>
5.1	SUMMARY .....	163
5.1.1	Plates without leading edge vortex shedding.....	163
5.1.1.1	Natural vortex shedding.....	163
5.1.1.2	Effect of transverse velocity perturbations .....	163
5.1.2	Plates with rectangular leading edges.....	164
5.1.2.1	Natural vortex shedding.....	164
5.1.2.2	Effect of transverse velocity perturbations .....	165
5.1.2.3	Reconciling the experiments of Nakamura <i>et al.</i> (1991) and Stokes & Welsh (1986) .....	167
5.1.2.4	Similarity in vortex shedding $St$ for three seemingly independent experiments.....	167
5.2	RECOMMENDED FUTURE STUDIES .....	168
<b>6</b>	<b>BIBLIOGRAPHY .....</b>	<b>171</b>
<b>7</b>	<b>APPENDICES.....</b>	<b>177</b>
APPENDIX 1	ESTIMATION OF UNCERTAINTIES .....	177
APPENDIX 2	PUBLICATIONS ARISING FROM THIS STUDY .....	191

## **Acknowledgments**

I wish to thank my supervisor Associate Professor John Sheridan for his guidance, encouragement & support, for assisting me to present at conferences, and for help with publications. My associate supervisor Associate Professor Kerry Hourigan also provided invaluable support, enthusiasm and positive input to the project, especially while he was with the CSIRO Building, Construction and Engineering (BCE) division.

Special thanks also goes to Mr Martin Welsh, formerly of the CSIRO BCE, for making the experimental facilities at CSIRO BCE available - without which this project would not have been possible. I am also extremely grateful to Dr Jie Wu, also from CSIRO BCE, who provided frequent assistance in the laboratory, as well as many helpful discussions.

I thank the many CSIRO Staff:

Mr Brook Dunstan, Ms Tracey Nicholls, Ms Marie Bond and Neil Hamilton for assistance with film processing, production of figures and overheads, and the production of videos.

Mr Graeme Flood, Mr Laurie Welch, Mr Ron Downie, Mr Tony Kilpatrick, Mr Ross Hamilton and Dr Peter Cooper for technical assistance in the laboratory.

Mr Ron Maxtead, Mr Jim Tynan and the other staff in the engineering workshop for the construction of most of the experimental apparatus used in the project.

Technical support was also provided by the Monash University Mechanical Engineering workshop.

I would like to thank Mr John Easton, Mr GOH Long Kim, Mr Wes Eadon, Mr Andrew McCluskey and Mr Mark Symonds (electronics) for their help.

Financial support in the form of an Australian Post Graduate Research Scholarship (APRA) is acknowledged.

I thank the following people for many useful discussions; Dr Moses Khor, Dr Julio Soria, Dr Mark Thompson and Dr Lachlan Graham.

Finally, this project would not have been possible without the support and encouragement of my family. In particular, I thank my parents for the many hours sacrificed to proof reading the manuscript, usually at short notice.

## **Statement of Originality**

To the best knowledge of the candidate, neither this thesis, nor any part of it, has been or is being concurrently submitted in candidature for any degree at this or at any other University.

---

Richard Howard Mills

19 March 2007



## Abstract

The flow over long rectangular prisms of various chord to thickness ( $c/t$ ) ratios has been investigated. The effect of periodic transverse velocity perturbations on the base pressure was investigated in the wind tunnel. Particle Image Velocimetry (PIV) experiments and flow visualisation were performed in the water tunnel to provide insight into the mechanism controlling vortex shedding from rectangular plates in the presence of transverse velocity perturbations. Particular interest was paid to vortex shedding from the trailing edge.

At low  $Re$ , vortex shedding from rectangular plates occurs naturally, but the frequency of shedding is strongly dependent on the  $c/t$  ratio. In the presence of sinusoidal transverse velocity perturbations, maximum base suction for plates with different  $c/t$  ratios was found to occur at frequencies corresponding to the natural vortex shedding frequency measured at low  $Re$  for each  $c/t$  ratio. While leading edge vortex shedding can be phase-locked to perturbations over a wide range of frequencies, PIV results and flow visualisation showed that vortex shedding at the trailing edge can only be phase-locked when the perturbation frequency was close to the natural shedding frequency. When this occurred, complex vortex interactions between vortices shed from the leading and trailing edges were observed in the near wake.

Since the convection velocity of vortices shed from the leading edge (L vortices) is independent of  $c/t$  ratio, the number of perturbation cycles, for a L vortex to be convected to the trailing edge depends on both the perturbation frequency and the plate  $c/t$  ratio. PIV results and flow visualisation showed that the phase in the perturbation cycle that L vortices pass the trailing edge determines whether strong vortex shedding occurred at the trailing edge.



## Nomenclature

$a$	spacing between two vortex rows, mm.
$b$	spacing between two vortices in a row, mm.
$c$	plate chord, mm.
$d$	cylinder diameter, mm.
$h$	height of backwards facing step, mm.
$l_f$	vortex formation length, mm.
$t$	plate thickness, mm.
$x$	streamwise distance, mm.
$\partial x$	streamwise distance between adjacent PIV gridpoints, mm.
$y$	cross-stream distance, mm. also amplitude of body motion, mm.
$\partial y$	cross-stream distance between adjacent PIV gridpoints, mm.
$X_R$	shear layer reattachment length, mm.
$A$	area, mm <sup>2</sup> .
$\phi$	vortex shedding phase angle, degrees.
$u'$	amplitude of perturbation velocity, ms <sup>-1</sup> .
$U_\infty$	free stream velocity, ms <sup>-1</sup> .
$U_o$	free stream velocity, ms <sup>-1</sup> .
$U_b$	velocity at edge of boundary layer at separation point, ms <sup>-1</sup> .

$U_{\text{conv}}$	convection velocity of vortices, $\text{ms}^{-1}$ .
$U_x$	streamwise component of velocity, $\text{ms}^{-1}$ .
$U_y$	cross-stream component of velocity, $\text{ms}^{-1}$ .
D	drag force, N.
$P_{\text{base}}$	time averaged base pressure, Pa.
$P_{\text{surface}}$	time averaged surface pressure, Pa.
$P_{\text{dynamic}}$	dynamic pressure, Pa.
$\Delta P$	pressure difference between two points, Pa.
f	vortex shedding frequency, Hz.
$f_s$	vortex shedding frequency, Hz.
$f_o$	natural vortex shedding frequency, Hz.
$f_p$	perturbation frequency, Hz.
$f_e$	oscillation frequency, Hz.
$\omega$	vorticity, $\text{s}^{-1}$ .
$\Gamma$	circulation, $\text{m}^2 \text{s}^{-1}$ .
$\nu$	kinematic viscosity, $\text{m}^2 \text{s}^{-1}$ .
SPL	Sound Pressure Level, dB.
$c/t$	plate chord to thickness ratio, dimensionless.
$Re$	<i>Reynolds</i> number defined as $\frac{U_{\infty} t}{\nu}$ , dimensionless.

$C_d$	Drag coefficient defined as $D/(1/2 \rho U_\infty^2 A)$ , dimensionless.
$C_{p_s}$	Surface pressure coefficient defined as $P_{\text{surface}}/(1/2 \rho U_\infty^2)$ , dimensionless.
$C_{p_b}$	Base pressure coefficient defined as $P_{\text{base}}/(1/2 \rho U_\infty^2)$ , dimensionless.
$C_{p_{b_0}}$	Base pressure coefficient in the absence of transverse velocity perturbations, dimensionless.
$C_{p_{b_{\max}}}$	Maximum base pressure coefficient measured with transverse velocity perturbations applied to the flow, dimensionless.
$\Delta C_p$	Difference in pressure coefficient between two points, dimensionless.
$St$	Strouhal number defined as $\frac{f_s t}{U_\infty}$ , dimensionless.
$St_c$	Strouhal number (based upon plate chord) defined as $\frac{f_s c}{U_\infty}$ , dimensionless.
$St_p$	Perturbation Strouhal number defined as $\frac{f_p t}{U_\infty}$ , dimensionless.
$n$	ILEV mode, dimensionless.

### Common Acronyms Used

A/D	Analogue to Digital converter.
CFD	Computational Fluid Dynamics.
CRO	Cathode Ray Oscilloscope
LEVS	Leading Edge Vortex Shedding
ILEV	Impinging Leading Edge Vortex.
TEVS	Trailing Edge Vortex Shedding.
L vortex	Vortex shed from the leading edge of a bluff body.

T vortex      Vortex shed from the trailing edge of a bluff body.

LDV      Laser Doppler Velocimetry.

PIV      Particle Image Velocimetry.



# 1. Introduction

The field of fluid dynamics encompasses a wide variety of processes. The flow of fluids around bluff bodies is one of these (often called bluff body aerodynamics), and is one which most of us encounter either directly or indirectly each day. Gaining a better understanding of bluff body flows will benefit many areas of design, including the design of buildings, bridges, transport vehicles and heat exchangers, to name a few.

Simple geometries like circular and rectangular cylinders lend themselves well to basic research, as they allow fundamental features of flows (like separation bubbles and vortex formation regions) to be studied in detail. This can then help in explaining many flow phenomena associated with more complicated geometries.

During the last few decades, experimental studies of flow over two-dimensional rectangular cylinders has allowed some important advances to be made in our understanding of many flow phenomena, especially of the effect of turbulence on the separating shear layer, the general understanding of the separated flow region near the leading edge, and in understanding the effect of controlled flow perturbations on vortex shedding and heat transfer.

## 1.1 Previous Research at the CSIRO DBCE

Research on flows around elongated rectangular plates enclosed in a duct was undertaken by Welsh & Gibson (1979). They found that loud acoustic resonances occurred at certain flow velocities due to strong vortex shedding from the plates. When this occurred, the vortex shedding frequency from the plates coincided with the resonant frequency of the duct.

Parker & Welsh (1983) investigated vortex shedding from elongated rectangular plates in an open jet wind tunnel. With loudspeakers placed either side of the models, they were able to simulate the resonant sound field which can occur for plates mounted in a duct with the advantage of being able to vary both the sound amplitude and frequency. They found that the

leading edge separation bubble shed vortices at the same frequency as the sound over a wide range of frequencies.

Cooper *et al.* (1986) investigated heat transfer from an elongated rectangular plate in the presence of transverse velocity perturbations; they found that the heat transfer coefficient was essentially a function of the time-mean reattachment length of the separation bubble. Since the application of transverse velocity perturbations at a natural shedding instability frequency of the separation bubble always decreased the separation bubble length, this had the effect of increasing the heat transfer coefficient. It was also noticed that the time mean drag on the plates usually increased in the presence of the velocity perturbations.

Stokes & Welsh (1986) investigated the feedback mechanism responsible for controlling the vortex shedding from elongated rectangular plates mounted in a duct, in the presence of a loud sound field at the duct resonant frequency. They found that for rectangular plates, the acoustic feedback that controlled vortex shedding had its source at the trailing edge of the plate; the generated sound reflected off the duct walls to affect the vortex shedding at the leading edge of the plate.

## **1.2 Objective of the Overall Research Program**

The objective of this research program is to improve our understanding of the mechanism(s) responsible for vortex shedding from elongated bluff bodies in the presence of externally applied transverse velocity perturbations, and hence understand the changes in base pressure in response to velocity perturbations. This objective has been translated into the “vortex interaction hypothesis” which is described later in this thesis, as is the experimental program devised to test the hypothesis.

## 2. Literature Review

### 2.1 Bluff Body Aerodynamics

Flows around bluff bodies can be distinguished from flows around streamlined bodies by the presence of regions of separated and often reattaching flow, a relatively high value of the drag coefficient ( $C_d$ ), and the presence of vortex shedding. Bluff bodies are frequently found in flows of engineering interest. The study of flows around simple geometries like circular cylinders, prisms of different cross section and inclined aerofoils, has significantly increased our understanding of many fundamental features of bluff body flows, especially during the last fifty years.

#### 2.1.1 Vortex Shedding

Vortex shedding from bluff bodies generally occurs for values of Reynolds number ( $Re$ )  $> 50$ , and can cause large amplitude vibrations of structures, sometimes leading to catastrophic failure or, more likely, fatigue failure. Vortex shedding also can be a source of unwanted noise. In fact, Strouhal (1878) was the first to recognise the relationship between the frequency of sound ( $f_s$ ) (called the aeolian tone) resulting from the flow over a cylindrical wire, the flow velocity ( $U_\infty$ ), and the wire diameter ( $d$ ). He expressed this relationship as a non-dimensional constant:  $St = f_s d / U_\infty$ , where  $St$  is now commonly known as the Strouhal number.

It was not until Bernard (1912), however, that it was realised that the production of a regular vortex street behind the cylinder was responsible for the production of the aeolian tone. At the same period, von Kármán & Rubach (1912) established a ratio  $a/b$  of 0.28 for the spacing ( $a$ ) between two vortex rows to the distance ( $b$ ) between two vortices in a row as a requirement for a stable vortex street to exist (see figure 2.1). Alternating vortex streets behind bluff bodies are now commonly called Kármán vortex streets.

Roshko (1955) showed that similarity exists between bluff body flows for different geometries. He studied the pressure recovery process in reattaching flows and found that the pressure distributions for all shapes tested collapsed onto a single curve when the pressure was normalised by the pressure at separation, and the streamwise displacement was normalised by the re-attachment length.

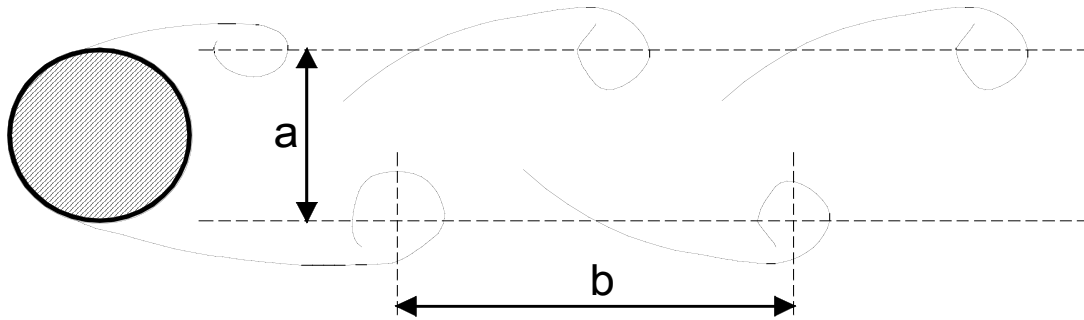


**Figure 2.1** Spacing between vortices in a von Kármán vortex street.

In a study of flow over a rectangular prism, Bearman (1967) showed the apparent similarity of vortex streets behind bluff bodies. He found that bluff body data roughly collapsed when his universal Strouhal number ( $S_b$ ) was plotted against the base pressure parameter  $K$  (where  $K = (1 - C_{p_b})^{0.5}$  and  $S_b = fb/U_b$  :  $f$  = vortex shedding frequency,  $b$  = longitudinal vortex spacing determined from the Kronauer stability criterion, and  $U_b$  = the velocity at the edge of the boundary layer at the separation point). In the same study, Bearman also noted that both the velocity of vortices and the longitudinal spacing between vortices were accurately predicted by the von Kármán vortex street drag formula.

## 2.2 Flow Instabilities

Examples of some naturally occurring flow instabilities of significance to engineers are free shear layer instabilities, bluff body shear layers, impinging shear layers, vortex street wakes, and the transition to turbulence of boundary layers. In recent times and with the aid of modern computers, renewed interest in the field of linear stability analysis has advanced our understanding of why many flows become unstable. The aim of performing a linear stability analysis is to predict if a given flow pattern is stable or not. Of course, a linear stability

analysis will only predict the onset of any flow instability for as the instability grows, the flow pattern is modified and it soon becomes non-linear.

The concepts of absolute/convective and local/global instabilities have helped us characterise the nature of typical flow instabilities. The instability of the velocity profile at a point in a flow is called a local instability. A global instability refers to the instability of the entire flow field.

Figure 2.2 illustrates responses to an impulse disturbance of an absolutely unstable system on the left, and of a convectively unstable system on the right. A physical interpretation of an absolutely unstable system, pioneered by Briggs (1964) while investigating plasma instabilities, is that a small amplitude impulsive disturbance grows exponentially in time at the source of the disturbance (Rockwell 1990). Such a system is said to be locally absolutely unstable (Huerre & Monkewitz 1990). On the other hand, the impulse disturbance of the convectively unstable system is convected away from the source, leaving the system to return to its original state in time.

Insert graph here (of abs. and conv. instable system responses to an impulse response)

**Figure 2.2** Sketch of a typical impulse response: (a) absolutely unstable flow; (b) convectively unstable flow; from Monkewitz & Nguyen (1987)

In the absence of any downstream impingement surfaces, the existence of a region of absolute instability is necessary for the existence of globally unstable oscillations of a shear flow (Rockwell 1990). A bluff body wake is a classical example of a globally unstable flow, due to the presence of a region of absolute instability within the wake. The placement of a

downstream impingement body in a convectively unstable shear flow can also complete the feedback loop needed to produce a global instability (Rockwell 1990) by providing an upstream feedback from the downstream surface to the shear layer at the upstream separation edge (Rockwell & Naudascher 1979).

### **2.2.1 Control of flow instabilities**

Generally speaking, flows which are locally convectively unstable everywhere, are highly receptive to external disturbances applied over a wide frequency range and are thus considered to be noise amplifiers (Huerre & Monkewitz 1990). It well known that mixing layers are convectively unstable, and it has been shown (Ho & Huerre 1984) that they are very sensitive to externally applied perturbations. The separated and reattaching shear layer from a long rectangular plate has also been shown to be convectively unstable (Soria & Wu 1992). This is consistent with the findings of Parker & Welsh (1983) who found that vortex shedding from the leading edge of long rectangular plates could be phase locked to transverse velocity perturbations over a wide range of frequencies.

Merati & Adrian (1992) investigated the feedback mechanism which amplified natural instabilities in a plane shear layer when it impinged on a downstream body. They found that locating a thin flat plate on the centreline of the shear layer in the region of exponential growth created periodic disturbances that fed back upstream to the initial instability. Depending on the distance between the separation splitter plate and the downstream plate, the shear layer amplitude was either increased or reduced by the feedback. The maximum amplification occurred when the distance between the feedback edge and the separation splitter plate edge was equal to an integer number of wavelengths of the initial instability frequency.

Flows which are globally unstable due to the presence of a region of absolute instability in the wake exhibit self excited oscillations, and can be categorised as oscillators (Huerre & Monkewitz 1990). Due to the naturally occurring self excited instability, they tend to be unresponsive to small amplitude perturbations. Only by applying perturbations of

sufficiently high amplitude to effectively alter the mean flow, can the flow be controlled by external perturbations.

The Kármán vortex shedding from a circular cylinder is an example of a globally unstable flow. It has a region of absolute instability in the wake, as well as the two separated shear layers that are locally convectively unstable. Karniadakis & Triantafyllou (1989) performed a direct numerical simulation of the flow about a circular cylinder in the presence of a periodic external forcing, and found that the response of the wake could be qualitatively represented by a two-parameter space inside a resonant horn as shown in figure 2.3

Insert graph here from Karniadakis and T. (1989)

JFM 199, 441-469 (figure 24 on p466)

**Figure 2.3** State selection diagram for laminar wakes, from Karniadakis & Triantafyllou (1989)

Small amplitude perturbations near the Kármán shedding frequency have little effect on vortex shedding. For perturbation amplitudes above the minimum threshold, perturbation frequencies within the lock-in boundary result in a near wake with a frequency equal to the perturbation frequency. For perturbation frequencies outside the receptivity boundary, the frequency in the near wake is equal to the natural vortex shedding frequency, while perturbation frequencies within the two regions between the lock-in boundary and the receptivity boundary result in a quasi-periodic wake, with both the perturbation frequency and the natural vortex shedding frequency present in the wake. Stansby (1976) found a similar response of vortex shedding to transverse oscillations of a circular cylinder in a series of wind tunnel experiments. Vortex shedding from a rectangular trailing edge of a body with an

aerofoil leading edge also shows similar response to perturbations compared to a circular cylinder with a minimum threshold perturbation level required in order for the vortex shedding to be modified (Wu *et al.* 1993). For perturbation levels above the threshold level, Lotfy & Rockwell (1993) found that a range of frequencies existed near the natural vortex shedding frequency where perturbations would result in a lock-in state.

## 2.3 Flows around Rectangular Prisms

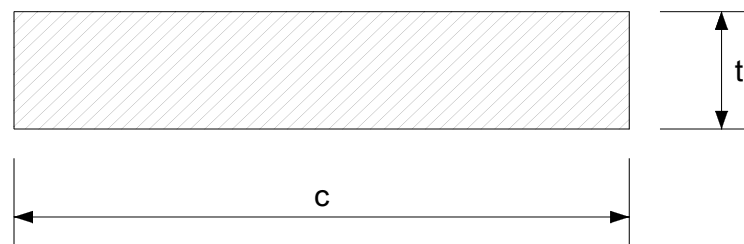


**Figure 2.4** Cross section of a rectangular prism of chord  $c$ , and thickness  $t$ .

Rectangular prisms or similar geometries can be found in many engineering applications, ranging from high rise office buildings and bridge decks, to the trash racks used to prevent rubbish from entering water ways.

A distinguishing feature of flows around rectangular prisms, compared to flows around circular cylinders, is the fixed separation point at the sharp leading edge corners.

Many factors can affect the flow around rectangular profiles of the form shown in figure 2.4. These include Reynolds number ( $Re$ ), chord to thickness ratio ( $c/t$ ), free stream turbulence, not to mention the complicated effects due to plate vibrations. Much progress has been made in recent times to further our understanding of how these factors can influence the flow, although most recent reviews on bluff body flows concentrate on the flow about circular cylinders. The book by Naudascher & Rockwell (1994) provides one of the most comprehensive recent reviews of flow about rectangular profiles.

### 2.3.1 Effect of $c/t$ ratio on shear layer development and $C_d$

Fage and Johansen (1927) appear to be the first to measure the drag coefficient ( $C_d$ ) for flow around a thin flat plate ( $c/t = 0.028$ ) placed normal to the oncoming air stream, and found that the drag coefficient was approximately 2.0. Additionally, by the late 1960's it was well known that for square cylinders ( $c/t = 1$ ),  $C_d$  is also approximately 2.0, so it was assumed that for intermediate  $c/t$  values  $C_d$  would remain constant at about 2.0. Nakaguchi *et al.* (1968) showed this assumption to be incorrect when they found that a maximum  $C_d$  of about 2.8 occurred when  $c/t = 0.62$ . For values of  $c/t > 1.0$ ,  $C_d$  steadily decreases to a value of about 1.0 for  $C_d = 5$  (see figure 2.5).

Insert graph here (from Norberg)

**Figure 2.5** Effect of varying  $c/t$  ratio on  $C_d$  for rectangular prisms (from Norberg 1993).

Bearman (1965) showed that the further downstream vortices form from the base of a bluff body, the lower the base suction and, hence, the lower the  $C_d$ . Bearman & Trueman (1972) used this argument to explain the cause of the high  $C_d$  associated with the  $c/t=0.62$  geometry. Essentially, as  $c/t$  is increased from zero, the shear layer curvature is initially unaffected by the presence of the afterbody so that the vortex formation position remains in the same location relative to the leading edge corners. However, the base of the body moves closer to the formation region, and this explains the increase in base suction up until  $c/t=0.62$ . At this stage the shear layers start to impinge on the trailing edge corners of the body. As  $c/t$  is increased further a complex equilibrium state is set up where the curvature of the shear layers increases due to the position of the trailing edge corners. As a result of this, the high base

suction can no longer be maintained and so we see the  $C_d$  steadily decrease towards a value of about 1.0 as  $c/t$  approaches 5.0.

### 2.3.2 Reynolds number effects on separation bubbles

For flow over long blunt flat plates where the separated shear layer always reattaches to the plate surface, Sasaki & Kiya (1991) defined three distinct regimes of shear layer development.

1. For  $80 < Re < 320$ , with  $Re$  based on plate thickness, the separated shear layer remains laminar up to the reattachment point and the separation bubble length increases with  $Re$  to a maximum of about  $6.5t$ . The first sign of an instability wave in the shear layer does not appear until  $Re \approx 315$ , but due to viscous forces remaining dominant, the shear layer does not roll up to form vortices.
2. For  $320 < Re < 380$ , the shear layer was observed to roll up and form  $\wedge$  shaped vortices (see figure 2.6(a)) due to the Kelvin-Helmholtz instability. These are arranged inline on the plate surface. The bubble length was observed to decrease rapidly with  $Re$ .
3. For  $Re > 380$ , horseshoe-like vortex structures that result from an amalgamation of vortices around the midpoint of the bubble appear. These are arranged on the plate surface in a staggered manner (see figure 2.6(b)).

As  $Re$  is increased above 380, the separated shear layer becomes thinner and rolls up further upstream. Also, the number of vortices undergoing the amalgamation process also increases and the resultant structures start to become more randomly distributed. The transition point, where the separated shear layer becomes turbulent, moves progressively upstream until at about  $Re = 2 \times 10^4$  (Ota *et al.* 1981) the shear layer is turbulent on separation. Hillier & Cherry (1981) noted that for low turbulence flows, shear layer data were virtually independent of  $Re$  for  $3.4 \times 10^4 < Re < 8 \times 10^4$ , a similar observation also being made by Parker & Welsh (1983). At these higher  $Re$ , and in a low turbulence flow, the reattachment length ( $X_R$ ) of the separation bubble has been reported by a number of authors to be approximately  $4.9t$ .

(a) (b)

**Figure 2.6** Flow visualisation of three dimensional structures in a separated shear layer, from Sasaki & Kiya (1991); (a)  $320 < Re < 380$ , (b)  $Re > 380$ .

Hillier & Cherry (1981) and Kiya & Sasaki (1983) have reported that the development of the shear layer is similar to that of a plane mixing layer over the first 60% of the separation bubble length. Over this portion, the shear layer thickness grows almost linearly, and the characteristic frequencies and lateral correlation scales correspond well to values found in plane mixing layers. These features indicate that the amalgamation of shear layer vortices occurs successively along the bubble. It is only over the last 40% of the bubble length that the reattachment surface appears to directly influence the nature of the separated shear layer. Vortices of size similar to the separation bubble are shed downstream with a reduced frequency of about  $0.6U_\infty/X_R$  (Kiya & Sasaki 1983), where  $U_\infty$  is the free stream velocity. The spacing between these vortices was estimated to be  $0.75X_R$ . (Kiya & Sasaki 1983).

Another feature noticed by several researchers is a low frequency flapping motion of the shear layer just downstream of the separation point. Cherry, Hillier & Latour (1984) noted that the flapping motion is associated with a large scale unsteadiness of the bubble, resulting in the low frequency flapping of the shear layer at a reduced frequency of approximately  $0.11U_\infty/X_R$ . Saathoff & Melbourne (1989) found that the occurrence of large negative peak pressures under the separation bubble of a sharp edged body are associated with the large vortex that forms with this low frequency flapping of the shear layer.

### 2.3.3 Effect of free stream turbulence

It is well known that free stream turbulence can significantly affect bluff body flows. While studying the effects of free stream turbulence on the flow around a square cylinder ( $c/t=1.0$ ), Vickery (1966) noticed that increasing the free stream turbulence decreased the drag on the cylinder. Bearman (1971) noticed the opposite effect when he performed a series of experiments on thin square and circular plates. This anomaly was not resolved until Gartshore (1973) recognised that small-scale free stream turbulence has the effect of significantly reducing the radius of curvature of the separated shear layer. After noticing that a thin rod placed on the stagnation stream line to generate vortices had the same effect on the shear layers as free stream turbulence, Gartshore suggested that the mean flow field acted to stretch the vorticity and create shear layers shed from the body containing intense, small-scale, streamwise vorticity. The shear layers containing this added vorticity will have greatly increased turbulent mixing, resulting in increased growth rate of the layers and their entrainment of fluid from inside and outside the wake. For the flows over the thin square and circular plates that Bearman (1971) studied, a decreased radius of curvature of the shear layers with increasing turbulence level resulted in a shorter vortex formation length and thus, an increase in drag. For the prism with  $c/t=1.0$ , the increased curvature of the shear layers meant that the shear layers reattached to the surface of the prism earlier, resulting in an increase in vortex formation distance and thus, the opposite effect on the drag was observed compared to a thin plate.

Hillier & Cherry (1981) investigated the effects of free-stream turbulence on mean and fluctuating pressure distributions on a long blunt flat plate. They showed that an increase in turbulence intensity ( $\sigma_w/u$ ) from about 0.1% to 6.5% caused a reduction of the mean reattachment length,  $X_R$ , from  $4.9t$  to  $2.7t$ , and a corresponding reduction in mean pressure at separation (see figure 2.7). The streamwise distributions of mean pressure were also found to be highly dependent on  $\sigma_w/u$ . (see figure 2.8). Kiya & Sasaki (1983) also reported that reducing the freestream turbulence intensity from 0.4% to 0.2% yielded a 5% longer separation bubble.

Insert graph here  
(from Saathoff & Melbourne (1997))  
figure 4

**Figure 2.7** Effect of free stream turbulence intensity ( $\sigma_u/u$ ) on the mean reattachment length ( $X_R$ ) of the separation bubble on a long rectangular plate (from Saathoff & Melbourne 1997).

Insert graph here  
(from Cherry & Hillier 1981)

**Figure 2.8** Effect of free stream turbulence intensity ( $\sigma_u/u$ ) on the time mean surface pressure under the separation bubble on a long rectangular plate.

Saathoff & Melbourne (1997) showed that peak pressure fluctuations occur when free-stream turbulence perturbations cause the separated shear layer to roll up near the leading edge. They found that an increase in  $\sigma_u/u$  produces stronger spanwise vortices and, as a result, an increase in the magnitude of pressure fluctuations. The magnitude of pressure fluctuations also increases with increasing turbulence scale due to two main effects:

- (i) An increase in spanwise coherence of vortices that are formed when the shear layer rolls up,
- (ii) a decrease in perturbation frequency which increases the duration of vorticity entrainment.

## 2.4 Vortex shedding from rectangular prisms

Vortex shedding from short bluff bodies is characterised by Kármán shedding, which results from the direct interaction of the two separated shear layers. Vortex shedding from rectangular prisms at high  $Re$  (ie.  $Re > 10000$  based on  $t$ ) has been grouped into four regimes by Parker & Welsh (1983), depending on plate chord to thickness ratio ( $c/t$ ).

- **Regime (a)** “On short plates with  $c/t < 3.2$ , flow separation occurs at the leading edge corners and the shear layers interact directly without reattaching to the plate surface, to form a vortex street.”
- **Regime (b)** “On longer plates ( $3.2 < c/t < 7.6$ ) the shear layers reattach to the trailing edge surface periodically in time. After reattachment the separation bubble grows enveloping the trailing edge and permitting fluid from within the bubble to pass into the vortex formation region, initiating a new vortex.”
- **Regime (c)** “For still longer plates ( $7.6 < c/t < 16$ ) the shear layers are always reattached upstream of the trailing edge and form a separation bubble which grows and divides in a random manner. This generates a boundary layer with discrete concentrations of vorticity (vortices) which move along the plate surface towards the vortex street formation region. The vortices are distributed randomly throughout the boundary layers and consequently produce irregular vortex shedding and no clear regular vortex street.”
- **Regime (d)** “For plates with  $c/t > 16$  the separation bubble fluctuates in length in the same manner as described in (c) but the vortices, which are distributed randomly in the boundary layers, diffuse before reaching the trailing edge. The characteristics of the boundary layers on each side of the plate approach those of the fully developed turbulent state and interact to form a regular vortex street not directly related to the formation of leading edge separation bubbles.”

Figure 2.9 shows the variation of vortex shedding  $St$  with plate chord to thickness ratio for  $Re > 10000$ .

Insert graph here (from Parker & Welsh(1983))  
 St vs c/t for rect prism's  
 (figure 2)

**Figure 2.9** Variation of vortex shedding  $St$  with  $c/t$  for elongated rectangular prisms, from Parker & Welsh (1983)

For plates with  $0 < c/t < 1.0$ ,  $St$  is approximately constant and equal to about 0.13 based on plate thickness. As  $c/t$  is increased further,  $St$  decreased until it reaches a minimum value of 0.065 when  $c/t = 3.2$ . A sudden jump in  $St$  occurs as  $c/t$  is increased beyond 3.2, indicating shedding in regime (b). For the shortest plates in regime (b), the shedding  $St$  is about 0.15, and steadily decreases to a value of only 0.07 for the longest plate ( $c/t = 7.6$ ). No regular vortex shedding was observed for plates in regime (c), but for longer plates in regime (d), the vortex shedding  $St$  approaches that for an aerofoil leading edge plate of similar length, indicating that vortex shedding is taking place at the trailing edge of the model, quite independently from the random fluctuations of the separation bubble at the leading edge.

Nakamura *et al.* (1991) investigated vortex shedding from rectangular plates of various  $c/t$  ratios. The studies were all performed at  $Re = 1000$ , based on plate thickness  $t$ . They observed an interesting feature that the Strouhal number based on plate length ( $St_c$ ) was approximately equal to  $0.6n$ , where  $n$  is an integer. As plate length was increased,  $St_c$  increased in a stepwise manner. When investigating flows over elongated H and  $\perp$  section prisms with  $c/t$  ratios from 2.0 to 8.0 at  $Re$  of 50000 or higher, Nakamura & Nakashima (1986) found that  $St_c$  was again almost constant and equal to 0.6. If the  $St$  measured by Parker & Welsh (1983) for flow around rectangular prisms in regime (b) are multiplied by plate  $c/t$  ratio, then  $St_c$  is also approximately constant to about 0.6 at high  $Re$ . At the higher  $Re$ , once  $c/t$  is increased above about 7, the regular vortex shedding breaks down meaning that no jumps to higher values of  $St_c$  are observed.

A physical interpretation of this staging in  $St_c$  is that there is always an integer number ( $n$ ) of vortices on a plate side, the number of which will depend on plate length. Figure 2.10 shows the variation in  $St_c$  with  $c/t$  as measured by Nakamura *et al.* (1991).

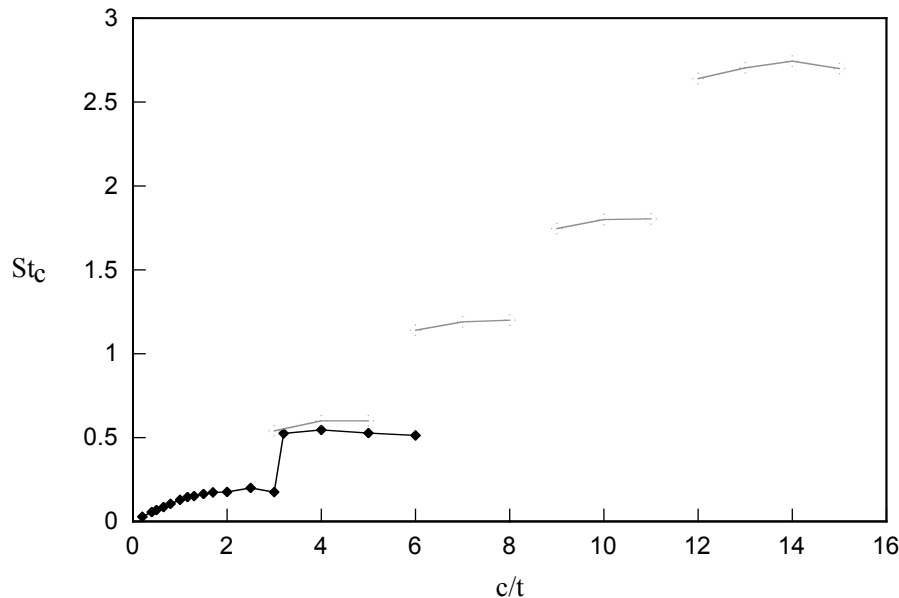


**Figure 2.10** Variation of vortex shedding Strouhal number for rectangular plates based on plate chord ( $St_c$ ), with  $c/t$  ratio for rectangular plates: (○  $Re = 1000$  (Nakamura *et al.* 1991), ◆  $Re > 10000$  (Parker & Welsh 1983))

#### 2.4.1 Impinging Leading Edge Vortex (ILEV) instability

The Impinging Shear Layer Instability mechanism was proposed by Nakamura & Nakashima (1986) to explain vortex formation from elongated bluff bodies and thus, the variations of  $St_c$  with  $c/t$  shown in figure 2.10. Naudascher & Rockwell (1994) more accurately called this the ILEV instability mechanism since for long plates ( $c/t > 7$ ), the leading edge shear layer does not impinge directly on the trailing edge. Rather, it is vortices shed from the leading edge separation bubble that do.

The ILEV instability mechanism is based on research reviewed by Rockwell & Naudascher (1978) that focused on the mechanism(s) controlling self-sustained oscillations of flow over a sharp edged cavity. Rockwell & Naudascher described three categories of self sustained fluid oscillations.

1. Fluid dynamic oscillations, where the instability of the cavity shear layer is enhanced by a feedback mechanism originating at the downstream corner of the cavity. The acoustic feedback wavelength is much larger than the cavity length, so the process can be considered to be a hydrodynamic one.
2. Fluid resonant oscillations, which are strongly coupled with resonant wave effects within the cavity. The acoustic wavelength is of the same order of magnitude as the cavity size.
3. Fluid-elastic oscillations that result from the periodic displacements of one or more of the cavity walls exerting feedback control on the separating shear layer.

For all three types of self sustained fluid oscillations defined by Rockwell & Naudascher, there is some sort of feedback control on the locally convectively unstable leading edge separating shear layer. Ho & Nosseir (1981) studied the feedback mechanism of a free jet impinging on a large flat plate mounted normal to the jet. They found that the feedback loop which controlled vortex formation in the free shear layers of the jet had two fundamental components. These were:

1. Large scale coherent vortex structures propagating downstream.
2. Upstream propagating pressure waves that travel at the speed of sound, generated by the impingement of the large scale coherent structures on the plate surface.

The upstream propagating pressure waves force the separating shear layer originating at the jet exit at a subharmonic of its “intrinsic most unstable frequency”, which results in a vortex amalgamation process (see figure 2.11) that was observed by Ho & Huang (1982) in experiments on a mixing layer. The vortex amalgamation completes the feedback loop, and is responsible for the generation of the large scale structures that impinge on the flat plate at intervals that are phase locked with the upstream propagating pressure waves.

Insert graph here (from Ho & Nosseir (1981))  
showing collective interaction  
of shear layer vortices at a  
sub harmonic of the forcing frequency.

**Figure 2.11** Collective interaction of mixing layer vortices to form large scale structures.

The ILEV instability mechanism, illustrated in figure 2.12, is a fluid resonant oscillation. The shear layer instability is greatly enhanced by the feedback control of the trailing edge discontinuity on the vorticity production at the separation point. Regular and periodic shedding of vortices (hereafter called an L vortices) occurs at the leading edge. As an L vortex shed during an earlier shedding cycle passes the trailing edge, a pressure pulse is generated which travels upstream to the receptive leading edge shear layer on the same side of the plate. This causes the L vortex that was forming at the leading edge on the same side to be shed, and a new L vortex to begin forming. In this manner, the wavelength of vortex shedding is locked to the plate chord. Plates with  $c/t$  between 3 and 5 have just one L vortex on each side, and thus shed vortices at ILEV mode  $n = 1$ . As  $c/t$  is increased from 3 to 5, the wavelength of these L vortices increases until a limit is reached, and the shedding jumps to the next ILEV mode ( $n = 2$ ).

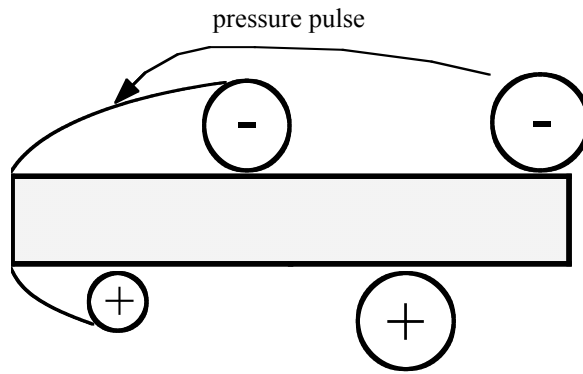


**Figure 2.12** Illustration of feedback mechanism which controls vortex shedding at low  $Re$  from rectangular plates (ILEV mode = 2).

Nakamura & Nakashima (1986) found from their work on the H section prisms that a plate with  $c/t = 5$  shed vortices from the leading edge at the same frequency with and without a splitter plate placed behind the trailing edge of the model. This indicates that the ILEV instability mechanism is one sided. Unlike vortex shedding from short bluff bodies, it is not dependent on the interaction of the two separated shear layers in the wake. It is worth noting that the  $Re$  for the H section prisms studied was 50000 or higher (based on  $t$ ), and the frequency spectrum of hot wire measurements made in the wake showed no sharp spectral peaks for plates with  $c/t > 8$ . This is consistent with the findings of Parker & Welsh (1983) for flow over rectangular plates at similar  $Re$ , who found that for rectangular plates with  $c/t > 7.6$ , no sharp spectral peaks were observed in the wake.

The study by Nakamura *et al.* (1991) on flows around rectangular plates found that the ILEV instability was present for plates with  $c/t$  up to 16. However, for plates with  $c/t > 6$ , Nakamura could not detect any regular vortex shedding for  $Re > 2000$ . As mentioned earlier, for low  $Re$  the shear layer separating from the leading edge corners is initially laminar, and remains so for up to approximately one plate thickness away from the leading edge. As  $Re$  is increased, the transition point moves further upstream, making the shear layer less sensitive to external disturbances. Also, the flow along the plate sides becomes increasingly three-dimensional as  $Re$  increases. These two things would combine to weaken the effect of any feedback mechanism for  $Re > 2000$ .

Naudascher & Rockwell (1994) characterised the different vortex shedding regimes for stationary rectangular cylinders based on  $c/t$  after Parker & Welsh (1983). As illustrated in figure 2.13, there are three possible classes of vortex formation: Class I-leading edge vortex shedding (LEVS), Class II-impinging leading edge vortices (ILEV) and Class III-trailing edge vortex shedding (TEVS) as  $c/t$  is increased.

I - LEVS	II - ILEV	III - TEVS
$c/t < 2-3$	$2-3 < c/t < 16$	$c/t > 16$

**Figure 2.13** Classes of vortex formation observed with increasing  $c/t$  for rectangular prisms (adapted from Deniz & Staubli 1997).

Nakamura *et al.* (1991) suggested that although the ILEV instability was not detectable for  $Re > 2000$ , this did not mean it was not present. They suggested that the regular shedding observed by Stokes & Welsh (1986) from a rectangular plate in a duct at high  $Re$  was a result of the ILEV instability being excited by the loud acoustic resonance set up at a duct  $\beta$ -mode (Parker 1967) resonant frequency. Stokes & Welsh showed that when the vortex shedding was locked to the acoustic resonant field in the duct, the acoustic feedback had its source at the trailing edge of the rectangular plates. The sound was reflected off the walls of the duct, before interacting with the separated shear layers to lock the vortex shedding to the duct  $\beta$ -mode resonant frequency. This is clearly an example of a category 2 type of self sustained oscillation defined by Rockwell & Naudascher (1978), and therefore different to the ILEV instability mechanism proposed by Nakamura *et al.* (1991). It is interesting to note the similarity between the acoustic Strouhal number at which peaks in the resonant sound pressure level occur for different length plates, and the ILEV shedding frequencies measured by Nakamura *et al.* (1991), as shown in figure 2.14. This is why Nakamura *et al.* (1991) suggested that the ILEV instability could be excited at  $Re > 2000$ . To date, no explanation for this contradiction between Stokes & Welsh (1986) and Nakamura *et al.* (1991) regarding the feedback mechanism controlling the vortex shedding from a plate in a duct in the presence of a resonant sound field has been offered. An explanation will be presented in chapter 4.

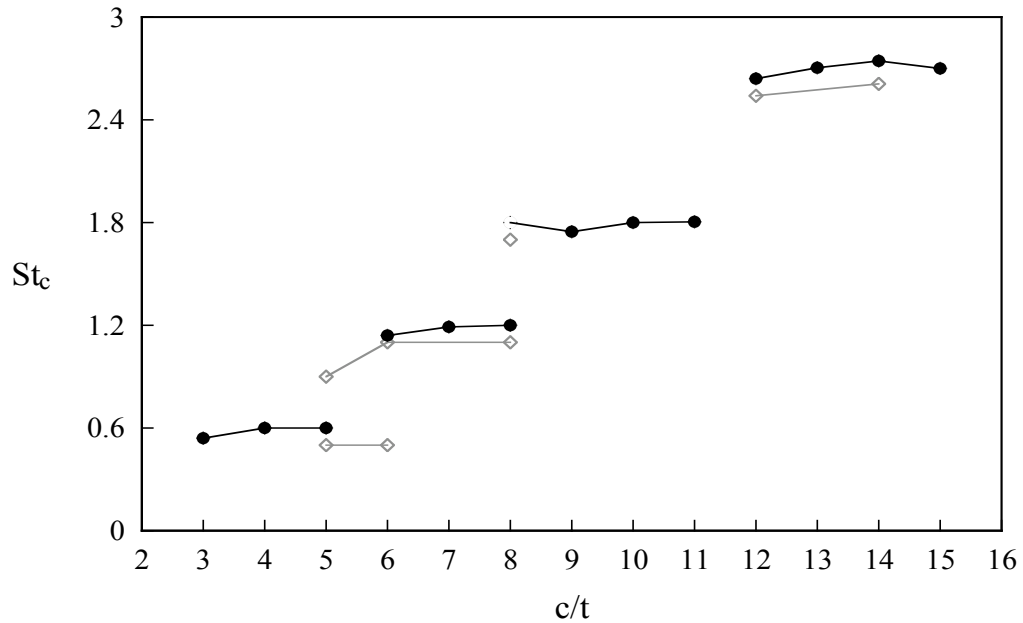


**Figure 2.14** Vortex shedding  $St$  for rectangular prisms of different  $c/t$  ratio's; • natural vortex shedding  $St$  ( $Re < 2000$ ) corresponding to ILEV instability frequency (Nakamura 1991), ◊ vortex shedding  $St$  corresponding to resonant shedding from plate in a duct (Stokes and Welsh 1986).

In order to better understand how the ILEV instability governs vortex shedding, Ohya *et al.* (1992) performed a computational fluid dynamics (CFD) study of flow around rectangular plates with  $c/t$  between 3 and 9. They observed good agreement in  $St_c$  with the wind tunnel results of Nakamura *et al.* (1991) for plate lengths up to  $7t$ , with the results of the  $c/t = 8$  and 9 plates differing, but still showing some evidence of the ILEV instability. The numerical study was a two dimensional one performed at a  $Re$  of 1000. Since the real flow is quite three dimensional at this  $Re$ , any coherence in vortices shed from the leading edge shedding would be significantly less than that assumed in the 2-D CFD study. This will result in artificially high values of circulation found in the numerical solution, and might account for the disagreement in the vortex shedding frequencies for the longest two plates investigated.

Nevertheless, the numerical study did reveal a feature of the flow that was not apparent previously. As the CFD simulation was run, initially there was no asymmetry to the flow, with the two separation bubbles growing symmetrically on both sides of the plate, and a pair of attached eddies forming at the rear. This process continued until the separation bubbles reached the trailing edge and began to interact with the attached eddies. This is when the asymmetry of the flow appeared, which eventually led to asymmetrical vortex shedding. The

shear layer separating from the leading edge reattaches to the sides of the plate to form a separation bubble which oscillates in length at a regular frequency. These oscillations are at the same frequency as the vortex shedding frequency, and result in a single L vortex being shed from the separation bubble per cycle. For the plates with  $3 < c/t < 5$ , only a single L vortex is detectable on the plates' side at any instant. For the plates in the next group ( $6 < c/t < 8$ ), there were always two L vortices present on the plate side at any instant. As  $c/t$  is increased, each jump in the  $St_c$  vs  $c/t$  curve (see figure 2.14) corresponds to an increase in ILEV mode, with the number of vortices on the side of the plate corresponding to the ILEV mode. This shedding of L vortices at the same frequency as the wake was expected, as it was detected by Nakamura *et al.* (1991).

The feature of the flow that had not been discovered previously was the shedding of vortices from the trailing edge of the plates (hereafter called T vortices). As an L vortex approaches the trailing edge, the reattached boundary layer separates again at the trailing edge and rolls up to form a T vortex, as shown in figure 2.15. The T vortex interacts with the approaching L vortex from the same side of the plate, and they are shed as a pair in the wake downstream. This interaction between L and T vortices occurs alternately on each side of the plate at the upper and lower trailing edge corners, and results in the formation of a regular vortex street.

Insert vorticity plot from Ohya (1992) showing T vortex.

**Figure 2.15** Vorticity plot showing formation of a vortex at the trailing edge of a rectangular plate (from Ohya *et al.* 1992).

As well as elongated rectangular, H and  $\perp$  sections, Nakamura (1996) found that vortex shedding from a variety of bluff body shapes with extended splitter plates was characterised by the ILEV instability. Consistent with earlier results, the ILEV instability for flow around a circular cylinder with a splitter plate could only sustain shedding of the  $n = 1$  mode at a  $Re$  of 5000 based on cylinder diameter, but the  $n = 2$  mode was observed at  $Re = 1600$ . Another

unrelated example of the ILEV instability was investigated by Nguyen (1990). He found that transverse vibrations of gates used to control open channel flows excited vortex shedding corresponding to ILEV modes 1 and 2.

## **2.5 The effect of periodic flow disturbances on bluff body flows**

The first documented effect of sound on a separating shear layer appears to be that by Leconte (1858) who noticed that certain notes on a violoncello caused a coal flame to jump in response. Almost a century later, Batchelor & Townsend (1945) investigated pure tones emanating from a wind tunnel at the University of Sydney and found them to be caused by an acoustic resonance between the turning vanes at each of the four corners of the tunnel. They noted that the sound wave formation was excited by the vortex shedding from the turning vanes which, in turn, was enhanced by the elastic vibrations of the turning vanes. In 1952, the self destruction of the old Tacoma Narrows bridge (which was graphically captured on film) was caused by wind conditions that resulted in strong vortex shedding from the bridge deck. Because the initial shedding frequency of the vortices was close to various natural structural modes, the bridge began to oscillate at this frequency and then lock the vortex shedding to the bridge oscillations. The last two examples are cases of a fluid elastic oscillation, as defined by Rockwell & Naudascher (1979). The application of a sound field to the flow about an aerofoil has been shown to delay flow separation (DeMeis 1986), allowing the aerofoil to operate efficiently at higher angles of attack than would be possible without the applied sound field.

Aside from being a fundamental challenge to researchers, examples like this provide ample motivation for research aimed at improving our understanding of flow-structure interactions, and how periodic flow perturbations affect the flow about bluff bodies. Some examples of possible flow perturbations are:

- flow induced vibration of a bluff body,
- the forced transverse or in-line vibration of a bluff object,

- applied transverse velocity perturbation to the mean flow field (global perturbation),
- rotational oscillation of a circular cylinder,
- sinusoidally oscillating jet applied directly to the separated shear layer (local perturbation),
- acoustic resonance initiated by vortex shedding and maintained due to favourable geometry.

### **2.5.1 Forced oscillations of bluff bodies**

In order to better understand the mechanisms that influence flow induced oscillations of bluff bodies, a common approach is to control the oscillations in order to eliminate the effects of structural damping and the various structural modes of vibration that can exist for a body, allowing oscillation amplitude and frequency to be varied independently. Reviews by Bearman (1984) and Griffin & Hall (1991) provide an excellent overview of the progress that has been made in this area. As with research on flows over stationary bluff bodies, the majority of work has focussed on circular cylinders and other relatively short bluff bodies, with only a few researchers investigating the effects of oscillating elongated bluff bodies.

Stansby (1976) investigated the effect on the base pressure ( $Cp_b$ ) of a circular cylinder subject to transverse oscillations. He found that the vortex shedding could be phase locked to the cylinder at oscillation frequencies near the natural Strouhal shedding frequency. For a fixed ratio of amplitude of cylinder vibration to cylinder diameter ( $y/d$ ), as the frequency of oscillation ( $f_e$ ) was increased past the natural shedding frequency ( $f_0$ ) of a stationary cylinder, a large phase shift between the cylinder motion and the vortex shedding was observed to coincide with a sudden change in  $Cp_b$  (see figure 2.16).

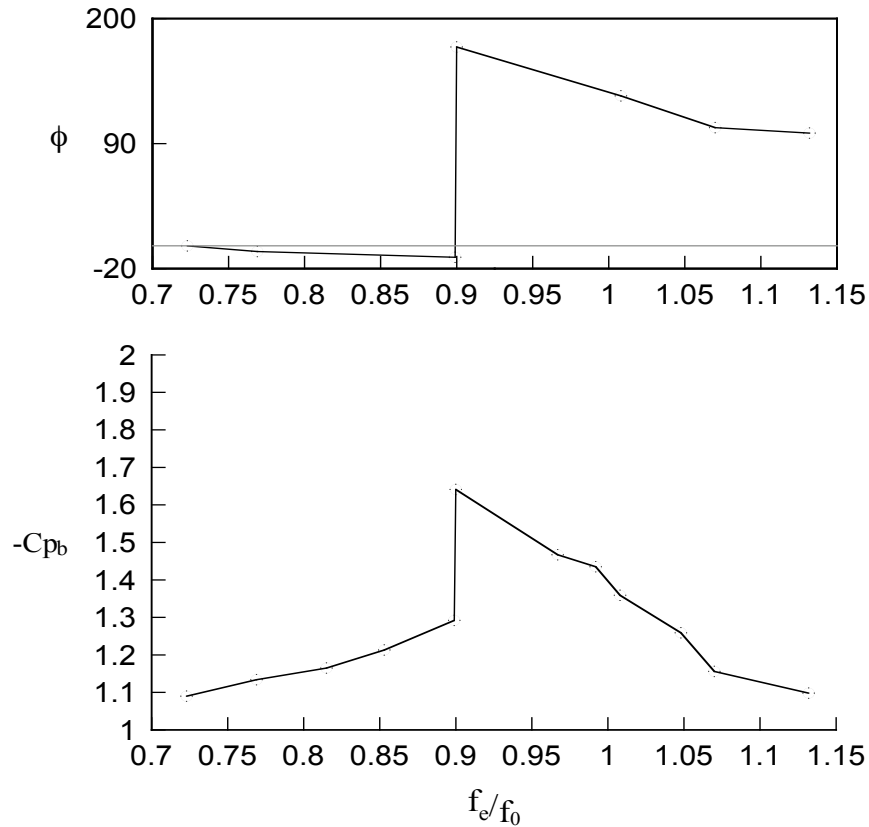


**Figure 2.16** Variation of (a) vortex shedding phase angle ( $\phi$ ) with cylinder frequency, (b) Base pressure coefficient ( $C_{pb}$ ) with cylinder frequency; both for  $y/d = 0.29$  (from Stansby 1976).

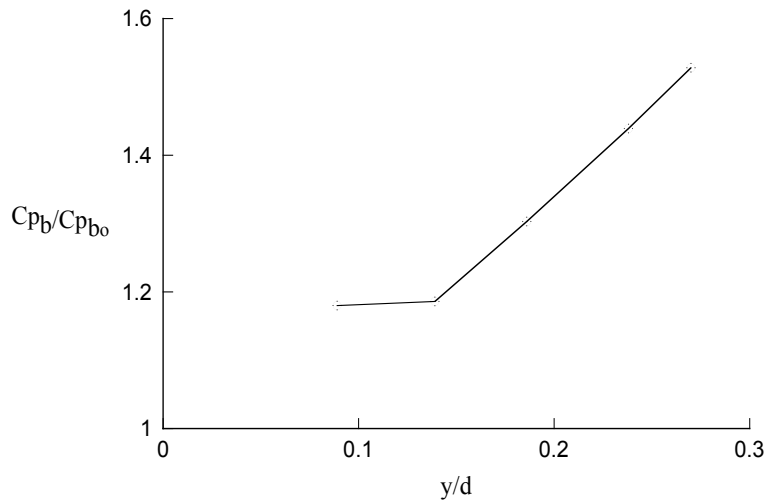


**Figure 2.17** Variation of the ratio of minimum base-pressure coefficients associated with an oscillating cylinder to the value for a stationary cylinder, with amplitude of cylinder vibration (from Stansby 1976).

As the ratio  $y/d$  was increased, the size of the change in  $C_{pb}$  was observed to increase (see figure 2.17). One other feature that Stansby did not draw attention to is that as  $y/d$  is increased, the frequency at which the phase jump in vortex shedding occurs decreases.

Stansby also found that by fixing the separation point at  $\theta = \pm 70^\circ$  with a thin circular rod, there was no organised effect due to lock on for  $y/d = 0.10$ , and the value of  $C_{p_b}$  is always close to the value for the stationary cylinder.

The results of Davies (1976) for a **D**-section cylinder show that for a value of  $y/d = 0.2$ , with the vortex shedding phase locked to the cylinder motion there was an increase in circulation ( $\Gamma_v/UD$ ) of the shed vortices of 35%. This result is consistent with the findings of Greenway & Wood (1973) who found that when vortex shedding was phase locked to the trailing edge of a long oscillating plate with an aerofoil leading edge and a rectangular trailing edge, the circulation of vortices in the wake was found to increase significantly. Griffin & Ramberg (1975) showed that there is an inverse relationship between the vortex strength in the wake of an oscillating cylinder and the length of the vortex formation region ( $l_f$ ). The drag coefficient was also found to increase with decreasing vortex formation length, which is consistent with the findings of Bearman (1967b) who studied the effects of base bleed on the drag of stationary bluff bodies.

Recently, there have been several studies on flows about oscillating rectangular cylinders with various  $c/t$  ratios (Bearman & Obasaju (1982); Bearman & Luo (1988), Nakamura & Nakashima (1986), Nakamura & Hirata (1989), Nakamura & Hirata (1991), and Deniz & Staubli (1997)). With the exception of Nakamura & Nakashima (1986) and Deniz & Staubli (1997), all of these studies were on short plates that fall into category I (LEVS) as described by Deniz & Staubli (1997), where there is no flow reattachment on the streamwise stationary bodies, and the interaction of the leading edge shear layers results in the shedding of a Kármán vortex street.

Nakamura & Hirata (1989) looked at the vortex shedding from oscillating rectangular prisms with  $c/t = 0.2-1.0$ , subject to vibrations of amplitude  $y/t = 0.1$ . For all plates tested, perturbations applied near the natural shedding frequency of a stationary rectangular cylinder resulted in the vortex shedding phase locking to the oscillations. For plates shorter than the critical value of  $c/t=0.6$  where for stationary cylinders the base pressure is a minimum, the

application of the oscillations reduced the base pressure. Associated with this was a shortening of the vortex formation length. The cylinder with  $c/t = 0.4$  was found to have the lowest base pressure and thus the highest drag. For the prisms with  $c/t > 0.6$  a recovery in base pressure was observed, as the shear layer-trailing edge interaction was enhanced, resulting in an increased radius of curvature of the shear layers and an increase in vortex formation length. Nakamura and Hirata (1991) showed that both the cylinders with  $c/t = 0.4$  and  $0.6$  showed significant changes in the phase angle between vortex shedding and cylinder oscillation near resonance. Bearman & Obasaju (1982) also observed large changes in the phase angle for square cylinders oscillating with amplitudes  $y/t = 0.05$  and  $y/t = 0.1$  when the frequency of oscillation was near the natural shedding frequency.

Deniz & Staubli (1997) studied the vortex shedding process from an oscillating rectangular prism with  $c/t = 2.0$  at  $Re = 10^5$ . When the oscillation frequency was equal to the Kármán shedding frequency of the stationary body ( $St = 0.078$  based on thickness) the vortex motion synchronised with the oscillations, resulting in increased intensity of shed vortices. There was no phase jump observed between the timing of vortex formation and body oscillation near this frequency. As the oscillation frequency was increased towards the frequency of impinging vortices on the trailing edge, vortices were formed at the trailing edge as well as the leading edge. These leading edge and trailing edge vortices were observed to coalesce and form a large vortex in the wake. When the oscillation frequency equalled the frequency of impinging vortices for a stationary cylinder, a phase jump between the lift forces on the body and the body motion was observed, due to a change in the timing of the formation of vortices at the trailing edge. The coalescence of trailing edge vortices with vortices of the same rotation from the leading edge was still observed to occur near the trailing edge of the cylinder. With further increases in oscillation frequency, the interaction between vortices formed on the same side of the cylinder at the leading and trailing edges respectively was delayed until after both vortices had been shed into the wake.

The process of vortex shedding from an oscillating rectangular trailing edge of a long plate fitted with an elliptical leading edge was investigated by Lotfy & Rockwell (1993). Over a

relatively narrow frequency range ( $0.95 \leq f_e/f_0 \leq 1.05$ ) (where  $f_e$  = oscillation frequency and  $f_0$  = natural shedding frequency of a stationary model) vortex shedding was observed to be phase locked to the trailing edge oscillations. The term phase locked means that the shedding pattern is highly repeatable from cycle to cycle. Over this frequency range, the small changes in  $f_e/f_0$  resulted in a change of almost  $180^\circ$  in the phase of vortex formation with regard to the trailing edge motion. Lotfy & Rockwell used a time clock analogy to explain the differences in phase angle, due to changes in the times required for vortex formation and departure from the trailing edge.

For frequencies outside this range ( $0.50 \leq f_e/f_0 < 0.95$  and  $1.05 < f_e/f_0 \leq 2.0$ ), the flow structure is not phase-locked to the trailing edge motion. A modulated flow structure is observed, as illustrated by the flow visualisation in figure 2.18. Each image is separated by one edge oscillation cycle, with the trailing edge at its uppermost position  $+\eta_{\max}$ . It takes a number of cycles for the large scale vortex U shed from the upper edge to form again at the same position. This is due to mode competition that occurs between the self excited global instability frequency  $f_0$  of vortex shedding for the stationary plate, and the perturbation frequency  $f_e$ . The wake frequency is equivalent to  $f_0$ , but the flow structure is modulated due to perturbations produced by the edge at the frequency  $f_e$ . This effect is illustrated in figure 2.19, which shows a comparison between the velocity fluctuation signal  $u(t)$  and the edge displacement signal.

For oscillating bluff bodies of various shapes, one common feature is that over a narrow range of frequencies of oscillation near the natural vortex shedding frequency of the stationary body, the vortex shedding will synchronise, or phase lock, with the body motion. Over this range of frequencies, large changes in the phase relationship between vortex shedding and body motion can be seen, although the occurrence and nature of the phase shift has been shown to be highly dependent on the afterbody geometry (Ongoren & Rockwell 1988). Substantial changes in the base pressure coefficient for short bluff bodies are also observed to coincide with this phase change if there is no interference on the vortex formation from the leading edge by the downstream surfaces of the body. For a bluff body with a significant

afterbody length, there is in fact no phase shift in vortex shedding from the leading edge observed as the body oscillation frequency is varied (Ongoren & Rockwell 1988).

### **2.5.2 Acoustic resonance associated with vortex shedding**

Until Parker (1966), the occurrence of resonance for plates mounted parallel to an airstream had been attributed to the natural vortex shedding frequency coinciding with a natural frequency of vibration for the plates. Parker performed a series of tests with a cascade of flat plates mounted in a wind tunnel (see figure 2.20) and showed that the acoustic resonances detected in the tunnel at various flow speeds were purely aerodynamic in nature. These resonances occurred when the acoustic wavelength associated with the vortex shedding from the trailing edge matched an integral multiple of the distance between the plates.

**Insert fig 2(a) from Lotfy & Rockwell,  
showing flow vis of shedding.**

**Figure 2.18** Downstream movement of vortex pattern during one cycle of modulation. Photos represent vortex pattern for successive edge oscillation cycles at  $f_e/f_o = 0.87$ . All photos taken at maximum positive position  $+\eta_{\max}$  of edge. Distance  $x_v$  is streamwise displacement,  $T$  is trailing edge thickness and  $N$  is number of cycles of edge oscillation (from Lotfy & Rockwell 1993).

Insert graph here (fig 3 from Lotfy & Rockwell 1993)  
showing modulated shedding from oscillating trailing edge.

**Figure 2.19** Modulated velocity signal  $u(t)$  in comparison with edge displacement signal  $\eta(t)$  and resultant phase difference  $(\phi_u - \phi_\eta)$  at frequency ratio  $f_c/f_o = 0.87$  (from Lotfy & Rockwell 1993).

Insert picture here (from Parker 1966)

**Figure 2.20** Experimental arrangement of parallel flat plates used by Parker (1966).

The importance of measuring the acoustic field inside the working section of a closed wind tunnel with a microphone was stressed by Welsh *et al.* (1990) when they summarised much of the research concerning the effect of sound on flow from bluff body objects. They stated that velocity perturbation levels as low as 0.1% compared to the free stream velocity can alter both the flow and the heat transfer characteristics without being obvious to the experimenter.

Welsh & Gibson (1979) performed a series of experiments on a square leading edge plate with  $c/t = 5$  in a duct, that initiated a sequence of studies at the CSIRO Highett into the effect of sound on flow past flat plates. In this study, they found that complex acoustic duct modes could be generated as a result of vortex shedding from the flat plate, with acoustic pressure levels as high as 146dB (*re* 20  $\mu$ Pa).

For most flow velocities tested, vortex shedding occurred at the natural plate shedding frequency. However, with the plate located in the centre of the duct, there were two distinct flow velocity regimes that were associated with loud acoustic resonance (see figure 2.21). For one of these regimes, the natural shedding frequency of the plate is equal to or slightly less than the Parker  $\beta$ -mode resonant frequency of the duct (see figure 2.22). The other regime occurred when the natural vortex shedding frequency was a subharmonic of the  $\beta$ -mode resonant frequency, and a step change in shedding frequency to the resonant

frequency resulted from the resonant sound “feeding back” onto the leading edge separating shear layer to lock the vortex shedding at this frequency.

Insert graph here (from Welsh & Gibson showing shedding  $St$  vs flow velocity, & 2 regions of flow lock on)

**Figure 2.21** The effect of flow velocity on acoustic resonance and vortex shedding frequency from a blunt flat plate mounted in a duct (from Welsh & Gibson 1979).

Insert diagram showing  $\beta$  mode of acoustic resonance in a duct

**Figure 2.22**  $\beta$ -mode acoustic field for rectangular plates mounted in a duct. Arrows show local direction and magnitude of the acoustic particle velocities; curved solid lines show isobars;  $\diamond$ , maximum RMS acoustic pressure.

The acoustic feedback that Welsh & Gibson (1979) noticed was shown to have its source at the trailing edge of the plate by Stokes & Welsh (1986). Using a potential flow model they

were able to show that vortices passing the trailing edge of the plate can produce large instantaneous contributions to the net acoustic power, because the directions of vortex motion and acoustic particle velocity are approximately orthogonal. The sign of acoustic power generated by a vortex as it is convected past the trailing edge depends on the phase in the acoustic resonance cycle at which the vortex passes the trailing edge. Since the resonant frequency of the duct is approximately constant, and the convection velocity of vortices once shed from the leading edge separation bubble is approximately constant, there exists discrete vortex shedding  $St$  at which resonance occurs. Although the vortex shedding mechanisms that govern vortex shedding from rectangular plates in the presence of a resonant acoustic field and the ILEV instability mechanism that occurs naturally at low  $Re$  are different, the feedback pressure pulse in each case is initiated as an L vortex passes the trailing edge of the plate. This is the reason for the similarity between the vortex shedding  $St$  for the two seemingly unrelated flows (see figure 2.14); this will be discussed in more detail in chapter 4.

Plates with rectangular leading and trailing edges can generate resonances at several discrete frequencies due to the separation of the vortex formation region at the leading edge and the acoustic feedback source at the trailing edge. In contrast, plates with semi-circular leading edges can only generate resonances over one range of flow velocity because they generate vortices at the same location as they generate sound (Welsh *et al.* 1984).

Stoneman *et al.* (1988) were able to modify the vortex shedding about a plate in a duct by placing a second plate downstream in tandem. For some velocities tested, the  $\beta$ -mode resonant field that existed with a single plate in the duct was suppressed by the placement of the second plate downstream, while at other velocities, resonances were found to occur at velocities that would not have generated resonance from a single plate. They found that the effect of the downstream plate depended on the spacing between the two plates ( $x/t$ ), based on the thickness of the upstream plate. At the velocity corresponding to loud acoustic resonance from the single plate, the SPL in the duct was observed to vary with the spacing of the plates in a periodic manner, showing maxima at some values of  $x/t$ , while for other values of  $x/t$ , the resonant shedding was suppressed and normal vortex shedding was resumed without

resonance. As can be seen from figure 2.23, the spacing between these maxima was equal to approximately  $x/t=3.75$ .

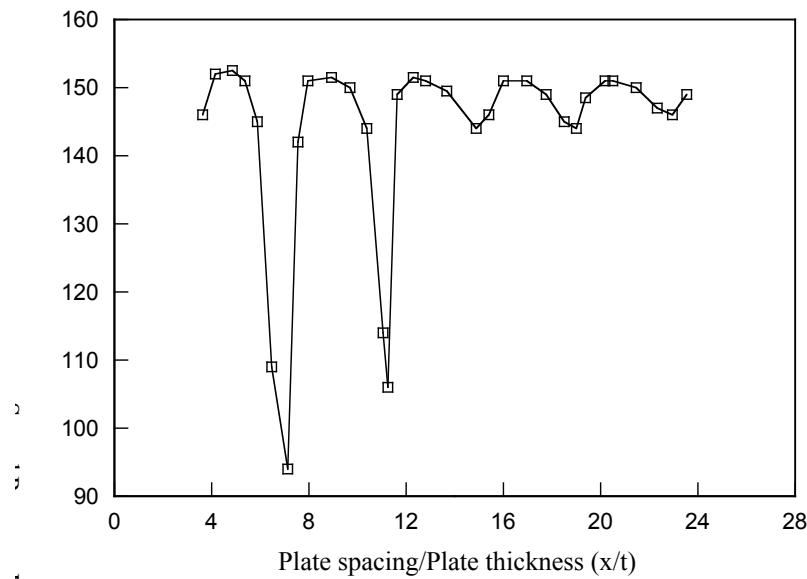


**Figure 2.23** Variation of SPL (at acoustic resonant frequency) with spacing between plates at a flow velocity of  $25.1 \text{ ms}^{-1}$  (from Stoneman *et al.* 1988).

Greenway & Wood (1973) observed resonant shedding from a plate in a duct with an elliptical leading edge and a rectangular trailing edge. They used a towing tank with a similar plate that was oscillated in a direction transverse to the mean flow direction to perform flow visualisation experiments and measure the circulation of vortices shed from the trailing edge using an early form of PIV. When the plate was oscillated at the natural vortex shedding frequency of a stationary plate, the trailing edge shedding was phase-locked to the oscillations and the circulation of the trailing edge vortex shedding increased significantly. Flow visualisation showed that the correlation of vortex shedding across the span was increased, and the vortices formed closer to the trailing edge of the body.

### 2.5.3 The effect of external velocity perturbations on vortex shedding

Blevins (1985) investigated the effect of a transverse sound field on vortex shedding from circular cylinders. The motivation for investigating the effect of sound on vortex shedding was to understand the acoustic feedback which occurs when vortex induced sound reflects from large stationary surfaces back to the cylinder surface. This sound reflection and feedback mechanism has been reported to be responsible for intense noise and vibration of

some tube-and-shell heat exchangers found in large power plants, often at amplitudes high enough to cause structural damage to the heat exchangers. Blevins found that vortex shedding from a cylinder could be phase locked to an applied sound field over a range of frequencies near the natural shedding frequency of the cylinder. When this happened, the coherence of the vortex shedding across the span increased substantially. As the sound pressure levels applied to the flow about the cylinder were increased, so too was the range of frequencies that the vortex shedding could be phase locked to the sound field. Blevins also found that it was the acoustic particle velocity which was responsible for the locking on of vortex shedding at the sound frequency, not the sound pressure fluctuations.

Knisely *et al.* (1986) investigated the effect of in-line velocity perturbations on vortex shedding from rectangular cylinders. For a cylinder with  $c/t=0.5$ , velocity perturbations of amplitude 1% of the free stream velocity could result in a decrease in base pressure of 18% compared to the value for steady flow. This decrease occurred when the perturbation frequency was equal to either twice or four times the natural vortex shedding frequency of the cylinder. Flow visualisation showed that associated with the decrease in base pressure there was an increase in shear layer curvature, a corresponding decrease in formation length, and an increase in the strength of vortex shedding. With perturbations applied at twice the natural shedding frequency, vortices were shed alternately from each side of the plate, one per cycle.

The effect of local velocity perturbations applied to the separated shear layer originating from a cylinder with its axis parallel to the mean flow has been investigated by Sigurdson & Roshko (1985). They observed that the pressure coefficient under the separation bubble and the time mean reattachment length of the shear layer were always decreased in the presence of the local velocity perturbations. The maximum change in pressure under the separation bubble occurred for perturbations applied at frequencies corresponding to wavelengths of vortex shedding similar to the separation bubble height. At high  $Re$ , these frequencies were lower than those of the initial Kelvin-Helmholtz instability, and corresponded to the frequency of the shedding type instability of the separation bubble. Table 2.1 shows that as the perturbation level was increased, the minimum pressure under the separation bubble

became more negative, and the reattachment length was also reduced for perturbations applied near the separation bubble shedding frequency.

Forcing level (% of free stream velocity)	$\% \Delta C_{p_s}$	$\% \Delta X_R/d$
4%	-10%	-19%
7.8%	-17%	-31%

**Table 2.1** Percent change in surface pressure coefficient ( $C_{p_s}$ ) under the separation bubble of an axisymmetric flow and of time mean reattachment length ( $X_R$ ), with perturbation level (from Sigurdson & Roshko 1985).

The flow over a backwards facing step has also been shown to be sensitive to externally applied velocity perturbations. Hasan (1992) found that the separated shear layer exhibited two modes of instability. The shear layer mode of instability scaled with the momentum thickness  $\theta$  at separation, while the step mode of instability scaled with the step height  $h$ . As with other separated and reattaching flows, the effect of applying velocity perturbations was to shift the reattachment point upstream.

Wu *et al.* (1993) used a water tunnel with moveable sidewalls to simulate the Parker  $\beta$ -mode acoustic field found in ducts. They investigated the vortex shedding from a plate with an elliptical leading edge and a rectangular trailing edge in the presence of transverse velocity perturbations applied at the natural shedding frequency. As with flows about circular cylinders, there was found to be a minimum perturbation level of 0.35% of free stream velocity required to phase lock the vortex shedding across the trailing edge of the plate. For natural vortex shedding and with perturbation levels below this threshold, vortex shedding was not well correlated across the span. For perturbation levels above the lock in threshold level, vortex shedding was well correlated across the span, giving insight into how the resonant sound field reported by Welsh *et al.* (1984) can enhance vortex shedding.

Wu *et al.* (1991) also investigated the wake oscillations due to the impingement of a laminar wake from an aerofoil on a second aerofoil placed downstream in tandem. Johnson & Loehrke (1984) investigated this problem, and showed that when the boundary layer from the upstream plate is laminar, a vortex impingement feedback mechanism is responsible for unsteadiness in the wake. Wu *et al.* (1991) were able to show that the impingement feedback

mechanism could be overridden by transverse velocity perturbations, with vortices being forced to shed at the applied oscillation frequency.

Parker & Welsh (1983) were able to simulate the Parker  $\beta$ -mode acoustic field that occurs in ducts by placing a plate in an open jet flow, and locating loudspeakers on either side of the plate. This gave them the added freedom of being able to vary the sound amplitude and frequency independently. They found that vortex shedding from the leading edge of rectangular plates with  $c/t$  in regime (c) could be locked to the applied sound frequency over a wide range of acoustic Strouhal numbers ( $St_p$ ), and that a regular vortex street was shed at the sound frequency for acoustic  $St_a$  between 0.05 and 0.25 based on plate thickness. When this occurred, the length of the separation bubble always decreased, and was found to oscillate at the applied sound frequency. They also found that the leading edge vortex shedding could only be locked to the sound frequency for plates in regimes (b) and (c), where periodic or permanent reattachment of the separated shear layer on the plate surface occurred. For the shorter plates, the applied sound field had no measurable effect on the vortex shedding process.

The effect of sound on heat transfer from bodies under flow separation has also been extensively studied. Richardson (1967) found that the heat transfer rate from tubes can be increased in the presence of an ambient sound field. Cooper *et al.* (1986) studied the effect of sound on the heat transfer rate from a rectangular flat plate and found that the overall heat transfer coefficient of the plate increased with the application of sound. They showed that the heat transfer coefficient was essentially only a function of the time mean reattachment length of the separation bubble, and also noticed that the aerodynamic drag on the plate generally increased when sound was applied. It was this finding that provided the motivation for this investigation, to gain insight into the mechanism that controls vortex shedding from elongated rectangular prisms in the presence of a transverse velocity perturbation, and thus understand how the base pressure is affected by the sound field.

Preliminary results were reported by Hourigan *et al.* (1993), as shown in figure 4.24. Large increases in base suction ( $-Cp_b$ ) were observed for plates with  $c/t = 10$  and 15 when the perturbation Strouhal number ( $St_p$ ) was equal to about 0.17, and the velocity perturbation level ( $u'/U_\infty$ ) was approximately 7%. However, there was found to be a strong dependence on  $c/t$ . A third plate with  $c/t = 13$  showed two smaller peaks in  $Cp_b$  at  $St_p$  of approximately 0.15 and 0.19, while there was a recovery in  $Cp_b$  at  $St_p = 0.17$ . It was hypothesised that the plate chord changes the position in the acoustic phase at which the leading edge vortices arrive at the trailing edge, and that interference with the trailing edge vortex shedding may then be responsible for the variations in  $Cp_b$ .

**Figure 4.24** Variation of  $Cp_b$  with  $St_p$  for rectangular plates of different  $c/t$  ratios in the presence of 7% transverse velocity perturbation.



### **3. Experimental Apparatus and Method**

The experiments were all performed in the Fluid Dynamics Laboratories of the CSIRO's Division of Building, Construction and Engineering, Highett. Two test rigs were used; an open jet wind tunnel for measuring surface pressures and flow visualisation using a smoke wire technique, and a closed circuit water tunnel for flow visualisation and Particle Image Velocimetry (PIV) experiments.

#### **3.1 Open Jet Wind Tunnel**

##### **3.1.1 Tunnel Design**

The wind tunnel used was a blow-down, open jet tunnel which was designed and constructed at the CSIRO Division of Building, Construction and Engineering, Highett. An open jet wind tunnel was used rather than a closed wall tunnel, to eliminate the possibility of acoustic resonances that can be excited by vortex shedding from bluff bodies in enclosed ducts (Welsh & Gibson 1979). The main drawback associated with the use of an open jet tunnel is the inherently higher free stream turbulence level compared to a conventional enclosed draw down type tunnel.

The wind tunnel is illustrated in figure 3.1. Air is drawn into the wind tunnel through a BS848 conical inlet. The conical inlet has four surface pressure tappings placed 100mm downstream of the inlet, and contains a honeycomb to minimise swirl in the inlet. Using these pressure tappings, the velocity in the working section can be calibrated to the pressure drop across the conical inlet. Air flow is supplied by a Richardson Pacific 11 blade centrifugal fan powered by a variable speed three phase A.C. motor controller. Flow from the fan passes through a wide angle diffuser containing four perforated plates, into a settling chamber containing a honeycomb and four nylon screens. It then passes through an 8:1 contraction into a 244mm by 244mm square outlet from which it exits to form a free jet. The tunnel could operate over a jet velocity range of 0 to 15ms<sup>-1</sup>.

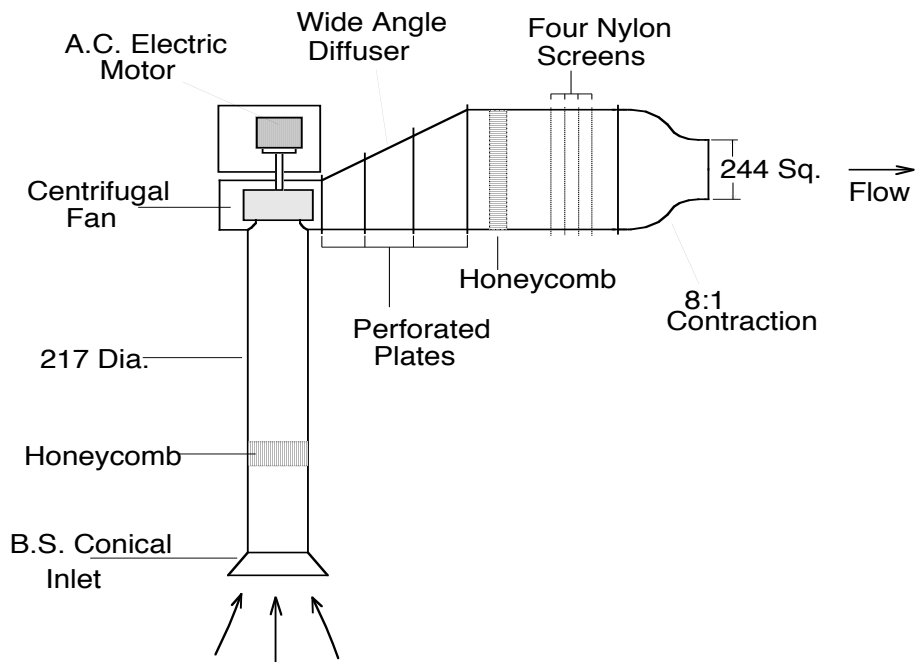


**Figure 3.1** Schematic of Open Jet Wind Tunnel.

A photograph of the working section (figure 3.2) and the illustration (figure 3.3) shows the location of the model in the working section, and the loudspeakers either side of the model to generate the transverse velocity perturbation.

Insert photo here  
of Wind Tunnel Working Section

**Figure 3.2** Photograph of wind tunnel working section.

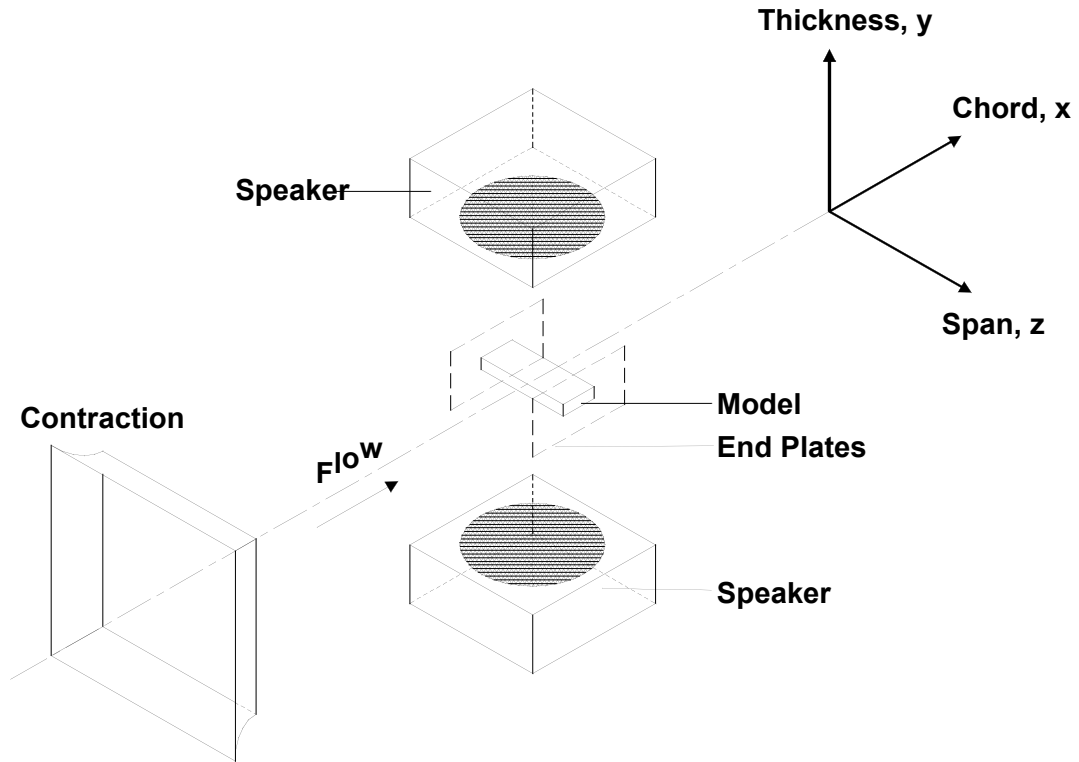


**Figure 3.3** Schematic of wind tunnel working section.

### 3.1.2 Tunnel Characteristics

#### 3.1.2.1 Velocity Profile

The uniformity of the airflow across the tunnel outlet was established by measuring the dynamic pressure with a pitot tube mounted on an X-Y traverse, at a series of regularly spaced points across the working section. The dynamic pressures measured were converted to velocities using equation (3.1), and the velocity was found to be constant to within  $\pm 0.5\%$  across the central core of the jet. Figure 3.4 shows the variation of tunnel velocity with position across the jet, taken at the horizontal centre span with the tunnel velocity held constant at  $11 \text{ ms}^{-1}$ , to within  $\pm 0.1 \text{ ms}^{-1}$ . For all experiments, the models were always placed entirely within the core of the jet.

$$P_{\text{dynamic}} = 1/2 \rho_{\text{air}} U_{\infty}^2 \quad (3.1)$$

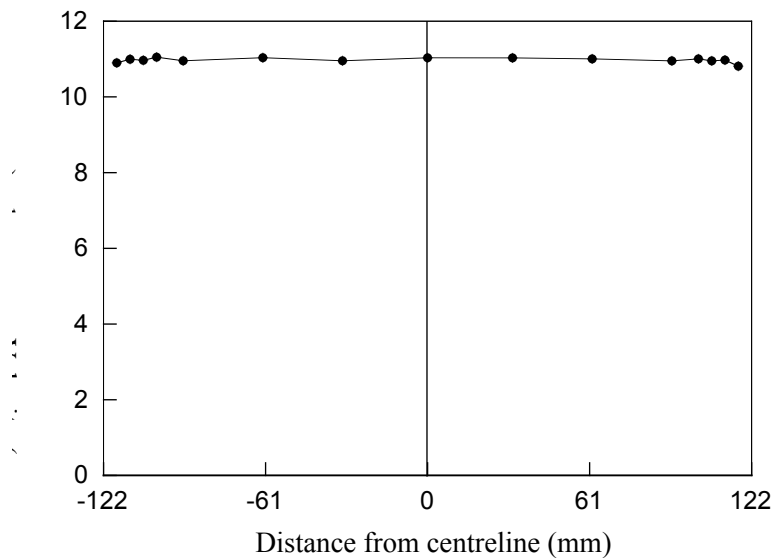


**Figure 3.4** Velocity profile across horizontal centre span of open jet.

### 3.1.2.2 Longitudinal turbulence intensity

A TSI hot wire probe was used to measure the velocity spectra and turbulence level of the free jet. Details of the hot wire anemometer are given later in section 3.1.3.3. The hot wire signal was digitally sampled, and converted to binary form. The turbulence level and energy spectra were calculated using the method described by Soria and Norton (1990). The area under the plot of Spectral Density vs Frequency represents the rms component of velocity, from which the turbulence intensity can be calculated.

The contribution to the rms velocity from the very low frequency components was found to be significant in many cases. Because any components less than 1 Hz are not regarded as turbulence, they were removed from the initial spectra, and the turbulence levels re-calculated. When calculating the turbulence level in the free jet, as well as removing any low frequency components from the spectra, a narrow band 50 Hz spike due to interference from the 240V, 50 Hz AC mains supply was observed in the spectra and also removed. This was achieved by setting the component of spectral density at 50 Hz to be the numerical average of the two components to either side. This method proved satisfactory in this case, as there were no major components at 50 Hz. However, care was taken when performing this step to make sure no information was lost from the original data by averaging the 50 Hz

component. To ensure that the spectral component observed at 50 Hz was due to the 50 Hz power supply and not a flow instability, the turbulence spectra at three different velocities ( $9 \text{ ms}^{-1}$ ,  $10 \text{ ms}^{-1}$  and  $11 \text{ ms}^{-1}$ ) were compared. All three showed a spectral peak at 50 Hz, with no other spectral components within  $\pm 6 \text{ Hz}$ .

The power density spectrums in figure 3.5 below show the variation of the energy spectrums with streamwise distance from the outlet of the free jet, measured with the jet velocity at  $10 \text{ ms}^{-1}$ . The major spectral components are seen to lie between about 5 Hz and 50 Hz

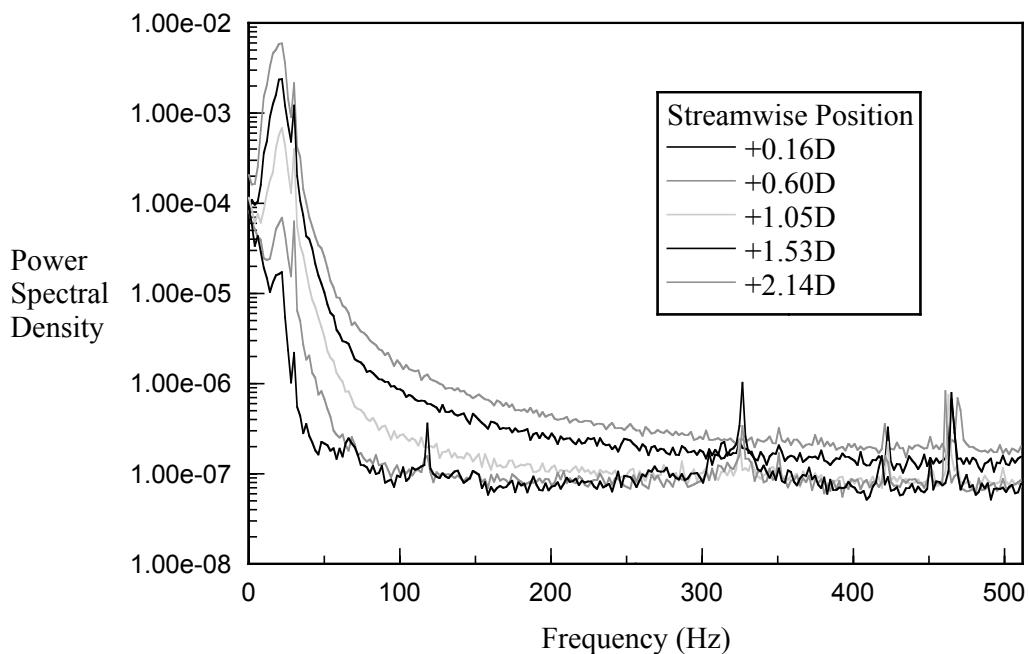


**Figure 3.5** Variation of Turbulence Spectra with Streamwise distance from the jet outlet.

Figure 3.6 shows how the longitudinal turbulence intensity ( $u'/U_\infty$ ) along the centre line of the jet varies with the streamwise distance from the tunnel outlet. The minimum turbulence level measured was 0.25% adjacent to the tunnel exit for velocities between  $6 \text{ ms}^{-1}$  and  $12 \text{ ms}^{-1}$  (with components less than  $1 \text{ Hz}$  filtered out). This increased to 1.0% at a distance of 1 outlet diameter downstream, and reached about 2.5% at the furthest point downstream at a distance of 2 outlet diameters. This variation of turbulence level is consistent with that expected of an open jet, and matches closely the results obtained by Michel & Froebel (1988).

They found that the increase in turbulence level in the open jet can be attributed to instabilities in the shear layers bounding the jet, magnifying with streamwise distance.

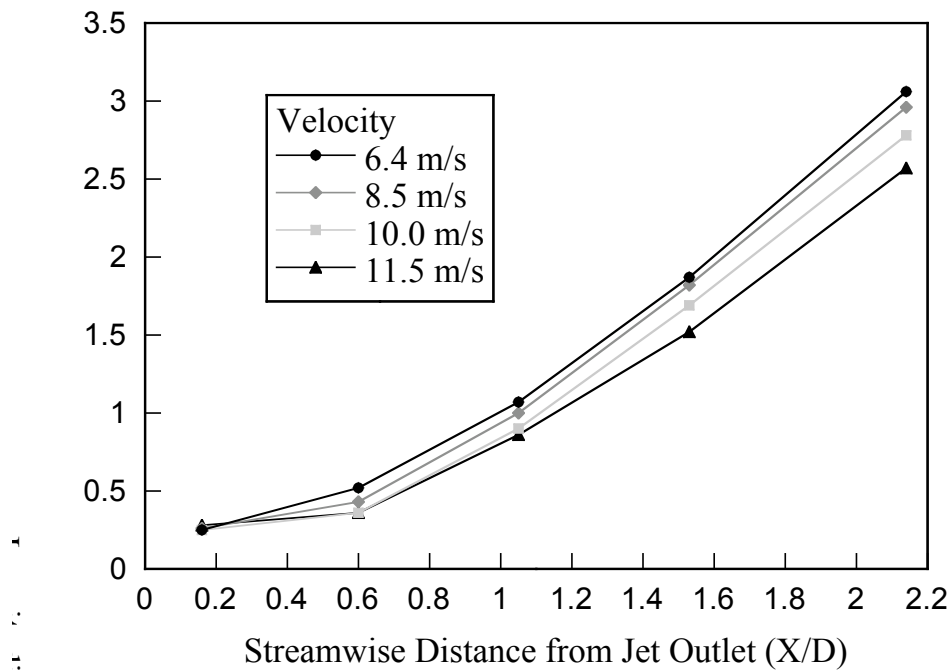


**Figure 3.6** Variation of turbulence intensity with streamwise distance from the outlet

### 3.1.3 Experimental Instrumentation and Models

#### 3.1.3.1 Data Acquisition and Processing

All wind tunnel data were digitally sampled using a Boston Technologies PC-30DS 12 bit Analogue to Digital (A/D) conversion board, which was interfaced with a 486 PC. The input range of the A/D board was -5V to +5V, giving a resolution of 2.44mV per bit. Eight A/D channels were available on the Boston A/D board, with the computer software able to control sample size and frequency. The maximum sample frequency was 100 kHz, while the sample size was limited by the available memory on the PC. Figure 3.7 shows a block diagram of the arrangement of experimental apparatus connected to the PC via the Boston A/D board. The Boston A/D board also had four digital interfaces, one of which was used to control the Scannivalve. The Scannivalve was used to connect the Setra 239E pressure transducer to the pressure tappings on the wind tunnel models, one at a time.



allowing the pressure transducer to be calibrated against the Betz manometer over its entire working range. Figure 3.9 shows the output from the pressure transducer in Pascals, compared to the pressure measured by the Betz manometer. A straight line was fitted through the data points using a least squares fit, with a correlation coefficient of 0.99998. Pressures measured with the Setra 239E pressure transducer were accurate to within 0.2 Pa (see Appendix 1).

The Setra 261-1 transducer measured the pressure drop across the conical inlet. Since this is proportional to the square of the velocity at the tunnel outlet, it allowed the pressure transducer attached to the conical inlet to be calibrated to allow the PC to automatically obtain the mean tunnel velocity.

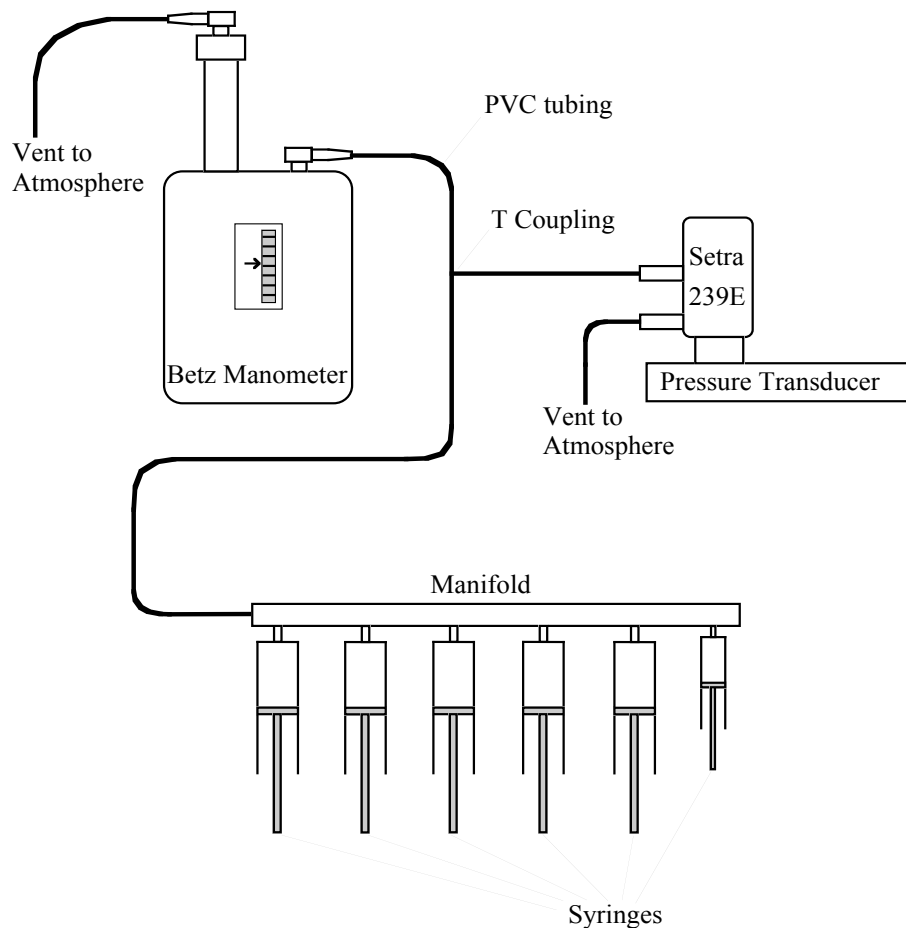


**Figure 3.8** Arrangement for calibration of Setra 239E Pressure Transducer.

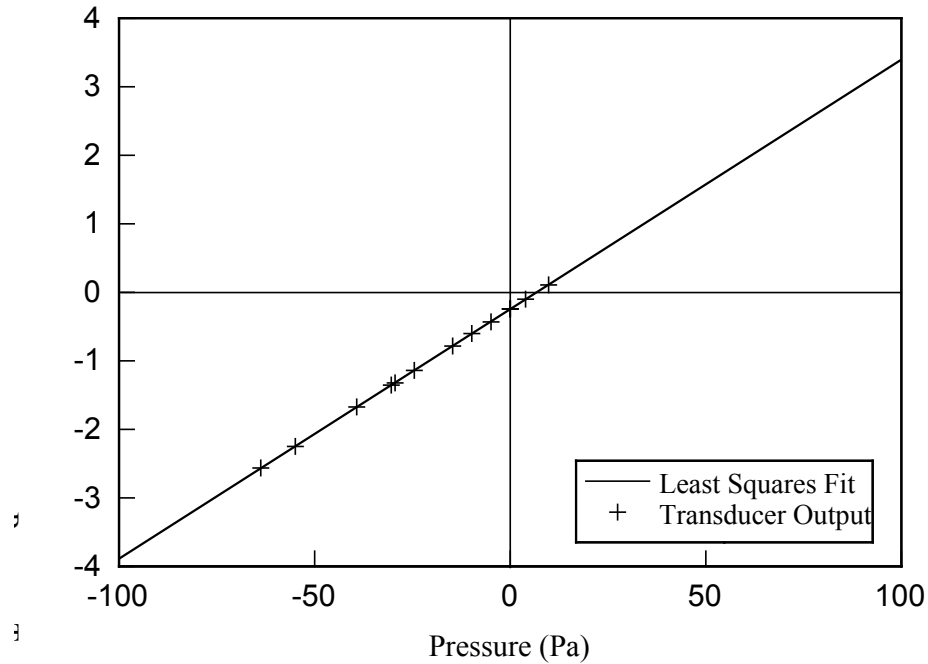


**Figure 3.9** comparison b/w Betz manometer and Setra 239E transducer.

Once the Setra 239E pressure transducer had been calibrated, it was used to calibrate the Setra 261-1 transducer connected to the conical inlet. A pitot tube was located in the centre of the working section, and was connected to the Setra 239E transducer in order to obtain the time mean tunnel velocity. The static pressure was measured from flush pressure tapings placed in the side walls of the outlet section. This allowed the Setra 261-1 transducer to be calibrated to the tunnel velocity over a velocity range from  $6 \text{ ms}^{-1}$  to  $15 \text{ ms}^{-1}$ , with the maximum error in  $U_{\infty}$  being less than 2% (see Appendix 1). Figure 3.10 shows the output from the pressure transducer after converting to metres per second, compared to the velocity calculated from the pressure drop across the pitot static tube according to the equation 3.1.

For both pressure transducers, a least squares linear fit was used to correlate the output voltage from the pressure transducers to the input pressure.

The sampling frequency was 2048 Hz for all surface pressure measurements. A sampling time of four seconds was used when measuring the time-averaged pressure, and the sound pressure level, which gave repeatable results to within 1%. With the vortex shedding frequency never being less than 50Hz, a sample time of four seconds captured data over at least 200 shedding cycles.

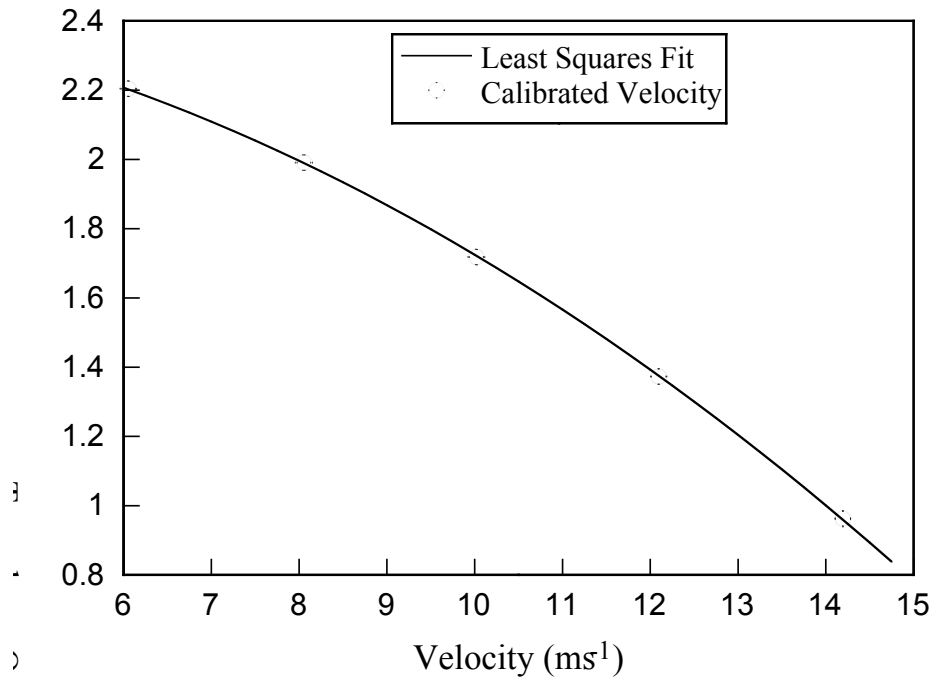


**Figure 3.10** Plot of Open Jet velocity against output from the Setra 261-1 transducer connected to the conical inlet

### 3.1.3.3 Hot Wire Anemometer

A TSI, IFA 100 two channel hot wire anemometer was used in conjunction with a single TSI 1210T1.5 hot wire probe. The diameter of the platinum-rhodium hot wire is 4 $\mu$ m and its length about 2mm, giving an aspect ratio of about 200. The single wire was mounted normal to the oncoming air stream to give a measure of longitudinal turbulence intensity.

The signal from the hot wire was low pass filtered at 500 Hz within the anemometer, and digitally sampled at 1000 Hz with the data acquisition system described in section 3.1.3.1. The sampling frequency of 1000 Hz was chosen in order to avoid aliasing. The hot wire signal was then converted to velocity using the three term calibrating equation recommended by Soria and Norton (1990).

In order to obtain sufficient resolution with the A/D converter when investigating the fluctuating component of velocity, the anemometer gain and offset were set to 20 and 1 respectively. This resulted in the signal covering as much of the -5V to +5V range of the A/D converter as possible.

### 3.1.3.4 *Wind tunnel models*

All the test plates were made from brass, using the Hitachi-Seiki VK45 numerically controlled milling machine in the CSIRO Engineering Workshop at Highett, and have a nominal thickness of 13mm  $\pm$ 0.02mm. Three of these rectangular plates have pressure tappings placed at regular intervals on one side and on the front and rear faces to enable time mean surface pressure coefficients to be measured (see figure 3.11). Of the three, two of them are identical having a  $c/t$  ratio of 3, no pressure tappings on the rear face, and one pressure tapping in the cover plate to aid in aligning the plates with the air flow. The third plate has a  $c/t$  ratio of 6, and has two pressure tappings placed in the cover (one 15mm from the leading edge, one 15mm from the trailing edge) to assist with alignment. All pressure tappings have an internal diameter of 1.0mm, and care was taken to ensure that the tap hole edges were sharp, and that they were flush with the model surface after insertion into the model. A series of spacer plates with no pressure tappings were also constructed having  $c/t$  ratios of 2,3,4,6 and 8. These allowed the overall plate length to be varied from  $6 < c/t < 16$  in integer steps. As well as these basic sections, which have rectangular profiles, two leading edge extensions were constructed; one with a semicircular nose profile and the other with a C4 aerofoil profile (Wallis 1977) to prevent separation before the trailing edge. A semicircular trailing edge extension was also constructed, which contained pressure tappings across the span.

End plates were constructed from 9mm thick perspex, and used in all tests. Figure 3.12 shows the dimensions of the end plates used. Their main function was to keep the acoustic field uniform around the model (Parker & Welsh 1983).

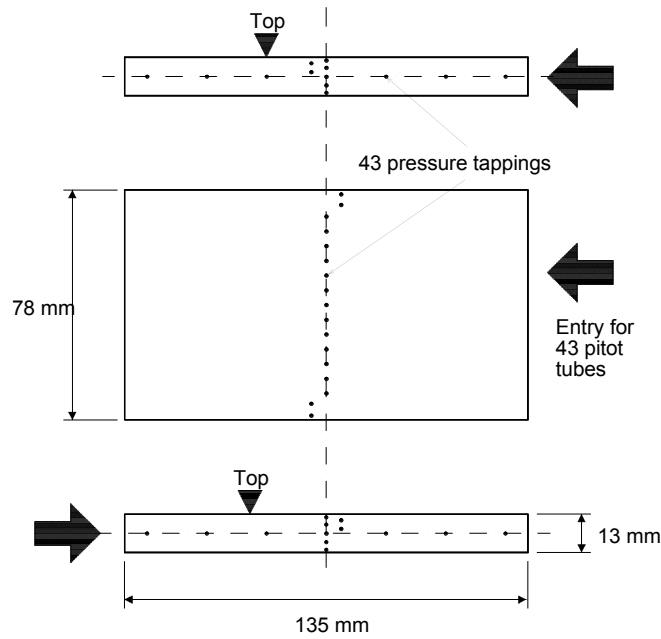


**Figure 3.11** Schematic showing placement of pressure tapings in brass plate.



**Figure 3.12** Illustration of end plates used with brass models in open jet wind tunnel.

### 3.1.3.5 Smoke wire

Flow visualisation was performed in the wind tunnel with the use of a smoke wire technique, described by Corke *et al.* (1977). A schematic of how the system was configured is shown below in figure 3.13.

A thin NiChrome wire of diameter 0.1mm was wiped with a cloth soaked in Castrol white technical oil. The oil subsequently formed into small drops on the wire; when an electric current was passed through the wire, the wire was heated and the oil subsequently vaporised

to form streaks of smoke. For the oil used, a voltage of 35 V proved to give the best smoke density with an air velocity of  $6\text{ms}^{-1}$ . The small wire diameter used was necessary so that the Reynolds number for the thin wire was no more than 40, leaving a steady wake with undistorted streaklines.

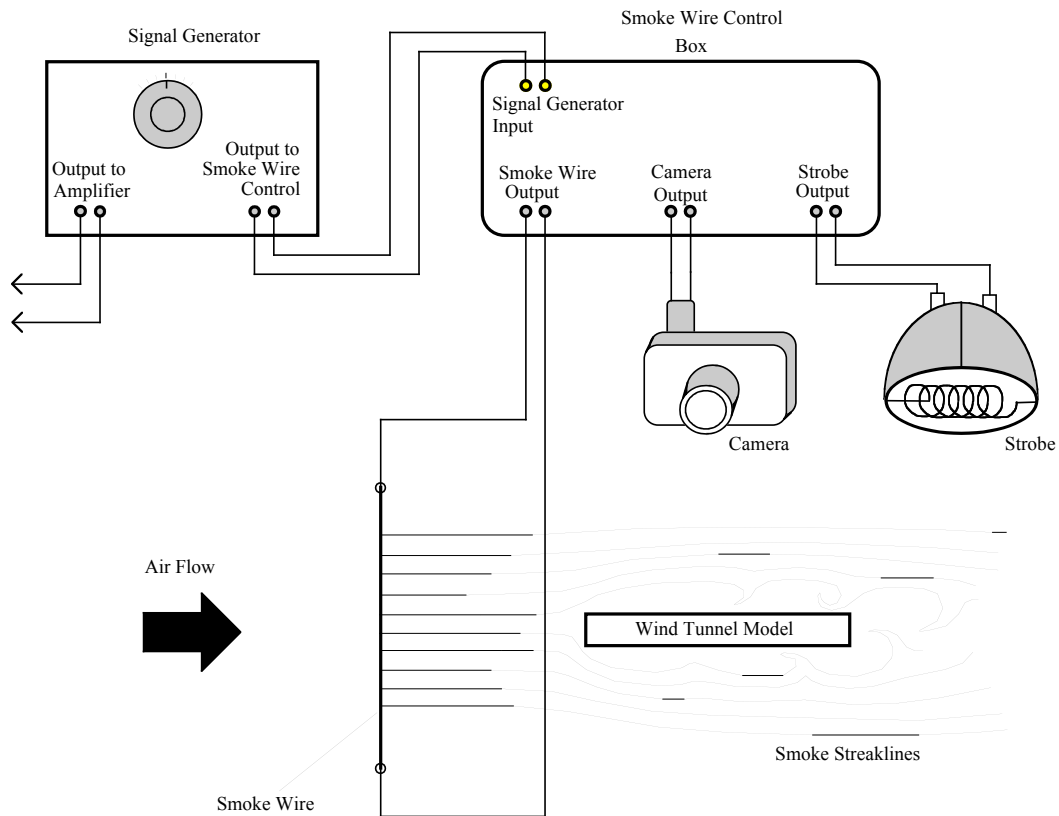


**Figure 3.13** Schematic showing configuration of smoke wire system.

An electronic circuit with a 50 V rectified D.C. power supply was designed at Monash University to supply the voltage across the smoke wire, and to also synchronise the triggering of the camera and strobe. The circuit had the provision for a small “preheat” voltage to be applied to the wire so that the delay between triggering the smoke wire circuit and the smoke actually appearing would be minimised. It was found to be unnecessary due to the small wire size, as the delay between the smoke wire being triggered and the smoke appearing was insignificant. The circuit also took an input in the form of a triangular wave from the signal generator used to generate the sinusoidal signal to drive the loud speakers, so that the strobe

could be triggered at predetermined phase points in the forcing cycle, while the shutter of the camera was open.

A 35mm Nikon F90X Single Lens Reflex camera was used to take the images, with Kodak TMax 400 ASA black and white film being used. A Photo Pro Electronics strobe with an energy output of 1 Joule per flash and a 20  $\mu$ s flash duration was used to illuminate the smoke streaks. The relatively short flash duration was required so that a clear image could be obtained, without blurring of the streaklines. Figure 3.14 below shows a typical image taken using the smoke wire technique.

**Figure 3.14** Flow visualisation using the smoke wire technique.

### **3.1.4 Transverse Velocity Perturbation**

#### ***3.1.4.1 Signal Generator, Amplifier and Speakers***

Loudspeakers were placed 185mm above and 185mm below the plate outside the jet, to generate a transverse velocity perturbation at an adjustable amplitude and frequency (see figure 3.3). With the models mounted midway between the speakers, the transverse velocity perturbation field generated by the speakers was similar to the Parker  $\beta$ -mode acoustic resonant field (Parker 1966) found to occur in ducts (see figure 2.22).

A Wavetek Model 145 20 MHz Pulse/Function Generator was used to generate a sine wave signal at different frequencies. The frequency of the signal was measured using a Venner Electronics Digital Counter Type TSA6636/2, which was connected to the signal generator in parallel with a stereo amplifier. The amplifier used was a YAMAHA stereo amplifier type A-700, while the speakers were a Lorantz Audio 12 inch single cone design, with a frequency range of 50 Hz to 1 kHz. The speakers were connected in antiphase, and could generate sound pressure levels of 120 dB (re 20  $\mu$ Pa) measured at the midchord position on the plate surface, when driven at a frequency of 100 Hz.

#### ***3.1.4.2 Measurement of transverse perturbation using LDV***

In order to allow direct comparison of wind tunnel data with data obtained from other experimental facilities, like the water tunnel, as well as CFD data, the size of the velocity perturbation applied to the mean flow was measured using a Laser Doppler Velocimetry (LDV) system. A TSI System 9100 Helium-Neon LDV system configured in a simple forward scatter arrangement was used, with no beam expansion or frequency shifting as illustrated in figure 3.15. A smoke generator was used to produce seeding particles. In order to achieve a zero mean velocity for the seeding particles in the working section, the entire room that the wind tunnel was in was filled with the seeding particles, which were allowed to settle for a period of several minutes.

Since measurements were being made on the sinusoidal perturbation field, only the maximum perturbation velocity was of interest. Using the LDV system, the highest frequency Doppler burst was measured at each location, in two directions orthogonal to each other. This was achieved using a Hewlett Packard 54600A Digital Storage CRO, which has a digitising frequency of 100 Mhz per channel. The triggering mechanism was set to “single” in order to catch a single Doppler burst. At each location, the first Doppler burst was recorded, its image was saved on the CRO, and when two Doppler bursts with higher frequency were captured, the second one was saved on the CRO. This process continued until over 100 bursts had been captured, with the one stored on the CRO being the highest frequency burst

and hence, representing the peak velocity of the perturbation at that location. To obtain the Doppler frequency, a period of 10 cycles of the burst was measured, and converted to frequency. This reduced the measurement error compared to just measuring the period of a single oscillation, with the measurement error being estimated at  $0.2\mu\text{s}$  in  $100\mu\text{s}$ , or 0.2%.

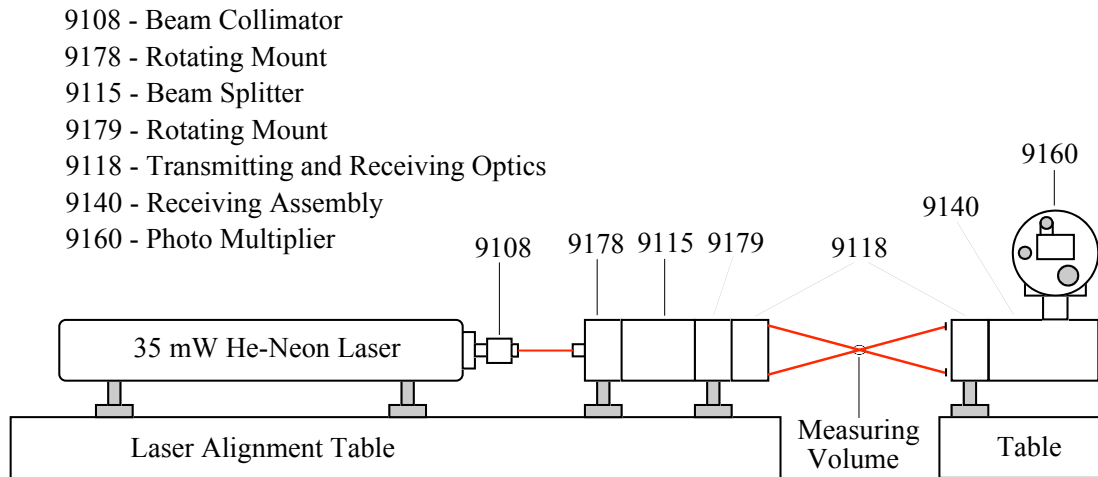


**Figure 3.15** Arrangement of components for the LDV system.

Figure 3.16 shows the perturbation velocity vector field as measured with the LDV system. Once the size of the velocity perturbation had been measured, a probe microphone positioned at the midchord position above the plate surface was then used to ensure that the sound pressure level (SPL) for all subsequent tests was held constant.

**Figure 3.16** Perturbation velocity vector field measured with LDV system.

Because the rms fluctuating pressure ( $P_{\text{rms}}$ ) is directly proportional to the maximum perturbation velocity (Parker and Welsh 1983), the microphone was used to measure the SPL needed for each experiment to generate velocity perturbations of a required amplitude.

## 3.2 Water Tunnel

### 3.2.1 Tunnel Design

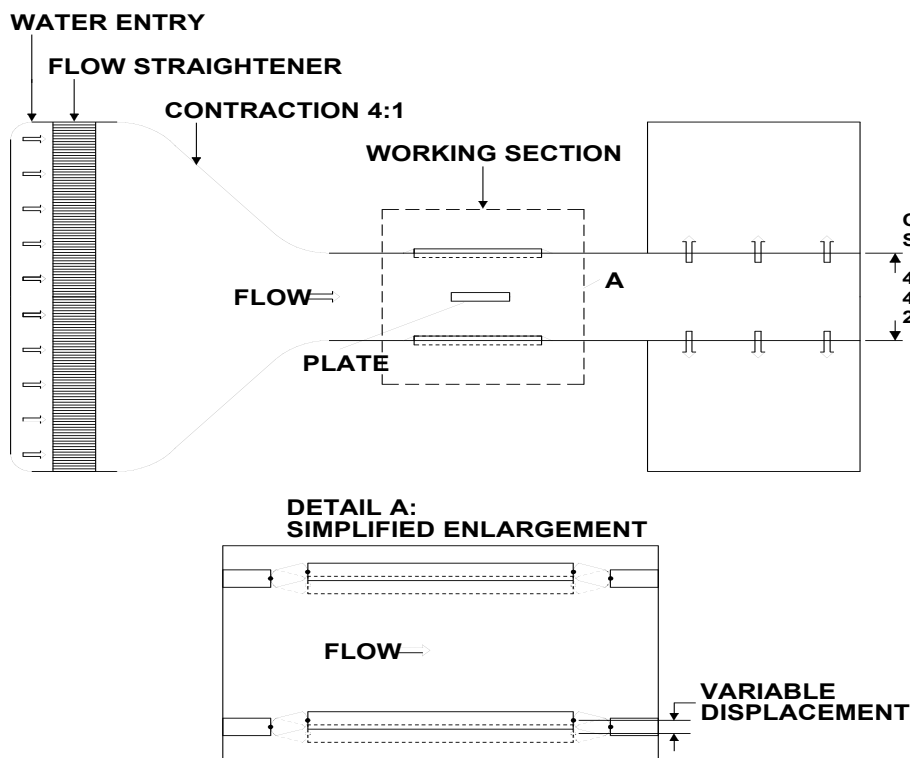
The water tunnel used was a low turbulence closed circuit design, which was designed and constructed at the CSIRO Division of Building, Construction and Engineering, Highett. A photo of the water tunnel is shown in figure 3.17, while a schematic of the water tunnel and working section is shown in figure 3.18.

A pump driven by an AC electric motor is used to generate the mean flow in the tunnel test section. Water is pumped through a diffuser incorporating screens into a settling chamber containing filter material, and a honeycomb section. The water then passes through a two dimensional four-to-one contraction with an outlet dimension of 244mm x 244mm, into a duct having the same cross section dimensions. There are three sections of the duct, all constructed of 20mm thick clear acrylic sheet. The first section is 660mm long, and is followed by the working section which is 770mm long, then a 440mm long section which is connected to an outlet reservoir.

The working section has flexibly mounted side walls to allow a velocity perturbation to be applied in a direction perpendicular to the mean flow. The applied velocity perturbation is similar to that imposed by a resonant acoustic  $\beta$ -mode. The two 400mm long moveable side walls have glass windows, and are rigidly connected to each other and sealed to the remainder of the test section by a thin flexible membrane. Harmonic oscillations of the side walls are produced by a Charles and Hunting variable speed drive made locally in Melbourne. The drive is connected to the sidewall support frame via a crank and connecting rod, which allows a variable stroke. The oscillation amplitude of the side walls can be varied from 0 to 5mm at frequencies between 0 and 6 Hz. A Schlumberger DG5 linear displacement transducer was

used to monitor the oscillating test section wall displacements, the output of which was recorded by the computer via the A/D board described in section 3.1.3.1.

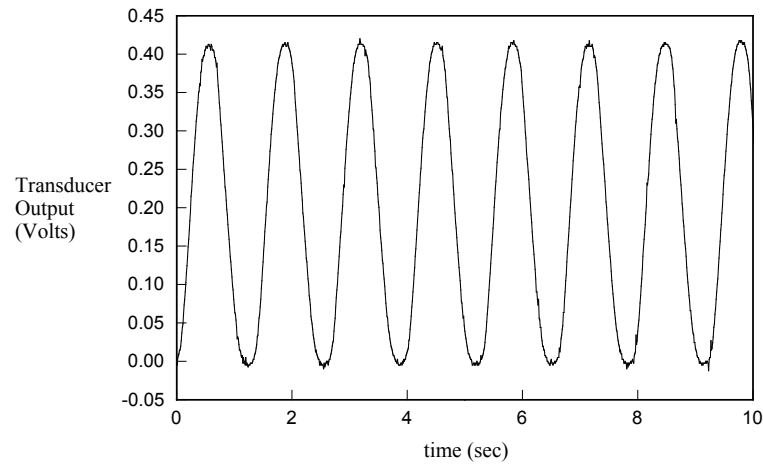
**Figure 3.17** Closed circuit water tunnel used.



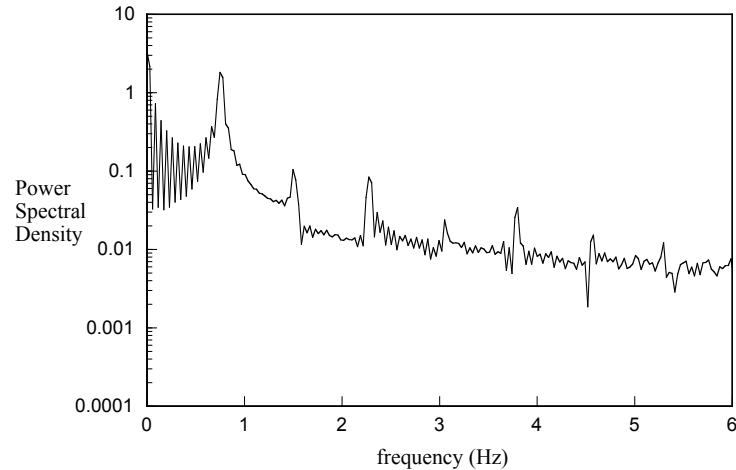
**Figure 3.18** Schematic of water tunnel working section

Figure 3.19 shows a typical output from the linear displacement transducer taken with the sidewalls oscillating at a frequency of 0.75 Hz and an amplitude of 0.4 mm. A fast fourier transform of the signal shown in figure 3.20, has a spectral peak at the side wall oscillation frequency, with the harmonics being at least 25 dB lower. Wu *et al.* (1993) measured the

perturbation velocity about a long plate in the same water tunnel at the CSIRO, and found that the magnitude of the velocity perturbation at the trailing edge was 1.43 times the velocity of the transverse oscillating wall. This allowed the velocity perturbation level about the models to be characterised by simply measuring the amplitude and frequency of the sidewall oscillations.



**Figure 3.19** Output from water tunnel sidewall linear position transducer.



**Figure 3.20** Spectrum of sidewall linear position transducer signal.

With the perturbations being periodic in nature, the phase of the perturbation cycle is defined relative to the perturbation velocity field as shown in figure 3.21. Assuming the perturbations are sinusoidal, the perturbation velocity at any time ( $t$ ) is given by the function  $u(t) = u' \sin(\omega t)$ , where the phase of the perturbation cycle at any time is equal to  $\omega t$ . Thus, a perturbation phase angle of 0 degrees gives the perturbation velocity to be zero but about to increase in the upwards direction, while 90 degrees denotes the maximum perturbation

velocity in the upwards direction. The perturbation phase of a PIV image is denoted by a large filled circle, as shown in figure 3.21 for a phase angle of 90 degrees.

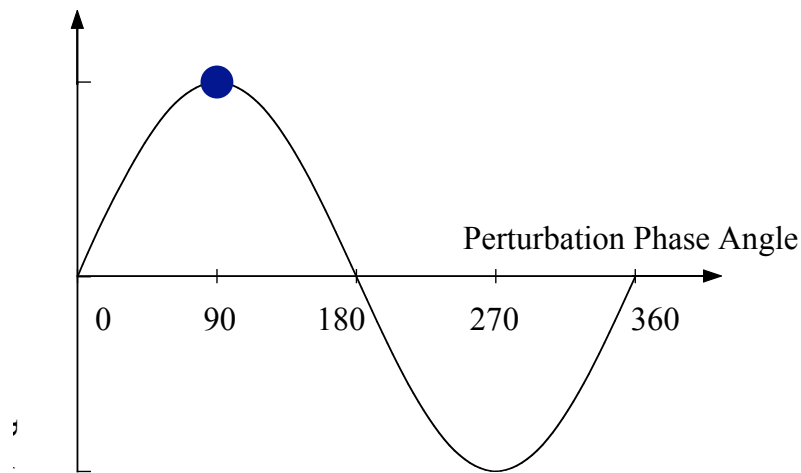


**Figure 3.21** Graph of perturbation velocity vs perturbation phase angle.

### 3.2.2 Tunnel Characteristics

The speed of the motor driving the pump was accurately controlled by a Danfoss AC 3-phase motor controller. The velocity ( $U_\infty$ ) in the working section can be varied between  $0 \text{ ms}^{-1}$  and  $0.4 \text{ ms}^{-1}$ , and the mean velocity variation, measured with a hot film and with PIV measurements, was less than  $\pm 0.5\%$  of  $U_\infty$  across the test section. For the velocities used in the experiments, the mean longitudinal turbulence level was approximately  $0.1\%$  of  $U_\infty$  at the tunnel speed of  $0.1 \text{ m/s}$  when band pass filtered between  $0.08\text{Hz}$  and  $20\text{Hz}$ . No distinct spectral peaks were observable in the natural turbulence spectrum within this frequency range. A full description of the tunnel characteristics is given by Wu *et al.* (1993)

### 3.2.3 Water Tunnel Models

Test plates were made from clear acrylic, in both the CSIRO Engineering Workshop, and the Monash University Mechanical Engineering workshop. All plates used spanned the  $244\text{mm}$  wide working section of the water tunnel. At the CSIRO, a plate with a  $c/t$  ratio of approximately 10 was constructed having a rectangular trailing edge, and a symmetrical C4 aerofoil leading edge profile (Wallis 1977) to prevent flow separation before the trailing edge. The thickness of this plate is  $12.4 \text{ mm}$ .

Five plates with rectangular cross sections were constructed at Monash University with  $c/t$  ratios ranging from 6 to 10 in integer steps. They were all constructed from the same sheet of acrylic, and each had a nominal thickness of 11.8 mm ( $\pm 0.1$  mm). Using these models avoided having to change the tunnel speed in order to keep the  $Re$  constant, and allowed the same relative velocity perturbation level to be easily applied to each model without changing the amplitude of the sidewall oscillation.

All models were located vertically on the centre line of the working section, as shown in figure 3.18. The  $Re$  for the PIV measurements ranged from 490 to 1100, based on plate thickness. The water temperature was approximately constant at 15°C for all experiments.

### 3.3 Particle Image Velocimetry (PIV)

Using the PIV technique, instantaneous velocities of a fluid can be measured over a region illuminated by a two dimensional sheet of light. The film-based high image density PIV technique used will be described in this section. Adrian (1991) reviewed the concept of high image density PIV, and the technique is now widely accepted as a reliable method of obtaining instantaneous velocity data for flows around bluff bodies. More recently, Grant (1997) has reviewed the PIV technique.

The flow was seeded with small flow-following particles, the motion of which are used to determine the flow velocity at discrete points in the fluid. The motion of the particles was recorded on film by pulsing a laser light source several times. Knowing the time between light pulses and the camera magnification, the displacement of particles was determined and, hence, their velocities. As long as the time between light pulses is small compared with time scales of fluid motion, then the time average velocity measured over the duration from the first pulse to the last will be a good approximation of the fluid velocity at the instant the first pulse was initiated. An example of a typical PIV image is shown in figure 3.22.

Film negatives were digitised, and interrogated over a regularly spaced grid of 64 x 64 pixel windows using an auto-correlation technique to determine the displacement between each

exposure within each window. By knowing the time between each exposure on a single frame, the velocity field could be calculated from the displacement field. Because auto-correlation was used, image shifting was employed to resolve near zero flow velocities in the near wake, and overcome the ambiguity associated with flow direction for reversing flows.

**Figure 3.22** PIV image, with image shift employed, of flow about a rectangular plate.

### **3.3.1 Flow seeding and illumination**

The flow was seeded with silver coated hollow glass particles that were  $< 40 \mu\text{m}$  in diameter, and close to neutrally buoyant. In order to minimise errors due to particle slip, it would seem best to choose the smallest particles possible. However, the resolution of the recording device must be considered, as well as the light scattering properties of the particles, which depends on particle size (Adrian 1991). With the largest particles used having a diameter of  $40 \mu\text{m}$ , the maximum particle slip velocity was less than 0.2% of free stream velocity (see Appendix 1).

One of the factors limiting the application of the PIV technique to high  $Re$  flows, is the available light intensity from the source. Insufficient light intensity results in poor data conversion rates, with velocity vectors unable to be resolved at a large number of gridpoints. This happens because the under-illuminated particles are indistinguishable from the background noise. To minimise the chance of this happening, lasers are commonly used in PIV systems, as they provide a high intensity, controllable light source. In this system, the

particles are illuminated using light from a continuous 6 W Argon-Ion laser. In order to obtain a PIV image, the laser light is first passed through a mechanical shutter connected to the 486 PC. The shutter can be controlled to generate laser light pulses with pulse durations of 1ms. A 50  $\mu\text{m}$  diameter multi-mode optical fibre cable was used to transmit the light, which was spread into a thin sheet using a cylindrical lens, and passed through a side wall of the working section. The thickness of the laser sheet was adjusted to 1mm by varying the spacing between the two lenses at the outlet of the fibre optics. Figure 3.23 shows a block diagram of the experimental arrangement used.

One major factor which limited the velocity of flows that could be measured using this system, was the minimum pulse duration obtainable from the mechanical shutter of 1 ms. However, if shorter pulse durations were able to be generated in order to measure higher velocity flows, a higher intensity laser would also be required, as the black and white film used was developed in order to obtain maximum contrast between the reflected light from particles, and the background fog on the film.

For all PIV images processed, 3 light pulses were used. This reduced the chance of false detection of pairs compared to using 2 pulses, both when automatically processing the image using the autocorrelation technique, and when manually editing regions of the flow where vectors were not resolved automatically. In order to be able to obtain a velocity vector from each interrogation window, particle concentrations of between 3-10 particles were considered adequate for each interrogation window (Wu 1994).

One method to overcome both problems of minimum pulse duration and the loss of light intensity of the light when it is refracting into a sheet, is to reflect the laser beam from a rotating multi-faceted mirror (Rockwell *et al.* 1993) into the working section of the water tunnel. As the laser beam is swept through the working section, it strikes each particle with its full intensity, and the time between successive pulses can be controlled by varying the rotational speed of the mirror.

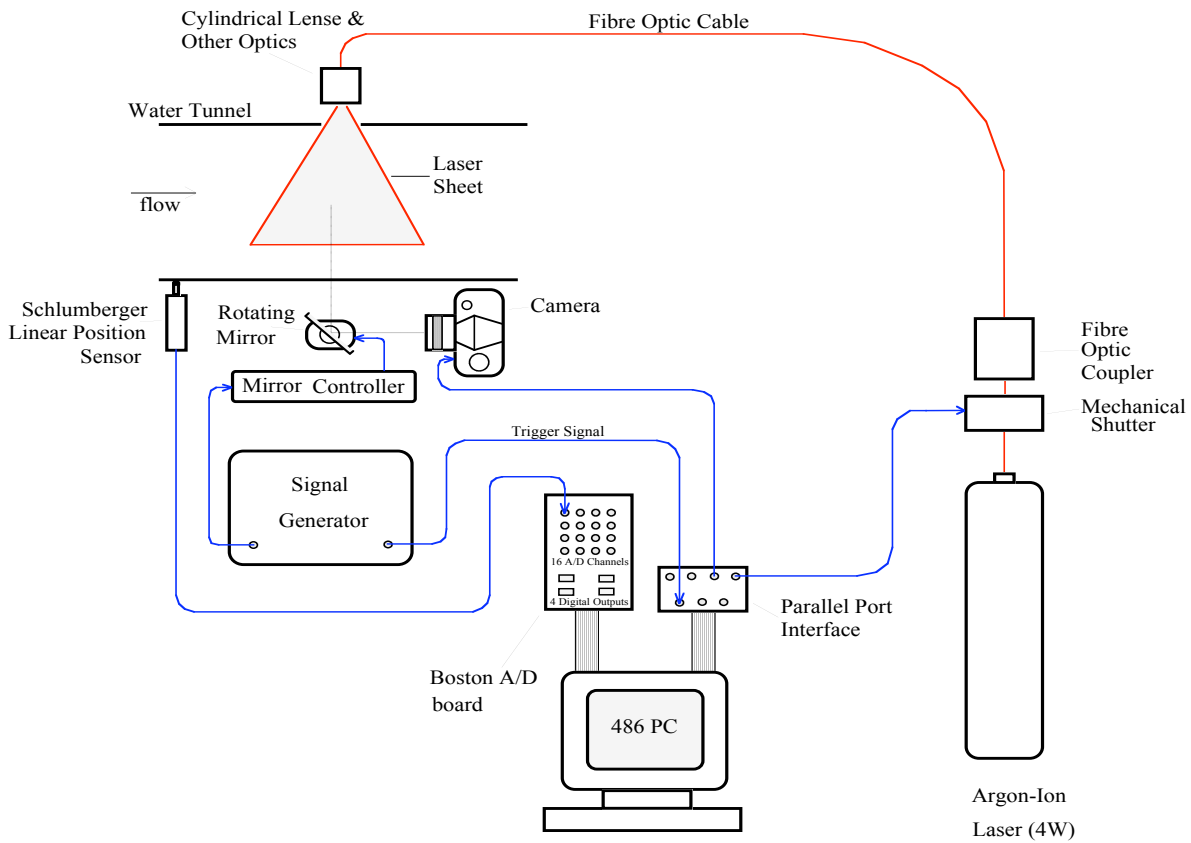


**Figure 3.23** Experimental set-up.

### 3.3.2 Image acquisition

A 35mm Nikon F90X Single Lens Reflex camera was used to record PIV images on to Kodak TMax 400 black and white film. The camera shutter was triggered by the 486PC, using a Nikon remote triggering lead connected to the parallel port of the PC. The PC was used to control the timing of camera triggering and laser pulsing to coincide with the velocity bias mirror being at the midpoint of its oscillation cycle (the velocity bias mirror is described in the next section).

In order to obtain enough light contrast from the film to be able to extract velocity data, an aperture of f4 was used, and the film was pushed two stops when processing to be effectively a 1600 ASA film. A Nikon Coolscan LS10 35 mm film scanner was used to digitise individual frames.

For this film based PIV system, the digital film scanner was a limiting factor on the resolution of the PIV images, as the film resolution was an order of magnitude higher than that of the scanner. The film used was Kodak T-Max 400 which has a resolution of approximately 300 lines/mm, giving the resolution of the 35mm film to be 10000 x 7500. The resolution of the scanner was 106.3 pixels/mm, giving the resolution of a digitised 35mm frame to be approximately 3543 x 2657 pixels.

In order to minimise the number of false or unresolved vectors produced by the autocorrelation, a minimum intensity threshold level of the digitised image was adjusted to remove background noise.

### **3.3.3 Bias Velocity Mirror**

To enable an autocorrelation technique to be used on reversing flows, a 50mm x 50mm plane mirror was used to reflect the image from the working section towards the camera (see figure 3.24). The mirror was mounted on the shaft of a General Scanning G325DT scanner, which was used to rotate the mirror at a constant angular velocity. A triangular wave from a Wavetek Model 145 20 Mhz Pulse/Function generator with a frequency of 0.66 Hz was used as the input to the General Scanning scanner controller. This resulted in a constant angular velocity of the mirror over the interval that the laser was being pulsed to obtain a PIV image.

The axis of rotation of the mirror was parallel with the sheet of laser light, and perpendicular to the mean flow direction. This allowed a bias velocity to be added to the image in the direction of the mean flow ( $U_{\infty}$  direction) so that all U velocity components would be positive. For the flows photographed, a bias velocity approximately equal to the freestream velocity allowed PIV data to be resolved without any ambiguity over the entire image frame. After obtaining a velocity vector field from the image, the bias velocity was then subtracted from the original velocity field to obtain the velocity field in the laboratory reference frame.

**Figure 3.24** Camera and bias mirror located above the water tunnel working section.

### **3.3.4 Image Processing**

Once digitised, individual PIV images were processed on a Silicon Graphics workstation using the program PIVFlow written by Dr. Nicholas Lawson at CSIRO. PIVFlow uses an auto-correlation technique to extract a grid of velocity vectors from the PIV image.

#### ***3.3.4.1 Interrogation window size and local velocity gradient***

Using the software PIVFlow, three choices of interrogation window size were available; 32 x 32 pixels, 64 x 64 pixels or 128 x 128 pixels. The resolution of the PIV image is highly dependent on the interrogation window size. Choosing a window that is too small, compared to the length of a typical particle streak, will result in a poor detection rate, as the chance of detecting a complete particle streak within a single interrogation window is reduced. Choosing a window larger than necessary, can result in poor accuracy in regions of high local velocity gradient, due to a single interrogation window containing traces from particles moving at significantly different velocities. For the PIV data presented in this thesis, an interrogation window size of 64 x 64 pixels was used. A 32 x 32 pixel interrogation window was tried, but poor data conversion rates were obtained, due to the window size being of similar size to the length of a typical particle streak. The 128 x 128 pixel interrogation window was also tried, and in regions away from the bluff body wake, provided reliable

results. However, in the wake and near the bluff body, where the velocity gradients are higher, the window size was too large.

### 3.3.4.2 *Interrogation grid spacing*

The PIVFlow software, which was used to interrogate PIV images, has a limit on the number of gridpoints that can be used of  $120 \times 80$ . Using the maximum grid resolution would result in a data file with 9600 velocity vectors. This restriction was not a limitation, as the maximum number of gridpoints used was  $110 \times 45$ . This number of gridpoints was chosen to ensure there was an overlap ratio of at least 50% between adjacent interrogation windows. An overlap between adjacent windows is used because pulsed particle streaks are rarely centred in the middle of the interrogation window. Using a 50% overlap ensures that the image signal of each particle is fully exploited.

Using the 50% overlap, the grid spacing on the image was 29 pixels. By taking an image of a measuring rule at the same distance from the camera focal plane as the laser sheet, the image scale was established to be 0.043 mm per pixel. This gave the magnification of the lens to be approximately 1:4.56, the interrogation window size to be 2.75 mm x 2.75 mm, and the effective spacing between adjacent grid points in the laser plane to be 1.25 mm.

### 3.3.4.3 *Autocorrelation technique*

The spatial autocorrelation function

$$R_{xx}(r_d) = \int I(r)I(r + r_d)dr \quad (3.2)$$

of the transmitted light intensity ( $I$ ) can be found by taking a fourier transform of the fringe pattern produced by coherent illumination of a PIV image. The variable  $r$  is the position in the film plane, while  $r_d$  is the displacement vector between members of an image pair. In order to avoid obtaining a vector field with entirely zero vectors due to the self correlation peak at the origin of each interrogation window, a DC mask with a radius set equal to the

radius (in pixels) of the largest particle was used. The autocorrelation peaks measured were then due to the two peaks at displacements of plus and minus the displacements between particle images. There was noise present in the autocorrelation due to film grain effects, effects of digitising an image, and incorrect particle pairing. To overcome the effect of this noise in the resultant velocity field, post processing of the PIV data is performed.

### **3.3.5 Post Processing**

The PIVFlow program also facilitated post processing of the PIV data, to remove any false vectors, and to smooth noise generated by the autocorrelation technique. A range of acceptable velocities for each image could be set to automatically remove false vectors outside this range. Individual grid points could also be manually edited to correct unresolved or false velocity vectors that fell within the acceptable velocity range. In regions where there was no data, velocity vectors could be calculated using a linear interpolation between surrounding gridpoints.

#### ***3.3.5.1 Data spatial filtering***

To overcome the random noise associated with digital image processing, spatial filtering techniques are frequently used. The PIVFlow program uses a low-pass Gaussian filter to smooth the PIV data after processing. Data smoothing is necessary to remove the noise associated with the autocorrelation of each interrogation window. For the images processed, smoothing the data using the low-pass Gaussian filter over a radius of 2 gridpoints (effectively over the area of each interrogation window since a 50% overlap between successive windows was used) produced the best results. The only regions of the flow where this choice of smoothing radius was not appropriate was for the gridpoints immediately adjacent to the bluff body, where high values of peak vorticity associated with the thin boundary layer were lost due to smoothing. This gave the appearance of a thicker boundary layer than was actually the case.

Using a larger smoothing radius would have resulted in underestimating the values of peak vorticity and circulation over the entire flow field, while a smoothing radius of only 1 gridpoint was not large enough to adequately smooth noise in the data.

### 3.3.5.2 Vorticity calculation

For a two-dimensional flow field with the velocity in the  $x$  direction being defined as  $U_x$  and the velocity in the  $y$  direction being defined as  $U_y$ , the vorticity  $\omega$  is defined as

$$\omega = \frac{\partial U_y}{\partial x} - \frac{\partial U_x}{\partial y} \quad (3.3)$$

The vorticity at a grid point  $(i,j)$  is found numerically from the discrete velocity data using a central difference scheme as shown below:

$$\frac{\omega}{U_\infty/t} = \frac{t}{U_\infty} \left( \frac{(U_y^{i+1,j} - U_y^{i-1,j})}{2(x^{i+1,j} - x^{i,j})} - \frac{(U_x^{i,j+1} - U_x^{i,j-1})}{2(y^{i,j+1} - y^{i,j})} \right) \quad (3.4)$$

where the vorticity is normalised by the free stream velocity ( $U_\infty$ ), and the model thickness ( $t$ ). A central difference scheme was used due to its second order of accuracy.

For the left hand grid boundary where  $i = 1$ ,  $\frac{\partial U_y}{\partial x}$  was approximated using a forward difference scheme:

$$\frac{\partial U_y}{\partial x} \approx \frac{(U_y^{i+1,j} - U_y^{i,j})}{(x^{i+1,j} - x^{i,j})} \quad (3.5)$$

Along the right hand grid boundary where  $i = \text{maximum}$ ,  $\frac{\partial U_y}{\partial x}$  was approximated using a backwards difference scheme:

$$\frac{\partial U_y}{\partial x} \approx \frac{(U_y^{i,j} - U_y^{i-1,j})}{(x^{i,j} - x^{i-1,j})} \quad (3.6)$$

For the top and bottom boundaries ( $j = 1$  and  $j = \text{maximum}$  respectively), the vorticity was not calculated as the flow was considered to be approximately uniform along these boundaries.

### 3.3.5.3 Calculation of circulation of vortex structures

The circulation ( $\Gamma$ ) of a vortex structure was found by integrating the vorticity ( $\omega$ ) calculated from the discrete velocity data over the area of the vortex ( $A$ ) according to the formula:

$$\frac{\Gamma}{U_0 t} = \frac{\int_A \omega dA}{U_0 t} \quad (3.7)$$

where  $dA$  is the area of the image covered by each grid point. The area of a vortex was defined by specifying a central point within the vortex, as well as a rectangular bounding box. All gridpoints within the bounding box were interrogated, with the circulation at gridpoints with vorticity of the same sign as and no less than 10% of the vorticity at central point being added to the circulation of the entire vortex. The circulation was normalised by the free stream velocity ( $U_0$ ), and the model thickness ( $t$ ).

### 3.3.5.4 Generation of velocity vector plots and vorticity contour plots

An ASCII data file in a form suitable to be read into the graphics program Tecplot could be generated by the program PIVFlow, to allow contour plots of vorticity, velocity vector plots and sectional streamline plots to be produced. Figure 3.25 below shows the velocity vector field calculated from the PIV image shown in figure 3.22 earlier, along with the calculated vorticity field.

- (a) Velocity Vector Plot  
(Stationary ref. frame)
- (b) Streamline Plot  
(Stationary ref. frame)
- (c) Streamline Plot  
(moving ref. frame)
- (d) Vorticity Plot

**Figure 3.25** See page 72 for caption.

**Figure 3.25** (a) Velocity vector field; (b) Sectional streamline plot (Lab reference frame), (c) Sectional streamline plot (reference frame moving with vortices), (d) Vorticity contour plot, calculated from a PIV image.

### 3.3.6 Flow Visualisation

Flow visualisation was performed in the water tunnel with the same hardware used to obtain the PIV images (see figure 3.23). Typically, the laser was pulsed 10 times with pulses of 2 ms in duration to obtain particle streak lines of suitable length. The bias velocity mirror was used to physically remove the mean flow velocity component, effectively placing the camera in a reference frame moving at the convection rate of the vortices.. This was useful in revealing vortex structures in the flow, as can be seen in figure 3.26.

Flow Vis Image

(moving ref. frame)

**Figure 3.26** Flow visualisation from water tunnel, using the velocity bias mirror.

## 4. Results and Discussion

Experimental measurements have been taken from elongated plates with rectangular trailing edges, and both aerofoil and rectangular leading edges. Surface pressure measurements and smoke wire visualisations were taken using the open jet wind tunnel described in section 3.1, while PIV measurements and flow visualisation images were taken in the closed circuit water tunnel described in section 3.2.

### 4.1 Plates with no leading edge vortex shedding

For long plates with aerofoil leading edges and rectangular trailing edges, there is no vortex shedding from the leading edge of the models. The boundary layers that form on each side of the models separate from the sharp corners at the trailing edge, and interact to form a Karman vortex street.

#### 4.1.1 Surface pressure measurements

The variation of  $C_{p_b}$  with  $c/t$  ratio is shown in figure 4.1, measured with the flow velocity at  $10 \text{ ms}^{-1}$ .

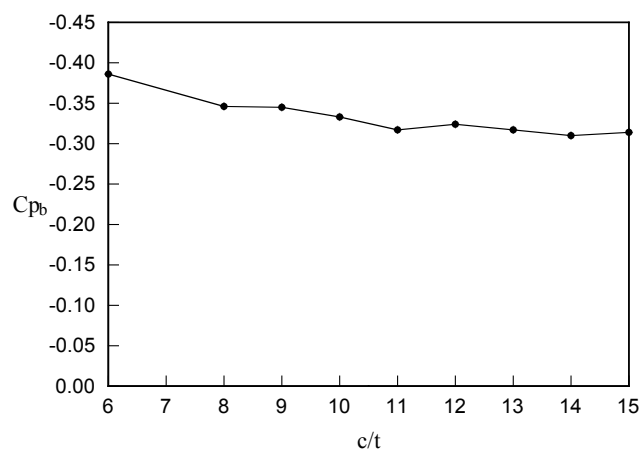


**Figure 4.1** Variation of  $C_{p_b}$  with  $c/t$  for a plate with an aerofoil leading edge and a rectangular trailing edge.

Bull *et al.* (1995) showed that the vortex shedding frequency from such plates depends on the boundary layer state at the plates trailing edge. For a laminar boundary layer at separation, the effect of increasing plate length is to thicken the boundary layers at separation, which

results in a wider wake and thus a lower  $St$ . Figure 4.2 shows the calculated variation in  $St$  with  $c/t$  for plates with thickness ( $t$ ) of 13 mm, and a flow velocity of  $10\text{ms}^{-1}$  using the formula

$$F_{t'} = 0.286Re_{t'} \quad (4.1)$$

from Bull *et al.* (1995) for large  $Re_{t'}$  and

$$St = \frac{ft}{U_{\infty}} \quad (4.2)$$

where  $Re_{t'} = U_{\infty}t'/\nu$ ,  $F_{t'} = ft'^2/\nu$ ,  $t' = t + 2\delta_*$ ,  $\nu$  = kinematic viscosity,  $f$  = vortex shedding frequency,  $\delta_*$  = boundary layer displacement thickness at separation, calculated using the relationship

$$\frac{\delta_*}{x} = \frac{C_{*L}}{Re_x^{1/2}} \quad (4.3)$$

with  $x = c$ , and  $C_{*L} = 1.7208$  for a laminar boundary layer.

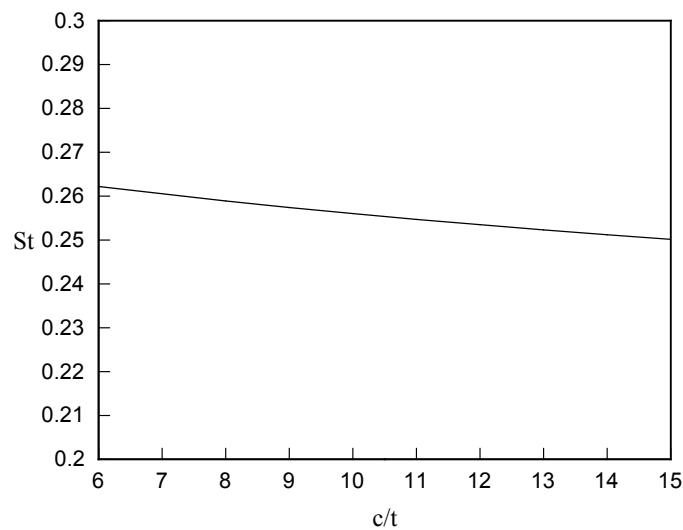


**Figure 4.2** Predicted variation in  $St$  with  $c/t$  using equations 4.1, 4.2 and 4.3, for a plate with an aerofoil leading edge and a rectangular trailing edge with  $t = 13$  mm and  $U_{\infty} = 10$   $\text{ms}^{-1}$  (used later in this section).

As for a stationary circular cylinder in smooth flow, as  $St$  decreases so does the magnitude of  $C_{pb}$  (Williamson 1996).

For a plate with a thickness ( $t$ ) of 13 mm,  $c/t = 10$  and a flow velocity of  $10$   $\text{ms}^{-1}$ , equation 4.1 gives the vortex shedding Strouhal number ( $St$ ) = 0.256 based on plate thickness.

#### 4.1.1.1 Effect of transverse velocity perturbations on $C_{p_b}$

As with most bluff body flows, the flow separating from the trailing edge of blunt based plates can be modified in the presence of small amplitude velocity perturbations. Due to the region of absolute instability in the near wake (Rockwell 1990), there exists a minimum velocity perturbation level required to overcome the natural instability characteristics of the flow before the vortex shedding is affected by the perturbations. For perturbations applied at the natural vortex shedding frequency, Wu *et al.* (1993) found that the minimum velocity perturbation level required to phase-lock the vortex shedding is approximately 0.35% of free stream velocity (ie  $u'/U_\infty = 0.0035$ ). Circular cylinders exhibit a similar response to perturbations applied at the natural vortex shedding frequency, as they also require a threshold perturbation level to be exceeded before vortex shedding locks on to the perturbations.

Figure 4.3 shows the variation of  $C_{p_b}$  with perturbation Strouhal number ( $St_p$ ) for a plate with  $c/t = 10$ , a flow velocity of  $10 \text{ ms}^{-1}$ , and a perturbation level ( $u'/U_\infty$ ) of 5%. The variation of  $C_{p_b}$  with  $St_p$  is remarkably similar to that observed by Stansby (1976) for a transversely oscillating circular cylinder (see figure 2.16). Stansby associated the sudden change in  $C_{p_b}$  with a large shift in the phase of vortex shedding with respect to the cylinder motion.

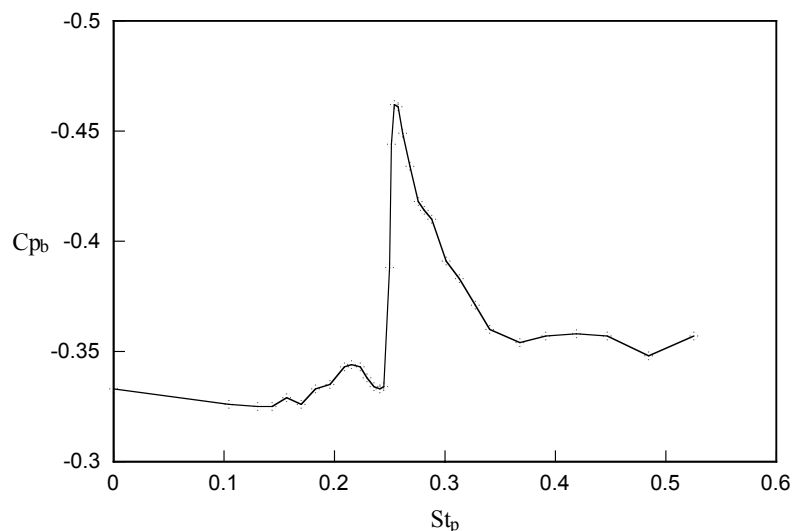


**Figure 4.3** Variation of  $C_{p_b}$  with  $St_p$  for  $u'/U_\infty = 5\%$  and  $U_\infty = 10 \text{ ms}^{-1}$ .

Lotfy & Rockwell (1993) performed a series of experiments on a model with an elliptical leading edge, and a trailing edge that could be oscillated transversely. They found that vortex shedding could be phase-locked to the trailing edge oscillations over the relatively narrow frequency range  $0.95 \leq f_e/f_0 \leq 1.05$  (where  $f_e$  = oscillation frequency and  $f_0$  = natural vortex shedding frequency from a stationary model). Within this frequency range, a small change in  $f_e/f_0$  resulted in a change of almost  $180^\circ$  in the phase of vortex formation with regard to the trailing edge motion. This suggests the possibility that the large change in  $Cp_b$  when  $St_p$  is near the natural vortex shedding  $St$  of 0.24 in figure 4.3 coincides with a large change in the phase of vortex shedding with respect to the transverse velocity perturbations.

For plates of different  $c/t$  ratios, a similar response to transverse perturbations of the same magnitude is observed, as shown in figure 4.4. Due to the variation of  $Cp_b$  with  $c/t$  when no perturbation is applied, the value of  $Cp_b$  for each plate length without perturbations applied has been subtracted from the data.

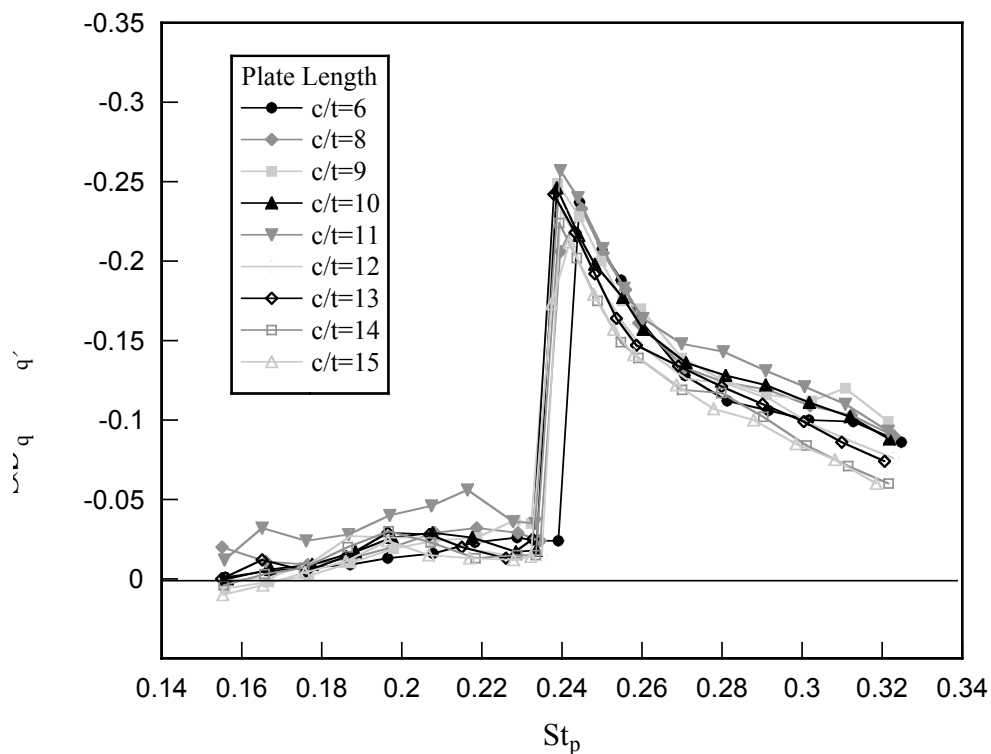


**Figure 4.4** Variation of change in  $Cp_b$  from  $Cp_b$  with no perturbation applied for different length plates, all with  $U_\infty = 10 \text{ ms}^{-1}$  and perturbation level = 5% of  $U_\infty$ .

The only effect of increasing plate length is thicker boundary layers at separation as discussed at the start of this chapter, so the relative independence of the  $Cp_b$  data from  $c/t$  shown in figure 4.4 is not surprising.

#### ***4.1.1.2 Effect of varying perturbation level***

Since varying the plate length has little effect on  $Cp_b$  as  $St_p$  is varied, only the effect of perturbation level on  $Cp_b$  for the plate with  $c/t$  ratio of 10 is presented in figure 4.5. As the relative perturbation level is increased, the size of the maximum change in  $Cp_b$  from the unperturbed flow value increases, as is shown in figure 4.6. This result is similar to that observed by Stansby (1976) for flow around a circular cylinder subject to forced transverse oscillations, where increasing the oscillation amplitude resulted in an increased change in  $Cp_b$ . Also consistent with the results of Stansby is the reduction in frequency at which the sudden change in  $Cp_b$  occurs as the relative perturbation level is increased. Further work is needed to establish whether the sudden change in  $Cp_b$  as  $St_p$  is increased is due to the flow suddenly phase-locking to the perturbations, or if it is due to already phase-locked vortex shedding undergoing a large phase shift relative to the perturbation cycle.

#### ***4.1.1.3 Effect of higher frequency perturbations***

Figure 4.7 shows the effect on  $Cp_b$  of applying perturbations at  $St_p$  as high as 0.9. As already discussed in this section, the natural vortex shedding  $St$  is approximately 0.25, and there is a peak in base suction when perturbations are applied at this frequency due to vortex shedding phase-locking to the perturbations. A second (small) peak in base suction occurs when  $St_p$  is approximately 0.5, which is twice the natural vortex shedding frequency. A third (large) peak in base suction is observed when  $St_p$  is approximately 0.75, which is three times the natural vortex shedding  $St$ . Flow visualisation revealed that large scale vortex shedding occurred at approximately  $St = 0.25$ , a subharmonic of the perturbation frequency when perturbations were applied at  $St_p = 0.75$ . The vortex shedding appeared enhanced by the perturbations, which was expected given the increased base suction measured in the wind tunnel. Further work is needed to investigate this effect more thoroughly.

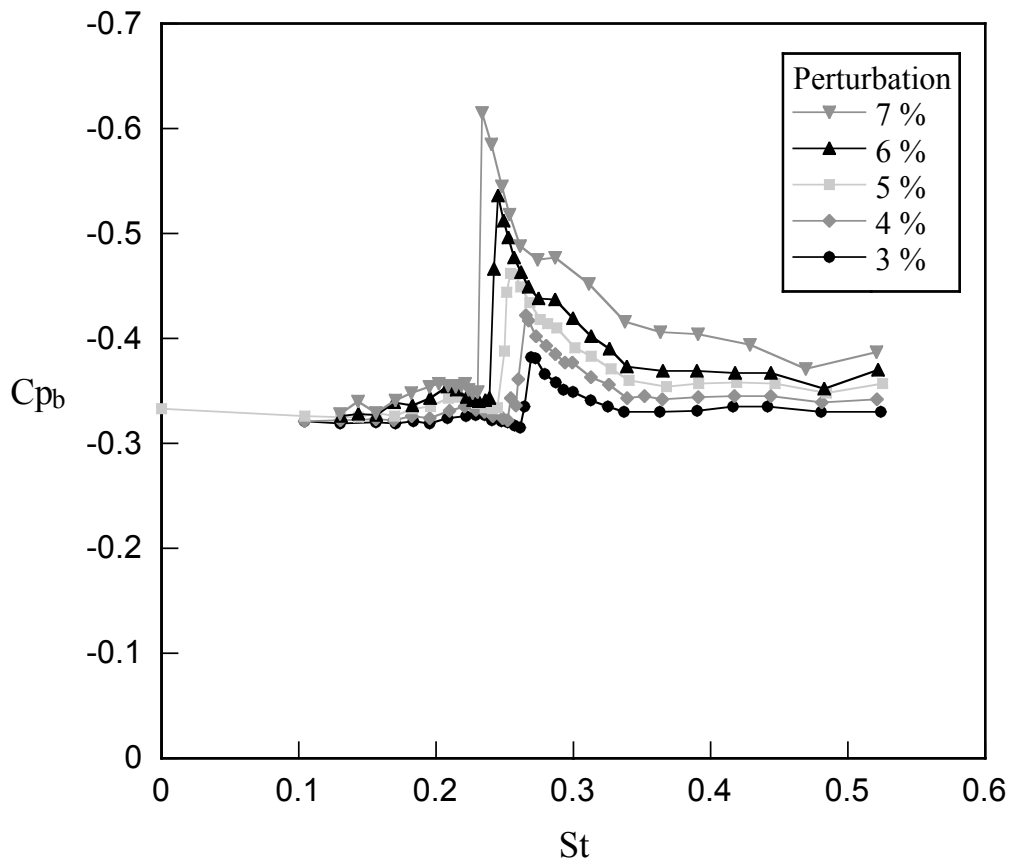


Figure 4.5 Effect of perturbation level on  $Cp_b$

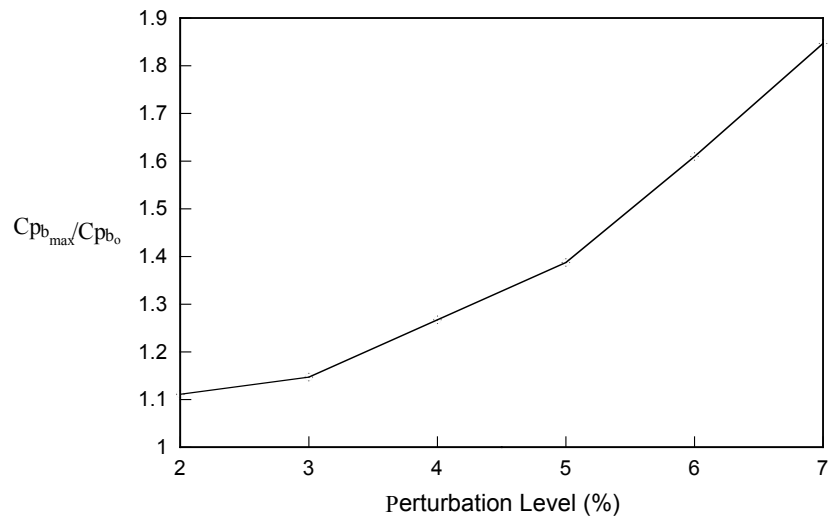
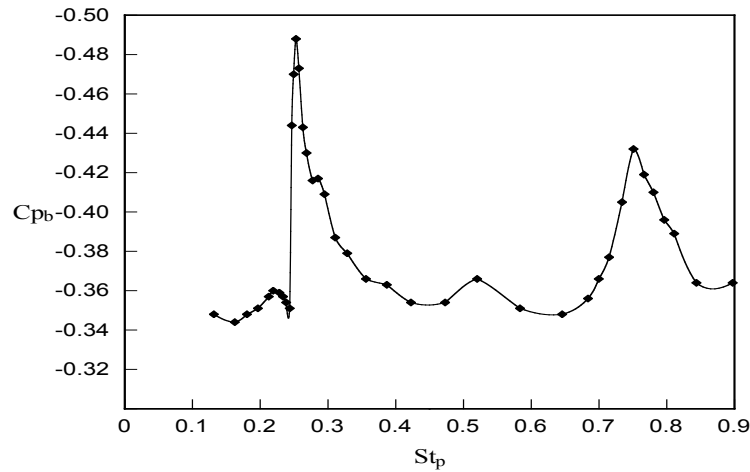


Figure 4.6 Variation of  $Cp_{b_{max}}/Cp_{b_0}$  with perturbation level for a  $c/t = 10$  plate.



**Figure 4.7** Variation of  $C_{p_b}$  with  $St_p$

#### 4.1.2 Particle Image Velocimetry measurements

Using PIV in the water tunnel, the effect of transverse velocity perturbations on the vortex shedding from the rectangular trailing edge of an aerofoil leading edge plate has been investigated. The aim of the PIV experiments was to gain insight as to why the large pressure drops measured in the wind tunnel experiments occur; in particular, to identify variations in the formation or location of flow structures. The Reynolds number for all PIV experiments on the aerofoil leading edge plate was 1100 based on plate thickness.

##### 4.1.2.1 No transverse velocity perturbations

Figure 4.8 shows velocity, sectional streamlines and vorticity fields, for a plate without transverse perturbation applied. The velocity vector plot 4.8(a) and the corresponding sectional streamline plot 4.8(b) were both generated with a stationary reference frame with respect to the laboratory, while the sectional streamline plot 4.8(c) was generated with the reference frame moving at  $0.75U_\infty$ , approximately the convection velocity of the vortices. Vortices of opposite sign are shed alternately from the trailing edge, to form a vortex street. This is clearly evident in the vorticity plot (figure 4.8(d)), which shows negative vorticity as dotted lines. The frequency of vortex shedding, calculated by measuring the time of twenty shedding cycles, was found to be 1.80 Hz. This gave a natural vortex shedding  $St$  of approximately 0.25, in close agreement with Bull *et al.* (1995) as discussed earlier.

Figure 4.9 shows a plot of the vertical velocity  $U_y$  against streamwise distance from the centre of the trailing edge, while figure 4.10 shows a contour plot of the vertical velocity  $U_y$  for the same PIV image as shown in figure 4.8. Both of these images show the wavelength of vortex shedding to be approximately  $4.0t$ .

ar8f09 - Velocity vector plot (Lab ref. frame)

(a)

ar8f09 - sectional streamlines (lab ref. frame)

(b)

ar8f09 - sectional streamlines (moving ref. frame)

(c)

**Figure 4.8** See page 81 for caption

## ar8f09 - Vorticity (no perturbation)

(d)

**Figure 4.8** PIV results on flow around a plate with an aerofoil leading edge ( $Re = 1100$ ), without any perturbation applied. (a) Velocity vector plot, (b) Sectional streamlines (lab reference frame), (c) Sectional streamlines (reference frame moving with vortices), (d) Vorticity.

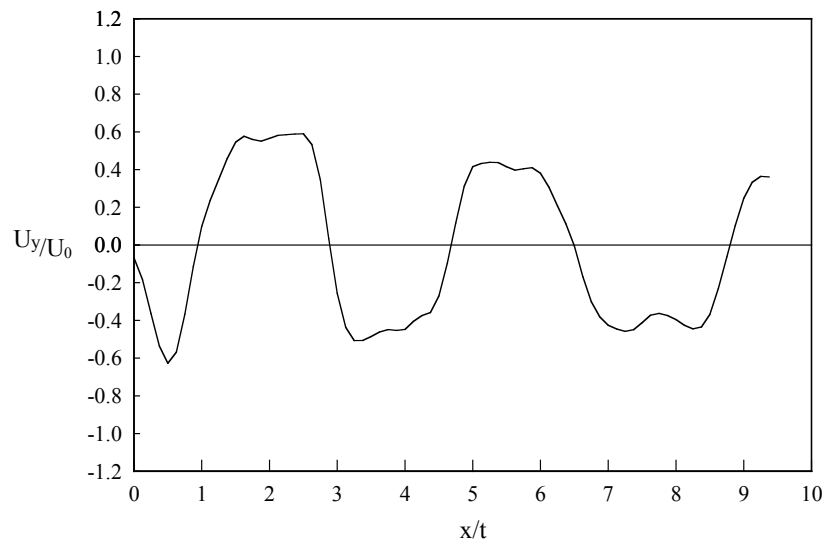


**Figure 4.9** Variation of  $U_y/U_0$  with streamwise distance from the trailing edge ( $x/t$ ).

ar8f09 - contour plot of  $U_y$ 

**Figure 4.10** Contour plot of  $U_y$  from a single PIV image of flow around an aerofoil leading edge plate without any perturbation applied.

A total of 10 PIV images were processed for the aerofoil leading edge model without any transverse velocity perturbation. Profiles of  $U_x$  were extracted from the PIV data at several streamwise locations and averaged, as shown in figure 4.11. These velocity profiles show a

top hat profile at the trailing edge. As  $x/t$  increases the wake spreads and the size of the velocity deficit decreases.

The same data is represented as a surface plot in figure 4.12, showing the velocity deficit in the wake. Had more PIV images been used in the averaging, the waviness evident in the figure would decrease.

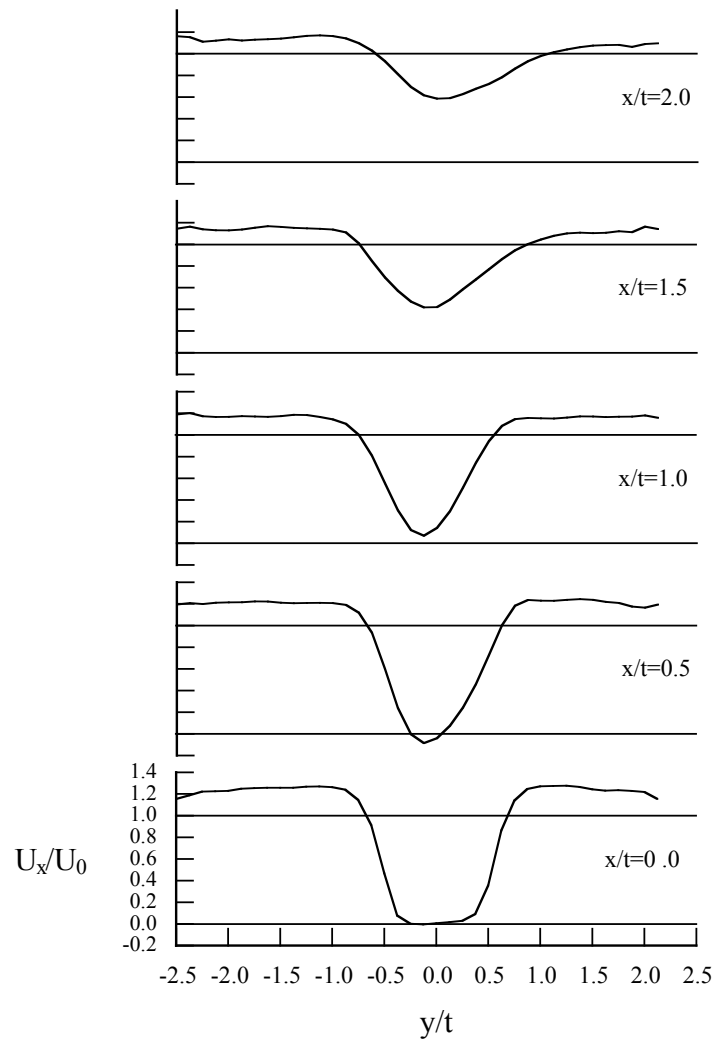


**Figure 4.11** Variation of  $U_x$  velocity profile across the wake with streamwise distance ( $x/t$ ), with no transverse velocity perturbation applied.

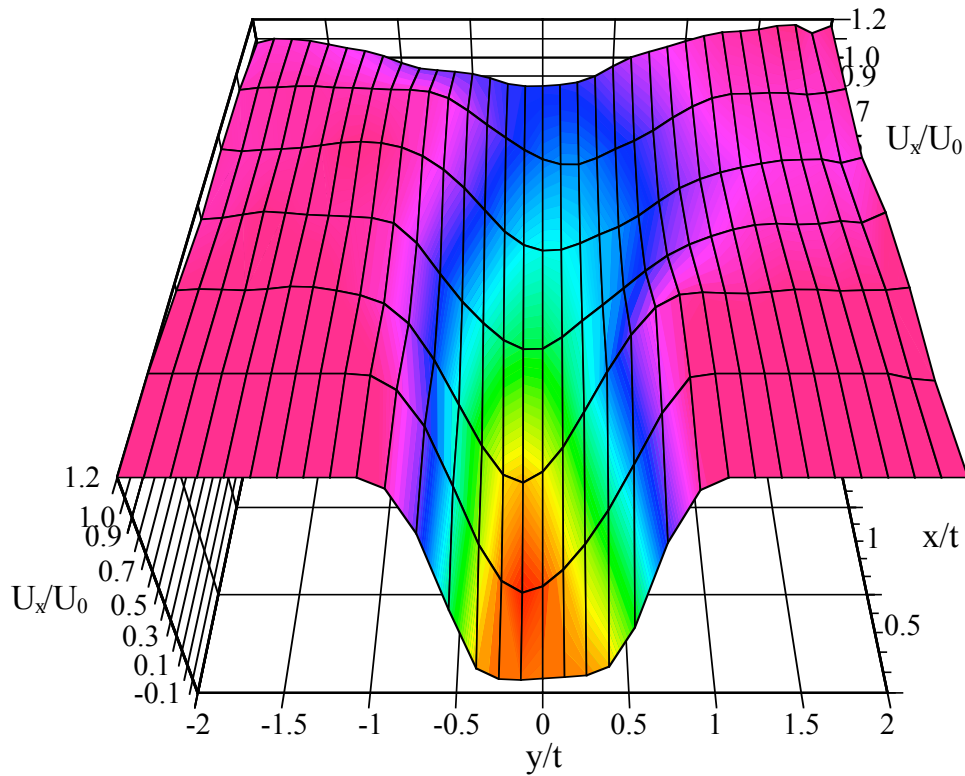


**Figure 4.12** Surface plot of  $U_x$  against streamwise distance ( $x/t$ ) and cross stream distance ( $y/t$ ), for the case with no transverse velocity perturbation applied.

A contour plot of  $U_x$  shown in figure 4.13 for the same PIV image as figure 4.8, shows the small region of reverse flow immediately behind the trailing edge of the model. The dark regions correspond to zero velocity, while the light regions correspond to high velocity.

ar8f09 - contour plot of  $U_x$

**Figure 4.13** Contour plot of  $U_x$  from a single PIV image of flow around an aerofoil leading edge plate without any perturbation applied.

#### 4.1.2.2 *Transverse velocity perturbation applied*

PIV measurements were made on flow about a plate with an aerofoil leading edge, in the presence of a 6% transverse sinusoidal velocity perturbation (see Chapter 3 for details of perturbation field and method of calculating perturbation phase). Figure 4.14 shows plots of velocity, sectional streamlines and vorticity when the moveable sidewalls used to generate the transverse velocity perturbation were in the lowest position. This corresponds to a phase angle of 0 degrees, with a perturbation velocity of 0 as indicated next to figure 4.14(a). The perturbation frequency was 1.65 Hz, giving  $St_p = 0.235$ . For this perturbation level, this was the lowest perturbation frequency for which the vortex shedding was phase-locked to the perturbation. This corresponds to the  $St_p$  for which the largest change in  $Cp_b$  was observed for a 6% velocity perturbation (see figure 4.3).

(a) ar9f15 - Velocity vector plot (perturbation 0 degrees)  
Lab ref. frame

(b) ar9f15 - sectional streamlines (perturbation 0 degrees)  
Lab ref. frame

**Figure 4.14** See page 85 for caption.

(c) ar9f15 - sectional streamlines (moving frame)

(perturbation 0 degrees)

(d) ar9f15 - Vorticity (perturbation 0 degrees)

**Figure 4.14** PIV results on flow around a plate with an aerofoil leading edge ( $Re = 1100$ ), with 6% transverse velocity perturbation applied at  $St_p = 0.235$ , (a) Velocity vector plot, (b) Sectional streamlines (lab reference frame), (c) Sectional streamlines (reference frame moving with vortices), (d) Vorticity; Perturbation phase =  $0^0$

Comparing the vorticity plots of figures 4.8 (d) and 4.14 (d), it can be seen that the spacing between vortices is reduced in the presence of the transverse perturbations, indicating a reduced convection velocity of vortices when phase-locked to the perturbations. Figure 4.15 shows a plot of  $U_y/U_0$  against streamwise distance from the centre of the trailing edge, while figure 4.16 shows a contour plot of  $U_y$  for the same PIV data as shown in figure 4.14.

These images show the wavelength of vortex shedding to be approximately  $3.8t$ . If the convection velocity of vortices remained unaffected by the application of transverse perturbations, then the spacing between vortices when  $St_p = 0.235$  should be  $4.26t$ . With a 6% transverse velocity perturbation applied at the lowest perturbation frequency that results in phase-locked vortex shedding, the convection velocity of vortices is only 89% of that for vortices shed from the model when no perturbation is applied. This is consistent with the findings of Davies (1976) for a transversely oscillating circular cylinder, where oscillating the cylinder at the natural vortex shedding frequency of the stationary cylinder increased the

circulation of the shed vortices by 35%, and reduced the convection velocity to only 90% of the convection velocity of vortices shed from a stationary cylinder.

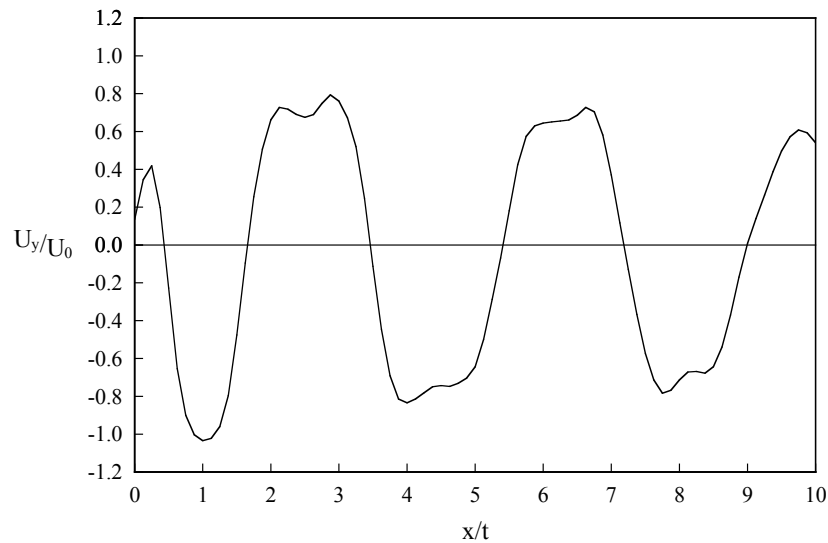


**Figure 4.15** Variation of  $U_y/U_0$  with streamwise distance from the trailing edge ( $x/t$ ).

ar9f15 - contour plot of  $U_y$

(perturbation 180 degrees - **actually 0**)

**Figure 4.16** Contour plot of  $U_y$  from a single PIV image of flow around an aerofoil leading edge plate with 6% transverse velocity perturbation applied at  $St_p = 0.235$ ; Perturbation phase = 0 degrees.

A total of 8 PIV images were processed for the aerofoil leading edge model with a 6% transverse velocity perturbation applied. The images selected were separated by 45 degree intervals in the perturbation cycle. It is recognised that a single image at each phase point is not sufficient to obtain a statistically significant average of the velocity data for that phase angle. However, profiles of  $U_x$  were extracted from the PIV data at several streamwise locations and averaged as shown in figure 4.17, and are useful in indicating the size of the velocity deficit in the wake. The same data are represented as a surface plot in figure 4.18. Compared to figure 4.12, there is a larger velocity deficit evident in figure 4.18 resulting from the lower convection velocity and higher circulation of vortices that occurs when the vortex

shedding is phase-locked to the transverse velocity perturbations. The slight waviness evident in the surface plot with increasing  $x/t$  is due to insufficient PIV images being processed, resulting in some phase dependency in the averaged data.

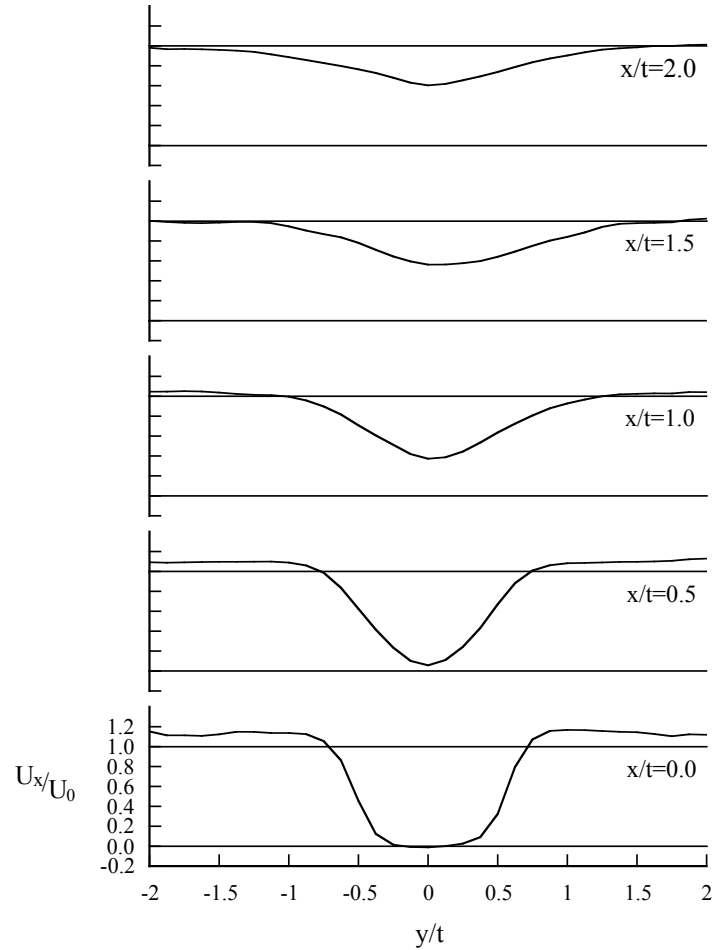


**Figure 4.17** Variation of  $U_x$  average velocity profile across the wake with streamwise distance ( $x/t$ ), 6% transverse velocity perturbation applied at  $St_p = 0.235$ .

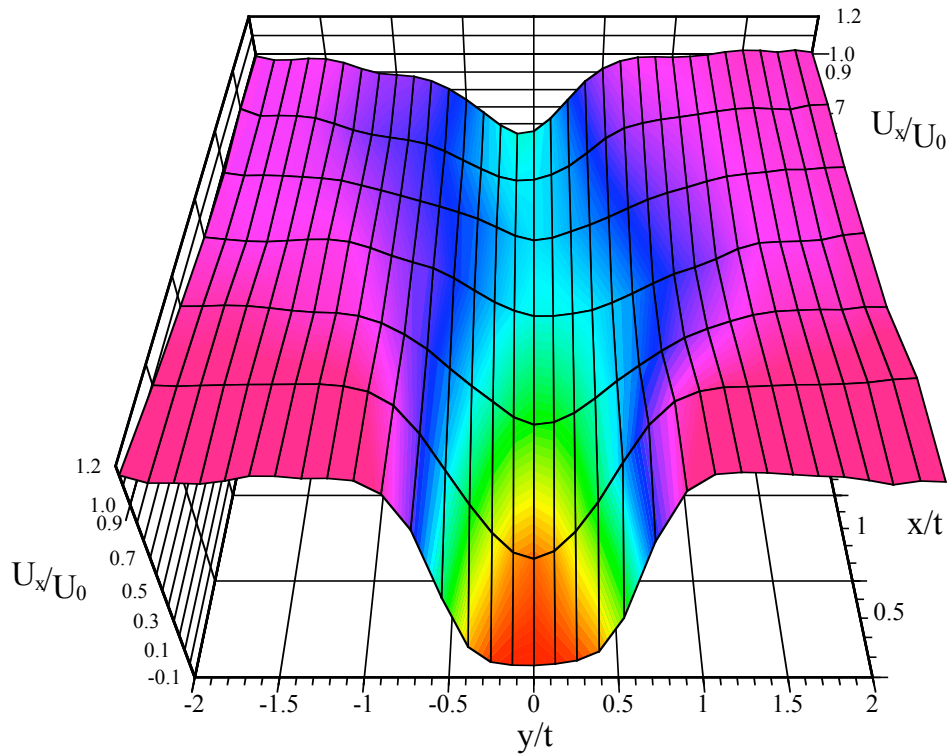


**Figure 4.18** Surface plot of  $U_x$  against streamwise distance ( $x/t$ ) and cross stream distance ( $y/t$ ), for the case with a 6% transverse velocity perturbation applied at  $St_p = 0.235$ .

Figure 4.19 shows a contour plot of  $U_x$  for the same PIV image as shown in figure 4.14, where the perturbation is at a phase angle of 0 degrees. Compared to figure 4.13, the dark region just behind the trailing edge representing slow moving or reversed flow is much smaller. This would suggest that the vortex formation length is smaller when vortex shedding is phase-locked to the perturbation field, an expected result given the higher base suction (see figure 4.3) and the observations of other researchers as discussed in Chapter 2.

show  
phase  
plot

ar9f15 - contour plot of  $U_x$

**Figure 4.19** Contour plot of  $U_x$  from a single PIV image of flow around an aerofoil leading edge plate with 6% transverse velocity perturbation applied at  $St_p = 0.235$ ; Perturbation phase angle = 0 degrees.

### 4.1.2.3 Relationship between circulation and base pressure

Equation 4.4 shows that the rate of circulation formation at a point on a surface is equal to the pressure drop along that surface (Morton 1984), as indicated in figure 4.20.

$$\int \frac{d\Gamma}{dt} dS = -\int \frac{\partial P}{\partial S} dS \quad (4.4)$$

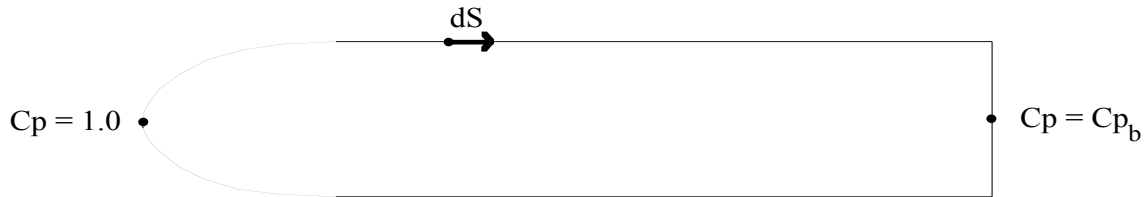


**Figure 4.20** Schematic of aerofoil leading edge model.

By integrating along either the upper or lower surface from the leading edge to the centre of the trailing edge, the rate of circulation generation about the entire model is equal to the change in pressure from the stagnation point at the leading edge to the trailing edge, as shown in equation 4.5.

$$\frac{d\Gamma}{dt} = -\Delta P \quad (4.5)$$

Integrating equation 4.5 over the period of one entire vortex shedding cycle gives:

$$\frac{\Gamma}{\Delta P} = \text{constant} \quad (4.6)$$

For two different cases of flow about a model like the one shown in figure 4.20, the relationship between circulation in the wake and pressure change about the surface of the model is given by equation (4.7):

$$\frac{\Gamma_1}{\Gamma_2} = \frac{\Delta P_1}{\Delta P_2} = \frac{\Delta C_{p1}}{\Delta C_{p2}} \quad (4.7)$$

Figure 4.21 shows the variation of circulation with streamwise distance from the trailing edge of the aerofoil leading edge model, both with and without transverse velocity perturbations applied.

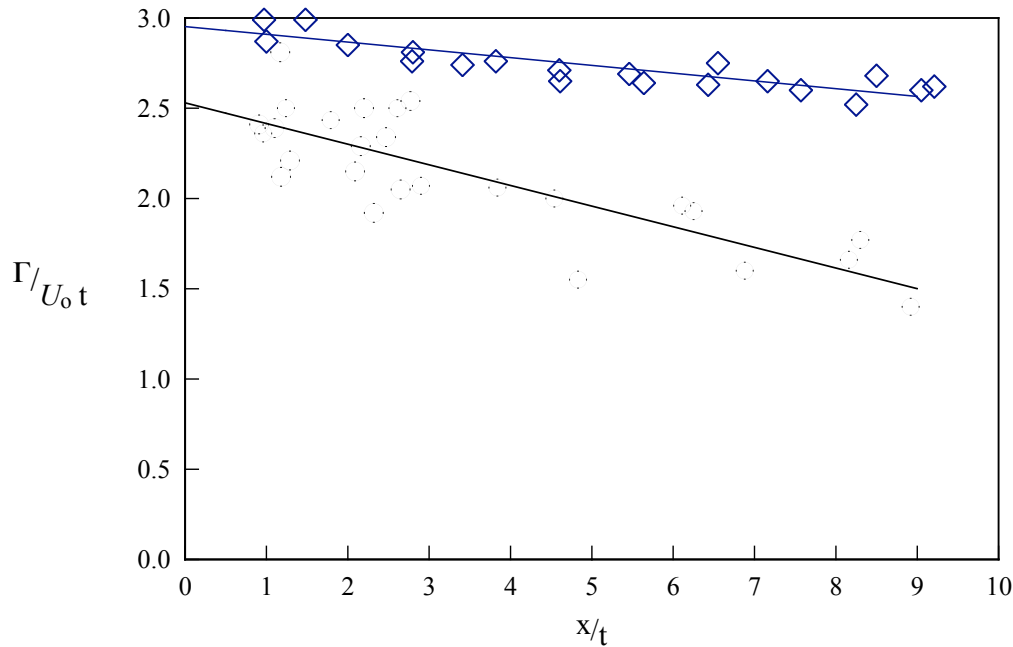


**Figure 4.21** Variation of normalised circulation with streamwise distance ( $x/t$ ) from the trailing edge of a plate with an aerofoil leading edge;  $\diamond$  with 6% velocity perturbation applied at  $St_p = 0.235$ ,  $\circ$  natural vortex shedding, dashed lines represent least squares lines of best fit.

Using the least squares lines of best fit through the two sets of data shown on figure 4.21 to extrapolate back to the trailing edge of the model, the circulation of vortices in the wake adjacent to the trailing edge is given in table 4.1. Also shown in table 4.1 is the change in pressure coefficient from the stagnation point at the leading edge of the model to the base of the model, both for the case of no transverse velocity perturbation applied, and for the case when a 6% transverse velocity perturbation is applied at  $St_p = 0.235$ .

<b>Circulation</b>	$\frac{\Gamma_1}{\Gamma_2}$	$\Delta C_p$	$\frac{\Delta C_{p1}}{\Delta C_{p2}}$
$\Gamma_1 = 2.53$ $\Gamma_2 = 2.95$	0.857	$\Delta C_{p1} = 1.33$ $\Delta C_{p2} = 1.54$	0.866

**Table 4.1** Comparison between circulation shed from a bluff body and the pressure change around it.

Using equation 4.7, the expected base pressure coefficient in the presence of a 6% velocity perturbation applied at  $St_p = 0.235$  is -0.552. This is within 3% of the base pressure

coefficient measured in the wind tunnel. Although the response to perturbations of only one level has been measured in the water tunnel, this result indicates that the extra circulation present in the wake when vortex shedding is phase-locked to transverse velocity perturbations corresponds with the large drop in base pressure.

There are other factors that can affect the base pressure of a bluff body. Bearman (1965) established that the base pressure is also directly affected by the vortex formation length. As the formation length decreased so did the base pressure, resulting in higher drag. The vortex formation length is often defined as the streamwise location along the centreline of the wake where the velocity fluctuations measured by a hot-wire are a maximum. With only 10 PIV images being processed for each case, there are not sufficient data to obtain an accurate estimate of formation length using this definition. However, figure 4.22 shows the variation of  $U_x$  (average at each streamwise location for all PIV images) with streamwise distance ( $x/t$ ) along the centreline of the wake for the case without any transverse perturbation applied and with a 6% transverse velocity perturbation applied. The region of reverse flow is smaller in the presence of transverse velocity perturbations, indicating that the formation length is reduced.

For circular cylinders subject to transverse oscillations close to the natural vortex shedding frequency, Griffin & Ramberg (1975) showed that an inverse relationship exists between vortex formation length and both vortex circulation and the drag on the cylinder. Thus, a decrease in vortex formation length, as suggested by figure 4.22, for the flow with vortex shedding phase-locked to the transverse perturbations is not unexpected, as it is a result of the more vigorous vortex shedding.

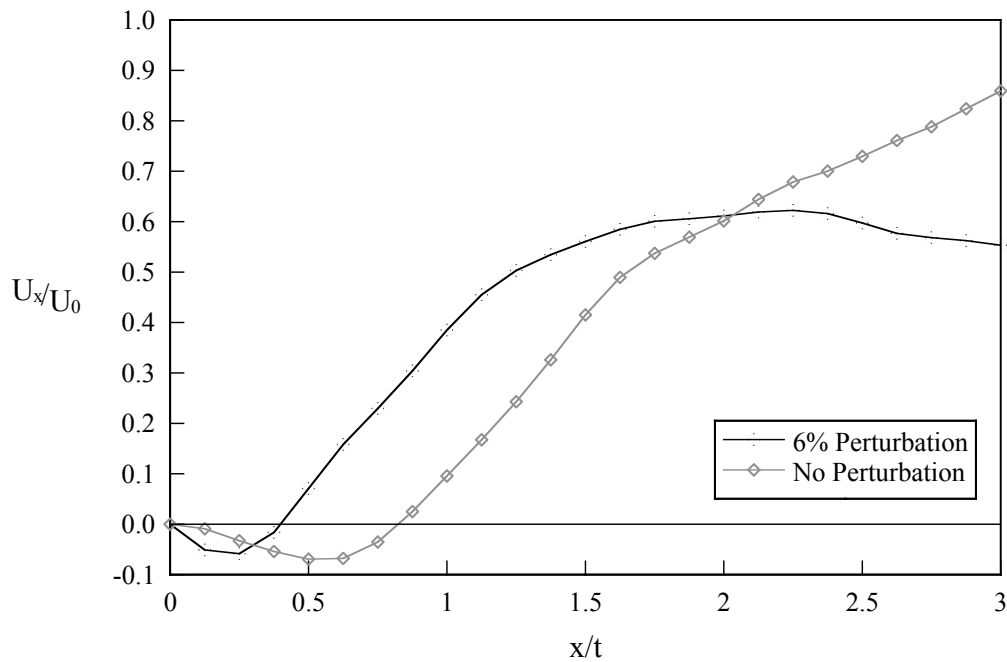


**Figure 4.22** Variation of streamwise component of velocity ( $U_x/U_\infty$ ) with streamwise distance from the centre of the trailing edge of a plate with an aerofoil leading edge.

### 4.1.3 Three dimensional effects

The base pressure measurements and PIV results presented in this section may give the impression that the vortex shedding from the trailing edge of a plate with an aerofoil leading edge is two dimensional (2-D). For flow over circular cylinders, three dimensional (3-D) effects are observed for  $Re$  greater than 190 (Williamson 1996), although Wu (1994) found evidence of 3-D structures at  $Re = 170$  which may be a function of free stream turbulence and end effects. Wu (1994) found that the circulation of streamwise vortices associated with mode B vortex shedding (Williamson 1996) in the wake of a circular cylinder was only 11% of the circulation of the spanwise vortices. Wu (1994) also found evidence of similar streamwise vortices in the wake of a plate with a semi-circular leading edge and a rectangular trailing edge, so it was expected that there would be streamwise structures in the wake of models with aerofoil leading edges. Figure 4.23 shows a flow visualisation image taken in the water tunnel of vortex shedding from a plate with an aerofoil leading edge and a rectangular trailing edge. The sheet of laser light was aligned to reveal the classical 2-D Kármán vortices in the wake. A feature of the flow that was not expected to be seen using

this technique was the existence of streamwise vortices embedded in the Kármán vortex street.

Flow Visualisation, of flow over an aerofoil leading edge  
plate - no perturbation applied  
Water tunnel image, showing streamwise vortex  
superimposed on primary spanwise vortices.  
**(have arrow pointing to 3D structure)**

**Figure 4.23** Vortex shedding from the rectangular trailing edge of a model with an aerofoil leading edge.

The PIV vorticity plot shown in figure 4.24 was generated from an image taken with the sheet of laser light aligned to reveal streamwise vortex structures. When vortex shedding was locked to transverse velocity perturbations, the streamwise structures appeared to be suppressed although no PIV data has been processed showing this; this would be worthy of further investigation. The intention of drawing attention to the existence of 3-D structures in the flow is not to draw any conclusion about the effect of three dimensionality on vortex shedding or  $C_{p_b}$ , but rather to acknowledge that 3-D structures are present.

PIV vorticity image of streamwise vortices in wake  
of aerofoil leading edge plate.

**Figure 4.24** Vorticity contour plot, with the laser sheet orientated in the same plane as the plate to reveal streamwise vortex structures in the wake.

Non-parallel vortex shedding also results in the formation of 3-D structures. Williamson (1989) showed that end conditions were responsible for non-parallel vortex shedding from circular cylinders, and Pickles *et al.* (1992) showed that parallel vortex shedding from models with aerofoil leading edges and rectangular trailing edges was also dependent on end conditions. Although vortex shedding from the base of a model with a semi-circular leading edge was regular in the absence of transverse velocity perturbations, Wu *et al.* (1993) showed that it was not well correlated across the span, indicating that the shedding was non-parallel. When transverse velocity perturbations were applied at a frequency close to the natural vortex shedding frequency, and at an amplitude sufficiently high to lock the vortex shedding to the perturbations, the vortex shedding was found to be well correlated across the span of the model (Wu *et al.* 1993), and therefore parallel.

## 4.2 Plates with rectangular leading and trailing edges

Experiments have been performed in the open jet wind tunnel on rectangular plates 13 mm thick, with chord to thickness ratios ( $c/t$ ) between 6 and 16. Surface pressure measurements and smoke wire visualisations were performed in the open jet wind tunnel at  $Re$  ranging between 5000 and 13000. The longitudinal turbulence intensity ( $u'/U_\infty$ ) at the location of the leading edge corner of all models tested was less than 0.3%. Parker & Welsh (1983) reported that for plates with  $c/t > 7.6$  in the absence of external flow perturbations, no regular vortex shedding is observed in the wake in this  $Re$  range. PIV measurements and flow visualisation were performed in the closed circuit water tunnel for  $Re = 490$ .

### 4.2.1 Surface pressure measurements and smoke wire flow visualisation

Figure 4.25 shows the variation of the surface pressure coefficient ( $C_{ps}$ ) over the upstream face of a rectangular plate with  $c/t = 10$ , and  $U_\infty = 10 \text{ ms}^{-1}$  ( $Re = 8667$ ). At the centre of the surface is a stagnation point, and as expected the pressure coefficient there is equal to 1.0. Changing plate  $c/t$  ratio had no measurable effect on the distribution of the pressure coefficient over the upstream face of the plates tested.

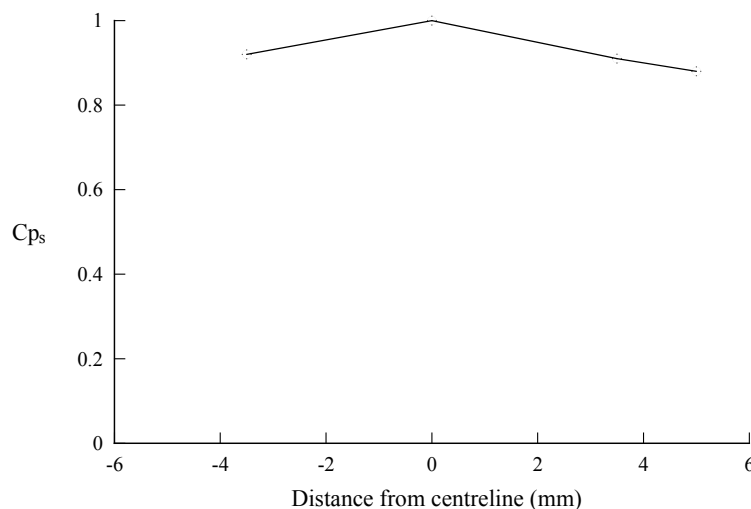


**Figure 4.25** Time mean surface pressure coefficient on upstream surface of a rectangular plate.

Figure 4.26 shows the variation of time mean  $C_{ps}$  along the streamwise surface of the same plate. A relatively high level of suction occurs under the separation bubble. After the

reattachment point of the separated shear layer, the magnitude of  $C_{p_s}$  remains less than 0.1 until within 1.5 plate thicknesses of the trailing edge corner of the plate. Also shown are data from Ram & Arakeri (1990) for the time mean surface pressure coefficient measured under the separation bubble of a long flat plate. Ram & Arakeri measured the time mean reattachment length of the separation bubble to be  $4.8t$ , with  $Re = 8600$  based on  $t$ , and the longitudinal turbulence intensity equal to 0.3%. The good agreement between the two sets of data indicates that the time mean reattachment length for the  $c/t = 10$  plate would also be  $4.8t$ , or 62.4 mm. For plates with  $c/t > 7.6$ , the variation of the surface pressure coefficient ( $C_{p_s}$ ) along the streamwise surfaces under the separation bubble of a rectangular plate is unaffected by plate length, since the time-dependent separated shear layer always reattaches to the plate surface. The smoke wire visualisation of the flow about a rectangular plate with  $c/t = 10$  in figure 4.27 shows that the shear layers on each side of the plate reattach well before the trailing edge.

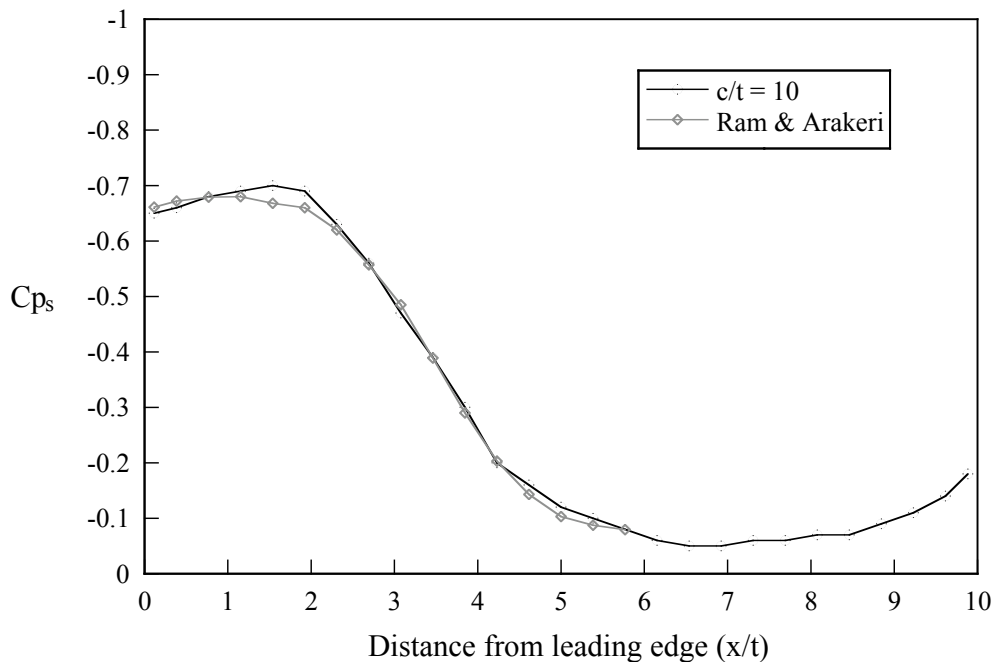
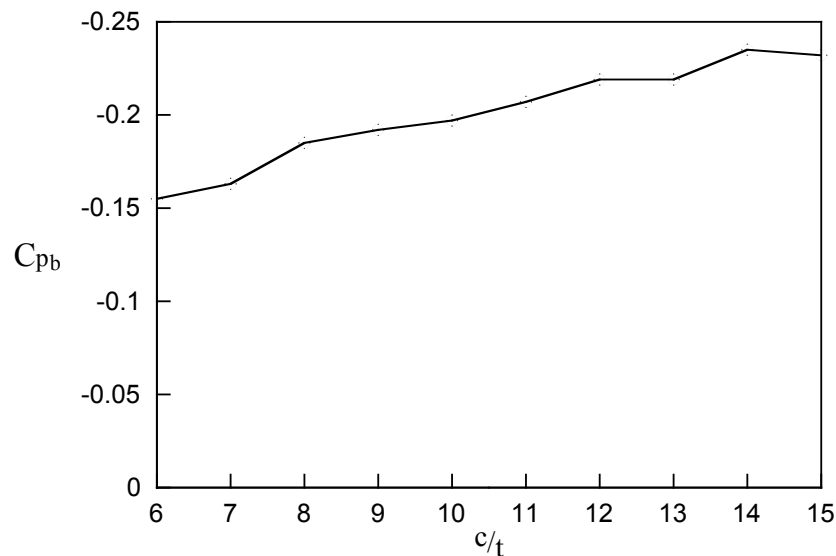


**Figure 4.26** Variation of surface pressure coefficient ( $C_{p_s}$ ) with distance from leading edge along streamwise surface of plate;  $\circ$   $c/t = 10$  ( $Re = 8667$ ),  $\diamond$  data from Ram & Arakeri (1990) for a long rectangular plate ( $Re = 8600$ ).

Smoke wire flow vis image -  $c/t=10$ ,  
 $c/t = 10$  NO PERTURBATION APPLIED.

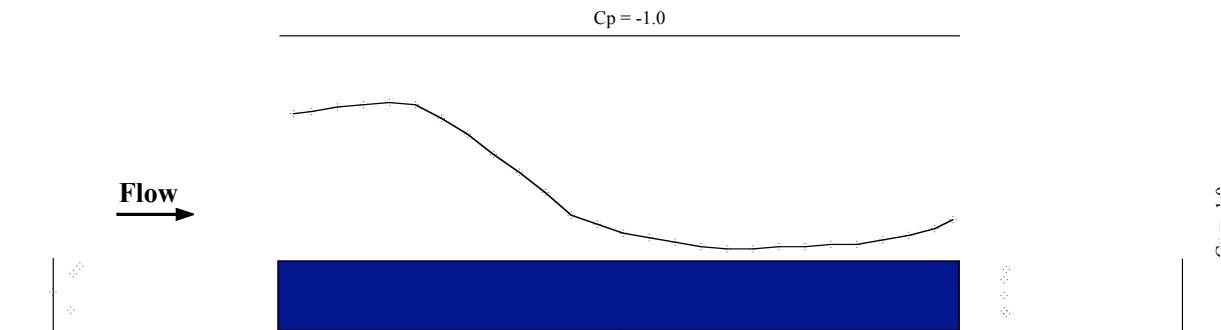
**Figure 4.27** Smoke wire visualisation of flow about a rectangular plate with  $c/t$  ratio = 10.

Figure 4.28 shows the variation of  $C_{p_b}$  with  $c/t$ , for  $U_\infty = 10 \text{ ms}^{-1}$ . The base suction ( $-C_{p_b}$ ) increases with  $c/t$  from a value of 0.16 for  $c/t = 6$ , to 0.23 for  $c/t = 15$ . Since the leading edge separation bubble sheds vortices randomly in time for plates with  $c/t > 7.6$ , as  $c/t$  is increased the patches of vorticity in the boundary layer become more diffused before reaching the trailing edge. Thus, as  $c/t$  is increased, the nature of the boundary layers at the trailing edge separation points on the sides of the plate approaches a fully developed turbulent state (Parker & Welsh 1983), and for plates with  $c/t > 16$ , regular vortex shedding occurs at the trailing edge. It is not surprising then that as  $c/t$  ratio is increased to 15, the value of  $C_{p_b}$  approaches the value for a plate with an aerofoil leading edge of the same  $c/t$  ratio (see figure 4.2).



**Figure 4.28** Variation of  $C_{p_b}$  with  $c/t$ , with  $U_\infty = 10 \text{ ms}^{-1}$ .

The variation of the time average surface pressure coefficient ( $C_{p_s}$ ) over all surfaces of the rectangular plate with  $c/t = 10$  with  $Re = 8667$  is shown in figure 4.29.  $C_{p_s}$  is not plotted on the lower streamwise surface since the results are identical due to flow symmetry.



**Figure 4.29** Variation of surface pressure coefficient around a rectangular plate with  $c/t = 10$ , when flow is unperturbed.

#### 4.2.1.1 Effect of transverse velocity perturbations

In section 4.1, the effect of transverse velocity perturbations on  $C_{p_b}$  for long plates with aerofoil leading edges was reported. The effect of perturbations above a minimum threshold level was to correlate the vortex shedding across the span of the model, and to increase the circulation and peak vorticity of the vortices shed. The vortex formation length was also observed to decrease. These factors, combined, result in a large decrease in  $C_{p_b}$  when the vortex shedding at the trailing edge phase-locks to the transverse perturbations.

For plates with rectangular leading edges, flow separation occurs at both the leading and trailing edges of the model. Parker & Welsh (1983) reported that rectangular plates with  $c/t$  between 6 and 16 can shed regular vortices to form a wake with the same frequency as transverse velocity perturbations, for perturbation Strouhal numbers ( $St_p$ ) between 0.05 and 0.25 ( $St_p$  based on plate thickness). Figure 4.30 shows the effect of transverse velocity perturbations applied at  $St_p = 0.17$  on the time mean surface pressure coefficient along the streamwise surface of a rectangular plate with  $c/t = 10$ , compared to  $C_{p_s}$  without any perturbation field applied. Data from Saathoff & Melbourne (1989) for flow over a long rectangular plate with an 8% free stream turbulence level are also presented for comparison, and show a strong similarity to the data for a 7% transverse velocity perturbation.

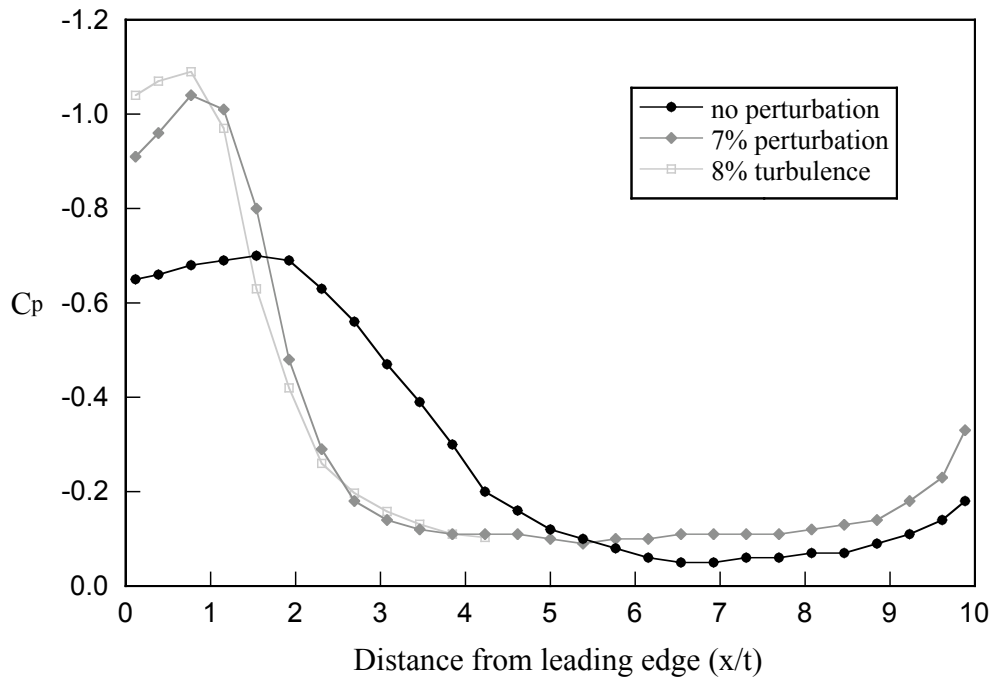


**Figure 4.30** Variation of  $C_{p_s}$  along the streamwise surface of a rectangular plate; •  $c/t = 10$  with no perturbation, ◆  $c/t = 10$  with 7% transverse velocity perturbation applied at  $St_p = 0.17$ , □ data from Saathoff & Melbourne (1989) for 8% free stream turbulence.

Smoke wire flow vis image -  $c/t=10$ ,

$c/t = 10$

PERTURBATION APPLIED.

**Figure 4.31** Smoke wire visualisation of flow about a rectangular plate with  $c/t$  ratio = 10.

With the vortex shedding at the leading edge phase-locked to the transverse velocity perturbations, the vortex formation length is significantly reduced, and the strength of shed vortices is increased, resulting in a much higher peak in the time mean  $C_{p_s}$  under the separation bubble. The effect of the transverse perturbations on increasing shear layer curvature and decreasing reattachment length can be seen by comparing figure 4.31 with figure 4.27.

A similar effect on leading edge vortex shedding is caused by high levels of free stream turbulence, even though the velocity perturbations due to free stream turbulence are random in nature (Saathoff & Melbourne 1997).

In a publication of some preliminary results of this study, it was reported by Hourigan *et al.* (1993) that surface pressure coefficients measured using different flow velocities were identical if the relative perturbation level was kept constant. Figure 4.32 shows the variation of  $C_{p_s}$  with streamwise distance from the leading edge of the plate with  $c/t = 10$  in the presence of 7% transverse velocity perturbation, for two different flow velocities.  $St_p$  was equal to 0.17 in both cases, and the good agreement between the two sets of data demonstrates the repeatability of the pressure measurements.

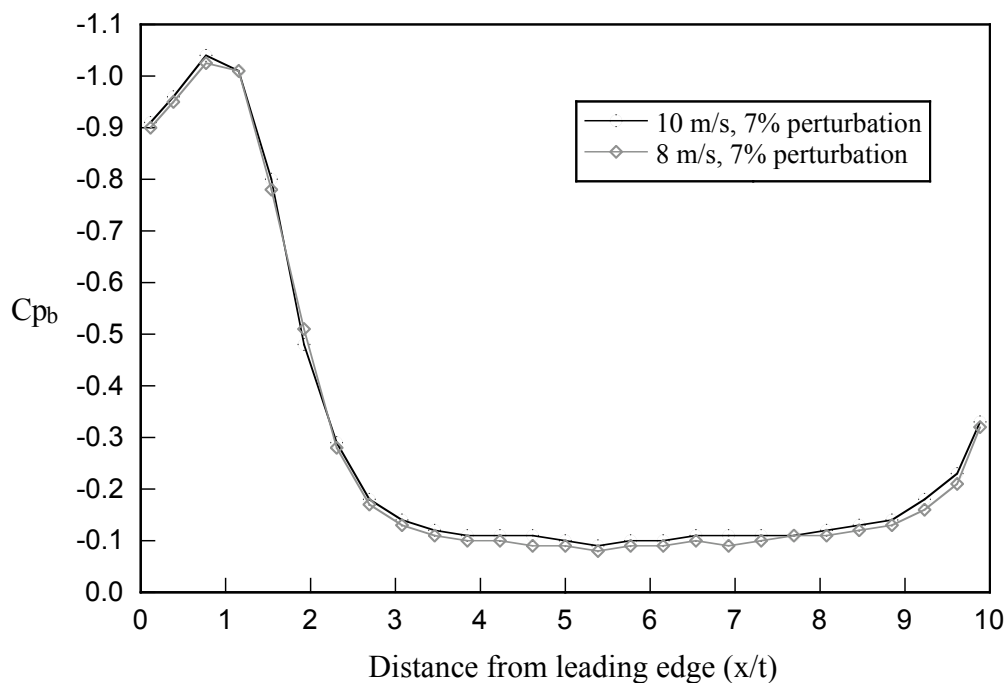


**Figure 4.32** Surface pressure coefficient for 7% velocity perturbation at two different flow velocities.

Cooper *et al.* (1986) found that the base pressure coefficient ( $C_{p_b}$ ) for a rectangular plate with  $c/t = 10$  always reduced in the presence of transverse velocity perturbations, although no explanation for the changes in  $C_{p_b}$  was offered. Figure 4.33 shows the effect on surface pressure across the span of the  $c/t = 10$  plate when a 7% transverse velocity perturbation is applied at a perturbation Strouhal number ( $St_p$ ) of 0.17.

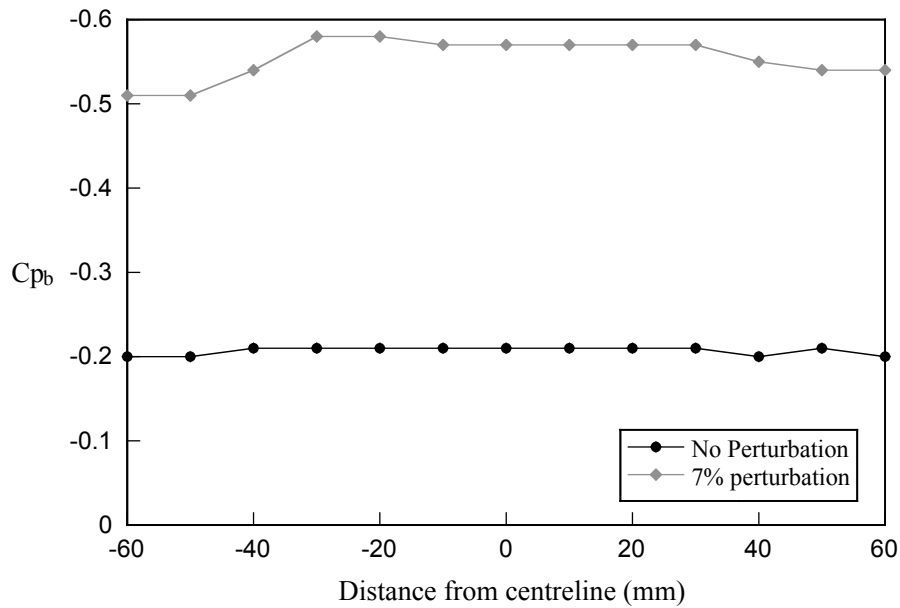


**Figure 4.33** Effect of 7% transverse velocity perturbation applied at  $St_p = 0.17$  on  $C_{pb}$  measured at pressure tappings across the span for a rectangular plate with  $c/t = 10$ .

Figure 4.34 illustrates the effect of transverse velocity perturbation on the time mean pressure coefficient over all surfaces of a rectangular plate. The perturbation level in this case was 7.0%, and the perturbation Strouhal number ( $St_p$ ) was 0.17.

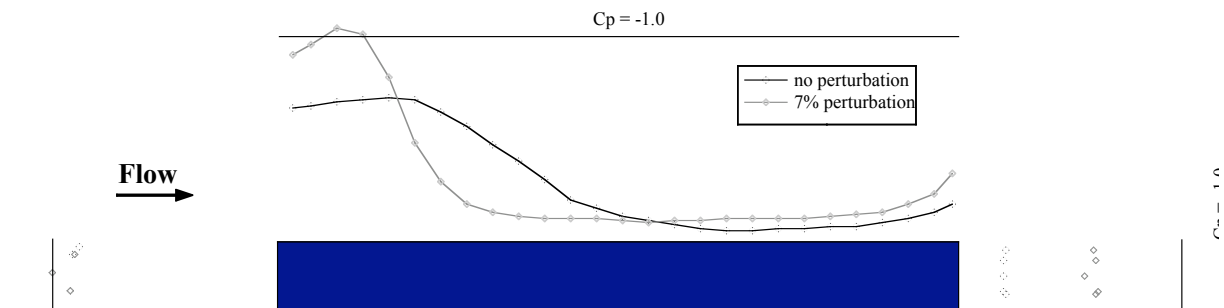


**Figure 4.34** Variation of surface pressure coefficient around a rectangular plate with  $c/t = 10$ , with and without transverse velocity perturbation applied.

It can clearly be seen that the effect of locking leading edge shedding to transverse velocity perturbations is to increase the suction under the separated shear layer, as well as reduce the time average length of the separation bubble. The base suction also shows a large increase, while the surface pressures on the upstream face are virtually unaffected.

The effect on  $C_{pb}$  of varying perturbation frequency is illustrated in figure 4.35 for a plate with  $c/t = 10$ , a 4.5% relative perturbation level and  $U_\infty = 10 \text{ ms}^{-1}$ . With no perturbations

applied ( $St_p = 0.0$ ),  $Cp_b = -0.195$ . Due to limitations of the loudspeakers used to generate the transverse velocity perturbations, it was not possible to apply velocity perturbations for  $St_p < 0.13$  at this perturbation level.

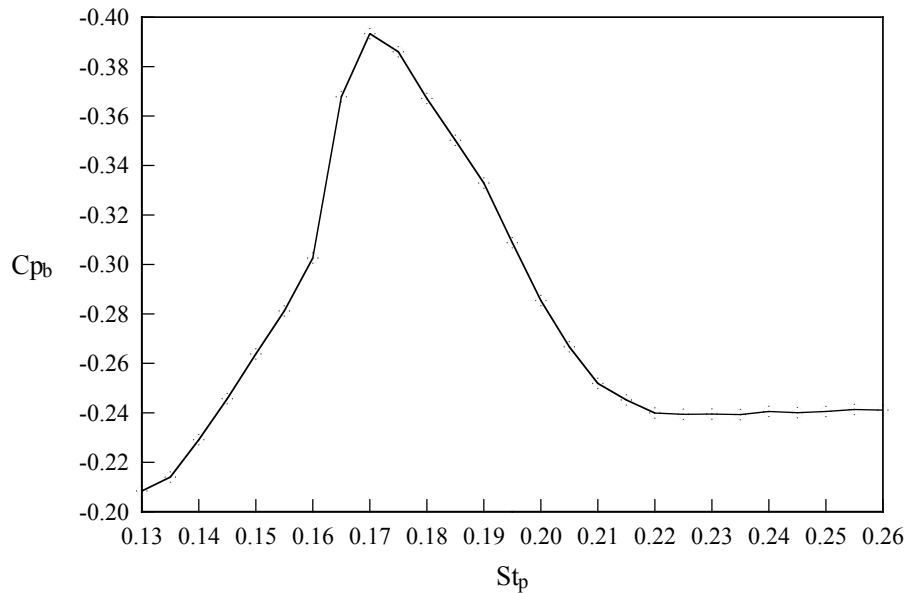


**Figure 4.35** Variation of  $Cp_b$  with  $St_p$  for  $c/t = 10$  plate,  $U_\infty = 10 \text{ ms}^{-1}$ , and 4.5% relative perturbation level.

Since there is no regular vortex shedding from rectangular plates with  $c/t$  between 8 and 16 in the absence of transverse velocity perturbations for  $Re \geq 2000$  (Parker & Welsh 1983), it is interesting to note that a peak in  $Cp_b$  of -0.393 occurs for  $St_p = 0.17$ . Parker & Welsh (1983) found that vortex shedding from the leading edge could be phase-locked to transverse velocity perturbations over a range of  $St_p$  from 0.05 to 0.25, resulting in a near wake with the same  $St$ . Therefore, over the entire range of  $St_p$  shown in figure 4.35, vortex shedding from the leading edge will have been phase-locked to the transverse velocity perturbations. Saathoff & Melbourne (1997) found that in turbulent flow, the turbulence length scale (inversely related to the frequency of turbulence fluctuations) had virtually no effect on the time mean surface pressure under the separation bubble of a long flat plate. Rather, it was the relative turbulence level which determined the surface pressure distribution under the separation bubble. With the relative perturbation level being kept constant as  $St_p$  was varied, the changes in frequency and thus spacing between vortices (which is analogous to turbulence length scale) shed from the leading edge had virtually no effect on the time mean surface

pressure coefficient under the separation bubble, and by itself does not explain the variations in  $Cp_b$  shown in figure 4.35 that occur as  $St_p$  is varied.

Nakamura *et al.* (1991) found that the Strouhal number for vortex shedding from rectangular plates with  $c/t = 10$  at  $Re = 1000$  was 0.18, which is close to the  $St_p$  that the peak in  $Cp_b$  shown in figure 4.35 occurs. A two dimensional laminar numerical simulation by Ohya *et al.* (1992) of flow about elongated rectangular plates at  $Re = 1000$  showed that regular vortex shedding from the trailing edge, as well as the leading edge, was a natural feature of the flow.

Hourigan *et al.* (1993) mentioned that flow visualisation in the water tunnel at the CSIRO Hightett showed the possibility of transverse velocity perturbations being able to phase-lock vortex shedding from both the leading edge and trailing edge of a rectangular plate with  $c/t = 10$ . For a plate with  $c/t$  ratio of 10, the similarity in Strouhal number between the natural vortex shedding frequency observed by Nakamura *et al.* (1991) at low  $Re$  and the  $St_p$  at which the peak in  $Cp_b$  occurs (see figure 4.35), suggests that the transverse velocity perturbations lock the vortex shedding at both the leading and trailing edges. Particle Image Velocimetry (PIV) and flow visualisation results presented in a later section of this chapter will show that this is in fact possible.

Stansby (1976) showed that transversely oscillating a circular cylinder at a frequency close to the natural vortex shedding frequency could result in vortex shedding phase-locking to the oscillations, resulting in a large rise in  $-Cp_b$ . It has been shown earlier (see figure 4.3) that for a plate with an aerofoil leading edge, when transverse velocity perturbations are applied at a frequency close to the natural vortex shedding frequency, the vortex shedding at the trailing edge phase-locks with the transverse velocity perturbations resulting in a large rise in  $-Cp_b$ .

It is hypothesised that the peak in  $Cp_b$  observed in figure 4.35 at  $St_p = 0.17$  is due to the transverse velocity perturbations locking vortex shedding at the trailing edge as well as the leading edge to the frequency of the perturbations. This hypothesis is supported by the results of a two dimensional computational fluid dynamics (CFD) simulation of the flow about a rectangular plate at  $Re = 400$  with  $c/t$  ratio of 10, as reported by Thompson *et al.*

(1997); they showed that transverse velocity perturbations applied at a frequency equal to the natural vortex shedding frequency ( $St = 0.18$ ) locked vortex shedding at both the leading and trailing edges, resulting in the most negative  $Cp_b$ . Applying perturbations at  $St_p = 0.16$  also resulted in trailing edge shedding being locked to the transverse perturbations, but the magnitude of  $Cp_b$  was less due to trailing edge vortices forming further away from the base of the plate. For perturbations applied at  $St_p = 0.20$ , the trailing edge shedding was still locked but very weak, and the magnitude of  $Cp_b$  was less than for both cases mentioned above.

The shape of the base suction ( $-Cp_b$ ) vs  $St_p$  curve in figure 4.35 shows that as  $St_p$  is either increased or decreased from the frequency that results in the peak value of  $-Cp_b$ , the base suction decreases steadily to a value that is close to the  $-Cp_b$  which is measured without transverse velocity perturbations applied. This smooth change in base suction indicates that vortex shedding at the trailing edge may be locked to the velocity perturbation for  $St_p$  both above and below the  $St_p$  that results in the highest base suction. This is supported by flow visualisation recorded on video, in the water tunnel, and by the CFD predictions of Thompson *et al.* (1997).

It is interesting to compare the shape of the curve in figure 4.35 with figure 4.3 shown in the previous section for a plate with an aerofoil leading edge and a rectangular trailing edge. For the aerofoil leading edge plate with  $St_p$  higher than the  $St_p$  that corresponds to the maximum base suction,  $-Cp_b$  decreases steadily towards the base suction measured without perturbations applied as  $St_p$  is increased. For  $St_p$  lower than the  $St_p$  that corresponds to the maximum base suction, as  $St_p$  is increased, there is virtually no change in  $-Cp_b$  until  $St_p$  reaches the critical value corresponding to the sudden increase in  $Cp_b$ . It was suggested that this sudden rise in base suction for a plate with an aerofoil leading edge, corresponds to a large phase shift in the vortex shedding compared to the perturbation cycle as  $St_p$  is increased past a critical value. The acoustic resonance observed by Welsh *et al.* (1984) for flow around a plate in a duct with a semi-circular leading edge and rectangular trailing edge was found to occur only at  $St$  above the natural vortex shedding frequency hence the name “lock up”. Resonant vortex shedding could not be generated when the resonant duct frequency was

below the natural vortex shedding frequency, just as there is little effect on  $Cp_b$  when  $St_p$  is below the lock on frequency (see figure 4.3).

#### 4.2.1.2 Effect of plate length on variation of $Cp_b$ in response to perturbations

Unlike plates with aerofoil leading edges, from which there is no leading edge vortex shedding, the changes observed in  $Cp_b$  as  $St_p$  is varied show a strong dependence on the plate  $c/t$  ratio for plates with rectangular leading edges. The dependence on  $c/t$  ratio of the  $St_p$  at which peaks in  $Cp_b$  occur is illustrated in figure 4.36, for two different plates with  $c/t = 8$  and 10 respectively. In both cases, the relative perturbation level was 4.5%, and  $U_\infty = 10 \text{ ms}^{-1}$ .

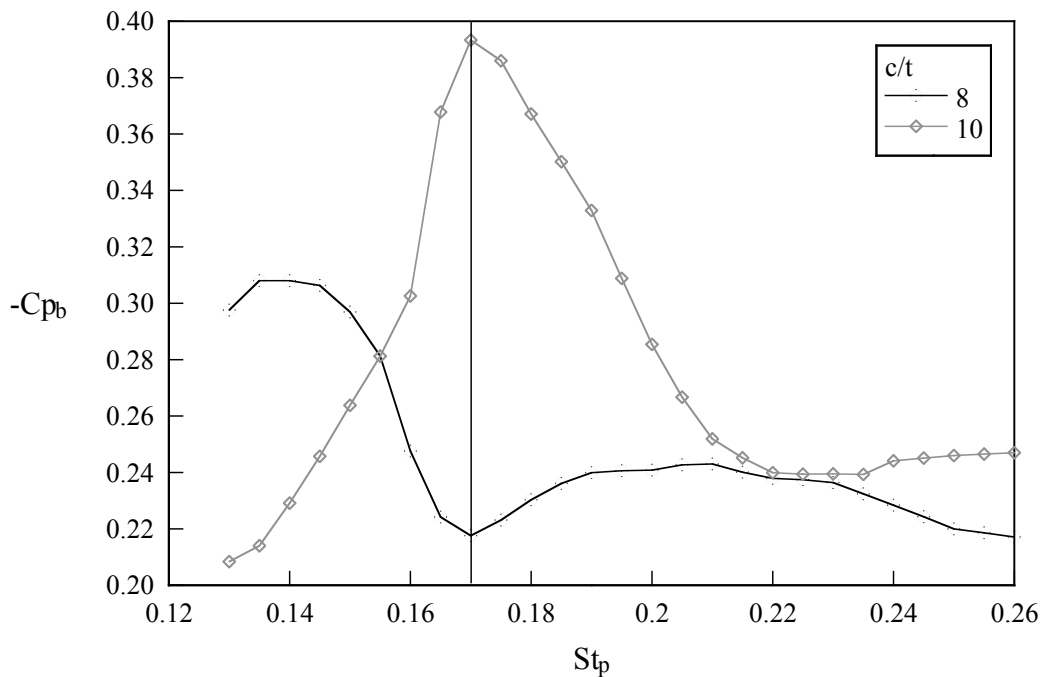


**Figure 4.36** Comparison of  $Cp_b$  vs  $St_p$  for plates with  $c/t = 8$  and 10;  $U_\infty = 10 \text{ ms}^{-1}$  and perturbation level = 4.5%.

For the plate with  $c/t = 8$ , there is a peak in  $-Cp_b$  when  $St_p = 0.138$ , indicating that vortex shedding at the trailing edge is locked to the perturbations at this frequency. As  $St_p$  is increased further there is a recovery in  $-Cp_b$ , with a local minimum occurring at  $St_p = 0.17$  indicating that the vortex shedding at the trailing edge is no longer locked to the perturbations. This is in contrast to the plate with  $c/t = 10$ , for which there is a maximum in  $-Cp_b$  at  $St_p = 0.17$ .

As discussed earlier in this section, vortex shedding from the leading edge is locked to the perturbation frequency, and occurs alternately from either side of the model. Stokes & Welsh (1986) found that leading edge vortices are always shed at the same phase in the perturbation cycle, independent of  $c/t$  ratio.

Assuming that the convection velocity of vortices is not affected by changes in plate  $c/t$  ratio, the plate chord changes the position in the acoustic phase at which the leading edge vortices arrive at the trailing edge. It was hypothesised by Hourigan *et al.* (1993) that interference with the trailing edge vortex shedding by the leading edge vortices may be responsible for the significant variation in  $-Cp_b$  between the two sets of data shown in figure 4.36. This hypothesis was called the vortex interaction hypothesis.

Figure 4.37 shows two smoke wire flow visualisation images of flow around rectangular plates in the presence of a 5% transverse velocity perturbation applied at  $St_p = 0.17$ . The phase of the perturbation cycle at which the images were taken is the same in each case; it can be seen that vortices shed from the leading edge are in similar streamwise locations, and the spacing between them is unaffected by the difference in  $c/t$  ratio of each plate. This shows that the convection velocity of vortices shed from the leading edge when locked to transverse velocity perturbations is unaffected by changes in  $c/t$  ratio, which is a necessary condition for the vortex interaction hypothesis to be valid.

$c/t = 8$

Smoke wire image of  $c/t=8$  plate  
Perturbation applied at  $St_p = 0.17$ .

$c/t = 10$ 

Smoke wire image of  $c/t=10$  plate  
(leading edge in same pos. as  $c/t=8$  plate)

**Figure 4.37** Flow visualisation of flow over rectangular plates with vortex shedding locked to transverse velocity perturbations;  $u'/U_\infty = 5\%$ ,  $St_p = 0.17$ .

Figure 4.38 shows the predicted locations of vortices surrounding two plates of different chord-thickness ratios, at two different phases of the perturbation cycle. Vortex shedding from the leading edge is phase-locked to the transverse velocity perturbations, and the phase of vortex formation and shedding at the leading edge relative to the phase of the perturbation cycle is unaffected by the position of the trailing edge. For the left hand pair of plates, the  $c/t = 10$  plate has a vortex that is starting to form at the trailing edge. The  $c/t = 8$  plate has a vortex that was shed from the lower leading edge passing the lower trailing edge corner at the same phase in the forcing cycle, which interferes with the vortex shedding at the trailing edge.

The two plates on the right hand side of figure 4.38 denote the predicted location of vortices surrounding the plate and in the wake after a further  $90^\circ$  of the perturbation cycle, showing the nearly fully formed vortex at the trailing edge of the  $c/t = 10$  plate.

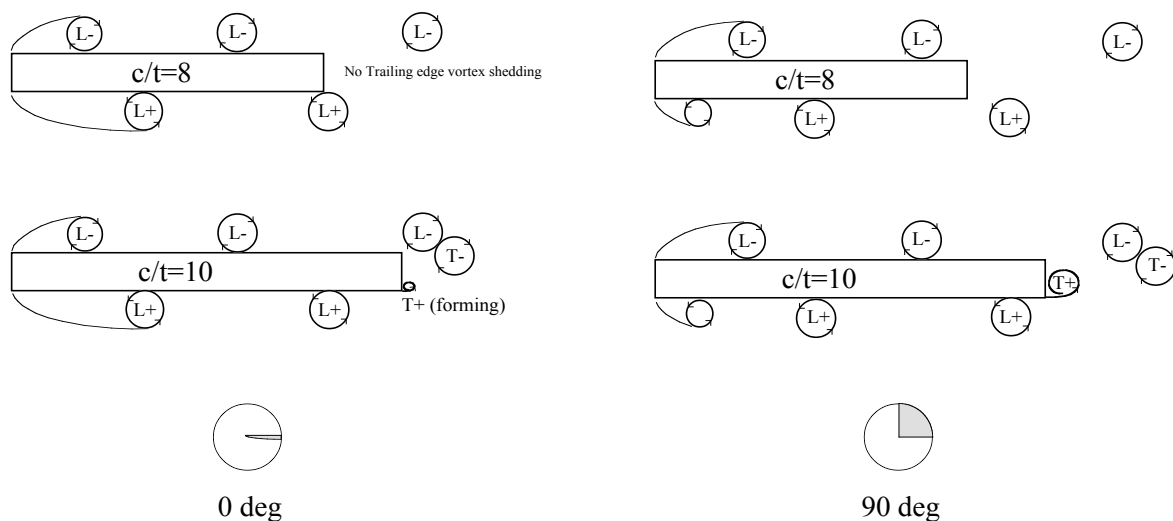


**Figure 4.38** Illustration of vortex shedding from two rectangular plates of different chord-thickness ratios, subject to transverse velocity perturbations of the same amplitude and frequency.

One experiment performed in order to test the vortex interaction hypothesis was to measure  $Cp_b$  for rectangular plates with  $c/t$  ranging from 6 to 16 in integer steps. The results for each plate  $c/t$  ratio are shown individually in figure 4.39 for a relative velocity perturbation level of 4.5%, and  $U_\infty = 10 \text{ ms}^{-1}$ . The same data are presented in figure 4.40 to better illustrate the effect on  $Cp_b$  of varying  $c/t$  ratio.

For all plate  $c/t$  ratios tested, the base suction ( $-Cp_b$ ) exhibited a local peak at some value of  $St_p$ . The value of  $St_p$  at which these peaks occur shows a strong dependence on  $c/t$  ratio. Figure 4.40 clearly shows that the peaks in  $-Cp_b$  occur in three distinct groups. This feature is again consistent with the vortex interaction hypothesis. In order to strengthen the argument in favour of the vortex interaction hypothesis, it needs to be established that vortex shedding at the trailing edge can in fact be simultaneously locked to the transverse velocity perturbations with the leading edge vortex shedding. PIV experiments were performed in the water tunnel to investigate this; the results are presented in a later section.

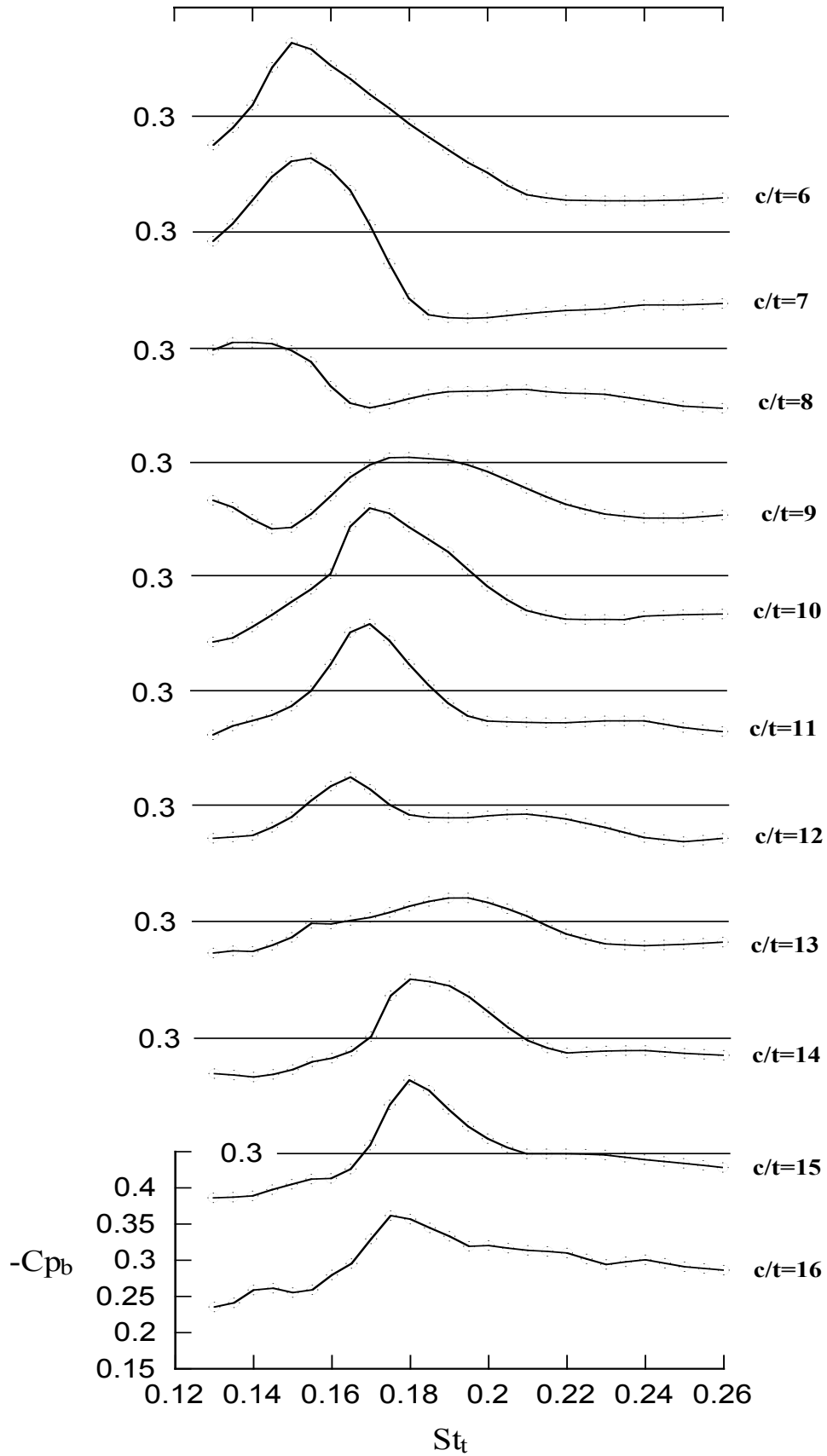


**Figure 4.39** Variation of  $C_{pb}$  with  $St_p$  for all rectangular plates; Perturbation level = 4.5%,  $U_\infty = 10 \text{ ms}^{-1}$ .

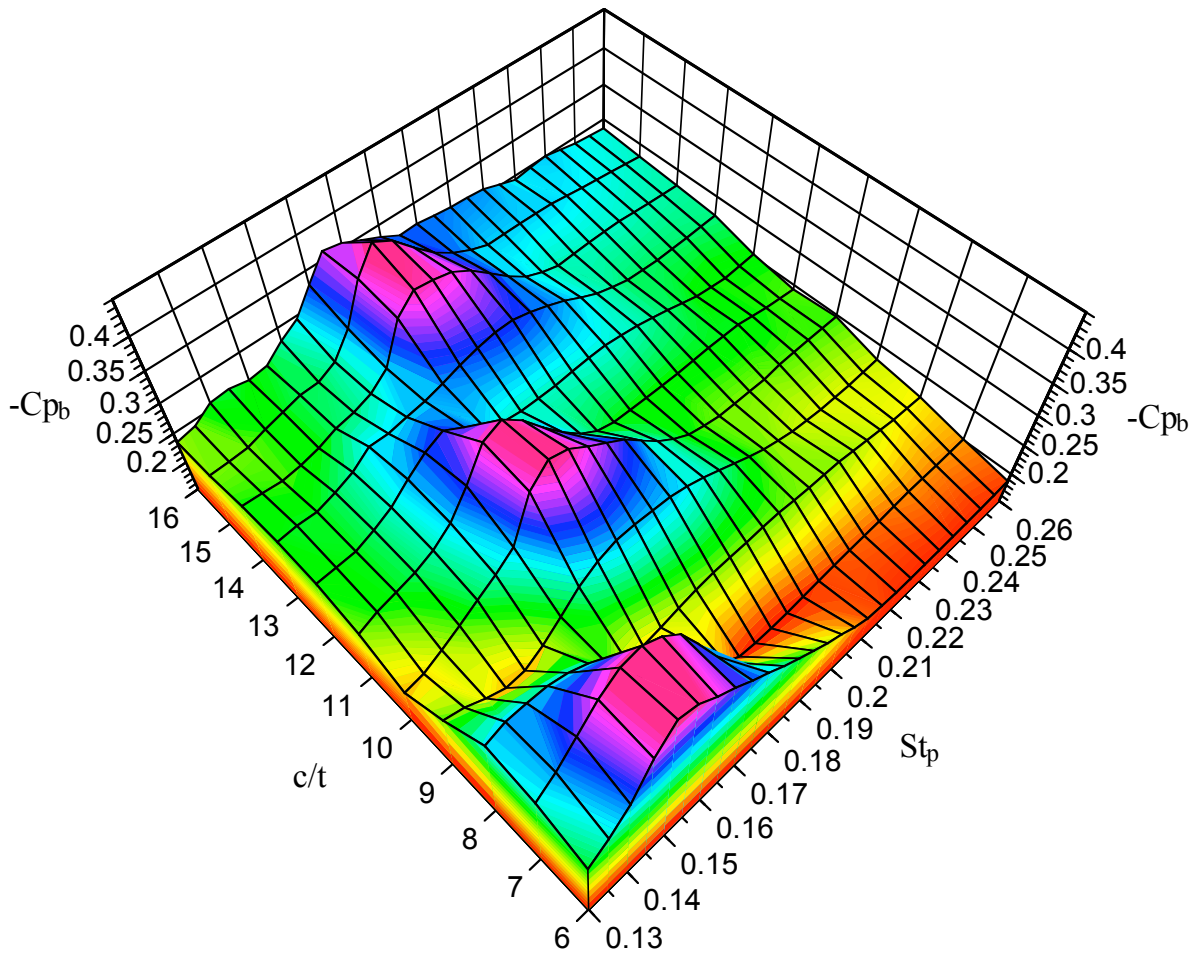


**Figure 4.40** Surface plot of base suction ( $-Cp_b$ ) as  $c/t$  and  $St_p$  are varied; relative perturbation level = 4.5%,  $U_\infty = 10 \text{ ms}^{-1}$ .

Table 4.2 lists the values of  $Cp_b$  and  $St_p$  at which peaks in  $Cp_b$  occur for each plate length tested, when the relative perturbation level is 4.5% and  $U_\infty = 10 \text{ ms}^{-1}$ . Figure 4.41 shows the difference between the peak values of  $Cp_b$  and the  $Cp_b$  measured in the absence of perturbations for each  $c/t$  ratio tested. Plates with  $c/t = 6, 7, 10, 11, 14, 15$  and  $16$ , show the largest peak values of  $Cp_b$ , with only a single peak occurring as  $St_p$  is increased. These plates will be referred to as the primary plates. For the other plates ( $c/t = 8, 9, 12$  and  $13$ ), the sizes of the peaks are significantly smaller. Even smaller secondary peaks are also found to occur for these other plates, which will be referred to as the intermediate plates. For the plate with  $c/t = 9$ , the size and  $St_p$  of the secondary peak was extrapolated from data, which will be presented later in this chapter, obtained when a lower perturbation level was applied.

$c/t$	$St_p$ of peak in $Cp_b$	$Cp_b$ (peak value)	$St_p$ of secondary peak in $Cp_b$	$Cp_b$ (secondary peak value)
6	0.150	-0.401	not present	
7	0.155	-0.402	not present	
8	0.1375	-0.308	0.210	-0.243
9	0.180	-0.307	0.116	-0.250 estimated
10	0.170	-0.393	not present	
11	0.170	-0.392	not present	
12	0.165	-0.338	0.210	-0.287
13	0.195	-0.332	0.155	-0.301
14	0.180	-0.381	not present	
15	0.180	-0.402	not present	
16	0.175	-0.362	not present	

**Table 4.2** Peak values of  $Cp_b$  and the values of  $St_p$  for which they occur ( $Re = 8667$ , 4.5% perturbation)

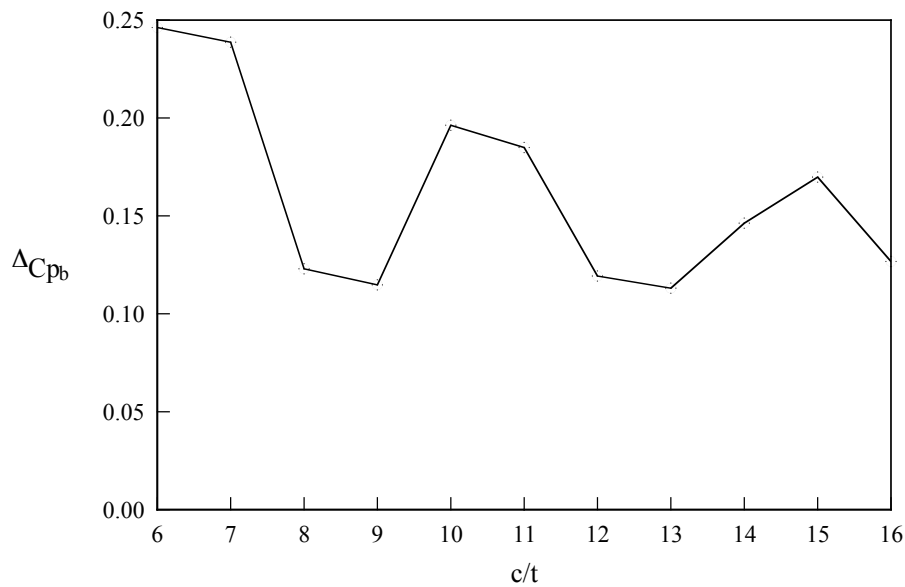


**Figure 4.41** Difference in  $Cp_b$  for each plate chord to thickness ratio ( $c/t$ ) tested between peak values of  $Cp_b$  and  $Cp_b$  measured without perturbation applied; relative perturbation level = 4.5%,  $U_\infty = 10 \text{ ms}^{-1}$ .

An important finding in support of the vortex interaction hypothesis is that for the intermediate plates, with perturbations applied at the same  $St_p$  that result in peaks in  $Cp_b$  for the primary plates, the magnitude of  $Cp_b$  is significantly reduced. This is consistent with the assumption that vortices shed from the leading edge (hereafter called L vortices) interfere with vortex shedding at the trailing edge depending on the phase in the perturbation cycle at which they arrive at the trailing edge.

As  $c/t$  is increased, the spacing between the peaks in  $Cp_b$  shown in figure 4.40 is approximately equal to  $4.0t$ . This also happens to be the same as the spacing between the peaks in  $\Delta Cp_b$  shown in figure 4.41. Although there is no regular vortex shedding from

rectangular plates in the absence of any flow perturbations for  $Re > 2000$  and with  $7.6 < c/t < 16$ , there is weak vortex shedding from the separation bubble on a long rectangular plate ( $c/t > 20$ ) of vortices with similar size to the separation bubble (Kiya 1983). Soria & Wu (1992) found that the separated shear layer from a rectangular plate is convectively unstable in nature, which is consistent with the fact that vortex shedding from the leading edge of long rectangular plates is receptive to flow disturbances over a wide range of frequencies. The response of a plane mixing layer to disturbances or perturbations in the flow shows a similar receptivity, and Hillier & Cherry (1981) found that the shear layer development over the first 60% of the separation bubble length is similar to that of a mixing layer. Only over the last 40% of the separation bubble length does the shear layer development differ from a mixing layer, due to the presence of the downstream reattachment surface of the plate. Although the shear layer is convectively unstable, the presence of the downstream reattachment surface causes a weakly periodic shedding of vortices from the separation bubble in the absence of other flow disturbances. Hot-wire measurements by Kiya & Sasaki (1983) showed a broad spectral peak at the reduced frequency of  $0.6U_\infty/X_R$ , and found the spacing between these vortices shed from the separation bubble to be approximately  $3.8t$ . This spacing between vortices is very close to the spacing between the peaks in  $Cp_b$  as  $c/t$  is increased, of approximately  $4.0t$ .

For long rectangular plates at low  $Re$  ( $Re < 2000$ ) and in the absence of external flow disturbances, a feedback mechanism called the Impinging Leading Edge Vortex (ILEV) instability characterises vortex shedding (see figure 2.12) as discussed in Chapter 2. Vortex shedding from the leading edges is and periodic, and is locked to the plate chord so that  $St_c = 0.6n$ , where  $n$  is an integer and equal to the ILEV mode. Depending on the plate  $c/t$  ratio, it may take several shedding cycles for an L vortex to pass the trailing edge. Since each feedback pulse is generated as an L vortex passes the trailing edge, as  $c/t$  ratio is varied, L vortices always pass the trailing edge at the same phase in the leading edge shedding cycle. Since T vortices and L vortices of like sign merge together in the near wake, T vortices are

always generated at the same phase in the leading edge shedding cycle regardless of  $c/t$  ratio and are shed just as the L vortex of the same sign approaches the trailing edge.

Nakamura *et al.* (1991) found that the most vigorous and regular vortex shedding occurred for plates with  $c/t = 6$  and 10, while the plate with  $c/t = 8$  shed vortices intermittently at two different frequencies. For the experiments performed in the open jet wind tunnel, as  $St_p$  was varied, the plates with  $c/t = 6$  and 10 showed single, large peaks in  $Cp_b$ , while the plate with  $c/t = 8$  showed two much smaller peaks in  $Cp_b$ , at frequencies close to the two possible ILEV frequencies for natural vortex shedding at low  $Re$ . This is reflected in figure 4.41, which shows the largest change in  $Cp_b$  measured for each  $c/t$  ratio tested.

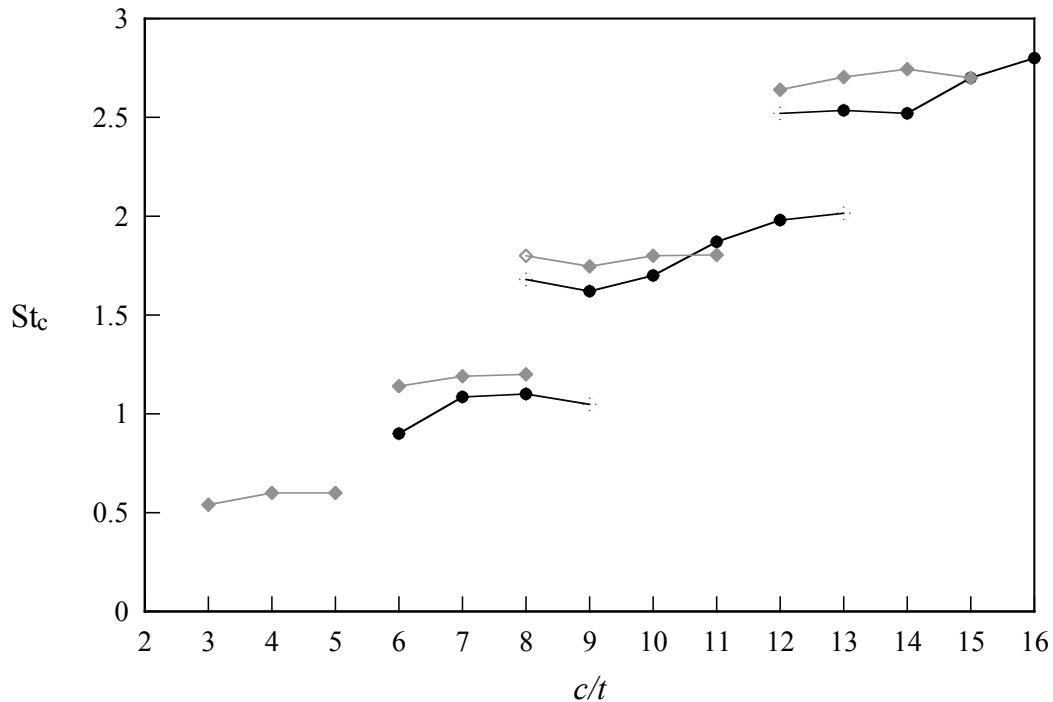


**Figure 4.42** Vortex shedding  $St_c$  for elongated rectangular plates; •  $St_p$  (based on plate chord) corresponding to peaks in  $Cp_b$  data (4.5% perturbation level), ♦  $St_c$  measured by Nakamura at  $Re = 1000$  (solid symbols indicate the primary peaks, open symbols indicate secondary peaks where detected).

The peaks of  $Cp_b$  observed in figure 4.40 appear to occur in distinct groups, similar to the  $St_c$  measured by Nakamura *et al.* (1991). Thus, the  $St_p$  data presented in table 4.2 at which peaks in  $Cp_b$  occur for each plate length has been multiplied by plate  $c/t$  ratio, and is presented in figure 4.42 along with the  $St_c$  that Nakamura measured at  $Re = 1000$ .

As discussed earlier, for rectangular plates in the presence of transverse velocity perturbations, L vortices are always shed at the same phase in the perturbation cycle regardless of  $c/t$  ratio (Stokes & Welsh 1986). The similarity between the two sets of data shown in figure 4.42 adds weight to the argument that peak values of  $C_{p_b}$  occur at  $St_p$  when L vortices pass the trailing edge at the same phase in the perturbation cycle regardless of  $c/t$  ratio. This adds further support to the vortex interaction hypothesis.

#### 4.2.1.3 Effect of perturbation level on $C_{p_b}$

Experiments were performed using relative perturbation levels of 3%, 4%, 4.5% and 5% compared to free stream velocity, while keeping the free stream velocity constant at  $10 \text{ ms}^{-1}$ . The results of these experiments are shown in figure 4.43 for plates with  $c/t$  ratios between 6 and 15. The aim of these experiments was to investigate how the perturbation level affected both the frequency at which peaks in  $C_{p_b}$  occurred, and the magnitude of the peaks in  $C_{p_b}$ .

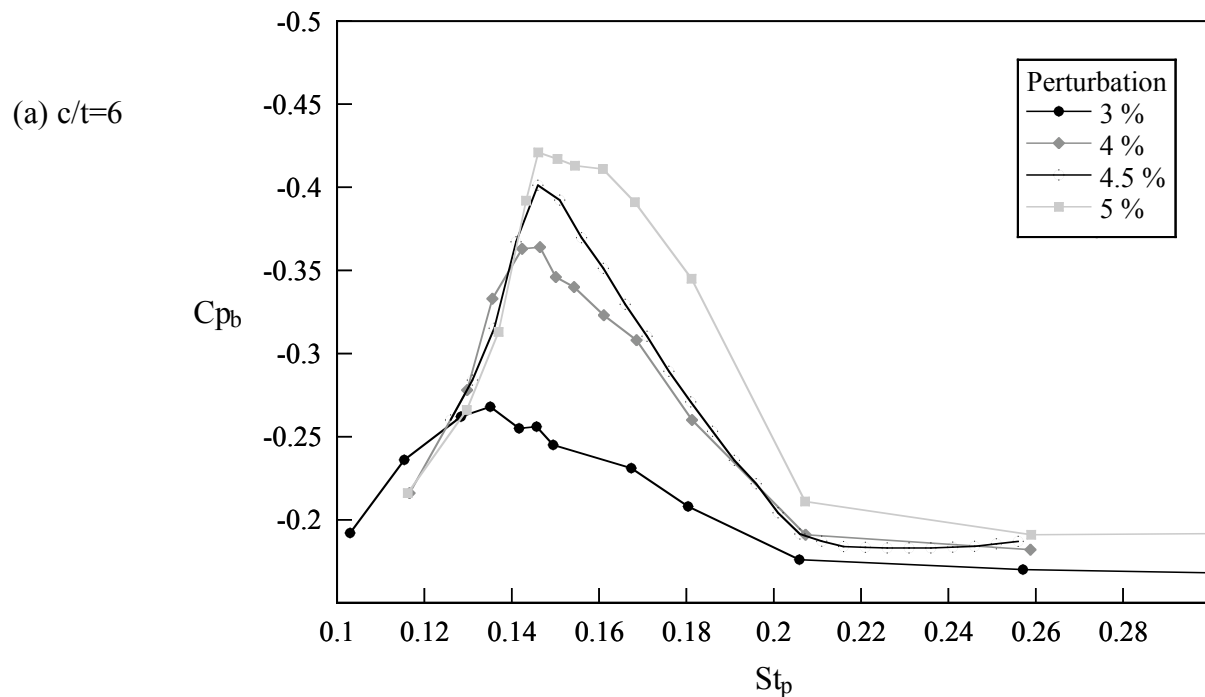


Figure 4.43 See page 119 for caption.

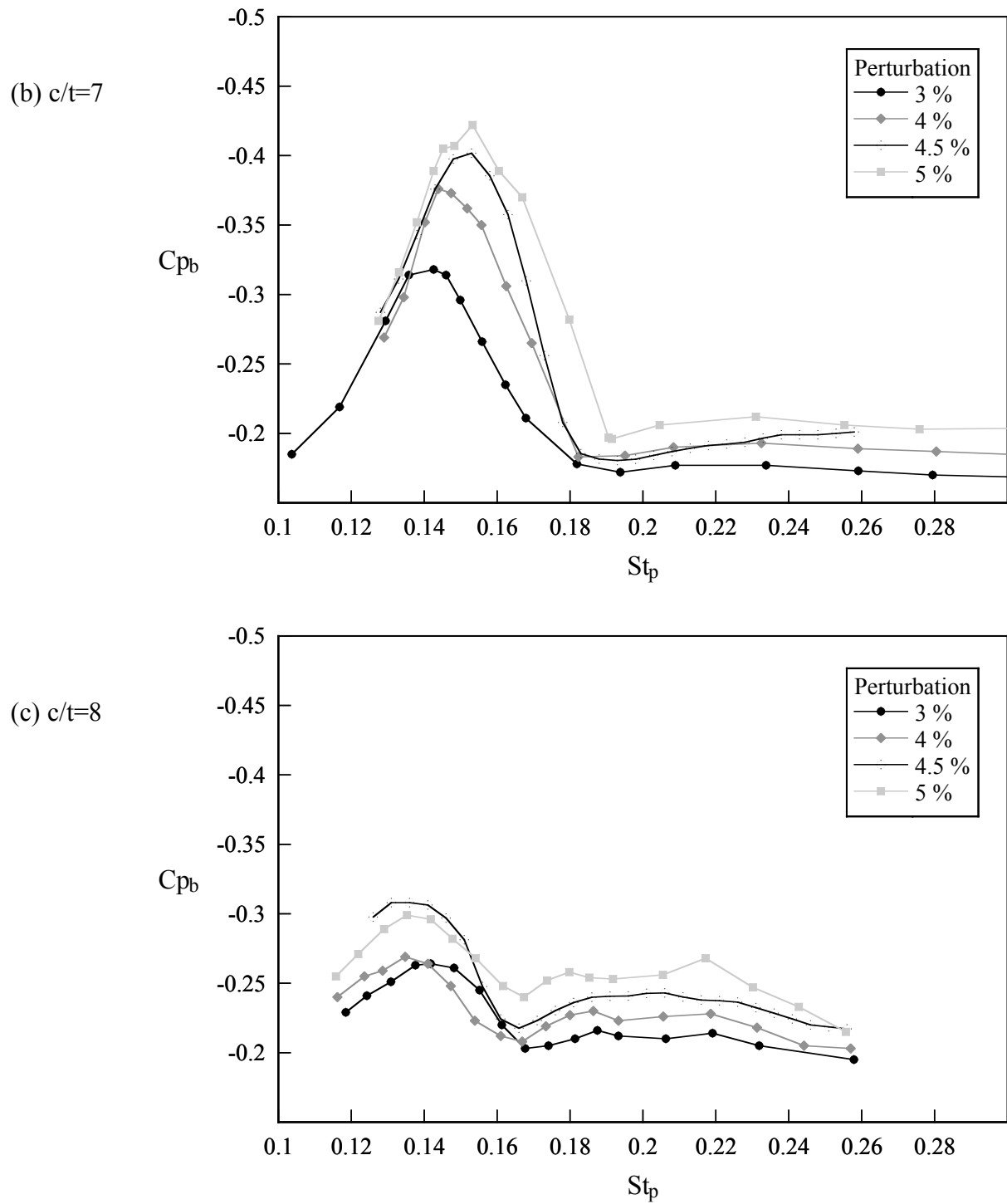


Figure 4.43 See page 119 for caption.

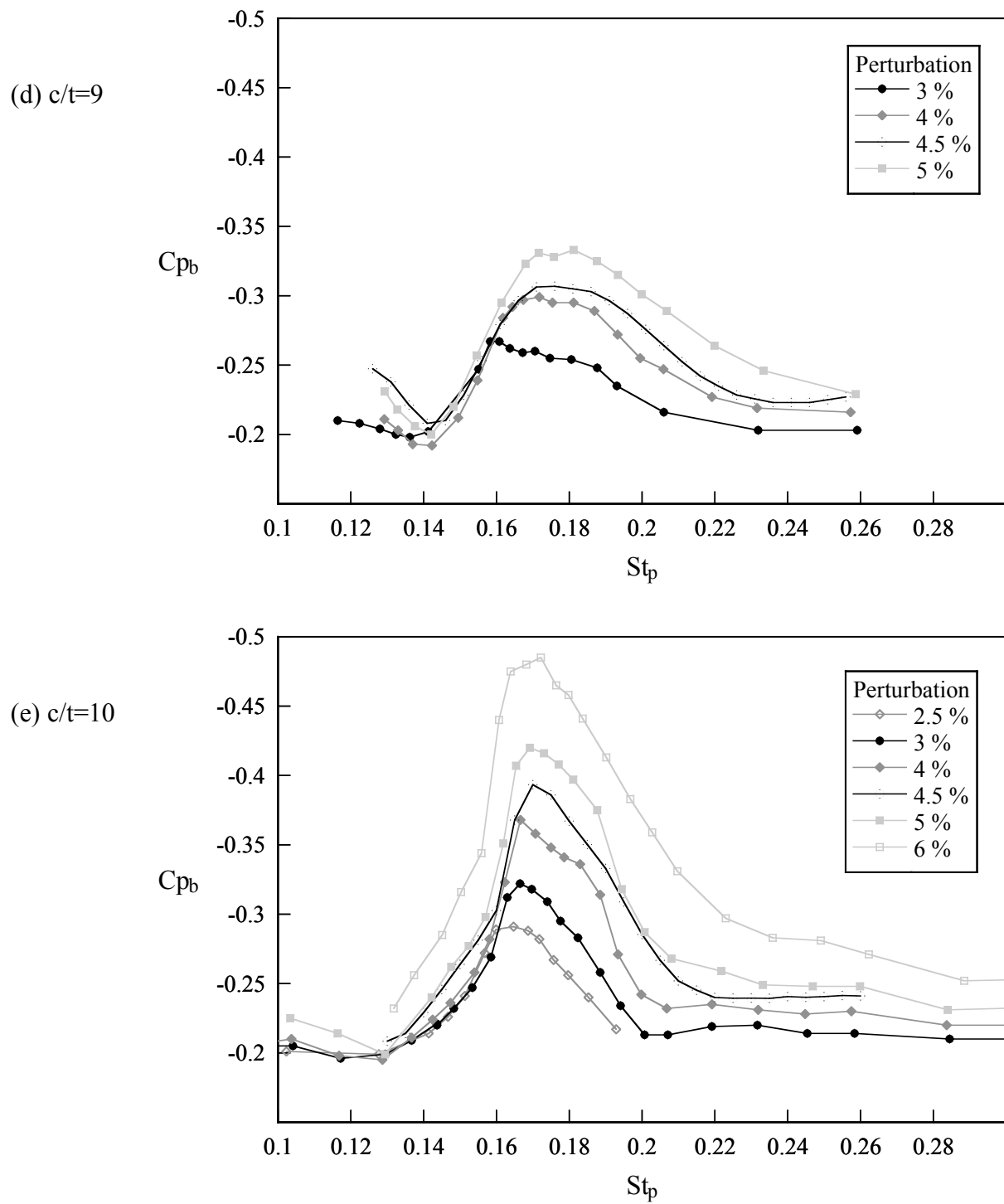


Figure 4.43 See page 119 for caption.

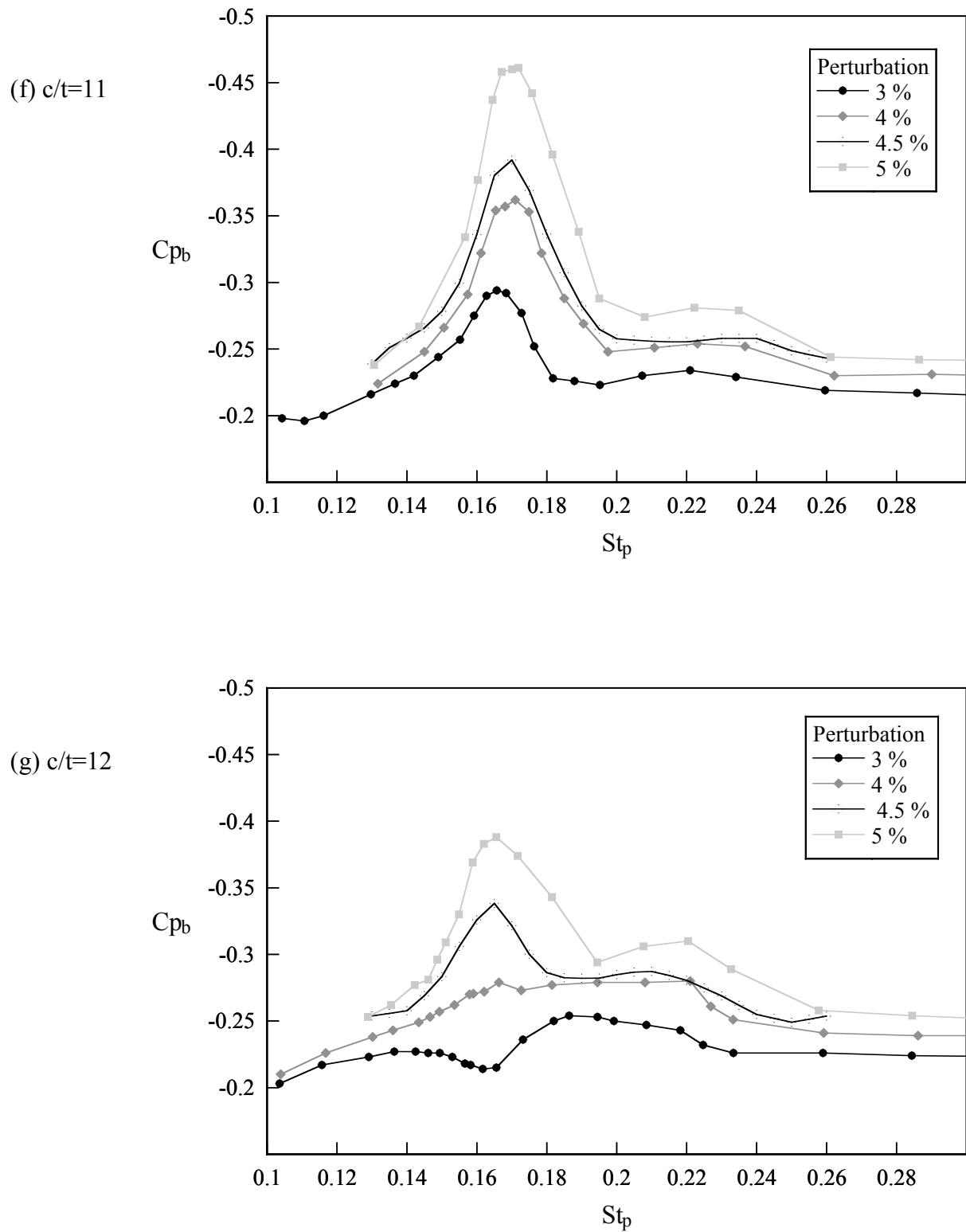


Figure 4.43 See page 119 for caption.

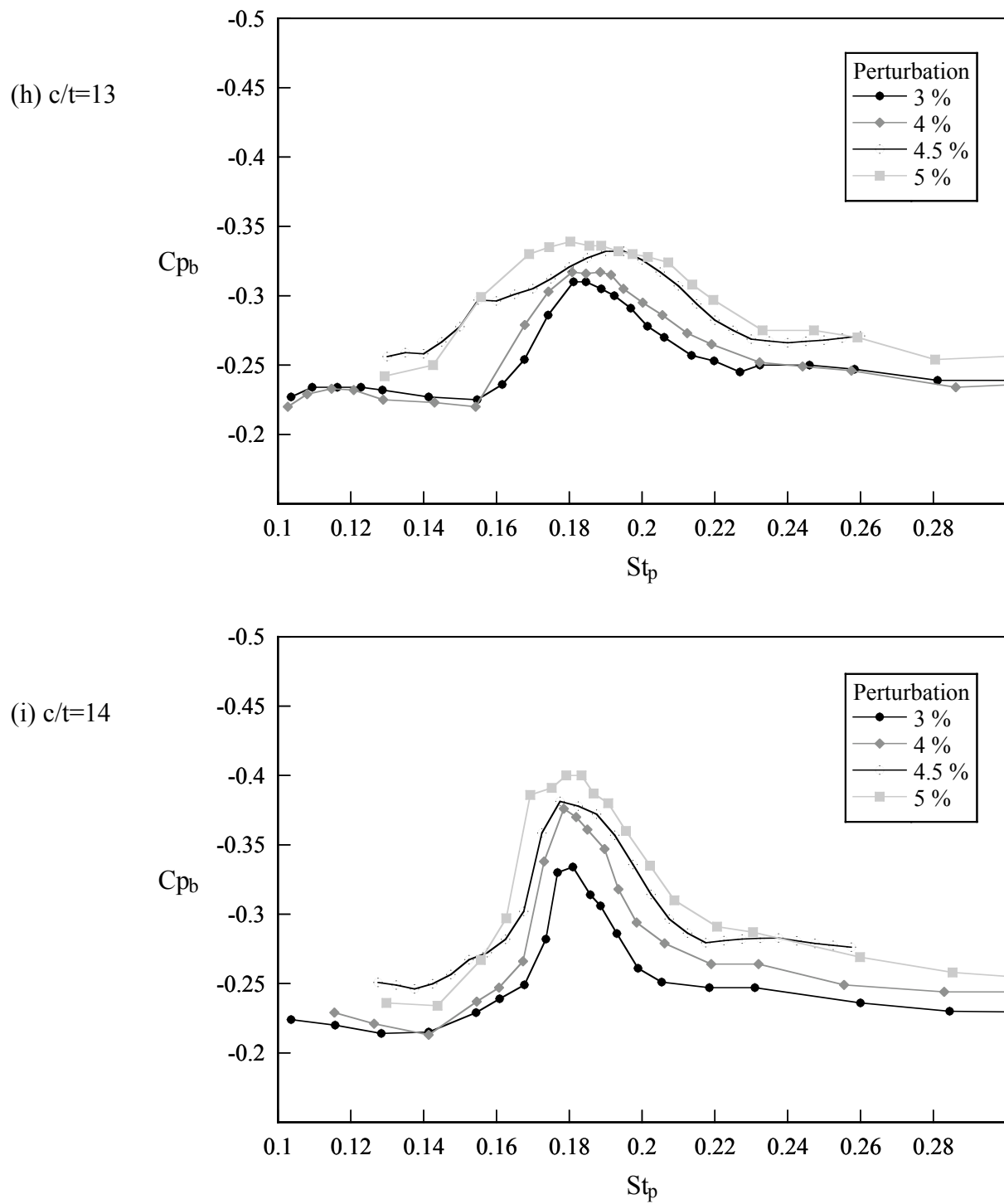
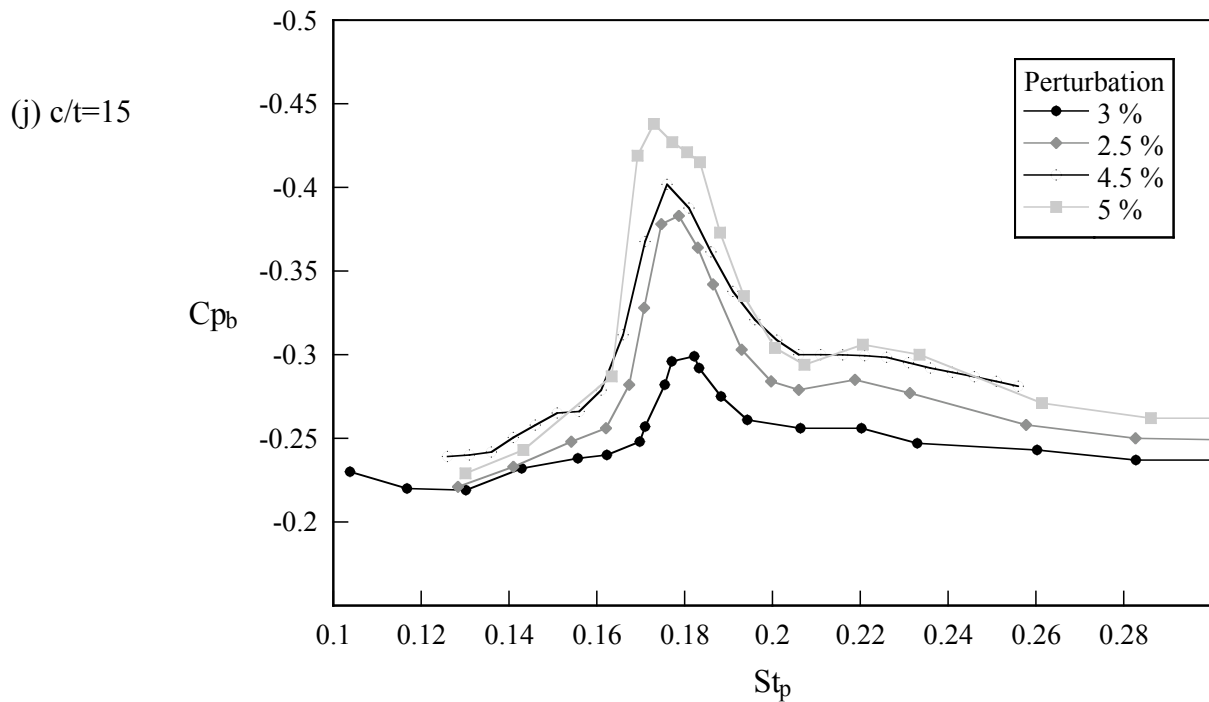


Figure 4.43 See page 119 for caption.



**Figure 4.43** Effect of varying perturbation level for plates with  $c/t$  between 6 and 16, on  $Cp_b$  as  $St_p$  is varied.

For all the primary plates ( $c/t$  ratios of 6,7,10,11,14 and 15), as the perturbation level is increased the magnitude of the peak in  $Cp_b$  reached increases. This was expected, given that increasing perturbation level on the flow about both a circular cylinder (Stansby 1976) and a plate with an aerofoil leading edge and a rectangular trailing edge increases the magnitude of the peak in  $Cp_b$ .

In general, as the perturbation level applied to the flow about a bluff body is increased, the range of frequencies over which vortex shedding can be locked to the perturbations increases. Thus, with increasing perturbation level the peaks in  $Cp_b$  would be expected to be broader, as was the case with the aerofoil leading edge plate. This is indeed the case for the primary plates, where only a single distinct peak is observed. Also, for all primary plates that are in regime c, as defined by Parker & Welsh (1983) (ie  $c/t > 7.6$ ), the  $St_p$  at which peaks in  $Cp_b$  occur show little variation as the perturbation level is varied.

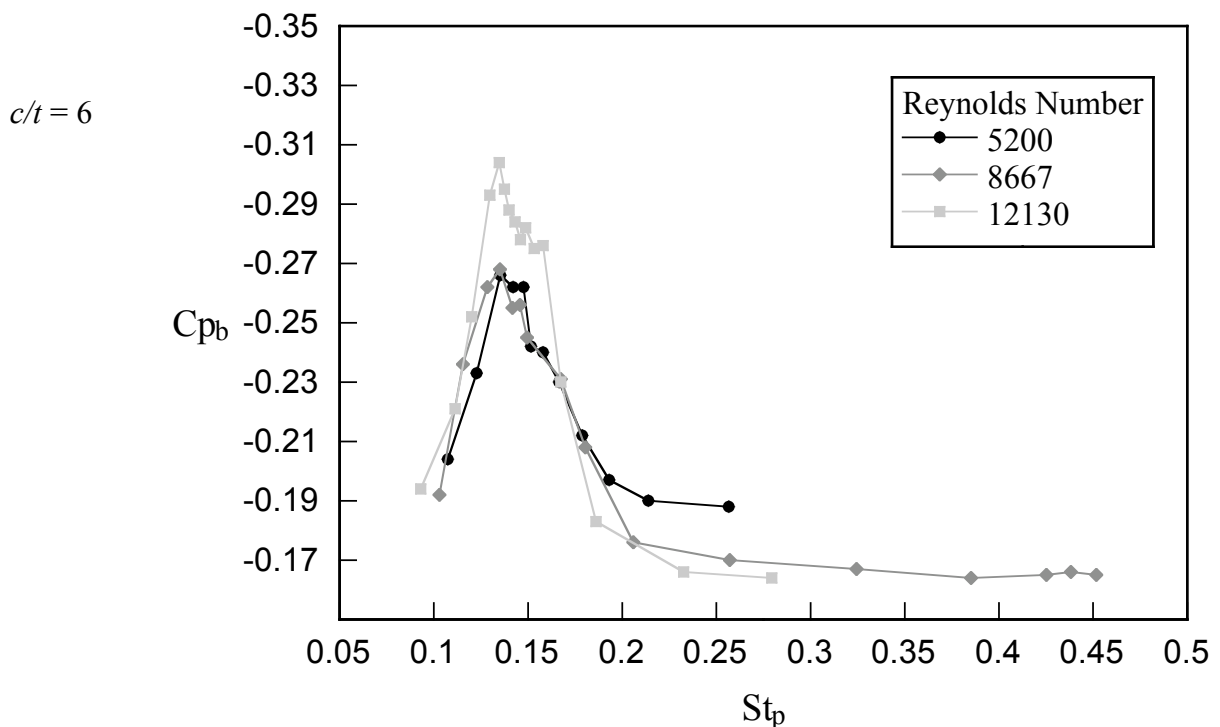
For the two primary plates with  $c/t$  ratios in regime b ( $c/t = 6$  and  $7$ ), in the absence of perturbations and for  $Re > 2000$  these plates shed vortices naturally at ILEV mode = 1 (see figure 2.10). When perturbations are applied, as the relative perturbation level is increased,

the  $St_p$  at which the maximum base suction occurs also increases, and approaches the frequency corresponding to ILEV mode 2 shedding.

For the intermediate plates, a slightly different behaviour is observed. Generally, as the perturbation level is increased so does the magnitude of the peak in  $Cp_b$ . However, the  $St_p$  at which peaks occur can be quite dependent on perturbation level. This is especially evident for the plate with  $c/t = 12$ . Assuming that L vortices can either enhance or interfere with the shedding of T vortices, the strength of L vortices locked to perturbations would increase as perturbation level increases, and thus the likelihood of L vortices affecting the shedding of T vortices. Further investigation is needed to explain this behaviour.

#### 4.2.1.4 Effect of Reynolds number on $Cp_b$

The effect of varying  $Re$  on  $Cp_b$  was also investigated. These results are shown in figure 4.44. Due to the limitations of the loudspeakers used to generate the transverse velocity perturbations, it was only possible to measure the effect of varying  $Re$  using a 3% velocity perturbation relative to the free stream velocity. Flow velocities used ranged between  $6 \text{ ms}^{-1}$  and  $14 \text{ ms}^{-1}$ , corresponding to a  $Re$  range of 5200 to 12130.



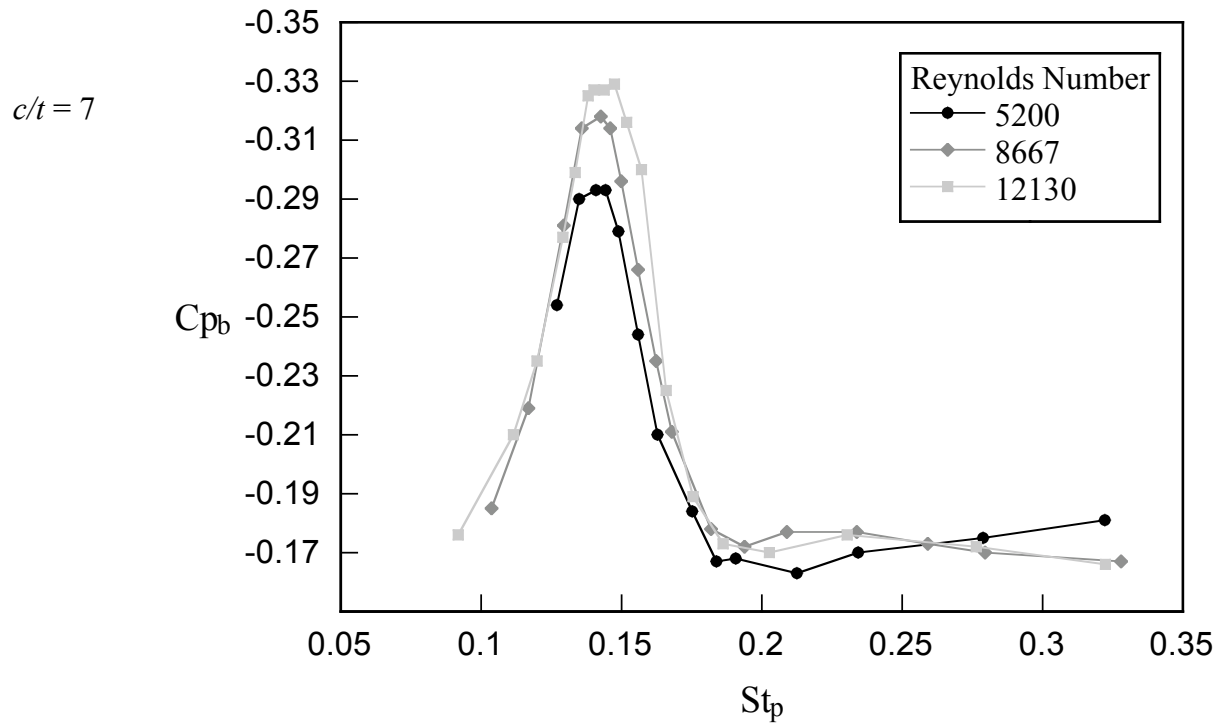
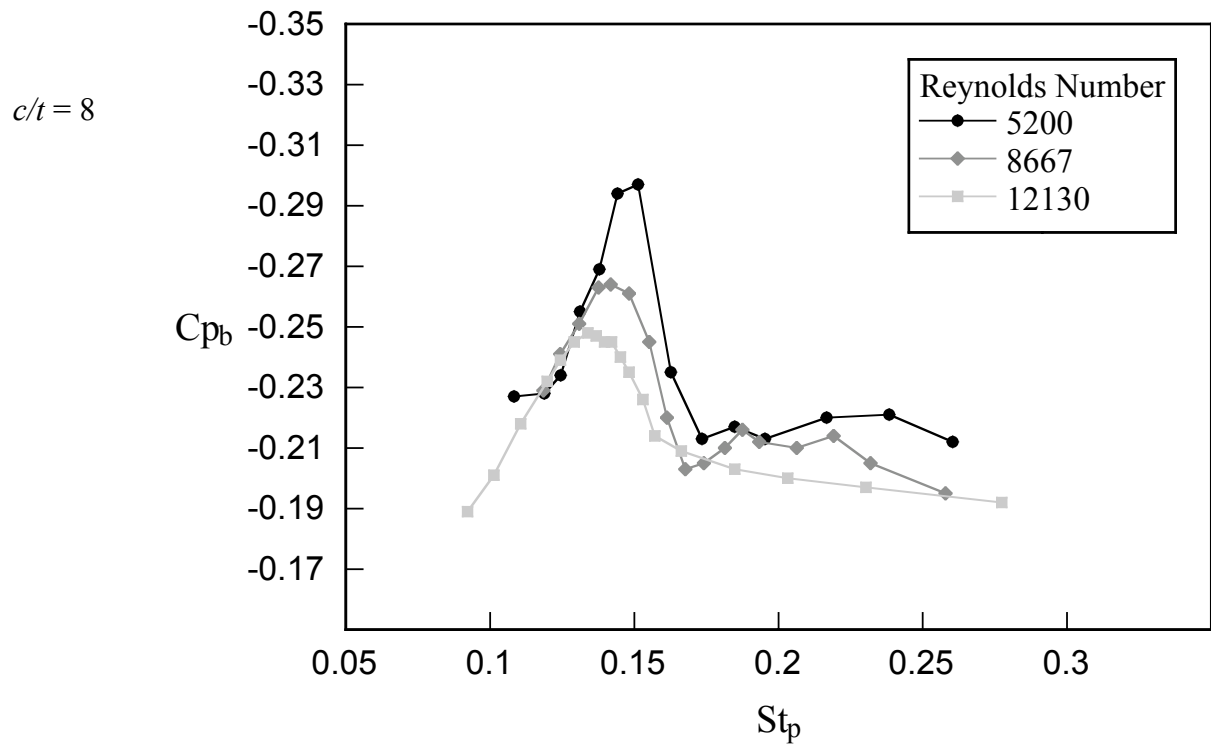
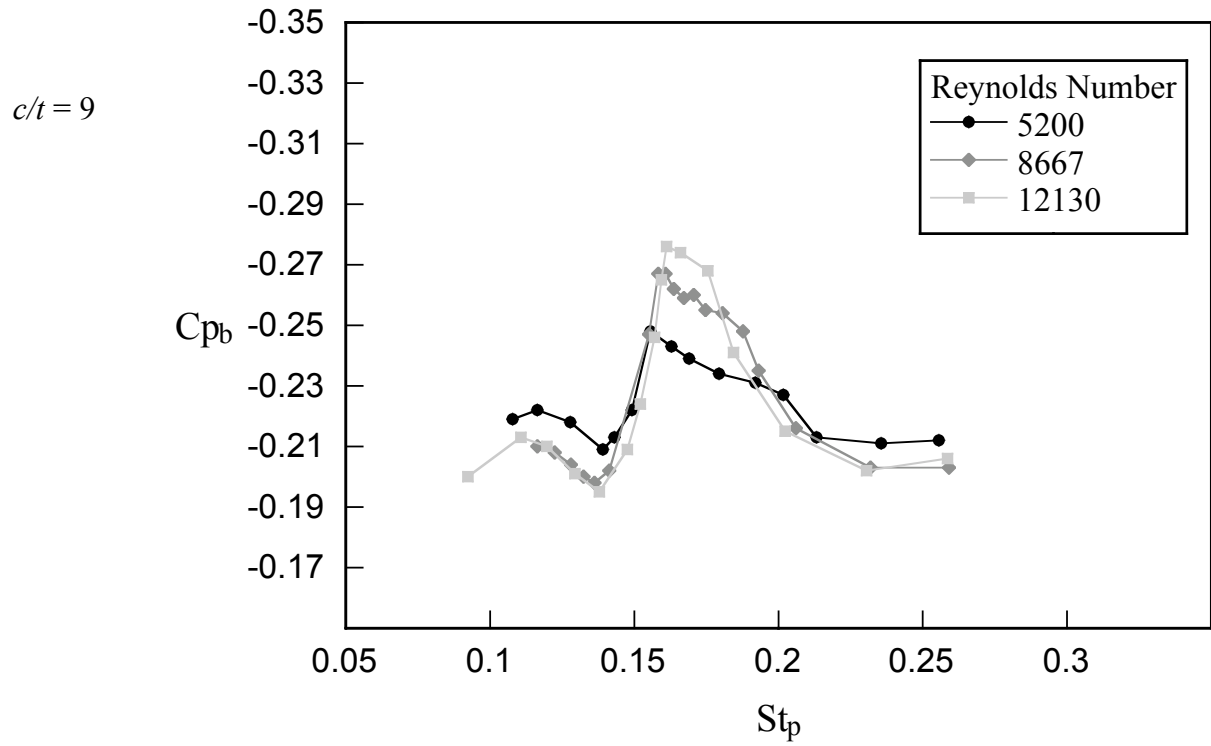
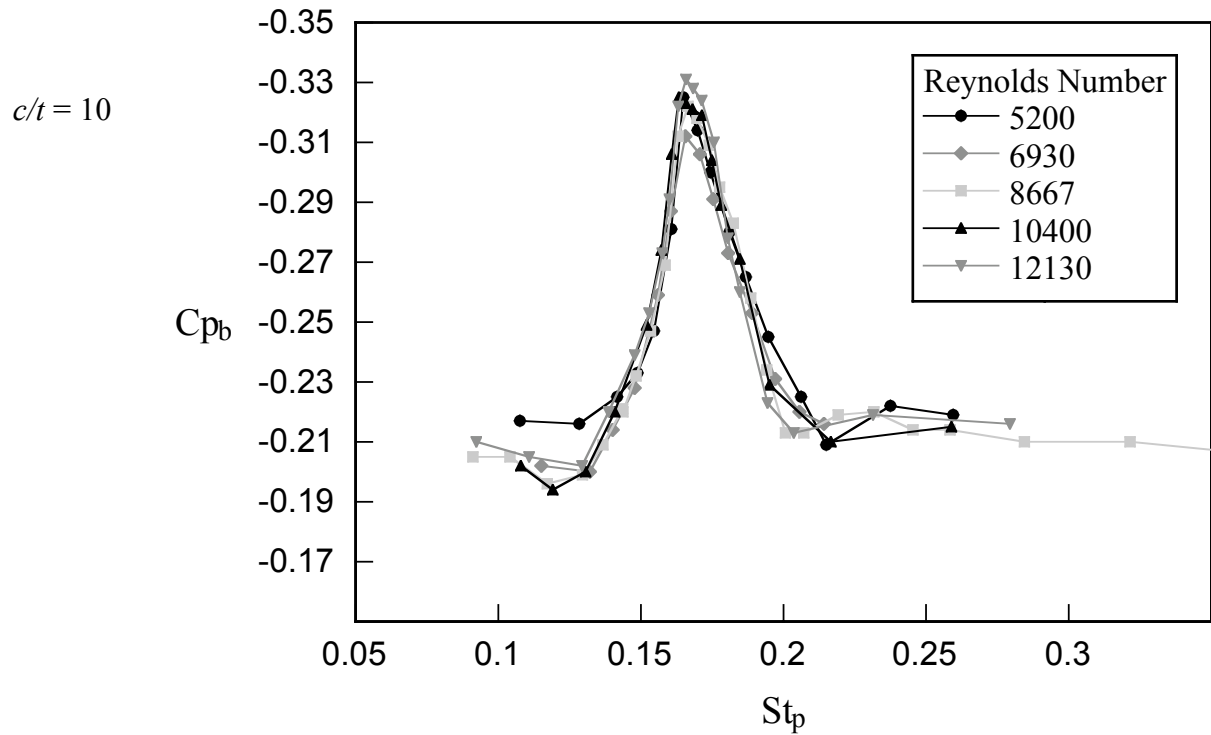


Figure 4.44 See page 125 for caption.





**Figure 4.44** See page 125 for caption.



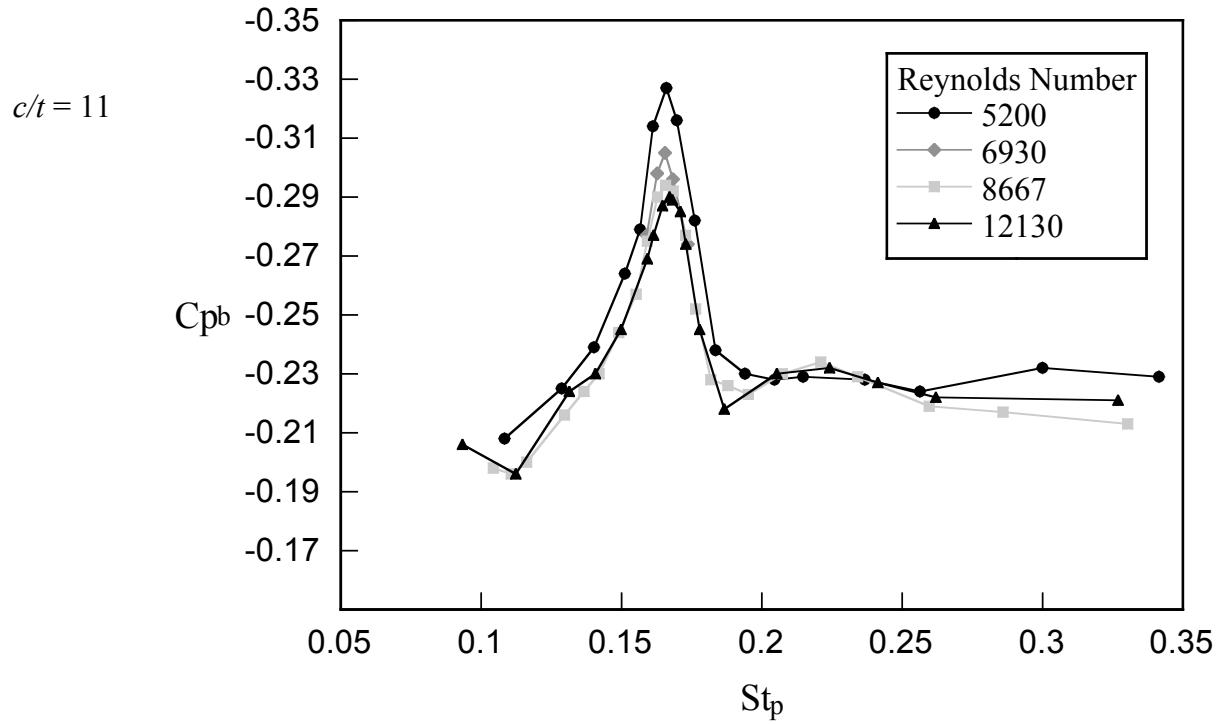
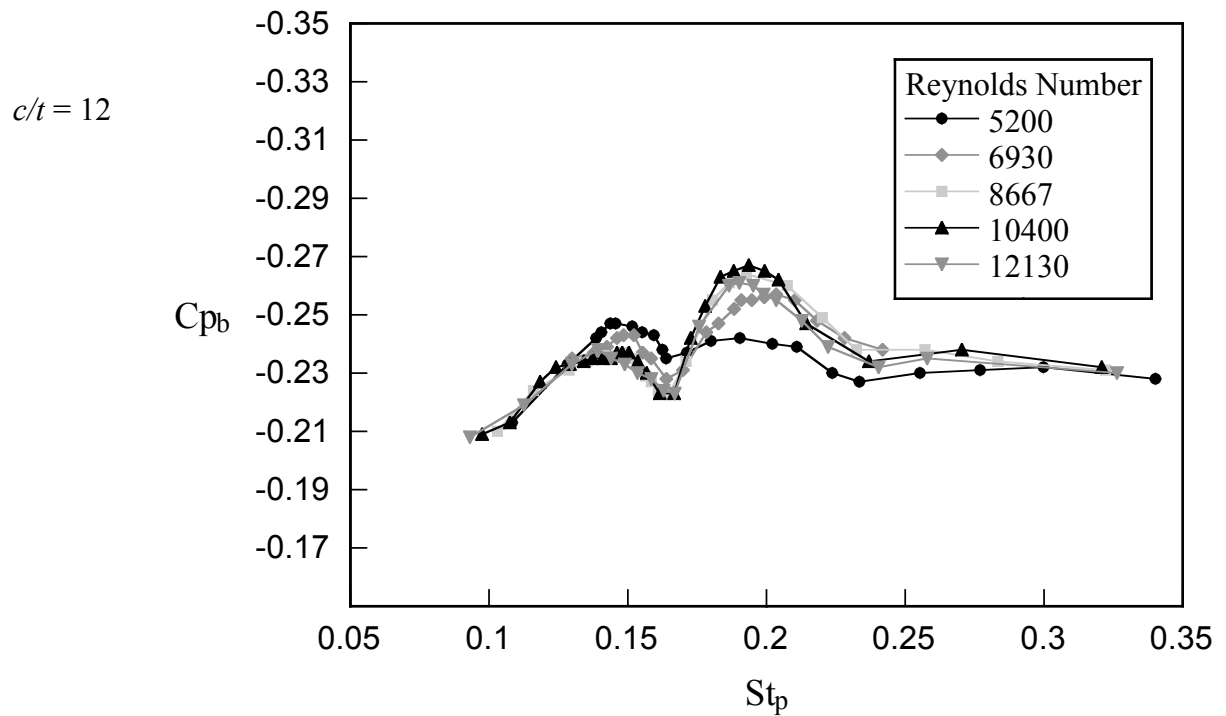


Figure 4.44 See page 125 for caption.



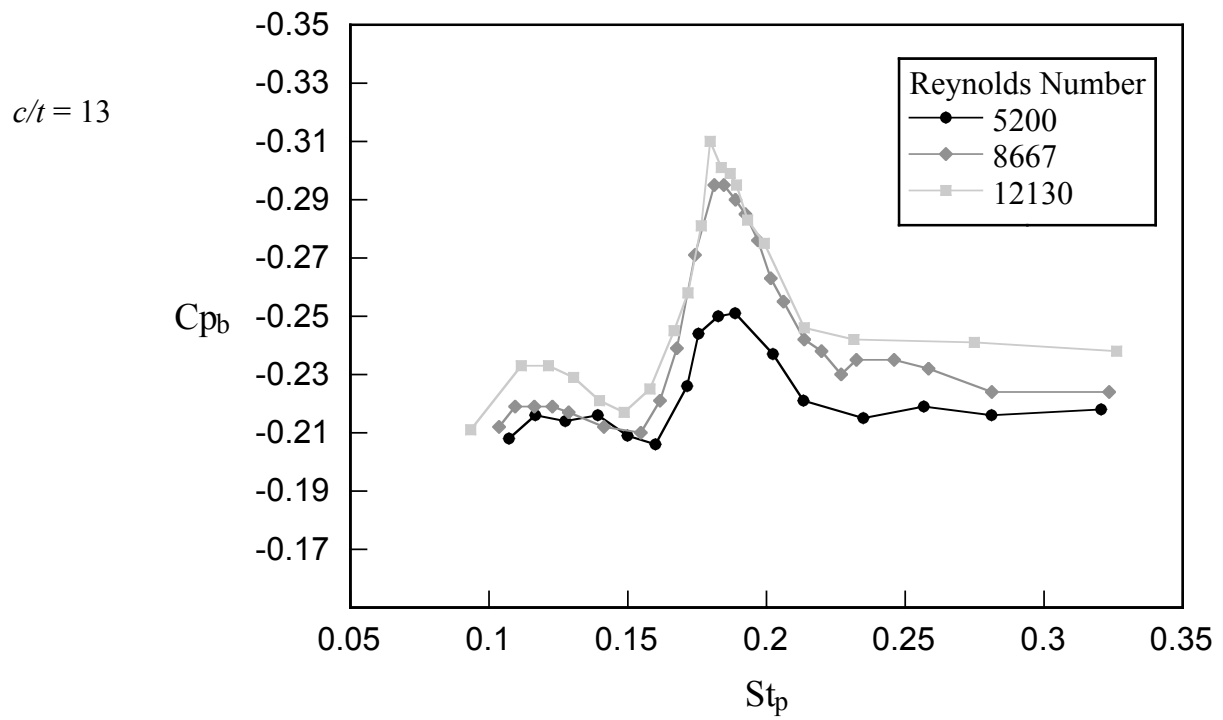
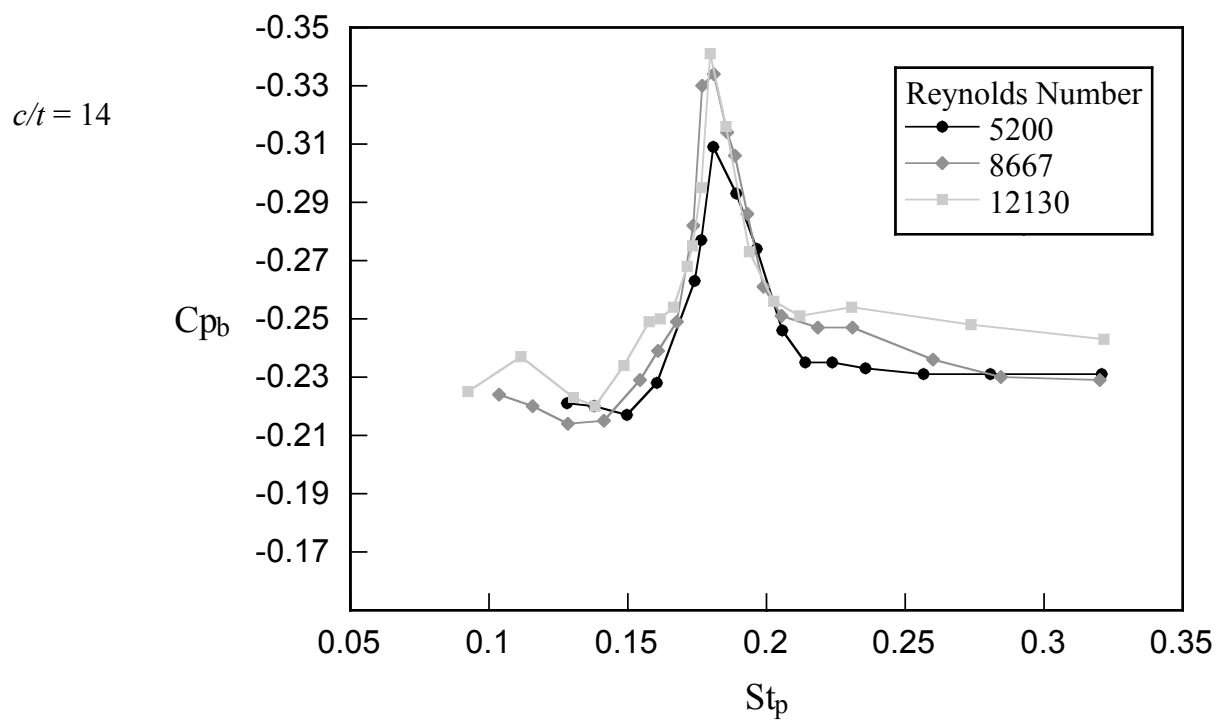
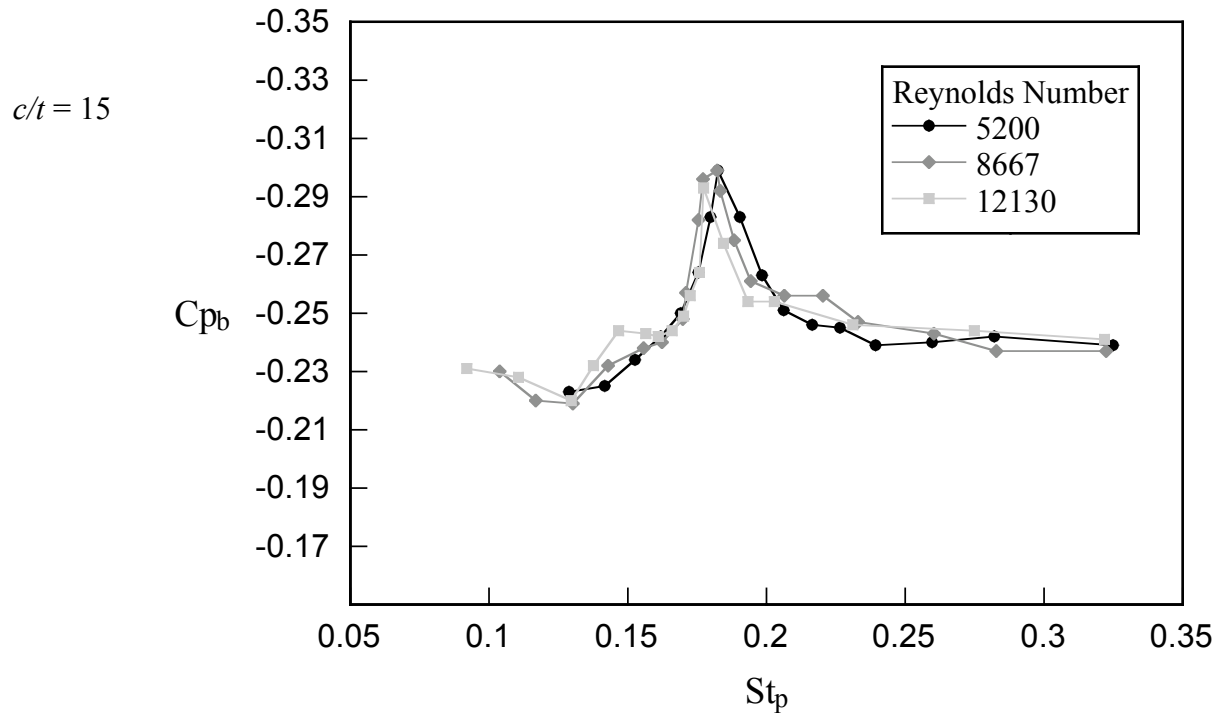


Figure 4.44 See page 125 for caption.





**Figure 4.44** Effect of varying  $St_p$  on  $C_{p_b}$  at different  $Re$ , for plates with  $c/t$  between 6 and 15; perturbation level in all cases was 3%.

For all plate  $c/t$  ratios tested, the  $St_p$  at which peaks in  $C_{p_b}$  occur was virtually independent of  $Re$ , and occurred at  $St_p$  close to the  $St$  measured by Nakamura *et al.* (1991) for the natural ILEV modes. However, for most plate  $c/t$  ratios the magnitude of the peaks in  $C_{p_b}$  showed some variation with  $Re$ . The exact nature of this variation is unclear, and is worthy of further investigation. However, a trend in the data was evident. Only two plates, with  $c/t$  ratios of 10 and 15, showed no variation with  $Re$  within experimental error. For intermediate length plates where two peaks were evident, the peak corresponding to the higher ILEV mode was always smaller at lower  $Re$ , while the opposite was found for the peak corresponding to the lower ILEV mode, where it was generally larger at lower  $Re$ .

#### 4.2.2 Particle Image Velocimetry (PIV) results and flow visualisation

PIV experiments have been performed on rectangular plates, with  $c/t$  varying between 6 and 10, in the water tunnel at CSIRO, Hightett. All PIV measurements on rectangular plates were performed with  $Re = 490$ , where the flow remains largely two dimensional even in the absence of transverse velocity perturbations. It was not possible to perform these experiments at the same  $Re$  used in the wind tunnel experiments, due to limitations of the PIV

system at higher velocities. Although the shear layer is laminar at  $Re = 490$  and the vortex structures shed from the leading edge are largely two dimensional, performing experiments at this low  $Re$  is justified because the effect of the transverse velocity perturbations used in the higher  $Re$  wind tunnel experiments is to suppress the downstream development of three dimensionality in the flow. Thus, when the higher  $Re$  flow is phase-locked to transverse velocity perturbations it can be considered to be quasi-two dimensional, consisting of regularly spaced spanwise vortices with an associated secondary three dimensional random component (Welch *et al.* 1986).

Flow visualisation was also performed in the water tunnel, for the same flows used for the PIV experiments.

#### ***4.2.2.1 Natural vortex shedding (no perturbations applied)***

Performing experiments at low  $Re$  also allowed a direct comparison to be made with the results of Nakamura *et al.* (1991) and Ohya *et al.* (1992), which were from experiments performed at  $Re = 1000$ . For  $Re < 2000$  and in the absence of external flow disturbances, a feedback mechanism called the Impinging Leading Edge Vortex (ILEV) instability characterises vortex shedding from long rectangular plates as discussed in chapter 2.

PIV results are shown in figure 4.45 for a rectangular plate with  $c/t = 6$ . The velocity vector plot (a) and the sectional streamline plot (b), both in a stationary reference frame, show the existence of a clockwise rotating vortex forming at the trailing edge of the model (T vortex). The choice of reference frame significantly affects the flow structures that can be observed when looking at either velocity vector plots or streamline plots. This is clear when looking at the velocity vector plot of (c) and the sectional streamline plot (d), both in a reference frame moving at the convection velocity of the vortices ( $U_{conv} = 0.75 U_{\infty}$ ), where the clockwise T vortex is not revealed. Also, a clockwise rotating L vortex on the upper side of the plate adjacent to the trailing edge can clearly be seen, whereas this was not obvious in plots (a) and (b). The vorticity plot (e) clearly shows both clockwise rotating L and T vortices near the upper trailing edge corner, as well as other vortices in the flow since vorticity is Galilean

invariant and hence is not affected by the choice of reference frame. The vorticity concentrations in the wake result from the merging of L and T vortices of like sign at the trailing edge before being shed into the wake.

Further evidence of the simultaneous shedding of L and T vortices can be seen in the flow visualisations in figure 4.46. As with the velocity vector plots and streamline plots, the choice of reference frame can greatly alter the interpretation of a flow visualisation image. Image (a) (in a fixed reference frame) clearly shows the formation of a clockwise rotating vortex at the trailing edge, while image (b) (in a reference frame moving with the vortices) only shows the presence of a clockwise rotating L vortex adjacent to the trailing edge. The flow visualisation of figure 4.47, taken approximately  $90^\circ$  later in the vortex shedding cycle than figure 4.46, shows that the L and T vortices have merged in the near wake. This vortex interaction process occurs for vortices from either side of the plate, with L and T vortices of like sign merging in the near wake to form a single vortex.

(for PIV images of 110,45 gridpoints)

(a) c6r1f17.tcp : velocity vector plot  
(lab reference frame)

(for PIV images of 110,45 gridpoints)

(b) c6r1f17.tcp : streamline plot  
(lab reference frame)

(for PIV images of 110,45 gridpoints)

- (c) c6r1f17.tcp : velocity vector plot  
(moving reference frame)

(for PIV images of 110,45 gridpoints)

- (d) c6r1f17.tcp : streamline plot  
(moving reference frame)

**Figure 4.45** See page 129 for caption.

(for PIV images of 110,45 gridpoints)

- (e) c6r1f17.tcp : vorticity contour plot

**Figure 4.45** PIV results for rectangular plate with  $c/t = 6$ , at  $Re = 490$ ; (a) Velocity vector plot (lab reference frame), (b) Sectional streamline plot (lab reference frame), (c) Velocity vector plot (reference frame moving at  $0.75U_\infty$  in the direction of the flow), (d) Sectional streamline plot (reference frame moving at  $0.75U_\infty$ ), (e) Vorticity contour plot.

- Flow vis image -  $c/t=6$ , showing trailing edge vortex in similar position to vorticity plot above
- (a) (Stationary Reference Frame)  
c6fv - f2
- Flow vis image -  $c/t=6$ , showing trailing edge vortex in similar position to vorticity plot above
- (b) (Moving Reference Frame)  
c6fv - f11

**Figure 4.46** Flow visualisation of flow about a rectangular plate with  $c/t = 6$ , at  $Re = 490$ ; (a) Stationary reference frame, (b) Reference frame moving with the vortices in the wake (using the bias velocity mirror).

- Flow vis image -  $c/t=6$ , showing merging of L and T vortices  $90^\circ$  later in cycle than image above
- (Moving Reference Frame)  
c6fv - f10

**Figure 4.47** Flow visualisation of flow about a rectangular plate with  $c/t = 6$ , at  $Re = 490$ ; image taken in reference frame moving with the vortices, approximately  $90^\circ$  later in vortex shedding cycle than figure 4.46.

Vorticity contour plots are presented in figure 4.48, showing the existence of both L and T vortices in the flow about rectangular plates with  $c/t$  ratios of 7, 8, 9 and 10. This confirms the CFD results of Ohya *et al.* (1992), which showed the shedding of both L and T vortices to be a feature of natural vortex shedding from elongated rectangular plates.

(a) (for PIV images of 110,45 gridpoints)  
 $c/t = 7$  c7r1f24.tcp : **vorticity** contour plot

(b) (for PIV images of 110,45 gridpoints)  
 $c/t = 8$  c8r1f10.tcp : **vorticity** contour plot

**Figure 4.48** See page 131 for caption.

(c) (for PIV images of 110,45 gridpoints)  
 $c/t = 9$  c9r1f07.tcp : **vorticity** contour plot

(d) (for PIV images of 110,45 gridpoints)  
 $c/t = 10$  c10r1f???.tcp : **vorticity** contour plot

**Figure 4.48** Vorticity contour plots for rectangular plates with different  $c/t$  ratios;  $Re = 490$ .

The natural vortex shedding frequencies for all the rectangular plates tested in the water tunnel at  $Re = 490$  are shown in Table 4.3, along with  $St_c$  for the same data, and  $St_c$  for the data presented by Nakamura *et al.* (1991) with  $Re = 1000$ .

$c/t$	$f_{\text{shed}} (Re = 490)$	$St_c (Re = 490)$	$St_c (Re = 1000)$
6	0.68 Hz	1.15	1.14
7	0.61 Hz	1.21	1.19
8	0.55 Hz	1.24	1.20
9	0.49 Hz	1.24	1.75
10	0.64 Hz	1.81	1.80

**Table 4.3** Vortex shedding frequencies for rectangular plates with ( $6 \leq c/t \leq 10$ ) at low  $Re$

Figure 4.49 shows the comparison between the results graphically. The similarity between the two sets of results indicates that the vortex shedding frequencies associated with the ILEV instability are not affected by changes in  $Re$  over the range in which it affects vortex shedding from long rectangular plates. The only difference in the two sets of results is the vortex shedding frequency for the plate with  $c/t = 9$ . Nakamura found that this plate shed vortices at the  $n = 3$  ILEV mode, while the model in the water tunnel shed vortices at the  $n = 2$  ILEV mode.

The exact mechanism by which a particular ILEV mode is selected remains unclear. One possible explanation for the difference in the shedding frequency for the  $c/t = 9$  plate is the difference in tunnel blockage ratio between the two sets of experiments. This would alter the convection velocity of L vortices, thus slightly affecting the spacing between them. Given the prescribed frequency of shedding, a higher convection velocity would result in a larger spacing between vortices for a given plate. The same effect on the spacing between L vortices would be observed by increasing the plate length slightly. This means that the  $c/t = 9$  plate, which shed vortices at the  $n = 2$  ILEV mode in the water tunnel, would shed vortices at the same frequency as a slightly shorter plate in a wind tunnel with a smaller blockage ratio. Another difference between the two experiments is the  $Re$ ; it is possible that  $Re$  affects the plate  $c/t$  ratio that vortex shedding changes from one ILEV mode to another.

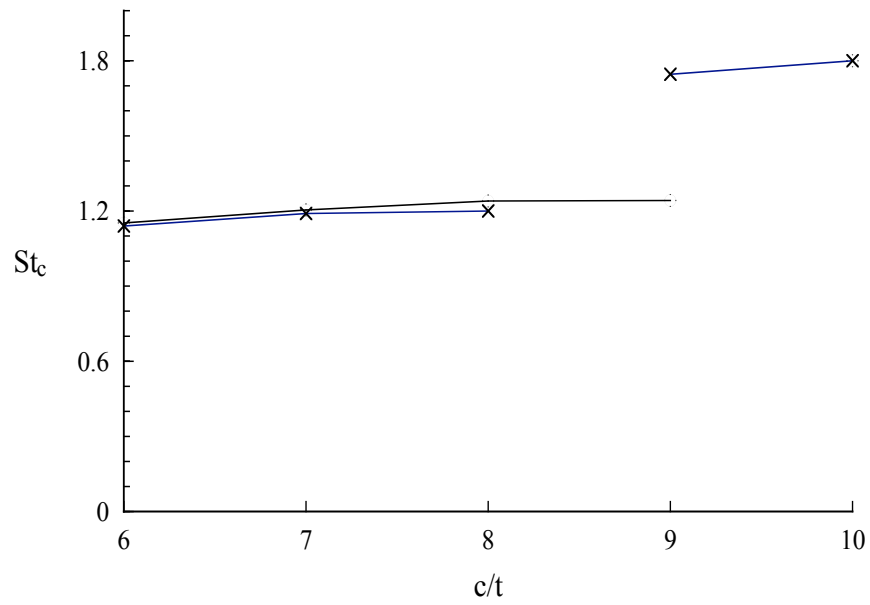


**Figure 4.49** Comparison of vortex shedding frequencies for rectangular plates with ( $6 \leq c/t \leq 10$ );  $\circ$   $Re = 490$ ,  $\times$   $Re = 1000$  (from Nakamura *et al.* 1991),

#### 4.2.2.2 *Transverse velocity perturbations applied at natural ILEV frequencies*

In order to test the vortex interaction hypothesis, the effect of applying transverse velocity perturbations at the natural ILEV frequency of each rectangular plate was investigated. Figure 4.50 shows the results of a single PIV image taken of the flow about a rectangular plate with  $c/t = 6$ , in the presence of a 5% velocity perturbation applied at a frequency of 0.68 Hz ( $St_p = 0.192$ ). This is the natural vortex shedding frequency for the same plate with an ILEV mode of 2. The perturbation phase angle is 270 degrees (see section 3.2.1), meaning that the perturbation velocity is a maximum in the downwards direction. The free stream velocity is  $41.8 \text{ mms}^{-1}$  ( $Re = 490$ ).

(for PIV images of 110,45 gridpoints)

c6r2f13.tcp : velocity vector plot

(a)

(lab reference frame)

**actually 270 deg.**

(for PIV images of 110,45 gridpoints)

(b)

c6r2f13.tcp : streamline plot

(lab reference frame)

**Figure 4.50** See page 134 for caption.

(for PIV images of 110,45 gridpoints)

- (c) c6r2f13.tcp : velocity vector plot  
(moving reference frame)

(for PIV images of 110,45 gridpoints)

- (d) c6r2f13.tcp : streamline plot  
(moving reference frame)

(for PIV images of 110,45 gridpoints)

- (e) c6r2f13.tcp : vorticity contour plot

**Figure 4.50** PIV results for rectangular plate with  $c/t = 6$  with 5% velocity perturbation applied at  $St_p = 0.192$ , and perturbation phase angle = 270 degrees; (a) Velocity vector plot (lab reference frame), (b) Sectional streamline plot (lab reference frame), (c) Velocity vector plot (reference frame moving at  $0.75U_\infty$  in the direction of the flow), (d) Sectional streamline plot (reference frame moving at  $0.75U_\infty$ ), (e) Vorticity contour plot.

At this frequency both the leading and trailing edge vortex shedding are phase-locked to the transverse velocity perturbations. Thompson *et al.* (1997) have numerically simulated this flow for a rectangular plate with  $c/t = 10$  with a 5% transverse velocity perturbation applied. Their results show a similar merging of L and T vortices at the trailing edge, when the perturbation frequency results in vortex shedding being locked at both the trailing and leading edges.

The vorticity plots presented in figure 4.51, show a full shedding cycle for the plate with  $c/t = 6$  under the same flow conditions as the results shown in figure 4.50.

$$\phi = 0^\circ$$

(for PIV images of 110,45 gridpoints)

c6r2f16.tcp : vorticity contour plot

$$\phi = 90^\circ$$

(for PIV images of 110,45 gridpoints)

c6r2f07.tcp : vorticity contour plot

$$\phi = 120^\circ$$

(for PIV images of 110,45 gridpoints)

c6r2f08.tcp : vorticity contour plot

**Figure 4.51** See page 137 for caption.

$$\phi = 150^\circ$$

(for PIV images of 110,45 gridpoints)

c6r2f09.tcp : vorticity contour plot

$$\phi = 180^\circ$$

(for PIV images of 110,45 gridpoints)

c6r2f10.tcp : vorticity contour plot

$$\phi = 210^\circ$$

(for PIV images of 110,45 gridpoints)

c6r2f10.tcp : vorticity contour plot

$$\phi = 240^\circ$$

(for PIV images of 110,45 gridpoints)

c6r2f10.tcp : vorticity contour plot

**Figure 4.51** See page 137 for caption.

$$\phi = 270^\circ$$

(for PIV images of 110,45 gridpoints)

c6r2f10.tcp : vorticity contour plot

$$\phi = 360^\circ$$

(for PIV images of 110,45 gridpoints)

c6r2f10.tcp : vorticity contour plot

**Figure 4.51** Vorticity contour plots for a rectangular plate with  $c/t = 6$ ,  $Re = 490$ , 5% velocity perturbation,  $St_p = 0.192$ ; perturbation phase angle is indicated next to each contour plot.

In between consecutive vortices shed from the leading edge, the flow reattaches to the surface of the plate. As this reattached boundary layer fluid is convected past the trailing edge, it rolls up to form a T vortex. From the vorticity plots of figure 4.51, the clockwise T vortex starts forming from the upper corner of the trailing edge at the phase in the perturbation cycle when the perturbation velocity is approximately zero (180 degrees). As the perturbation cycle continues, the perturbation velocity increases in the downwards direction which, combined with the induced velocity from the T vortex of opposite sign formed during the previous half cycle, causes the boundary layer fluid to roll up tightly and form a new T vortex. This process occurs on either side of the plate. It is interesting to compare the vorticity plots of figure 4.51 at phase angles of 0 degrees and 180 degrees. It appears that the vortex shedding is not quite symmetrical with respect to the top and bottom surfaces of the plate. The L vortex adjacent to the upper side of the trailing edge when the phase angle is 180 degrees is further advanced along the side of the plate than the corresponding L vortex

adjacent to the lower side of the trailing edge when the phase angle is 0 degrees. While no explanation for this asymmetrical shedding has been found, it is interesting to note that Thompson *et al.* (1995) observed a similar asymmetry in the vortex shedding in their two dimensional numerical simulation of the flow.

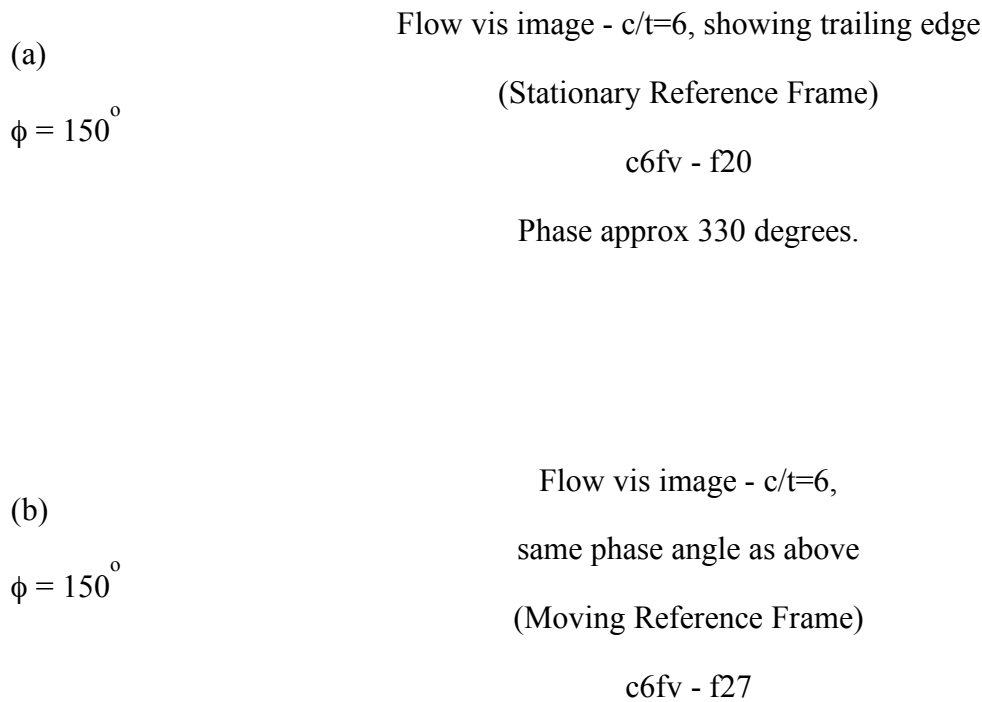


**Figure 4.52** Flow visualisation of flow about a rectangular plate with  $c/t=6$ , at  $Re=490$ , 5% velocity perturbation,  $St_p=0.192$ ; (a) Stationary reference frame, (b) reference frame moving with the vortices in the wake.

Figure 4.52 shows two flow visualisation images taken of the flow with  $c/t=6$  and a 5% transverse velocity perturbation applied at  $St_p=0.192$ . The sidewalls are close to the uppermost position and moving slowly upwards, corresponding to a phase angle of 150 degrees. A clockwise rotating T vortex has almost completed forming from the reattached boundary layer fluid from the lower side of the trailing edge, while a clockwise rotating L vortex is approaching the lower side of the trailing edge. On the side of the plate adjacent to the upper trailing edge corner is reattached boundary layer fluid that will form an anti-clockwise rotating T vortex in the next half cycle of vortex shedding. An image



- (c)
- (for PIV images of 110,45 gridpoints)
- c7r2f27.tcp : velocity vector plot
- (moving reference frame)
- 
- (d)
- (for PIV images of 110,45 gridpoints)
- c7r2f27.tcp : streamline plot
- (moving reference frame)
- 
- (e)
- (for PIV images of 110,45 gridpoints)
- c7r2f27.tcp : vorticity contour plot

**Figure 4.54** PIV results for rectangular plate with  $c/t = 7$  with 5% velocity perturbation applied at  $St_p = 0.172$ ,  $Re = 490$ , and perturbation phase angle = 270 degrees; (a) Velocity vector plot (lab reference frame), (b) Sectional streamline plot (lab reference frame), (c) Velocity vector plot (reference frame moving at  $0.75U_\infty$  in the direction of the flow), (d) Sectional streamline plot (reference frame moving at  $0.75U_\infty$ ), (e) Vorticity contour plot.

Figure 4.54 shows the PIV results from a single image taken of the flow about a rectangular plate with  $c/t = 7$  in the presence of a 5 % velocity perturbation applied at a frequency of 0.61 Hz ( $St_p = 0.172$ ). This is the natural vortex shedding frequency for the plate with  $c/t = 7$ , at which it sheds vortices corresponding to an ILEV mode of 2. The perturbation phase angle is 270 degrees.

Applying a 5% transverse velocity perturbation to the flow around a plate with  $c/t = 7$  at the same frequency as the natural vortex shedding frequency results in vortex shedding at both the leading and trailing edges being phase-locked to the perturbations, as for the plate with  $c/t = 6$ . Comparing figure 4.54 with figure 4.51 for the plate with  $c/t = 6$ , both show a clockwise rotating vortex forming at the trailing edge when the perturbation phase angle is 270 degrees. This vortex appears to form from the reattached boundary layer fluid between L vortices on the upper surface of the plate. Although the perturbation frequency is different in the two cases, the difference in plate length means that the L vortices shed from the upper leading edge corner pass the trailing edge at a phase in the perturbation cycle of approximately 0 degree, while L vortices on the lower side pass the trailing edge at a phase in the perturbation cycle of approximately 180 degrees. The phase in the perturbation cycle at which the T vortices form appears to be the same for both plate lengths.

$$\phi = 0^{\circ}$$

(for PIV images of 110,45 gridpoints)

c7r2f18.tcp : vorticity contour plot

$$\phi = 90^{\circ}$$

(for PIV images of 110,45 gridpoints)

c7r2f9.tcp : vorticity contour plot

**Figure 4.55** See page 142 for caption.

$$\phi = 180^{\circ}$$

(for PIV images of 110,45 gridpoints)

c7r2f1.tcp : vorticity contour plot

$$\phi = 270^{\circ}$$

(for PIV images of 110,45 gridpoints)

c7r2f27.tcp : vorticity contour plot

**Figure 4.55** Vorticity contour plots for a rectangular plate with  $c/t = 7$ ,  $Re = 490$ , 5% velocity perturbation,  $St_p = 0.172$ ; perturbation phase angle is indicated next to each contour plot.

Figure 4.55 shows four vorticity plots, each a quarter of a perturbation cycle apart in phase, for a plate with  $c/t = 7$  under the same flow conditions as figure 4.54.

As for the plate with  $c/t = 6$ , T vortices merge in the near wake with vortices of the same sign that were shed from the leading edge during the previous perturbation cycle. Also evident, is an asymmetry in the vortex shedding. Like the  $c/t = 6$  plate, L vortices being convected along the upper surface of the plate are further advanced along the plate compared to L vortices on the lower surface 180 degrees later in the perturbation cycle. The asymmetry in the vortex shedding is clearest when comparing the vorticity plots for the 90 degree and 270 degree phase angles in figure 4.55. For the plot where the phase angle is 90 degrees, the clockwise L and T vortices from the upper side of the plate have almost completely merged into a single vortex. In contrast, the plot where the phase angle is 270 degrees shows that the anti-clockwise L and T vortices from the lower side of the plate are clearly identifiable as separate vortices. These vortices eventually merge as they are convected away from the

model. However, vorticity from the L vortex remains identifiably separate from the T vortex with which it merges, even after the completion of one full shedding cycle from when the T vortex was shed.

These results for the two plates with  $c/t = 6$  and  $7$  show that transverse velocity perturbations applied at the frequency corresponding to the natural ILEV shedding frequency for each plate resulted in vortex shedding being phase-locked to the perturbations. Transverse velocity perturbations were applied at frequencies corresponding to the natural ILEV mode for plates with  $c/t = 8$ , and  $10$ . However, the vortex shedding from the plate with  $c/t = 9$  could not be locked to the transverse perturbations at the frequency corresponding to ILEV mode 2, this being the natural vortex shedding frequency measured in the water tunnel. For this plate, perturbations were applied at a frequency corresponding to ILEV mode 3 (the natural frequency measured by Nakamura *et al.* (1991)). Figure 4.56 shows vorticity contour plots for these three different length plates, with the phase of the perturbation cycle for each case indicated.

For all three plate lengths shown in figure 4.56 vortex shedding at both the leading and trailing edges was phase-locked to the perturbations.

(a)

(for PIV images of 110,45 gridpoints)

$c/t = 8$

c8r2f28.tcp : vorticity contour plot

(phase = 355)

**Figure 4.56** See page 144 for caption.

- (b) (for PIV images of 110,45 gridpoints)  
 $c/t = 9$  c9r2f8.tcp : vorticity contour plot  
 (phase = 15)
- (c) (for PIV images of 110,45 gridpoints)  
 $c/t = 10$  c10r2f10.tcp : vorticity contour plot  
 (phase = 0)

**Figure 4.56** Vorticity contour plots for the flow around rectangular plates of different  $c/t$  ratio's in the presence of transverse velocity perturbations applied at the natural ILEV frequency for each plate; phase angle indicated.

As mentioned earlier in this chapter, when leading edge shedding is phase locked to the sinusoidal perturbation field, L vortices are shed at the same phase in the perturbation cycle regardless of  $c/t$  ratio. Depending on both  $c/t$  ratio and perturbation frequency, it can take several perturbation cycles for a L vortex to reach the trailing edge. The phase in the perturbation cycle at which a L vortex passes the trailing edge depends on both the  $c/t$  ratio and the perturbation frequency, as the convection velocity of vortices along the side of the plate is relatively independent. For all five plate lengths tested (ie. 6,7,8,9 and 10) adjusting the frequency to equal that of the natural ILEV mode changes the spacing between adjacent L vortices on the sides of the plate. The result of this is that in all cases, L vortices shed from the upper leading edge corner pass the trailing edge when the phase of the perturbation cycle is approximately 0 degrees. Also, when the phase of the perturbation cycle is 0 degrees the clockwise rotating T vortex that was forming from the fluid that separated from the upper trailing edge corner is shed as the L vortex on the upper side approaches the trailing edge

corner, before the two vortices interact in the near wake. Thus, it has been demonstrated that strong trailing edge shedding can occur for different length plates when transverse velocity perturbations are applied at a frequency corresponding to a natural ILEV mode. This corresponds to frequencies which resulted in maximum values of base suction in the wind tunnel experiments (see figure 4.41).

#### 4.2.2.3 *Transverse velocity perturbations applied at non ILEV frequencies*

To further test the hypothesis that vortices shed from the leading edge (L vortices) can interfere with the vortex shedding at the trailing edge (T vortices) depending on the phase in the perturbation cycle at which they arrive at the trailing edge, PIV and flow visualisation data were collected for transverse velocity perturbations applied at frequencies half way between ILEV modes for each plate (ie.  $St_p = 0.6 (n+0.5)$ ).

- (a) (180 degrees)  
(for PIV images of 110,45 gridpoints)  
c7r3f26.tcp : velocity vector plot  
(lab reference frame)
- (b) (for PIV images of 110,45 gridpoints)  
c7r3f26.tcp : streamline plot  
(lab reference frame)

**Figure 4.57** See page 146 for caption.

(c)

(for PIV images of 110,45 gridpoints)

c7r3f26.tcp : velocity vector plot

(moving reference frame)

(d)

(for PIV images of 110,45 gridpoints)

c7r3f26.tcp : streamline plot

(moving reference frame)

(e)

(for PIV images of 110,45 gridpoints)

c7r3f26.tcp : vorticity contour plot

**Figure 4.57** PIV results for rectangular plate with  $c/t = 7$  with 6.5% velocity perturbation applied at  $St_p = 0.212$ , and perturbation phase angle = 180 degrees; (a) Velocity vector plot (lab reference frame), (b) Sectional streamline plot (lab reference frame), (c) Velocity vector plot (reference frame moving at  $0.75U_\infty$  in the direction of the flow), (d) Sectional streamline plot (reference frame moving at  $0.75U_\infty$ ), (e) Vorticity contour plot.

Figure 4.57 shows the results from a single PIV image of the flow with a plate of  $c/t = 7$  in the presence of a 6.5 % velocity perturbation applied at a frequency of 0.75 Hz ( $St_p = 0.212$ ) which corresponds to an ILEV mode of 2.5.

Figure 4.57 (a) shows the velocity vector field in a stationary frame of reference, with the longer vortex formation length behind the trailing edge being evident by the large region of low velocity fluid. From the sectional streamline plot (d) and the vorticity contour plot (e), it is clear there is no trailing edge vortex shedding in this case. This is because the clockwise rotating L vortex on the upper side of the plate adjacent to the trailing edge arrives at the trailing edge at a phase in the perturbation cycle of 180 degrees which interferes with vortex shedding at the trailing edge. With the phase of the perturbation cycle equal to 180 degrees, the perturbation velocity will increase in the downwards direction as the cycle continues, resulting in the reattached boundary layer fluid adjacent to the lower trailing edge corner being convected past the trailing edge and into the wake, without rolling up to form a T vortex.

If the phase of the perturbation cycle was 0 degrees (ie. 180 degrees different), then the reattached boundary layer fluid adjacent to the trailing edge on the lower side of the plate in figure 4.57 would be in the correct position for an anti-clockwise rotating T vortex to form. This is the case when the perturbation frequency is equal to a natural ILEV frequency; this could be achieved by either changing the perturbation frequency or the  $c/t$  ratio.

Figure 4.58 shows a full cycle of vortex shedding under the same flow conditions as for figure 4.57; it can be seen that L vortices are convected into the wake, where they interact to form an alternating vortex street. No T vortices are formed. The interaction of L vortices of opposite sign in the wake explains how Parker & Welsh (1983) measured vortex shedding in the wake for  $0.05 < St_p < 0.25$

$$\phi = 0^\circ$$

(for PIV images of 110,45 gridpoints)

c7r3f04.tcp : vorticity contour plot

$$\phi = 90^\circ$$

( )

(for PIV images of 110,45 gridpoints)

c7r3f25.tcp : vorticity contour plot

$$\phi = 170^\circ$$

(350)

(for PIV images of 110,45 gridpoints)

c7r3f26.tcp : vorticity contour plot

$$\phi = 285^\circ$$

(105)

(for PIV images of 110,45 gridpoints)

c7r3f03.tcp : vorticity contour plot

**Figure 4.58** Vorticity contour plots for a rectangular plate with  $c/t = 7$ ,  $Re = 490$ , 5% velocity perturbation,  $St_p = 0.212$ ; perturbation phase angle is indicated next to each plot.

Figure 4.59 compares two PIV images from plates with  $c/t = 7$ , both at a phase angle of 180 degrees in the perturbation cycle but with different perturbation frequencies. Clearly shown is how L vortices can interfere with the vortex shedding at the trailing edge. The top image has the perturbation frequency equal to the natural ILEV mode 2 ( $St_p = 0.172$ ). It shows a strong anti-clockwise rotating T vortex in the near wake, and the presence of reattached boundary layer fluid adjacent to the upper trailing edge corner which is about to be convected past the trailing edge to roll up and form a clockwise rotating T vortex. The other image is for a frequency corresponding to an ILEV mode of 2.5 ( $St_p = 0.212$ ) and shows no T vortices being formed. Instead of reattached boundary layer fluid being adjacent to the upper trailing edge corner when the phase of the perturbation cycle is 180 degrees, the fluid there is part of an L vortex which interferes with the formation of a T vortex.

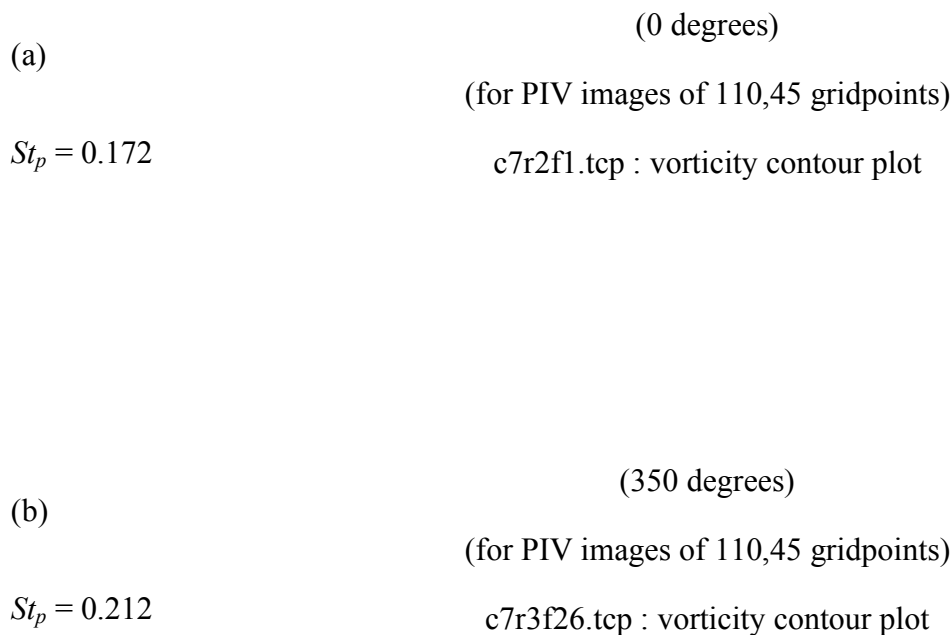


**Figure 4.59** Vorticity contour plots of flow about a rectangular plate with  $c/t = 7$  in the presence of transverse velocity perturbations showing the effect of changing perturbation frequency on trailing edge vortex shedding; perturbation phase angle for both plots is approximately 180 degrees.

The difference in the size of the region of low velocity fluid behind the trailing edge for the two images shown in figure 4.59 is illustrated by the contour plots of the  $U_x$  component of velocity shown in figure 4.60. In the absence of trailing edge vortex shedding, there is a much larger region of stagnant fluid behind the trailing edge, corresponding to a much greater vortex formation length.

- (a) (0 degrees - **actually 180**)  
 (for PIV images of 110,45 gridpoints)  
 $St_p = 0.172$  c7r2f1.tcp :  $U_x$  contour plot
- (b) (350 degrees)  
 (for PIV images of 110,45 gridpoints)  
 $St_p = 0.212$  c7r3f26.tcp :  $U_x$  contour plot

**Figure 4.60** Contour plots of  $U_x$  for flow about a rectangular plate with  $c/t = 7$ ,  $Re = 490$ , 5% velocity perturbation, perturbation phase angle = 180 degrees;  $St_p$  is indicated next to each plot.

Although the vortex formation length has not been measured directly here, figure 4.61 shows the difference in average  $U_x$  for the two cases and how this varies with distance from the trailing edge ( $x/t$ ) (after averaging over four images covering one shedding cycle).

Figure 4.61 and the contour plots of  $U_x$  shown in figure 4.60 clearly show that when there is regular shedding of T vortices at the trailing edge, the vortex formation length is significantly reduced. Perturbations applied at the natural ILEV frequency for the plate with  $c/t = 7$  of  $St_p = 0.172$  in the wind tunnel resulted in a large negative  $C_{pb}$ , a consequence of the strong trailing edge vortex shedding and correspondingly shorter vortex formation length that was

observed in the water tunnel. A much smaller negative  $Cp_b$  was measured in the wind tunnel when  $St_p = 0.212$ , which is consistent with the results from the water tunnel which showed no trailing edge vortex shedding and a correspondingly longer vortex formation length for perturbations applied at this frequency.

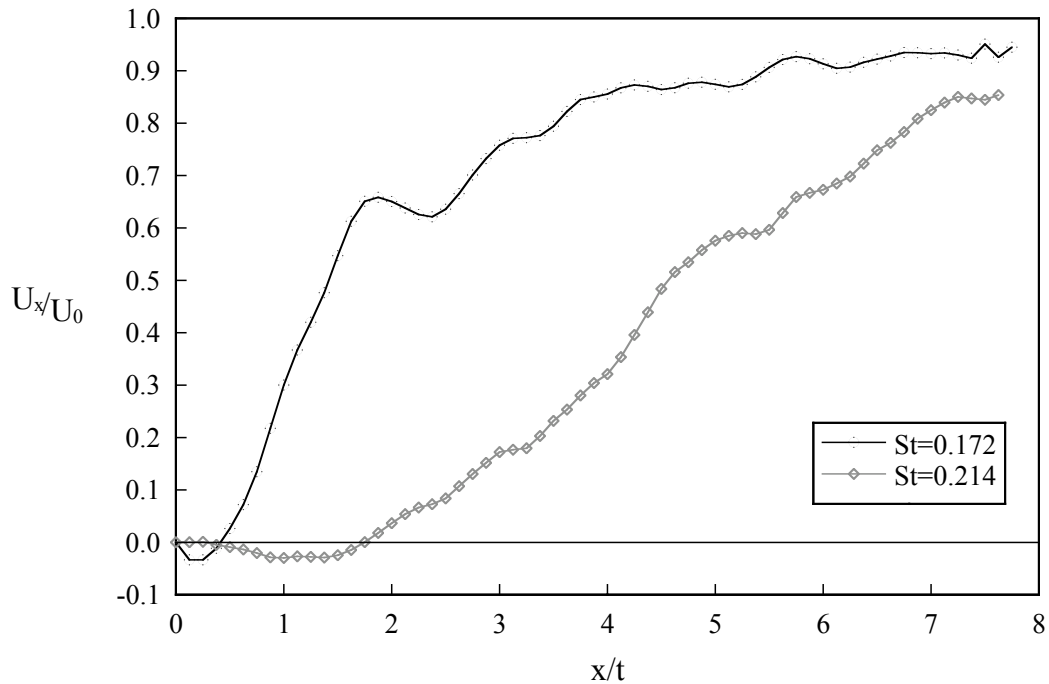


**Figure 4.61** Variation of average  $U_x$  component of velocity with normalised distance from the trailing edge ( $x/t$ ) for two different perturbation frequencies.

Flow visualisation images were taken of the flow over plates with  $c/t = 6$  and  $8$  when a 7% velocity perturbation was applied at frequencies corresponding to an ILEV mode of 2.5. in each case. Figure 4.62 shows an image for each plate in which the phase angle of the perturbation cycle is approximately 270 degrees. It can clearly be seen that there is no shedding of T vortices in either case, due to L vortices interfering with their formation by arriving at the trailing edge at the wrong phase of the perturbation cycle.

$c/t = 6$

Flow vis image -  $c/t=6$ ,  
 same phase angle as f27 above, but higher freq. with no t.e. shedd.  
 (Moving Reference Frame)  
 c6fv - f34

$c/t = 8$

Flow vis image -  $c/t=8$ ,  
 same phase angle as above, no t.e. shedd.  
 (Moving Reference Frame)  
 c8fv - f??

**Figure 4.62** Flow visualisation of flow about rectangular plates of different  $c/t$  ratios, with perturbations applied at frequencies corresponding to ILEV mode 2.5; image taken in reference frame moving with the vortices in the wake.

For the plate with  $c/t = 8$ , the frequency of perturbation corresponding to ILEV mode 2.5 is 0.685 Hz ( $St_p = 0.193$ ). This is within 1% of the natural vortex shedding frequency of the plate with  $c/t = 6$  corresponding to an ILEV mode of 2, and supports the vortex interaction hypothesis by showing that changing the plate length while keeping the perturbation frequency constant changes the time for L vortices to be convected from the leading edge to the trailing edge, and thus the phase in the perturbation cycle that L vortices arrive at the trailing edge.

Thompson *et al.* (1997) performed CFD simulations of the flow around long rectangular plates in the presence of periodic transverse velocity perturbations. Although the simulations were two dimensional and performed at  $Re = 400$ , they found a good qualitative agreement with the experimental results discussed in this chapter. The vorticity contour plots in figure

4.63 show the effect of changing perturbation frequency on the computed vortex shedding from a plate with  $c/t = 10$ , which appear similar to the PIV results shown in figure 4.59.

Thompson et al  
vorticity plots

(a)  $St_p = 0.16$

(b)  $St_p = 0.18$

(c)  $St_p = 0.20$

**Figure 4.63** Computed vorticity contour plots for the flow around a rectangular plate with  $c/t = 10$  in the presence of transverse velocity perturbations (from Thompson *et al.* 1997); Perturbation phase is 0 degrees.

For the three cases shown, vortex shedding was locked at both the leading and trailing edges, with the phase in the perturbation cycle being the same for each plot. The natural shedding  $St$  for this plate was found to be approximately 0.18, and when perturbations were applied at this frequency the highest base suction was observed. The other two vorticity plots are for  $St$  of 0.16 and 0.20. It can clearly be seen that L vortices arrive at the trailing edge at different phases in the perturbation cycle depending on  $St_p$ , and this affects the strength of T vortices that are shed. When  $St = 0.20$ , the T vortices formed are very weak and do not wrap around the base of the plate as they do for the other two cases resulting in much lower base suction.

Thompson et al. (1997) also observed a similar dependency of the calculated  $Cp_b$  on plate  $c/t$  ratio in the presence of transverse perturbations to that measured experimentally (see figure 4.38), as shown in figure 4.64. Comparing  $Cp_b$  for the two plates when  $St_p = 0.18$ , the plate with  $c/t = 10$  shows a maximum base suction. Increasing the  $c/t$  ratio to 13 while keeping  $St_p$  constant at 0.18 alters the phase in the perturbation cycle that L vortices pass the trailing edge, and the base suction is a local minimum due to much weaker shedding of T vortices.

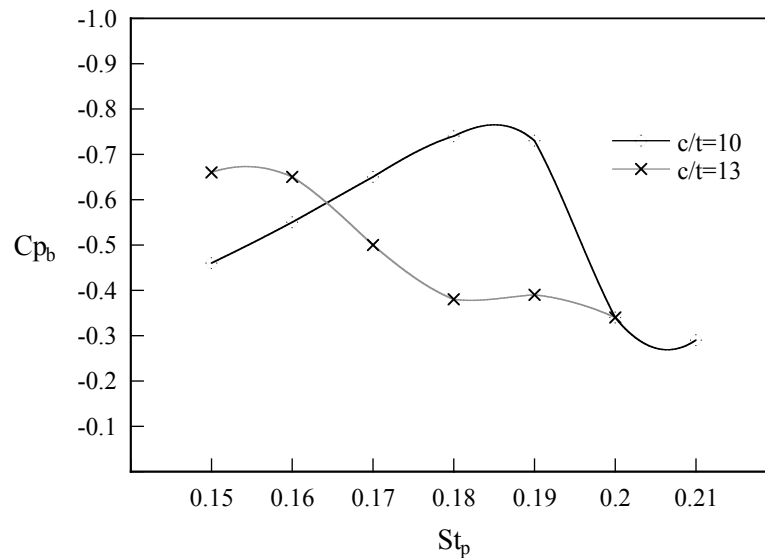


**Figure 4.64** Computed base pressure coefficient as a function of Strouhal number for different chord to thickness ratio plates (from Thompson *et al.* 1997).

### 4.2.3 Reconciling the experiments of Nakamura *et al.* (1991) and Stokes & Welsh (1986).

As discussed already in this chapter, vortex shedding from rectangular plates at low  $Re$  is characterised by the ILEV instability, where  $St_c = 0.6n$ . Figure 4.65 illustrates how vortex shedding is locked to the plate chord. Vortex shedding from the leading edge is periodic, and L vortices may take several shedding cycles to be convected past the trailing edge once shed from the leading edge separation bubble. Since the leading edge shedding responds to pressure pulses that are generated as L vortices pass the trailing edge, L vortices always pass the trailing edge at the same phase in the leading edge shedding cycle regardless of  $c/t$  ratio. Nakamura *et al.* (1991) showed that the convection velocity of L vortices along the sides of the plates is almost independent of the  $c/t$  ratio. Figure 4.65 also shows how the frequency of vortex shedding varies with plate  $c/t$  ratio so that L vortices take an integer number of leading edge shedding cycles to reach the trailing edge.

The ILEV instability is hydrodynamic in nature, meaning that the feedback pressure pulses travel upstream to control the leading edge shedding directly and almost instantaneously. As  $Re$  is increased above 2000, increased turbulence breaks down or overrides the feedback path, resulting in a loss of regular vortex shedding.

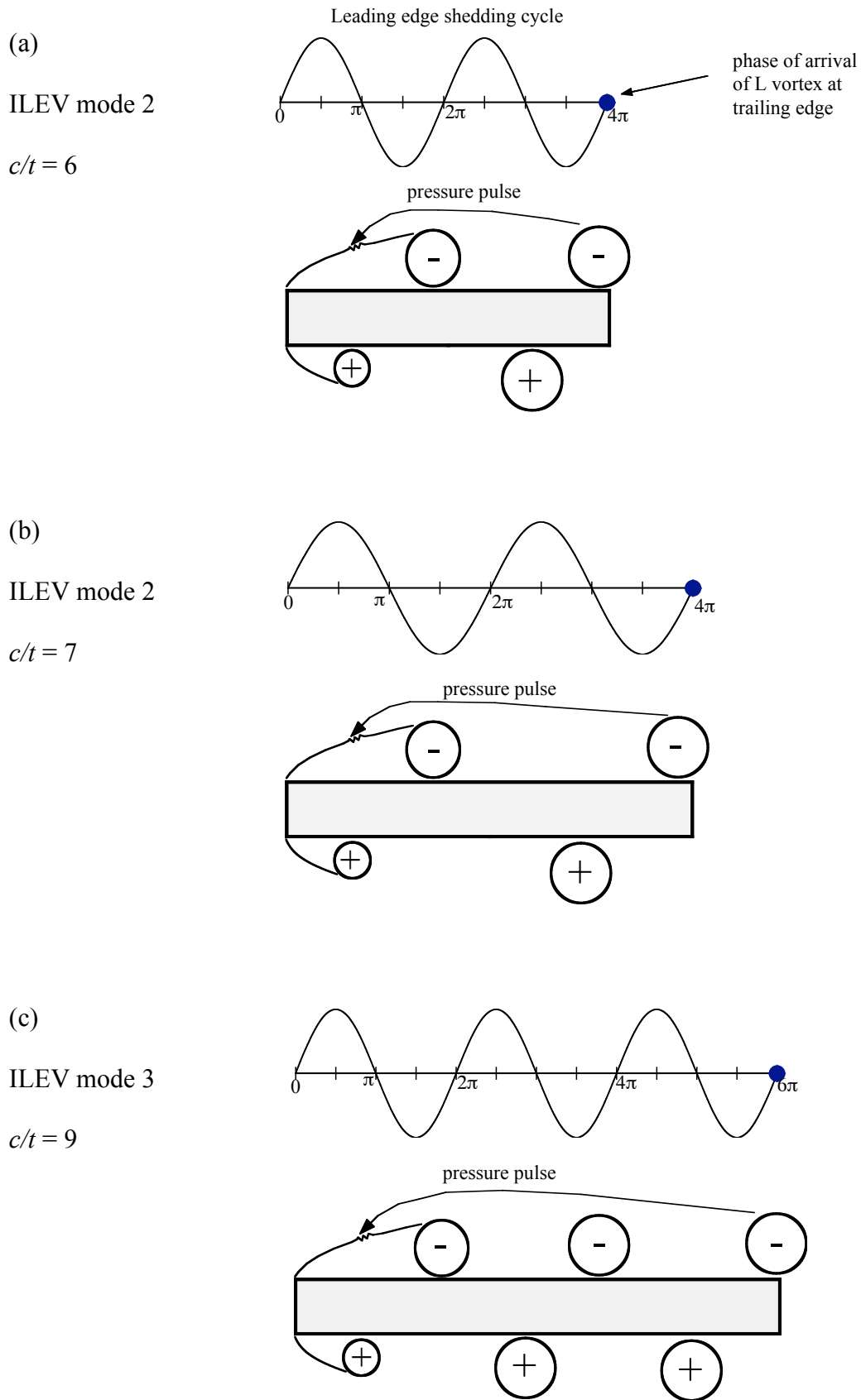


**Figure 4.65** Illustration of ILEV shedding mechanism, showing the effect on spacing between L vortices of changing plate  $c/t$  ratio. L vortices always pass the trailing edge at the same phase in the leading edge shedding cycle regardless of  $c/t$  ratio.

Despite there being no evidence of the ILEV instability occurring naturally for  $Re > 2000$ , Nakamura *et al.* (1991) suggested that for rectangular plates located centrally in a duct, the resonant peaks reported by Stokes & Welsh (1986) due to vortex shedding at  $Re > 10000$  were a result of the ILEV instability being excited. Nakamura *et al.* (1991) believed that this explained the similarity between the  $St$  of resonant peaks measured by Stokes & Welsh and the  $St$  corresponding to natural ILEV shedding frequencies (see figure 2.14, Chapter 2).

This is a different explanation to that offered by Stokes & Welsh. They showed that the pressure pulses that sustained the resonant transverse acoustic duct  $\beta$  mode were generated as an L vortex passed the trailing edge, but only if the phase of the acoustic cycle was such that the acoustic particle velocity was in the same direction as the particle velocity due to the pressure pulse. As shown in figure 4.66, the pressure pulses generated at the trailing edge are reflected off the duct walls before interacting with the leading edge shear layer. Leading edge shedding is controlled by the acoustic perturbations, and is locked to the frequency of the transverse duct mode with one L vortex being shed per acoustic cycle. As mentioned earlier, L vortices are always shed at the same phase in the acoustic cycle regardless of  $c/t$  ratio. Depending on the plate  $c/t$  ratio, they may take several acoustic cycles before they pass the trailing edge. Since the resonant acoustic cycle is only sustained when L vortices pass the trailing edge at a certain phase in the cycle, vortex shedding is locked to the plate  $c/t$  ratio in a similar manner to the natural ILEV shedding at low  $Re$ . This is illustrated in figure 4.67.

Although it may be possible for the ILEV instability to augment the feedback control of the resonant acoustic cycle on the leading edge vortex shedding, the ILEV instability by itself is not responsible for the resonant vortex shedding observed by Stokes & Welsh (1986). The similarity in  $St$  between the two seemingly unrelated experiments performed at different  $Re$  is due to the feedback pressure pulses being generated in each case as an L vortex passes the trailing edge, even though the feedback paths are different. In this way, L vortices always pass the trailing edge at the same phase in the leading edge shedding cycle for both cases, regardless of  $c/t$  ratio.

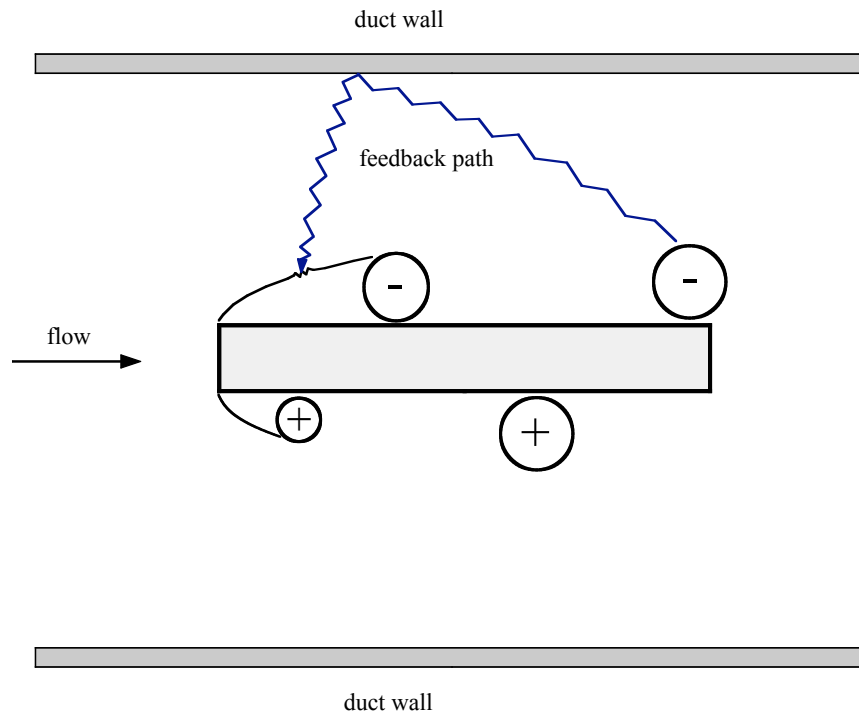


**Figure 4.66** Illustration of the feedback path from source at trailing edge, to the leading edge shear layer.

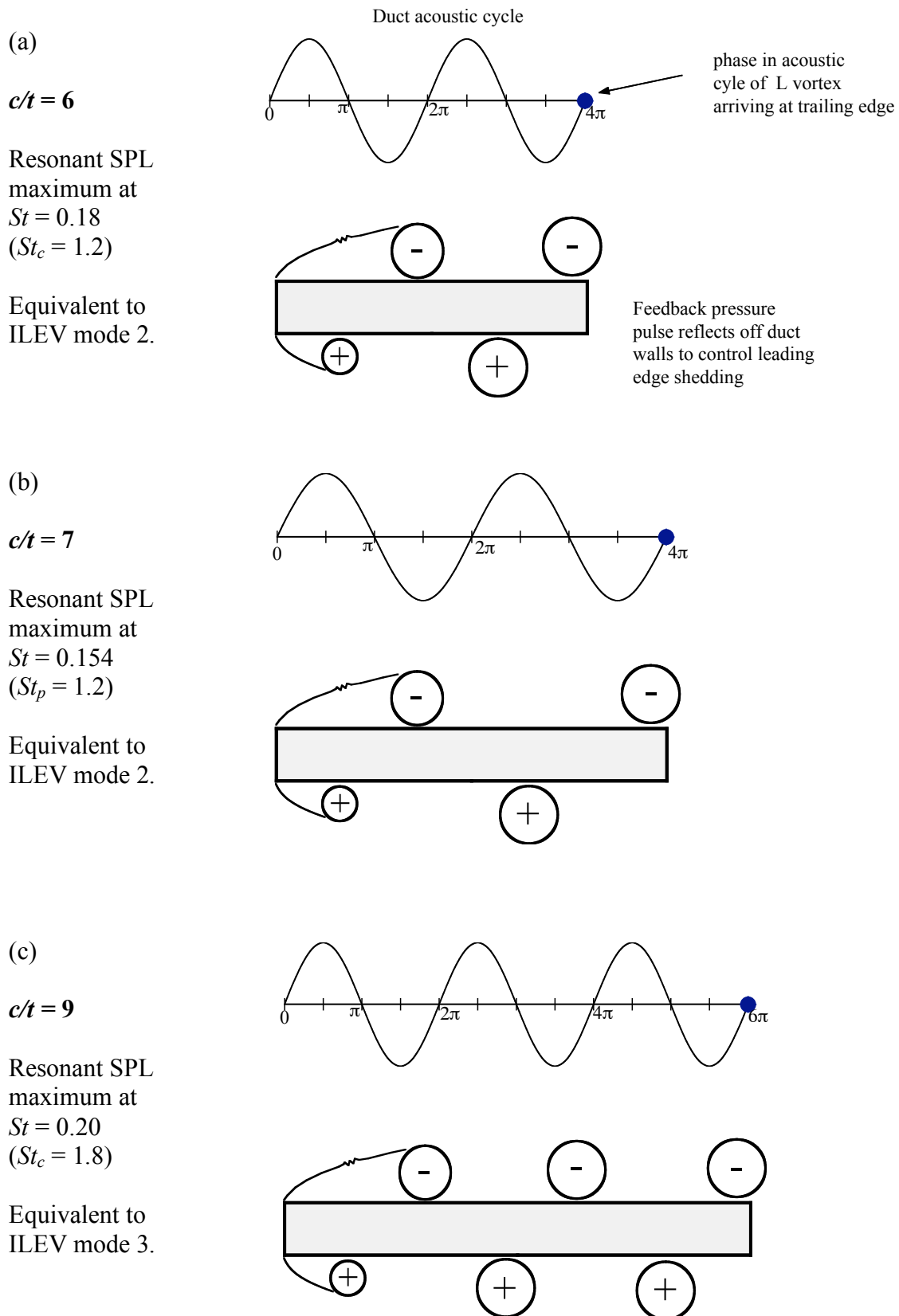


**Figure 4.67** Illustration of resonant shedding from rectangular plates located in a duct, showing the effect on spacing between L vortices of changing plate  $c/t$  ratio; L vortices always pass the trailing edge at the same phase in the acoustic resonance cycle regardless of  $c/t$  ratio.

#### 4.2.4 Similarity in vortex shedding $St$ for the three seemingly independent experiments

As shown earlier in this chapter (see figure 4.42), the results of this study show that when the  $St_p$  at which peaks in base suction occur are multiplied by plate chord they are similar to the  $St_c$  corresponding to the natural ILEV frequencies.

Peaks in base suction occur when strong trailing edge shedding is excited by the transverse velocity perturbations generated by loudspeakers located on either side of the rectangular plates. T vortices are shed when the perturbation frequency is equal to a natural, low  $Re$ , ILEV frequency. L vortices are convected at a constant velocity independent of  $c/t$  ratio. Thus, the phase in the perturbation cycle at which they pass the trailing edge depends on both the perturbation frequency and the  $c/t$  ratio. This is illustrated in figure 4.68 (a) where perturbations applied at a natural ILEV frequency for  $c/t = 6$  result in L vortices passing the upper trailing edge corner at 0 degrees in the perturbation cycle, thus allowing T vortices to form. Changing the perturbation frequency (4.68 (b)) changes the number of cycles it takes for an L vortex to be convected to the trailing edge. The L vortex now passes the trailing edge at a phase in the perturbation cycle of 180 degrees. At this phase for which it interferes with trailing edge shedding and no T vortices form. Figure 4.68 (c) illustrates the effect of applying perturbations at the same frequency as in figure 4.68 (b), but for a plate with a different  $c/t$  ratio. Now the L vortices take an extra half cycle before they pass the trailing edge, meaning that they pass the trailing edge at 0 degrees in the perturbation cycle. Thus, there is strong shedding of T vortices in figure 4.68 (c), as in figure 4.68 (a).

T vortices are shed when the perturbation frequency results in L vortices passing the trailing edge at the same critical phase in the perturbation cycle, for any  $c/t$  ratio. This occurs at the natural ILEV frequencies, although the occurrence of peaks in base suction when the perturbation frequency is equal to the natural ILEV frequency of a plate is not due to the ILEV instability being excited. As with the resonant shedding in the duct observed by Stokes & Welsh (1986), leading edge shedding is controlled by the transverse perturbations and not by any direct feedback in the form of pressure pulses from the trailing edge.

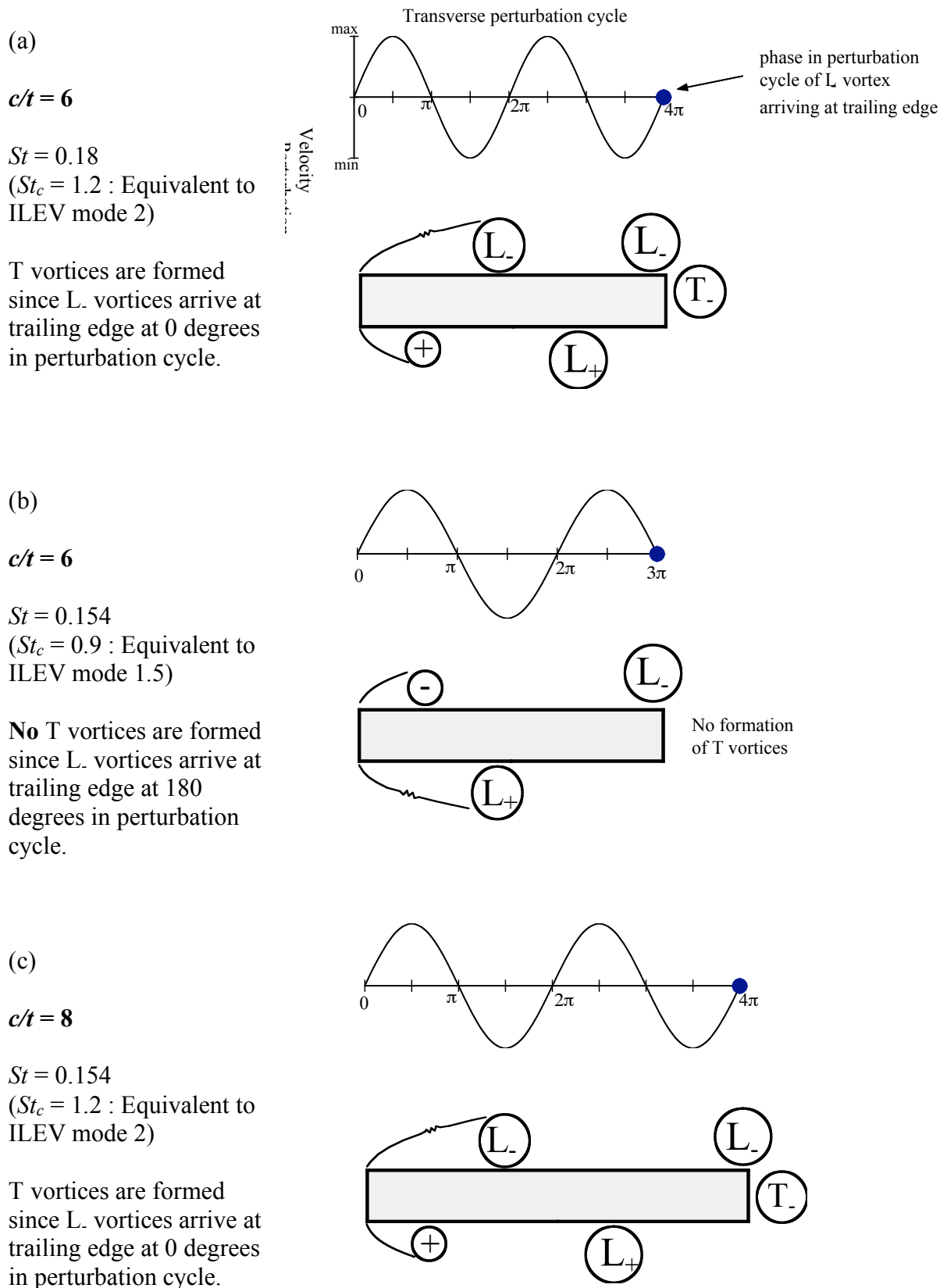


**Figure 4.68** Illustration of shedding from rectangular plates in the presence of transverse velocity perturbations, showing the effect on trailing edge shedding of changing the phase in the perturbation cycle that  $L$  vortices pass the trailing edge; Peaks in base suction occur when T vortices are shed, due to  $L$  vortices always pass the trailing edge at the same phase in the acoustic resonance cycle regardless of  $c/t$  ratio.

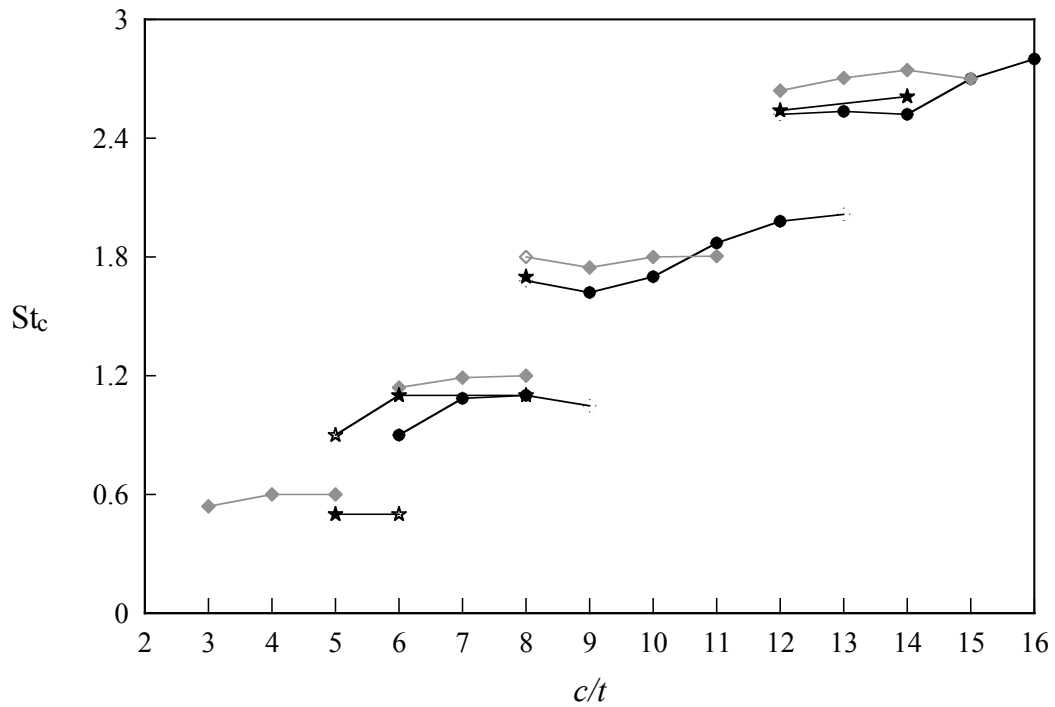


**Figure 4.69** Vortex shedding  $St_c$  for elongated rectangular plates; •  $St_p$  (based on plate chord) corresponding to peaks in  $Cp_b$  data (4.5% perturbation level), ◆  $St_c$  measured by Nakamura at  $Re = 1000$ , ★  $St$  measured by Stokes & Welsh (1986).

Although the mechanism controlling leading edge shedding for the three independent experiments of Nakamura *et al.* (1991), Stokes & Welsh (1986) and this study are different, the similarity in the  $St_c$  data shown in figure 4.69 for the three experiments is due to the dependency in each case of L vortices passing the trailing edge at the same critical phase in the leading edge vortex shedding cycle, regardless of  $c/t$  ratio.



## 5. Conclusions

### 5.1 Summary

The current study examines the effect of externally applied global flow perturbations on vortex shedding from elongated bluff bodies and the resulting effect on base suction ( $-Cp_b$ ). The major findings are summarised below.

#### 5.1.1 Plates without leading edge vortex shedding

##### 5.1.1.1 *Natural vortex shedding*

The base suction was measured for models with aerofoil leading edges and rectangular trailing edges. In the absence of any externally applied perturbations, the base suction was found to decrease slightly as the  $c/t$  ratio was increased. This is due to a thickening of the laminar boundary at separation, resulting in a wider wake and a lower vortex shedding  $St$ .

Flow visualisation and PIV measurements in the water tunnel showed that the natural vortex shedding has a strong streamwise component of vorticity, and as shown by Wu *et al.* (1993) is only weakly correlated across the span.

##### 5.1.1.2 *Effect of transverse velocity perturbations*

In another set of experiments finite amplitude transverse velocity perturbations were superimposed on the mean flow. As the perturbation frequency was increased the base suction remained almost constant before suddenly increasing to a maximum at a frequency just below the natural vortex shedding frequency ( $f_0$ ). The size of the peak in base suction was found to increase with increasing perturbation level, while the perturbation frequency at which the jump in base suction occurred was found to decrease with increasing perturbation level.

As the perturbation frequency was raised above  $f_0$ , the base suction was observed to recover to a value close to that found when no perturbations were applied.

A second small peak in base suction was found to occur when the perturbation frequency equalled  $2f_0$ , while another large peak was measured as the perturbation frequency approached  $3f_0$ . When the perturbation frequency was equal to  $3f_0$ , large scale vortex shedding was observed to occur at a frequency close to the natural shedding frequency ( $f_0$ ), a subharmonic of the perturbation frequency.

When perturbations were applied at a frequency close to  $f_0$ , flow visualisations showed that vortex shedding was phase-locked to the velocity perturbations at the frequency and perturbation level that resulted in a peak value of base suction. Particle Image Velocimetry (PIV) results showed that the increase in base suction coincides with increased circulation of the vortices shed from the trailing edge, and a reduction in vortex formation length. Another factor contributing to the higher base suction was the increase in spanwise correlation of vortex shedding when it was phase-locked.

Due to the absence of vortex shedding from the leading edge, the frequency at which peak values of base suction occurred showed only a weak dependence on  $c/t$  ratio. Vortex shedding at the trailing edge was found to be dependent on the state of the boundary layer at separation, as well as the frequency and amplitude of any applied transverse velocity perturbations.

### **5.1.2 Plates with rectangular leading edges**

#### **5.1.2.1 Natural vortex shedding**

Vortex shedding from elongated rectangular plates is characterised by the ILEV instability at low  $Re$  ( $Re < 2000$ ), as first reported by Nakamura *et al.* (1991). Vortices are shed at  $St_c = 0.6n$ , where  $n$  is an integer and is equal to the ILEV mode. The ILEV mode shows a strong dependence on  $c/t$  ratio, hence  $St_c$  increases in a stepwise manner as  $c/t$  ratio is increased.

PIV data from this study confirms the CFD results of Ohya *et al.* (1992) who found that vortex shedding occurred at both the leading and trailing edges at the natural ILEV frequency.

Similar complex vortex interactions were observed near the trailing edge between L and T vortices of like sign, which combined and were convected downstream in the wake.

Vortex shedding from the leading edge is regular, but controlled by pressure waves propagating upstream from the trailing edge that are generated as L vortices pass the trailing edge. Because of this, L vortices always pass the trailing edge at the same critical phase in the leading edge shedding cycle regardless of  $c/t$  ratio. Since the convection velocity of L vortices along the sides of the rectangular plates is relatively independent of  $c/t$  ratio (Nakamura *et al.* 1991), the requirement that L vortices pass the trailing edge at the same critical phase in the leading edge shedding cycle results in the vortex shedding frequency varying with  $c/t$  ratio.

For  $Re > 2000$ , the ILEV feedback mechanism is too weak to affect vortex shedding, the result being that no vortices are shed from plates with  $c/t \geq 7$  (Parker & Welsh 1983).

#### **5.1.2.2 Effect of transverse velocity perturbations**

Large changes in base suction were observed as the  $St_p$  was varied. Peak values of base suction were measured for all  $c/t$  ratios tested, however the  $St_p$  at which peak values occurred showed a strong dependence on  $c/t$  ratio. They occurred at  $St_p$  that closely matched the natural ILEV shedding  $St$  measured by Nakamura *et al.* (1991). This suggested that peaks in base suction occurred when L vortices passed the trailing edge at the same critical phase in the perturbation cycle, regardless of  $c/t$  ratio.

Parker & Welsh (1983) showed that transverse velocity perturbations can phase-lock leading edge vortex shedding over a wide range of frequencies, resulting in a vortex street being shed at the perturbation frequency. When leading edge shedding is phase-locked, L vortices are always shed at the same phase in the perturbation cycle regardless of  $c/t$  ratio or perturbation frequency. Smoke wire flow visualisation images from this study confirmed the findings of Nakamura *et al.* (1991) which showed that the convection velocity of vortices shed from the leading edge is not affected by the position of the trailing edge, and is therefore independent

of  $c/t$  ratio. Thus, the number of perturbation cycles for an L vortex to be convected to the trailing edge once shed from the leading edge separation bubble depends on only the perturbation frequency and the plate  $c/t$  ratio.

PIV measurements and flow visualisation showed that vortex shedding at the leading and trailing edges can be simultaneously phase-locked to transverse velocity perturbations when the perturbation  $St_p$  is close to a natural ILEV frequency. When this occurs, L vortices were found to always pass the trailing edge at the same critical phase in the perturbation cycle regardless of  $c/t$  ratio.

Applying perturbations at a  $St_p$  not equal to a natural ILEV frequency results in phase-locked vortex shedding from the leading edge, and a near wake with a frequency equal to the perturbation frequency. This is consistent with the findings of Parker & Welsh (1983). However, vortex shedding at the trailing edge is either very weak or non-existent. PIV results and flow visualisation showed trailing edge vortices did not form because L vortices arrive at the trailing edge at a phase in the perturbation cycle where they interfere with trailing edge shedding. T vortices are only shed when L vortices arrive at the trailing edge at a certain critical phase in the perturbation cycle. The frequencies that this occurs for different  $c/t$  ratios correspond to the natural ILEV frequencies.

Peaks in base suction occur when trailing edge shedding is excited by the transverse perturbations. The two dimensional CFD results of Thompson *et al.* (1997) confirm this finding. They also showed that the shedding of T vortices is highly dependent on the phase in the perturbation cycle at which L vortices pass the trailing edge.

### **5.1.2.3 Reconciling the experiments of Nakamura *et al.* (1991) and Stokes & Welsh (1986)**

For  $Re > 10000$ , Stokes & Welsh (1986) showed that vortex shedding from rectangular plates located centrally in a duct could generate loud resonant sound at the duct  $\beta$ -mode (a transverse mode) resonant frequency. The  $St$  at which maximum sound pressure level occurred for plates with different  $c/t$  ratios closely matched the ILEV frequencies measured

by Nakamura *et al.* (1991). Because of this, Nakamura *et al.* (1991) suggested that the vortex shedding observed by Stokes & Welsh (1986) was due to the ILEV instability being excited by the resonant sound in the duct. Stokes & Welsh (1986) showed that leading edge shedding was locked to the transverse velocity perturbations associated with the resonant acoustic field in the duct, clearly a different vortex shedding mechanism to the ILEV instability mechanism, which relies on pressure pulses being fed back upstream directly to the leading edge shear layer to control leading edge shedding. The reason for the similarity in  $St$  between the two experiments is due to the fact that the pressure pulses which control leading edge shedding in both cases are generated when  $L$  vortices pass the trailing edge, and therefore occur at the same critical phase in the leading edge shedding cycle.

#### ***5.1.2.4 Similarity in vortex shedding $St$ for three seemingly independent experiments***

Peaks in base suction occur when trailing edge shedding is excited by transverse velocity perturbations. As already mentioned, this is dependent on  $L$  vortices passing the trailing edge at a certain critical phase in the perturbation cycle and thus, the leading edge shedding cycle.

This is the reason for the similarity in the  $St$  vs  $c/t$  relationship for the three seemingly different sets of experiments of Nakamura *et al.* (1991), Stokes & Welsh (1986) and the current study.

## **5.2 Recommended future studies**

1. In the water tunnel, use PIV to investigate the effect on plates with aerofoil leading edges of varying perturbation level on the increased circulation of vortices in the wake that was measured when perturbations were applied at the frequency corresponding to maximum base suction.

2. Obtain pressure measurements from water tunnel models, to directly link wind tunnel measurements to PIV results.
3. Using hot film and pressure sensors in the water tunnel, investigate possibility of a phase jump between vortex shedding and the applied perturbations occurring at the same frequency at which the peak in base suction occur for plates with aerofoil leading edges.
4. Initial experiments showed that streamwise vorticity in the wake was reduced when vortex shedding was phase-locked to transverse velocity perturbations. Further work is needed to investigate the origin of streamwise vortex structures, and the influence of perturbations on them.
5. In the water tunnel, use PIV and flow visualisation to investigate the vortex shedding mechanism responsible for the large peak in base suction at three times the natural shedding frequency ( $3f_0$ ) for plates with aerofoil leading edges.
6. Using a hot wire in the wind tunnel and hot film in the water tunnel, measure vortex formation length in the presence of perturbations, for both aerofoil leading edge plates and rectangular plates. This could then be used to better correlate the base suction measurements from the wind tunnel to the PIV measurements from the water tunnel.
7. Fluctuating base pressure measurements would give another indication of the strength and frequency of trailing edge vortex shedding from rectangular plates in the wind tunnel.
8. Investigate the effect of multiple frequency perturbations  $f_1 + f_2 = f^*$ , to see which frequency is selected (if any) both at the leading edge, and in the wake.
9. Apply perturbations locally at the leading edge only and locking leading edge shedding to the perturbations; the effect on trailing edge shedding of varying leading edge shedding frequency could be investigated without having a global perturbation field affecting trailing edge shedding. The same could be done to investigate the effect of changing

---

trailing edge perturbation frequency on the leading edge shedding by applying perturbations locally at the trailing edge only.



## 6. Bibliography

1. Adrian R.J. 1991. Particle-imaging techniques for experimental fluid mechanics. *Ann. Rev. Fluid Mech.* **23**, 261-304.
2. Batchelor G.K. & Townsend A.A. 1945. Singing corner vanes: A note on a peculiar double resonant sustained oscillation occurring in a wind tunnel. *C.S.I.R. Division of Aerodynamics*, Note 62.
3. Bearman P.W. 1965. Investigation of the flow behind a two-dimensional model with a blunt trailing edge and fitted with splitter plates. *J. Fluid Mech.*, **21**, 241-255.
4. Bearman P.W. 1967. On vortex street wakes. *J. Fluid Mech.*, 28 part 4, 625-641.
5. Bearman P.W. 1967b. The effect of base bleed on the flow behind a two-dimensional model with a blunt trailing edge. *Aeronautical Quarterly*, **18**, 207-224.
6. Bearman P.W. 1971. An investigation of the forces on flat plates normal to a turbulent flow. *J. Fluid Mech.*, **46** part 1, 177-198.
7. Bearman P.W. 1984. Vortex shedding from oscillating bluff bodies. *Ann. Rev. Fluid Mech.*, **16**, 195-222
8. Bearman P.W. & Luo S.C. 1988. Investigation of the aerodynamic instability of a square-section cylinder by forced oscillation. *J. Fluids and Structures*, **2**, 161-176.
9. Bearman P.W. & Obasaju E.D. 1982. An experimental study of pressure fluctuations on fixed and oscillating square-section cylinders. *J. Fluid Mech.*, **119**, 297-321
10. Bearman P.W. & Trueman D.M. 1971. An investigation into the flow around rectangular cylinders. *Aeronautical Quarterly*, **23**, 229-237.
11. Bernard H. 1912. Formation de centres de giration a l'arriere d'un obstacle en mouvement. *C.R. Hebd Seances Acad. Sci.* **147**, 49-59.
12. Blevins R.D. 1985. The effect of sound on vortex shedding from cylinders. *J. Fluid Mech.* **161**, 217-237.
13. Briggs R.J. 1964. Electron stream interaction with plasmas. Research Monograph No 29, Cambridge, Mass., MIT Press.
14. Bull M.K., Li Y. & Pickles J.M. 1995. Effects of boundary layer transition on vortex shedding from thick plates with faired leading edge and square trailing edge. *Proc. 12th Australasian Fluid Mech. Conf.*, 231-234.
15. Cherry N.J., Hillier R. & Latour M.E.M.P. 1984. Unsteady Measurements in a Separated and Reattaching Flow, *J. Fluid Mech.*, **144**, 13-46.
16. Cooper P.I., Sheridan J.C. & Flood G.J. 1986. The effects of sound on forced convection over a flat plate. *Int. J. Heat & Fluid Flow*, **7** part 1, 61-68.

17. Corke T., Koga D., Drubka R. & Nagib H. 1977. A new technique for introducing controlled sheets of smoke streaklines in wind tunnels. *ICIASF '77 Record*, 74-80.
18. Davies M.E. 1976. A comparison of the wake structure of a stationary and oscillating bluff body, using a conditional averaging technique. *J. Fluid Mech.* **75** part 2, 209-231.
19. DeMeis R. 1986. Sounding a happy note for lift. *Aerospace America*, August, 10-11.
20. Deniz S. & Staubli T. 1997. Oscillating rectangular and octagonal profiles: interaction of leading and trailing edge vortex formation. *J. Fluids Structures*, **11**, 3-31.
21. Fage A. & Johansen F.C. 1927. On the flow of air behind an inclined flat plate of infinite span. *ARC R&M*, No. 1104.
22. Gartshore I.S. 1973. The effects of freestream turbulence on the drag of rectangular two dimensional prisms. *The University of Western Ontario, Canada*. **BLWT-4-73**.
23. Grant I. 1997. Particle image velocimetry: a review. *Proc. Inst. Mech. Eng.*, **211** Part C, 55-76.
24. Greenway M.E. & Wood C.J. 1973. The effect of a bevelled trailing edge on vortex shedding and vibration. *J. Fluid Mech.*, **61**, 323-335.
25. Griffin O.M. & Hall M.S. 1991. Review-Vortex shedding lock on and flow control in bluff body wakes. *ASME J. Fluids Eng.* **113**, 526-537.
26. Griffin O.M. & Ramberg S.E. 1975. On vortex strength and drag in bluff-body wakes. *J. Fluid Mech.* **69** part 4, 721-728
27. Hasan M.A.Z. 1992. The flow over a backward facing step under controlled perturbation: laminar separation. *J. Fluid Mech.*, **238**, 73-96.
28. Hillier R. & Cherry N.J. 1981. The effects of stream turbulence on separation bubbles. *J. Wind Eng. & Ind. Aero.*, **8**, 49-58.
29. Ho C.M. & Huang L.S. 1982. Subharmonics and vortex merging in mixing layers. *J. Fluid Mech.*, **119**, 443-473.
30. Ho C.M. & Huerre P. 1984. Perturbed free shear layers, *Ann. Rev. Fluid Mech.*, **16**, 365-424.
31. Ho C.M. & Nosseir N.S. 1981. Dynamics of an impinging jet. Part 1. The feedback phenomenon. *J. Fluid Mech.*, **105**, 119-142.
32. Hourigan K., Mills R.H., Thompson M.C., Sheridan J., Dilin P. & Welsh M.C. 1993. Base pressure coefficients for flows around rectangular plates. *J. Wind Eng. & Ind. Aero.*, **49**, 311-318.
33. Huerre P. & Monkewitz P.A. 1990. Local and global instabilities in spatially developing flows. *Ann. Rev. Fluid Mec.*, **22**, 473-537.

34. Johnson C.O. & Loehrke R.I. 1984. An experimental investigation of wake edge tones. *American Institute of Astronautics and Aeronautics Journal*, **22**, 1249-1253.
35. von Kármán T. & Rubach H. 1912. Über den Mechanismus des Flüssigkeits- und Luftwiderstandes. *Phys. Z.*, **13** part 2, 49-59.
36. Karniadakis G. E. M. & Triantafyllou G.S. 1989. Frequency selection and asymptotic states in laminar wakes. *J. Fluid Mech.*, **199**, 441-469.
37. Khor M. 1996 The character of the near-wake instability of the circular cylinder. *PhD Thesis*, Monash University, Melbourne, Australia.
38. Kiya M. & Sasaki K. 1983. Structure of a turbulent separation bubble. *J. Fluid Mech.*, **137**, 83-113.
39. Knisely C., Matsumoto M. & Menacher F. 1986. Rectangular cylinders in flows with harmonic perturbations. *J. Hydraulic Eng.*, **112** No 8., 690-704.
40. Leconte J. 1858. On the influence of musical sounds on the flame of a jet of coal gas. *Phil. Mag.* **15**, 235-239.
41. Lotfy A. & Rockwell D. 1993. The near wake of an oscillating trailing edge: mechanisms of periodic and aperiodic response. *J. Fluid Mech.*, **251**, 173-201.
42. Merati P. & Adrian R.J. 1992. Feedback amplification of a plane shear layer by impingement on a downstream body. *J. Fluids Struct.* **6**, 415-436.
43. Michel U. & Froebel E. 1988. Lower limit for the velocity fluctuation level in wind tunnels. *Experiments in Fluids*, **6**, 45-54.
44. Moffat R.J. 1988. Describing the uncertainties in experimental results. *Exp. Therm. and Fluid Sci.*, **1**, 3-17.
45. Monkewitz P.A. 1988. The absolute and convective nature of instability in two dimensional wakes at low Reynolds number. *Physics of Fluids*, **31** part 5, 999-1006.
46. Monkewitz P.A. & Nguyen L.N. 1987. Absolute instability in the near wake of two-dimensional bluff bodies. *J. Fluids Struct.* **1**, 165-184.
47. Morton B.R. 1984. The generation and decay of vorticity. *Geophys. Astrophys. Fluid Dynamics*. **28**, 277-308.
48. Nakaguchi H., Hashimoto K. & Muto S. 1968. An experimental study on aerodynamic drag of rectangular cylinders. *Journal of the Japan Society of Aeronautical and Space Sciences*, **16**, 1-5.
49. Nakamura Y. & Nakashima M. 1986. Vortex excitation of prisms with elongated rectangular, H and T cross-sections. *J. Fluid Mech.*, **163**, 149-169.

50. Nakamura Y. & Hirata K. 1989. Critical geometry of oscillating bluff bodies. *J. Fluid Mech.*, **208**, 375-393.
51. Nakamura Y. & Hirata K. 1991. Pressure fluctuations on oscillating rectangular cylinders with the long side normal to the flow. *J. Fluids Structures*, **5**, 165-183.
52. Nakamura Y., Ohya Y. & Tsuruta H. 1991. Experiments on vortex shedding from flat plates with square leading and trailing edges. *J. Fluid Mech.*, **222**, 437-447.
53. Nakamura Y. 1996. Vortex shedding from bluff bodies with splitter plates. *J. Fluids Structures*, **10**, 147-158.
54. Naudascher E. & Rockwell D. 1994. Flow induced vibrations- An engineering guide. *A.A.Balkema: Rotterdam: Brookfield*.
55. Nguyen D.T. 1990. Gate vibrations due to unstable flow separation. *ASCE Journal Hydraulic Eng.*, **116** part 3, 342-361.
56. Norberg C. 1993. Flow around rectangular cylinders: Pressure forces and wake frequencies. *J. Wind Eng. and Ind. Aero.*, **49**, 187-196.
57. Ohya Y., Nakamura Y., Ozono S., Tsuruta H. & Nakayama R. 1992. A numerical study of vortex shedding from flat plates. *J. Fluid Mech.*, **236**, 445-460.
58. Ongoren A. & Rockwell D. 1988. Flow structure from an oscillating cylinder Part 1. Mechanism of phase shift and recovery in the near wake. *J. Fluid Mech.*, **191**, 197-223.
59. Ota T., Asano Y. & Okawa J. 1981. Reattachment length and transition of the separated flow over blunt flat plates. *Bull. JSME*, **24**(192), 941-947.
60. Parker R. 1966. Resonance effects in wake shedding from parallel plates: some experimental observations. *J. Sound Vib.*, **4** part 1, 62-72.
61. Parker R. 1967. Resonance in wake shedding from parallel plates: calculation of resonant frequencies. *J. Sound Vib.*, **5**, 332-343.
62. Parker R. & Welsh M.C. 1983. Effects of sound on flow separation from blunt flat plates. *Int. Journal Heat and Fluid Flow*, **4** part 2, 113-128.
63. Pickles J.M., Bull M.K. & Li Y. 1992. Effects of boundary layer transition on vortex shedding from thick plates with faired leading edge and square trailing edge. *Proc. 11th Australasian Fluid Mech. Conf.*, 31-34.
64. Ram H.S.G. & Arakeri V.H. 1990. Studies on unsteady pressure fields in the region of separating and reattaching flows. *ASME Journal Fluids Eng.*, **112**, 402-408.
65. Richardson P.D. 1967. Effects of sound and vibration on heat transfer. *Appl. Mech. Rev.*, **20**, 201-217.
66. Rockwell D. 1990. Active control of globally unstable separated flows. *ASME Symposium on Non-steady Fluid Dynamics*. FED-Vol **92**, 379-394.

67. Rockwell, D. & Naudascher, E. 1978. Review- self sustaining oscillations of flow past cavities, *ASME Journal Fluids Eng.*, **100**, 152-165.
68. Rockwell, D. & Naudascher, E. 1979. Self-sustained oscillations of impinging free shear layers. *Ann. Rev. Fluid Mech.*, **11**, 67-94.
69. Rockwell D., Magness C., Towfighi J., Akin O. & Corcoran T. 1993. High image-density particle image velocimetry using laser scanning techniques. *Exp. Fluids*, **14**, 181-192.
70. Roshko A. 1955. On the wake and drag of bluff bodies. *J. Aero. Sci.*, **22**, 124-132.
71. Sasaki K. & Kiya M. 1991. Three dimensional vortex structure in a leading edge separation bubble at moderate Reynolds numbers. *ASME J. Fluids Eng.*, **113**, 405-410.
72. Saathoff P.J. & Melbourne W.H. 1989. The generation of peak pressures in separated/reattaching flows. *J. Wind Eng. and Ind. Aero.*, **32**, 121-134.
73. Saathoff P.J. & Melbourne W.H. 1997. Effects of free-stream turbulence on surface pressure fluctuations in a separation bubble. *J. Fluid Mech.* **337**, 1-24.
74. Sigurdson L.W. & Roshko A. 1985. Controlled unsteady excitation of a reattaching flow. *AIAA Shear Flow Control Conference*, AIAA-85-0552.
75. Soria J. 1993. Particle Image Velocimetry, *Workshop on Laser Diagnostics in Fluid Mechanics and Combustion*, Melbourne, Australia, 5.1-5.18
76. Soria J. & Norton M.P. 1990. A study of the three term hot wire system equation and analog linearization based on it. *Exp. Thermal Fluid Sci.* **3**, 346-353.
77. Soria J. & Wu J. 1992. The character of the instability of the separated shear layer from a square leading edge flat plate. *Proc. 11th Australasian Fluid Mech. Conf.*, 391-394.
78. Stansby P.K. 1976. Base pressure of oscillating cylinders. *Proc. ASCE J. Eng. Mech.*, **102**, 591-600.
79. Stoneman S.A.T., Hourigan K., Stokes A.N. & Welsh M.C. 1988. Resonant sound caused by flow past two plates in tandem in a duct. *J. Fluid Mech.*, **192**, 455-484.
80. Stokes A.N. & Welsh M.C. 1986. Flow-resonant sound interaction in a duct containing a plate; Part II: Square leading edge. *J. Sound Vib.* **104**, 55-73.
81. Strouhal V. 1878. Uber eine besondere ort der tonne regung, *Ann. Phys. Chem.*, **5** part 10, 216-251.
82. Thompson M.C., Mills R., Sheridan J. & Hourigan K. 1995. Simulation of acoustically forced flows around long rectangular plates. *Proc. 12th Australasian Fluid Mech. Conf.*, 513-516.

83. Thompson M.C., Tan B.T. & Hourigan K. 1997. Simulation of perturbed flows past long blunt plates. *ASME Fluids Engineering Division Summer Meeting June 22-26, FEDSM97-3675*.
84. Vickery B.J. 1966. Fluctuating lift and drag on a long cylinder of square cross-section in a smooth and in a turbulent stream. *J. Fluid Mech.*, **25**, 481-494.
85. Wallis R.A. 1977. The F-series aerofoils for fan blade sections. *The Institute of Engineers Australia, Mech. Eng. Trans.*, 12-20.
86. Welsh M.C. & Gibson D.C. 1979. Interaction of induced sound with flow past a square leading edge plate in a duct. *J. Sound Vib.* **67**, 501-511.
87. Welsh M.C., Stokes A.N. & Parker R. 1984. Flow-resonant sound interaction in a duct containing a plate, Part I: Semi-circular leading edge. *J. Sound Vib.* **67**, 510-511.
88. Welsh M.C., Hourigan K., Welch L.W., Downie R.J., Thompson M.C. & Stokes A.N. 1990. Acoustics and Experimental Methods: The influence of sound on flow and heat transfer. *Exp. Thermal & Fluid Sci.* **3** part 1, 138-152.
89. Williamson C.H.K. 1989. Oblique and parallel modes of vortex shedding in the wake of a circular cylinder at low Reynolds numbers. *J. Fluid Mech.*, **206**, 579-627.
90. Williamson C.H.K. 1996. Vortex dynamics in the cylinder wake. *Ann. Rev. Fluid Mech.*, **28**, 477-539.
91. Wu J. 1994. Three dimensional vortex structures in the wake of a bluff body. *PhD Thesis*, Monash University, Melbourne, Australia.
92. Wu J., Soria J., Hourigan K., Welsh M.C. & Welch L.W. 1991. Flow-excited acoustic resonance in a duct: The feedback mechanism. *5th International Conference on Flow Induced Vibration, Brighton, U.K.*, 21-23 May, 1991.
93. Wu J., Sheridan J., Soria J., Welsh M.C. & Hourigan K. 1993. Experimental investigation of vortex shedding from a plate: effect of external velocity perturbation. *J. Wind Eng. and Ind. Aero.* **49**, 401-410.

# Appendix 1.

## Calculation of the uncertainties in the experimental quantities

When an equation describing a result is a pure product such as equation A1.1, then the relative uncertainty can be found using equation A1.2 (Moffat 1988).

$$R = X_1^a X_2^b X_3^c \cdots X_M^m \quad (\text{A1.1.})$$

$$\frac{\delta R}{R} = \left\{ \left( a \frac{\delta X_1}{X_1} \right)^2 + \left( b \frac{\delta X_2}{X_2} \right)^2 + \cdots + \left( m \frac{\delta X_M}{X_M} \right)^2 \right\}^{1/2} \quad (\text{A1.2.})$$

When several independent variables are used in the function  $R$ , the individual terms are combined by a root-sum-squared method, as shown in equation A1.3 (Moffat 1988).

$$\delta R = \left\{ \sum_{i=1}^N \left( \frac{\partial R}{\partial X_i} \delta X_i \right)^2 \right\}^{1/2} \quad (\text{A1.3.})$$

### A1.1 Pressure Transducer

Surface pressures on wind tunnel models were measured using a Setra 239E pressure transducer, with a working range of -115 Pa to +130 Pa. The output voltage  $V_{pt}$  was directly proportional to the pressure difference across the pressure transducer ( $\Delta P_{pt}$ ). The transducer was calibrated against the height of a column of water measured using a Betz micro-manometer, which was connected in parallel to a manifold to generate the required pressures. The equation used to calculate the pressure difference measured by the Betz micro-manometer is:

$$\Delta P_{\text{Betz}} = \rho_{\text{H}_2\text{O}} g \Delta h \quad (\text{A1.4.})$$

where  $\rho_{\text{air}}$  is the density of air,  $\rho_{\text{H}_2\text{O}}$  is the density of water,  $g$  is the acceleration due to gravity and  $\Delta h$  is the height of the water column in the micro-manometer.

The uncertainty in the pressure measured by the Betz micro-manometer was:

$$\frac{\delta \Delta P_{\text{Betz}}}{\Delta P_{\text{Betz}}} = \left( \frac{\delta \rho_{\text{H}_2\text{O}}}{\rho_{\text{H}_2\text{O}}} + \frac{\delta g}{g} + \frac{\delta \Delta h}{\Delta h} \right) \quad (\text{A1.5.})$$

The Betz micro-manometer used in this study could resolve the water column height to within  $\pm 0.02$  mm;  $\delta(\Delta h) = 0.02$  mm. The following physical data were used in the calculations:  $\rho_{\text{H}_2\text{O}} = 998$  kg/m<sup>3</sup> and  $g = 9.81$  m/s<sup>2</sup>. The relative uncertainties  $\delta \rho_{\text{H}_2\text{O}}/\rho_{\text{H}_2\text{O}}$  and  $\delta g/g$  were all less than 1%. It was estimated conservatively that the effects of  $\delta \rho_{\text{H}_2\text{O}}/\rho_{\text{H}_2\text{O}}$  and  $\delta g/g$  would cause  $\delta \Delta P_{\text{Betz}}/\Delta P_{\text{Betz}}$  to increase by 0.5%, that is:

$$\frac{\delta \Delta P_{\text{Betz}}}{\Delta P_{\text{Betz}}} = \left( \frac{\delta \Delta h}{\Delta h} + 0.005 \right) \quad (\text{A1.6.})$$

The Betz micro-manometer was used to calibrate the Seta 239E pressure transducer, which was used both to measure the velocity in the wind tunnel using equation A1.7, and to measure the surface pressures on the experimental models. The wind tunnel velocity ranged from 6 m/s to 14 m/s. Table A.1.1 shows the uncertainties in the dynamic pressures that the Betz manometer could be expected to measure at both 6 m/s ( $P_{\text{dynamic}} = 21.65$  Pa) and 14 m/s ( $P_{\text{dynamic}} = 117.9$  Pa), where the dynamic pressure is given by equation A1.7, and  $\rho_{\text{air}} = 1.203$  kg/m<sup>3</sup>. The magnitude of the smallest base pressure coefficient was approximately 0.2, which was equal to a pressure drop of approximately 4.0 Pa when the flow velocity was 6 m/s, and a pressure drop of 12.0 Pa when the flow velocity was 10 m/s. The uncertainty for pressure readings of 4.0 Pa and 12.0 Pa on the Betz manometer are also shown in table A1.1.

$$P_{\text{dynamic}} = \frac{1}{2} \rho_{\text{air}} U_{\infty}^2 \quad (\text{A1.7.})$$

$\Delta h$ (mm)	$\Delta P_{\text{Betz}}$ (Pa)	$\delta(\Delta h)/\Delta h$ (%)	$\delta\Delta P_{\text{Betz}}/\Delta P_{\text{Betz}}$ (%)	$\delta\Delta P_{\text{Betz}}$ (Pa)
0.41	4.0	4.9	5.4	0.22
1.23	12.0	1.6	2.1	0.25
2.21	21.65	0.90	1.4	0.30
12.0	117.9	0.17	0.67	0.79

**Table A1.1** Pressure measurement using the Betz micro-manometer.

The Setra 239-E pressure transducer could resolve pressures to within  $\pm 0.5$  Pa, after calibration against the Betz micro-manometer. The graph shown in figure A1.1 shows the two worst case fit's from the calibration data for the Setra pressure transducer, along with the line of best fit.

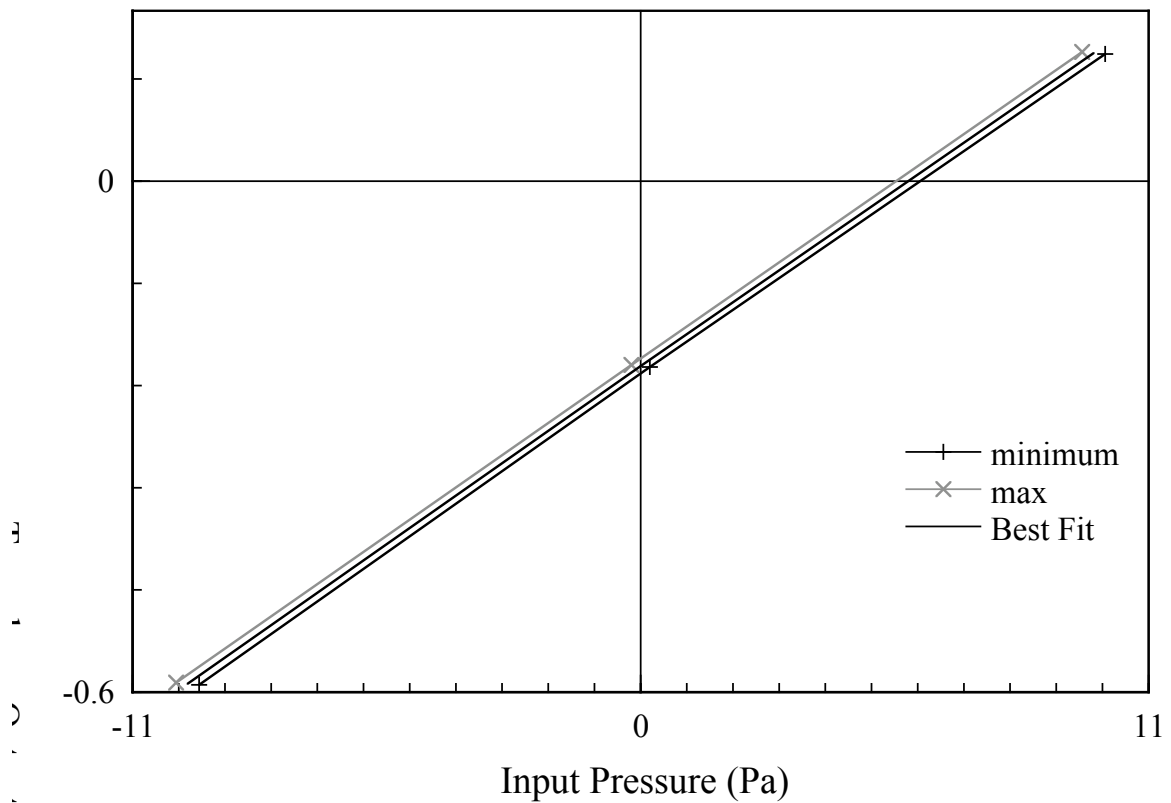


**Figure A1.1** The relationship between Setra pressure transducer output voltage, and input pressure measured with the Betz micro-manometer.

## A1.2 Wind Tunnel Flow Measurement

### A1.2.1 Pitot-static Tube

The flow speed in the wind tunnel was derived from the dynamic pressure measured with the pitot-static tube. The dynamic pressure is the difference between the total and static pressures, and was measured directly with a Setra 239E pressure transducer, and as the height of a water column with a Betz micro-manometer. The equation for the tunnel velocity is:

$$U_{ps} = \sqrt{\frac{2\Delta P_{Setra}}{\rho_{air}}} = \sqrt{\frac{2\rho_{H_2O} g\Delta h}{\rho_{air}}} = \sqrt{\frac{2\Delta P_{Betz}}{\rho_{air}}} \quad (A1.8.)$$

where  $\Delta P$  is the direct reading from the pressure transducer,  $\rho_{air}$  is the density of air,  $\rho_{H_2O}$  is the density of water,  $g$  is the acceleration due to gravity and  $\Delta h$  is the height of the water column in the micro-manometer.

$\delta\rho_{air}/\rho_{air} = 0.5\%$  (ie. for a standard atmosphere of 101.3 kPa, variation b/w 99.0 and 103.0 gave  $\delta P_{air} = \pm 2$  kPa, and an associated  $\delta\rho_{air} = \pm 0.006$  kg/m<sup>3</sup>).

The uncertainty in the flow speed measured with the pitot-static tube connected to the Setra 231-E pressure transducer was:

$$\frac{\delta U_{ps}}{U_{ps}} = \frac{1}{2} \left[ \left( \frac{\delta\Delta P_{Setra}}{\Delta P_{Setra}} \right)^2 + \left( \frac{\delta\rho_{air}}{\rho_{air}} \right)^2 \right]^{1/2} \quad (A1.9.)$$

where  $\delta\Delta P_{Setra} = 0.5$  Pa, and  $\delta\rho_{air}/\rho_{air} = 0.5\%$ .

Table A1.2 shows the uncertainty in the flow speed measured with the pitot-static tube, over the range of operating velocities used (6 m/s to 14 m/s).

$\Delta P_{Setra}$ (Pa)	$U_{ps}$ (m/s)	$\delta(\Delta P_{Setra})/\Delta P_{Setra}$ (%)	$\delta U_{ps} / U_{ps}$ (%)	$\delta U_{ps}$ (m/s)
-------------------------	----------------	---	------------------------------	-----------------------

21.65	6.0	2.3	1.2	0.07
60.15	10	0.8	0.49	0.05
117.9	14	0.4	0.32	0.04

**Table A1.2** Pitot-static tube measurements using the Setra pressure transducer.

### A1.2.2 Pressure Transducer Calibration

The difference between the static pressure measured by the four pressure tapings located inside the conical inlet and the static pressure inside the laboratory was directly proportional to the square of the velocity in the wind tunnel working section. A Setra 261-1 pressure transducer with a working range of -600Pa to 600 Pa was connected to all four pressure tapings in parallel to read the average pressure drop across the conical inlet. Since the voltage output from the transducer was directly proportional to the pressure drop across it, it was calibrated to automatically give the wind tunnel velocity.

Errors in the transducer output arise from the digitisation error during calibration, and from the error between the line of best fit through the calibration points and the velocity data from the pitot static tube pressure reading. The errors in the velocity measured with the pitot static tube have been calculated (see section A1.2.1), and were included in the error analysis.

Table A1.3 gives the calculated uncertainties in the velocity measured with the pressure transducer connected to the conical inlet. Figure A1.2 shows the relationship between the transducer output and the wind tunnel velocity. The curves representing the uncertainty limits are also shown in figure A1.2.

$U_{\infty}$ (m/s)	$\delta U_{\infty} / U_{\infty}$ (%)	$\delta U_{\infty}$ (m/s)
6.150	1.26	0.078

8.056	0.75	0.060
10.007	0.62	0.063
12.016	0.74	0.089
12.864	0.82	0.106

**Table A1.3** Velocity measurement error using the pressure transducer connected to the conical inlet of the open jet wind tunnel.

The equation of best fit for the calibration of the transducer to the tunnel velocity was

$$U_{\infty} = \sqrt{-128.6624 \times V_{\text{out}} + 323.5597} \quad (\text{A1.10.})$$

where  $U_{\infty}$  = tunnel speed (m/s), and  $V_{\text{out}}$  = transducer output (Volts).

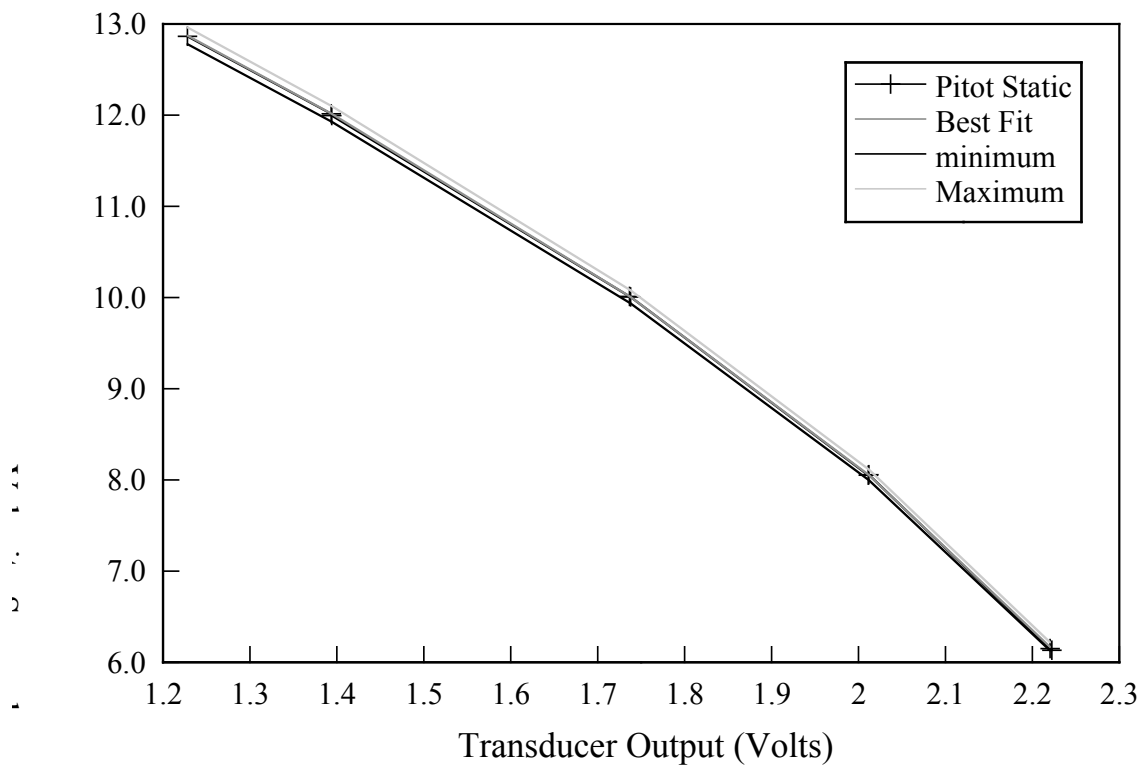


**Figure A1.2** The relationship between the pressure transducer output and the working section flow speed. The data from the pitot static tube used to calibrate the transducer is shown for comparison.

### A1.3 Model thickness measurements

The thickness of the plates used in all experiments was measured with a micrometer to an accuracy of  $\pm 0.01$  mm.

The thickness ( $t$ ) of all models used in the wind tunnel tests was 13.0 mm. They were machined using an N.C. milling machine to  $\pm 0.025$  mm. The maximum deviation in model thickness was 0.2% of  $t$ , showing the model thickness to be quite uniform along the entire span.

Models with four different thicknesses were used in the water tunnel experiments. The maximum deviation in  $t$  was  $\pm 0.1$  mm. The thinnest model used had a thickness of 10 mm, giving the largest deviation in model thickness to be 1%.

#### **A1.4 Sound Pressure Level Measurements**

The sound pressure level (SPL) in the working section of the wind tunnel was measured using a Brüel & Kjær 1/2 inch microphone, as described in chapter 3. The microphone was calibrated using a Brüel & Kjær pistonphone, and the standard error in the measured SPL after calibration will be  $\pm 0.39$ dB, or 4.3% (from Brüel & Kjær instruction manual for type 4133/34 microphone).

#### **A1.5 Hot-wire Anemometry Measurements**

The uncertainties associated with the hot-wire anemometer measurements have already been calculated by Khor (1996), for the same hotwire anemometer and same data acquisition system used in these experiments. The relative error associated with hot-wire velocity measurements was 6.2% (ie.  $\delta U/U = 6.2\%$ ). The error associated with measuring the auto-spectrum of each velocity time series was found to be 12.5%

#### **A1.6 Particle Image Velocimetry Measurements**

Several parameters affect the accuracy of results from the PIV system. Among these, are particle size, particle seeding concentration, light intensity, interrogation window resolution, interrogation window size, the local velocity gradient and interrogation grid spacing. Some of these have been already discussed in chapter 3.

### A1.6.1 Particle Slip Velocity

The velocity of the fluid is measured from the displacement of particle tracers. It is important to know how faithfully the particles follow the fluid motion. The particle slip velocity can be expressed as (Soria 1993):

$$\left(\frac{\Delta U}{U}\right)^2 = \left(\frac{\Delta \rho}{\rho}\right)^2 \frac{d_p^2 f}{10\nu} \quad (\text{A1.11.})$$

where  $d_p$  is the particle size,  $f$  is frequency and  $\Delta \rho$  is the difference in density between the particles and the fluid. In the present application,  $d_p < 40\mu\text{m}$ ,  $f < 2\text{Hz}$  and  $\Delta \rho/\rho < 0.1$ . The resultant slip velocity  $\Delta U/U < 0.2\%$ , which is negligible for any practical fluid velocity measurement.

### A1.6.2 Grid spacing

Choice of grid spacing can affect the scale of structures that can be resolved, as well as the accuracy of calculations of vorticity and circulation. In all cases, a 64x64 pixel interrogation window was used, with a 54% overlap ratio between adjacent gridpoints, giving a grid spacing of 30 pixels. In order to investigate the effect of halving the grid spacing (ie. doubling the resolution), an overlap of 77% was used giving a grid spacing of 14 pixels. Figure A1.3 shows a comparison between the velocity and vorticity fields for the two different overlap ratios used, calculated from the PIV image used in figure 4 with a perturbation phase of 240 degrees. Clearly the vortex structure forming from the upper trailing edge corner is not fully resolved when using the larger grid spacing. For the four large scale vortex structures in figure A1.3, peak vorticity was underestimated using the larger grid spacing by an average of 9%, while circulation differed by 5%.

Vector plot, using  
55% overlap

Vector plot, using  
80% overlap

Vorticity plot

Vorticity plot

(a)

(b)

**Figure A1.3** PIV velocity and vorticity fields calculated from the same image using different overlap ratios between adjacent gridpoints; (a) Overlap ratio = 55%, (b) Overlap ratio = 80%.

For all PIV results presented in chapter 4, a grid spacing of 30 pixels was used as this adequately resolved vortex structures the same size as the thickness of the plates used.

### A1.6.3 Overall accuracy

Using the same water tunnel, laser, seeding particles and using a 64x64 pixel interrogation window, Wu (1994) established that for a flow of uniform velocity, the maximum error in the magnitude of velocity vectors found was 5%  $U$  (where  $U$  is the actual flow velocity), with a  $1.0^\circ$  uncertainty in the orientation.

## A1.7 Derived Quantities

### A1.7.1 Reynolds Number

The Reynolds number for the wind tunnel experiments was calculated using the formula

$$Re = \frac{U_{\infty} t}{\nu_{air}} \quad (A1.12.)$$

The relative uncertainty in  $Re$  for this study was the sum of the relative errors in the free-stream velocity ( $U_{\infty}$ ), the model thickness( $t$ ), and the kinematic viscosity( $\nu_{air}$ ). These added up to approximately 5%;  $\delta Re/Re = 5\%$ .

### A1.7.2 Pressure Coefficient

Pressure coefficients were calculated from pressure readings from tappings in the wind tunnel models using the equation

$$C_p = \frac{\Delta P_{Setra}}{\frac{1}{2} \rho_{air} U_{\infty}^2} \quad (A1.13.)$$

The uncertainty in the pressure coefficient calculated was

$$\frac{\delta C_p}{C_p} = \left( \left( \frac{\delta \Delta P_{Setra}}{\Delta P_{Setra}} \right)^2 + \left( \frac{\delta \rho_{air}}{\rho_{air}} \right)^2 + 2 \left( \frac{\delta U_{\infty}}{U_{\infty}} \right)^2 \right)^{1/2} \quad (A1.14.)$$

with  $\delta \rho_{air}/\rho_{air} = 0.5\%$ .

Table A1.4 shows the uncertainty in the pressure coefficients measured at different flow speeds.

$U_{\infty}$ (m/s)	$\Delta P_{Setra}$	$C_p$ (non dimensional)	$\delta U_{\infty}/U_{\infty}$ (%)	$\delta \Delta P_{Setra}/\Delta P_{Setra}$	$\delta C_p/C_p$ (%)	$\delta C_p$
6.0	1.65	-0.2	1.25	2.3	2.434	0.0049
6.0	1.65	-0.5	1.25	2.3	2.434	0.0122
10.0	60.15	-0.2	0.62	0.8	1.438	0.0029

10.0	60.15	-0.5	0.62	0.8	1.438	0.0072
14.0	117.9	-0.2	1.0	0.4	1.703	0.0034
14.0	117.9	-0.5	1.0	0.4	1.703	0.0085

**Table A1.4** Pressure coefficient calculated using equation A1.13.

### A1.7.3 Perturbation Frequency

The perturbation frequency was measured to an accuracy of 0.05 Hz ( $\delta f_p = 0.05$  Hz). With the lowest frequency being 50 Hz, the greatest error in  $f$  was 0.1% ( $\delta f_p/f_p = 0.1\%$ ).

### A1.7.4 Perturbation Strouhal Number

The perturbation Strouhal number ( $St_p$ ) was calculated using the equation

$$St_p = \frac{f_p t}{U_\infty} \quad (\text{A1.15.})$$

where  $f_p$  = perturbation frequency,  $t$  = model thickness, and  $U_\infty$  = free stream velocity.

The uncertainty in  $St_p$  was found using the equation

$$\frac{\delta St_p}{St_p} = \left[ \left( \frac{\delta f_p}{f_p} \right)^2 + \left( \frac{\delta t}{t} \right)^2 + \left( \frac{\delta U_\infty}{U_\infty} \right)^2 \right]^{1/2} \quad (\text{A1.16.})$$

with  $\delta t/t = 0.2\%$  and  $\delta f_p/f_p = 0.1\%$ . Table A1.5 shows the uncertainty in  $St_p$  over the range of velocities and  $St_p$  used.

$U_\infty$ (m/s)	$St_p$	$\delta U_\infty/U_\infty$ (%)	$\delta(St_p)/St_p$ (%)	$\delta St_p$
6.0	0.1	2.3	2.31	0.0023
6.0	0.17	2.3	2.31	0.0039
6.0	0.25	2.3	2.31	0.0058

10.0	0.1	0.8	0.83	0.0008
10.0	0.17	0.8	0.83	0.0014
10.0	0.25	0.8	0.83	0.0021
14.0	0.1	0.4	0.46	0.0004
14.0	0.17	0.4	0.46	0.0008
14.0	0.25	0.4	0.46	0.0012

**Table A1.5** Calculation of errors in  $St_p$ .

### A1.8 Repeatability of pressure measurements

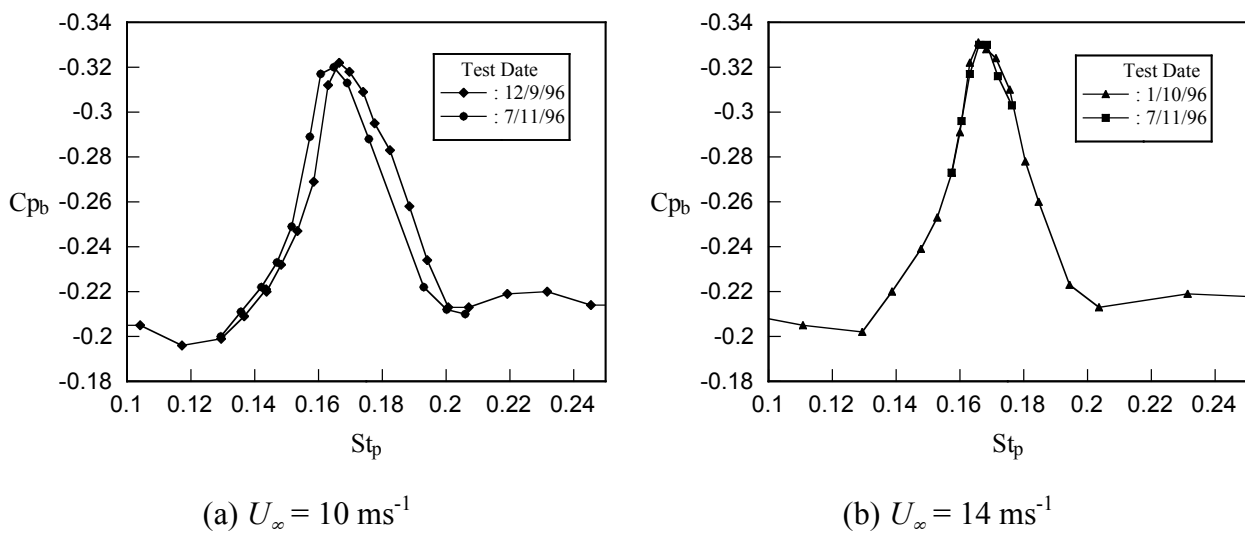


**Figure A1.4**  $Cp_b$  for a rectangular plate with  $c/t = 10$  and 3% velocity perturbation applied; measurements taken on different days to check repeatability of measurements, wind speed indicated below each graph.

Figure A1.4 shows graphically the results of checks made to ensure the repeatability of pressure measurements made in the wind tunnel with transverse velocity perturbations applied was acceptable. The error in the measurements shown in figure A1.4(b), when the wind speed was  $14 \text{ ms}^{-1}$ , is negligible. The difference in the results evident in figure A1.4(a) can be attributed to an error in  $St_p$  of approximately 3%; more than the error predicted in table A1.5, but within acceptable limits.



## **A2. Hello**

This page is blank, and is not to be included in the thesis.  
This is my slack way of increasing the heading number to A2.

## **Appendix 2.**

### **Publications arising from this study**

#### **A2.1 Refereed Conference Publications**

#### **A2.2 Refereed Journal Publications**

